2021

Wave and Tide Influence on Headland Bypassing and Shelf Scale Sand Transport

King, Erin Victoria

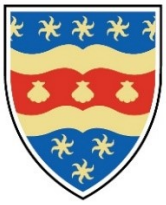

UNIVERSITY OF
PLYMOUTH

WAVE AND TIDE INFLUENCE ON HEADLAND BYPASSING AND SHELF SCALE SAND TRANSPORT

by

ERIN VICTORIA KING

A thesis submitted to the University of Plymouth
in partial fulfilment for the degree of

DOCTOR OF PHILOSOPHY

School of Biological and Marine Sciences

February 2021

Acknowledgements

I would like to thank my Director of Studies, Prof. Daniel Conley, for the opportunity to pursue this PhD, his guidance, belief, and continued support throughout my journey at the University of Plymouth. Thank you for your support achieving this.

I am also very grateful for the guidance and support of my wider supervisory team, Prof. Gerd Masselink and Dr. Nicoletta Leonardi. You have been a source of inspiration and support throughout this process. To my whole supervisory team, I am grateful for the opportunities for travel, learning, teaching and fieldwork that working with you has given.

To Jak McCarroll, your insights, discussions and advice have been especially valued over the last few years. Likewise, Tim Scott, and all who have shared insights and comments on the publications arising from this research. Thanks also to Kit Stokes for the modelling discussions, and the wider Coastal Processes Research Group team, especially those involved in the fieldwork without which the modelling in this study would not have been possible.

To my colleagues and friends in the postgrad community at Plymouth, thank you for your support and friendship: Maxine, Kat, Lewis, Nieves, Diego, Oli, Mark, Olivier and Marcus. Meeting you all has been a highlight of my experience in Plymouth.

Finally, to my friends and family, your support, encouragement and belief has been a cornerstone for me to rely on. To Madre, Jon and Christine, thank you for always sticking by, encouraging, and believing in me through this PhD and beyond.

Author's Declaration

At no time during the registration for the degree of Doctor of Philosophy has the author been registered for any other University award without prior agreement of the Doctoral College Quality Sub-Committee.

Work submitted for this research degree at the University of Plymouth has not formed part of any other degree either at the University of Plymouth or at another establishment.

The PhD supervisory team consisted of Prof. Daniel Conley (Director of Studies) and Prof. Gerd Masselink from the School of Biological and Marine Sciences, University of Plymouth, and Dr. Nicoletta Leonardi from the School of Environmental Sciences, University of Liverpool.

This research was in part funded by U.K. Natural Environment Research Council grant (NE/M004996/1; BLUE-coast project).

Relevant scientific seminars, project meetings and conferences were regularly attended throughout the duration of this thesis at which work was presented, and several papers were prepared for publication. These are listed below:

Refereed Journal Publications

King, E. V., Conley, D. C., Masselink, G., Leonardi, N., McCarroll, R. J., & Scott, T. (2019). The impact of waves and tides on residual sand transport on a sediment-poor, energetic, and macrotidal continental shelf. *Journal of Geophysical Research: Oceans*, 124, 4974 – 5002. https://doi.org/10.1029/2018JC014861

King, E. V., Conley, D. C., Masselink, G. & Leonardi, N. (2021). Predicting dominance of sand transport by waves, tides and their interactions on sandy continental shelves. *Journal of Geophysical Research: Oceans*, 126, e2021JC017200. https://doi.org/10.1029/2021JC017200

King, E. V., Conley, D. C., Masselink, G., Leonardi, N., McCarroll, R. J., Scott, T., & Valiente, N. G. (2021). Wave, Tide and Topographical Controls on Headland Sand Bypassing. *Journal of Geophysical Research: Oceans*, 126, e2020JC017053. https://doi.org/10.1029/2020JC017053

McCarroll, R. J., Masselink, G., Valiente, N. G., Scott, T., **King, E. V.** & Conley, D. (2018). Wave and Tidal Controls on Embayment Circulation and Headland Bypassing for an Exposed, Macrotidal Site. *Journal of Marine Science and Engineering*, 6(3), 94. https://doi.org/10.3390/jmse6030094

McCarroll, R. J., Masselink, G., Valiente, N. G., Wiggins, M., Scott, T., Conley, D. C. & **King, E. V.** (2020). Impact of a headland-associated sandbank on shoreline dynamics. *Geomorphology*, 355, 107065. https://doi.org/10.1016/j.geomorph.2020.107065

Stokes, C., Poate, T., Masselink, G., **King, E. V.**, Saulter, A. & Ely, N. (2021). Forecasting coastal overtopping at engineered and naturally defended coastlines. *Coastal Engineering*, 164, 103827. https://doi.org/10.1016/j.coastaleng.2020.103827

Valiente, N. G., Masselink., G., McCarroll, R. J., Scott, T., Conley, D. C. & **King, E. V.** (2020). Nearshore sediment pathways and potential sediment budgets in embayed settings over a multi-annual timescale. *Marine Geology*, 427, 106270. https://doi.org/10.1016/j.margeo.2020.106270

McCarroll, R. J., Masselink, G., Valiente, N. G., **King, E. V.**, Scott, T., Stokes, C. & Wiggins, M. (2021). An XBeach derived parametric expression for headland bypassing. *Coastal Engineering*, 103860. https://doi.org/10.1016/j.coastaleng.2021.103860

Conference Presentations

King, E. V., Conley, D. C., Masselink, G., Leonardi, N., McCarroll, R. J., Scott, T. & Valiente, N. G. (2020). Wave, Tide and Morphological Controls on Embayment Circulation and Headland Sand Bypassing. Conference: 2020 EGU General Assembly. Virtual Presentation. https://doi.org/10.5194/egusphere-egu2020-781

King, E. V., Conley, D. C., Masselink, G., Leonardi, N., McCarroll, R. J., Scott, T. & Valiente, N. G. (2020). Wave, Tide and Morphological Controls on Embayment Circulation and Headland Sand Bypassing. Conference: 2020 Young Coastal Scientists and Engineers Conference. Virtual Presentation.

King, E. V., Conley, D. C., Masselink, G., Leonardi, N., McCarroll, R. J., & Scott, T. (2019). The Impact of Waves and Tides on Residual Sand Transport on a Sediment-poor, Energetic and Macrotidal Continental Shelf. *Geophysical Research Abstracts*, 21, April 2019. Conference: 2019 EGU General Assembly. EGU2019-5535. Oral Presentation.

King, E. V., Conley, D. C., Masselink, G., Leonardi, N., McCarroll, R. J., & Scott, T. (2019). The Impact of Waves and Tides on Residual Sand Transport on a Sediment-poor, Energetic and Macrotidal Continental Shelf. February 2019, Conference: 2019 PlyMSEF Conference. Oral Presentation.

King, E. V., McCarroll, R. J., Conley, D. C., Leonardi, N. & Masselink, G. (2018). Modelling Wave and Tide Impacts on Sediment Transport and Morphology on an Exposed Macrotidal Coastline with Delft3D. February 2018, Conference: 2018 Ocean Science Meeting, Poster. https://doi.org/10.13140/RG.2.2.11098.03527

Valiente, N. G., McCarroll, R. J., Masselink, G., Scott, T., Conley, D. C. & **King, E. V.** (2019). Circulation and Sediment Fluxes on a Macrotidal, Exposed and Embayed Coastline. *Coastal Sediments 2019*, 539 – 552. https://doi.org/10.1142/9789811204487_0048

Valiente, N. G., Masselink, G., McCarroll, R. J., Saulter, A., Scott, T., Conley, D. C. & **King, E. V.** (2020). Modelling nearshore sediment fluxes in embayed settings over a multi-annual timescale. Conference: 2020 EGU General Assembly. Virtual Presentation. https://doi.org/10.5194/egusphere-egu2020-7875

McCarroll, R. J., Valiente, N. G., **King, E. V.**, Masselink, G., Scott, T. & Conley, D. (2018). The interaction of mega-rips and tidal regime as a mechanism for headland bypassing. Conference: 2018 Ocean Science Meeting. Presentation.

Grants Awarded

European Geosciences Union: Roland Schlich Early Career Scientist's Travel Support grant, 2020.

Plymouth Marine Science and Education Foundation: Travel Support Grant, 2020.

Word count of main body of thesis: 40 957

Signed……

Date……07/08/2021……

Abstract

Name: Erin Victoria King

Title: Wave and Tide Influence on Headland Bypassing and Shelf Scale Sand Transport

Waves and tidal currents resuspend and transport littoral and shelf sediments, and it is important to understand the processes impacting the net transport of sand, with implications for various topics including benthic habitats, marine operations, marine spatial planning, and long-term coastal change. Continental shelf areas comprise ~8% of global sea floor, and embayed beaches separated by rocky headlands represent 50% of global shorelines. These areas host a large proportion of global marine economic activity and recreation. Sandy sediments are potentially mobilised by wave-induced currents across > 40% of the earth's shelf. Mobilised sediments are susceptible to net transport by tidal residual currents and currents induced by wave asymmetry due to wave shoaling. Net sand transport pathways govern the transport and fate of littoral and shelf sand, influencing bedform morphology, contaminant dispersal, sediment distribution, and morphological evolution. Quantification of the potential for longshore bypassing of sand around headlands is necessary for evaluation of coastal sediment budgets and long-term coastal change. The processes driving net sand transport at shelf, regional and littoral scales, including headland bypassing, will form the focus of this thesis.

Shelf-scale assessments of the dominant drivers of sand transport often do not fully consider wave-tide interactions (WTI), due to the computationally intensive coupled numerical modelling required. WTI non-linearly enhance bed shear stress and apparent roughness due to interaction between the wave and current bottom boundary layers, change the current profile, and modulate wave forcing, The influence of WTI on headland bypassing is an area of ongoing research, and while bypassing rates have been shown to be predictable for idealised headlands, it remains to test the predictability of headland bypassing for realistic headland morphologies and sediment availability. In this thesis, it is shown that WTI can dominate net sand transport in mixed tide and wave energy conditions, the dominant forcing mode and potential magnitude of net sand transport are predictable from readily available data, and headland bypassing rates can be parameterised under wave-dominated conditions, depending upon headland cross-shore length, surf zone width, headland toe depth and spatial sediment coverage.

Sand transport in energetic macrotidal environments can be heavily influenced by waves. Median (50% exceedance) waves generally enhance net sand transport in the tidal direction, while extreme (1% exceedance) waves can dominate net sand transport, increasing it by an order of magnitude and potentially reversing transport direction. A novel continental shelf classification scheme is presented, based on wave, tide and WTI dominance of net sand transport. Here, "WTI" includes radiation stresses, stokes drift, enhanced bottom friction and bed shear stress, current and depth-induced wave refraction, Doppler shift and wave-blocking. Application of this

scheme to the macrotidal South West UK shelf shows WTI are a dominant or sub-dominant contributor to net sand transport under extreme waves and spring tides.

To enable application of this classification scheme to wider shelf areas in a computationally efficient way, a k-Nearest Neighbour (kNN) algorithm was trained on model data using readily available uncoupled wave and tide parameters, median grain size and water depth. The dominant mode and magnitude of net sand transport were predicted with 81.9% and 90.8% accuracy, respectively. This kNN classifier was applied to the Northwest European shelf over a synthetic, statistically representative year. The relative influence of waves, tides and WTI varies across the shelf, dependent upon variability in wave exposure, tidal regime, grain size and local bathymetry. Net sand transport in meso-macrotidal areas is tide-dominated, while shallow regions with finer sediments such as Dogger Bank and the German/ Denmark Shelf areas are wave-dominated. WTI dominate on the Netherlands (NL) Shelf and in deeper areas of the North and Celtic Seas. Observed sand wave morphologies on the NL Shelf vary significantly between dominant sand transport modes under extreme waves and spring tides (95% confidence level). Sand waves increase in length and asymmetry, and decrease in height, for increased wave dominance.

To examine the controls on headland sand bypassing, numerically modelled bypassing rates are quantified for 29 headlands along the macrotidal, wave-exposed North Coast of Cornwall under varied forcing conditions. Bypassing is wave-dominated under energetic (>5% exceedance) waves, with tides acting as a secondary control. WTI dominate bypassing for median waves. Non-uniform sediment coverage can reduce headland bypassing by several orders of magnitude when sand is unavailable at the headland toe. A primary control on bypassing is headland cross-shore length relative to surf zone width, whilst toe depth is an important secondary control. By adapting and developing an existing parameterisation, bypassing rates are predictable with a Mean Absolute Error of a factor of 4.6. Only two of the 29 headlands block headland bypassing along this coastline under all forcing conditions, indicating the potential ubiquity of headland bypassing on embayed coasts.

The findings of this thesis emphasise the critical need to consider wave-tide interactions when considering net sand transport in energetic environments globally, where previously tides alone or uncoupled waves may have been considered. The kNN approach applied here can efficiently indicate the dominant processes driving sand transport under a variety of conditions and across large spatial domains, of value to modellers in similar environments. This method will allow efficient inter-regional comparison and sensitivity testing to changing climate conditions. This work demonstrates headland bypassing is amenable to parameterisation in wave-dominated conditions. Such parametrisations of bypassing in realistic settings are entirely novel and the ability to predict bypassing within an order of magnitude is highly useful. This thesis highlights the extent to which headland bypassing occurs with implications for embayed coasts worldwide.

Contents

List of figures and captions

List of tables and captions

1 Introduction

1.1 Context and motivation

Continental shelf areas comprise ~8% of global sea floor, extending from the coastline to the shelf break marked by an increase of slope at a depth of typically ≲ 200m towards oceanic depths (IHO, 2008; Harris et al., 2014). This area hosts a large proportion of global marine economic activity, recreation, and is of increasing importance for marine renewable energy activities (Constanza et al., 1997; deHaas et al., 2002; Németh et al., 2003; Roetert et al., 2017; Cieślikiewicz et al., 2018; Cheng et al., 2020; Uncles et al., 2020). Sandy sediments are potentially mobilised by wave-induced currents over > 40% of the earth's shelf (Harris & Coleman, 1998), and it is important to understand the processes impacting their transport and deposition. The residual (net) transport of shelf sediments provides the regional context for coastal sediment transport. Embayed sandy beaches comprise ~ 50% of global shorelines (Short & Masselink, 1999). It is important to understand sand transport at coastal and shelf scales, including processes driving sediment exchange cross-shore between the beach and inner shelf, and longshore between embayments (e.g., van der Molen, 2002; Vieira da Silva et al., 2016, 2018; Thom et al., 2018; Wiggins et al., 2019; McCarroll et al., 2019, Under Review-a; Valiente et al., 2019a, b, 2020).

Net sand transport describes the net movement of sand driven by waves, wind and tidal currents (Stride, 1963; Pingree & Griffiths, 1979, 1980; Pattiaratchi & Collins, 1988; van der Molen, 2002). Net sand transport pathways govern the transport and fate of continental shelf sand, influencing bedform morphology, contaminant dispersal, and distribution of littoral and shelf sediments (Stride, 1963; Pingree & Griffiths, 1979; Pingree & Le Cann, 1989; Harris & Collins, 1991; van der Molen, 2002; Lewis et al., 2015; Cieślikiewicz et al., 2018; Leonardi & Plater, 2017; Luijendijk et al., 2017; Damen et al., 2018; Wang et al., 2019; Uncles et al., 2020). Tidal asymmetry resulting from non-linear tidal dynamics, in addition to interactions with variable bathymetry, coastal topography and bed friction, drives tidal residual currents relevant to transport of sediments in suspension (Pingree & Griffiths, 1979; Zimmermann, 1981; Leonardi et al., 2015; Leonardi & Plater, 2017). Wave action can resuspend shelf sediments, enabling transport by the residual tidal current, as well as transport due to currents induced by wave asymmetry resulting

from wave shoaling (Pattiaratchi & Collins, 1988; van der Molen, 2002; Thompson et al., 2019).

Across the continental shelf, variability in sediment characteristics, wave climate, tidal regime, bathymetry and coastal topography result in variable impacts of wave and tidal forcing on net sand transport (van der Molen, 2002; Porter-Smith et al., 2004; Harris et al., 2014; Aldridge et al., 2015; Bricheno et al., 2015). Variations between wave and tide-dominated sand transport impacts net sand transport direction (Pattiaratchi & Collins, 1988), sand wave morphology and migration (Van Dijk & Kleinhans, 2005; Campmans et al., 2018a,b; Damen et al., 2018), and benthic habitats (Harris, 2014). In mixed tide and wave energy environments, wave-tide interactions are important to consider. These interactions influence the benthic boundary layer and vertical current profile, non-linearly enhancing bed shear stress and apparent roughness (Kemp & Simmons, 1982, 1983; Olabarrieta et al., 2010; Tambroni et al., 2015).

Full assessment of wave and tidal drivers of net sand transport at the shelf scale including wave-tide interactions remains to be performed. Whilst the influence of wave-tide interactions on sand transport have been investigated in the laboratory (Kemp & Simmons, 1982, 1983; Olabarrieta et al., 2010), and through simplified modelling (Tambroni et al., 2015), regional and shelf-scale assessments of net sand transport often focus on wave and tidal forcing in an un-coupled form (Porter-Smith et al., 2004; Neill et al., 2010; Xing et al., 2012; van der Molen, 2014), or waves or tides are focussed on in isolation (e.g., Pingree and Griffiths, 1979; Leonardi & Plater, 2017). Given the non-linear enhancement of bed shear stress due to a thinner benthic boundary layer under combined waves and currents, enhanced resuspension from increased turbulence due to dissipation in the bottom wave boundary layer, wave-induced streaming in the bottom boundary layer, and non-linear peak orbital velocities, excluding wave-tide interactions may underestimate net sand transport in combined conditions (van Rijn et al., 2007).

The relative influence of wave-tide interactions across the continental shelf versus tides and wave alone remains to be quantified, including to assess the spatial and temporal variability of wave-tide interaction processes across the continental shelf resulting from differences in tidal regime, wave climate and bathymetry. Such an assessment could benefit numerical modelling efforts in different shelf areas,

revealing the dominant forces that need to be included to accurately and efficiently simulate sediment transport. It is also of potential benefit to inform where it is suitable to apply models or parameterisations of a process which assume dominance of waves or tides, such as models of headland bypassing (McCarroll et al., 2021b) or tide-dominated sand wave evolution (Besio et al., 2007). Chapter 2 examines the impact of waves, tides and their interactions on net sand transport, including a more in-depth review of the current literature (Section 2.1) and a detailed overview of wave-tide interactions as considered in this thesis (Section 2.3.2), while a more in depth review of shelf scale assessments can be found in Section 3.1.

Net sand transport in the alongshore, around headlands, is known as headland bypassing (Evans, 1943). Headland bypassing is an important component of the littoral cell sediment budget influencing sediment supply, morphological evolution, long term coastal change and subsequent management of the coastal zone (Goodwin et al., 2013; Duarte et al., 2014; Vieira da Silva et al., 2016, 2018; Ribeiro et al., 2017; McCarroll et al., 2019; Wiggins et al., 2019; Valiente et al., 2019a, b, 2020). Understanding the controls on headland bypassing is important for accurate modelling and prediction (Vieira da Silva et al., 2018; Valiente et al., 2020; McCarroll et al., 2021a, b). There remains a need to quantify the contributions of waves, tides and their interactions on this process, whilst also determining the relative influence of other environmental and morphological variables, to enable better understanding and prediction of bypassing rates. This is the focus of Chapter 4, and a detailed review of headland bypassing is presented in Section 4.1.

There has not yet been an analysis at scale of net sand transport on continental shelves with representation of wave tide interactions. With the advent of new shelf scale model reanalyses of waves and hydrodynamics with eddy permitting/ resolving hydrodynamic resolutions (Holt & Proctor, 2008; O'Dea et al., 2012; Saha et al., 2014; Holt, 2017; McConnell et al., 2017; Saulter, 2017), and greater availability of bathymetric and remote sensing data (Bentamy & Fillon, 2012; EMODnet Bathymetry Consortium, 2016) this is now possible. However, numerical models are computationally and labour expensive to develop and run at large spatial scales, high resolutions and with coupled hydrodynamic and wave forcing to capture wave tide interactions. A barrier to conducting shelf scale analyses of net

sand transport including wave tide interactions is the ability to conduct such an assessment at scale in an efficient way. This same computational constraint applies to modelling of coastal sediment budgets with headland bypassing, where much higher resolutions are required to adequately capture circulations around headlands (e.g., Vieira da Silva et al., 2016; McCarroll et al., 2018, 2021b; Valiente et al., 2020).

This thesis examines the relative impacts of waves, tides and their interactions on shelf-scale net sand transport and headland bypassing, quantifying their contributions to sand transport rates under varied environmental forcing and morphological settings. Recent work demonstrates potential for sediment transport beyond the morphological depth of closure (Valiente et al., 2019), which emphasises a need to consider regional sediment transport pathways which may influence sediment transport at the littoral scale. This thesis therefore will examine net sand transport at three scales: Chapter 2 will examine sediment transport at the regional scale of the South West UK shelf area, Chapter 3 extends the regional scale analyses to the scale of the Northwest European continental shelf, and Chapter 4 will examine littoral scale sediment transport with an emphasis on headland bypassing. This will enable a more rounded view of sediment transport to be gained including the influence of waves, tides and their interactions at different scales. Methods including machine learning classification prediction and parameterisations of the complex processes involved in net sand transport and headland bypassing are explored and developed alongside numerical models to enable computationally efficient and large scale estimations of transport rates and dominant environmental forcings to be made. The following section outlines the aims and objectives of this thesis, including a brief overview of each chapter.

1.2 Aims, objectives and thesis outline

The overall aims of this thesis are to advance our knowledge of the role of waves and tides on sand transport at coastal and shelf scales by: (i) advancing our understanding and quantification of the impact of waves, tides and their interactions on net sand transport; (ii) understanding how net sand transport varies across the continental shelf and how that relates to observed sediment distributions and bed morphology; and (iii) furthering our understanding of the extent, drivers and predictability of headland bypassing on embayed coastlines. The following chapters address these broader aims as follows:

1.2.1 Chapter 2

This chapter aims to determine under what conditions waves, tides and their interactions exert an important influence on regional sand transport pathways. This is achieved by means of the following objectives:

(i) Categorisation of the spatially varying contributions of waves and tides under different forcing conditions with applications for other exposed, macrotidal coastlines.

(ii) Comparison of potential sand transport pathways, major partings and convergences to known sediment size distributions and observed bedforms to verify the potential sand transport approach.

(iii) Improving understanding of the conditions where waves change or reverse sand transport pathways relative to tides alone.

(iv) Quantification of the contribution and importance of non-linear wave-tide interactions.

In this chapter a fully coupled numerical model is created and validated to simulate waves, hydrodynamics and sand transport for the South West UK and a portion of the Celtic shelf using Delft3D (Booij et al., 1999; Lesser et al., 2004; van Rijn, 2007a, b). Simulations are conducted with varied combinations of wave and tidal forcing to quantify the contributions of waves, tides and their non-linear interactions on net sand transport. Sand transport pathways are identified for the region including major partings and convergences, and the behaviour of these pathways with respect to variable environmental forcing is discussed. A novel classification

scheme is presented for the dominance of wave, tides or their interactions on sandy continental shelves.

1.2.2 Chapter 3

This chapter builds on Chapter 2 and aims to apply a data driven method to predict the dominant sand transport drivers and sand transport magnitude on sandy continental shelves, allowing assessment of the impact of waves, tides and wave-tide interactions at scale with a computationally efficient method. This is achieved by means of the following objectives:

(i) Determination of a list of readily available environmental and morphological variables with predictive capacity for the dominant sand transport mode and order of magnitude;
(ii) Using results of sand transport rates obtained through a validated numerical model to train a k-Nearest Neighbour (kNN) classifier for dominant sand transport class and order of magnitude;
(iii) Collating environmental and morphological predictors across a sandy continental shelf with highly varied environmental conditions;
(iv) Using the trained kNN classifier to assess the dominant transport mode and sand transport magnitude across the shelf.

In this chapter a kNN classifier is trained on uncoupled wave, tide and bathymetric data to predict the dominance of waves, tides or their interactions on net sand transport rates, using an expanded set of modelling scenarios building on the modelling conducted in Chapter 2. This is then used to estimate the dominant drivers of sand transport and sand transport magnitude across the Northwest European continental shelf, using environmental predictors collated from uncoupled shelf-wide modelling reanalyses. Comparisons are made between predicted dominance classes and observed sand wave morphology on the Netherlands shelf.

1.2.3 Chapter 4

This chapter focuses on coastal scale modelling of sand transport to assess headland bypassing on an exposed, macrotidal and embayed coastline. This chapter aims to test the applicability of existing headland bypassing parameterisations against

realistic headland morphologies, and to expand the parameterisations to include the influence of headland underwater expression, sediment availability and embayment morphology. It also aims to quantify the impact of tides and non-linear wave-tide interactions on headland bypassing rates. This is achieved by means of the following objectives:

(i) Quantifying headland and embayment morphologies and sediment spatial variability across an exposed, macrotidal and embayed region of coast;
(ii) Determining sand bypassing rates for headlands along this coastline under various physical forcing conditions using a validated coupled hydrodynamic, wave and sediment transport model;
(iii) Testing the performance of the parameterisation as presented in McCarroll et al. (2021b) against realistic headland morphologies, and suggesting improvements; and
(iv) Examining the impact of tidal currents and wave-current interactions on headland bypassing relative to wave-only forcing.

In this chapter a fully coupled, 3D numerical model of the North Coast of Cornwall is developed with a focus on rocky headlands to simulate headland bypassing. Bypassing rates are determined for variations of wave and tidal forcing. Sediment spatial variation is determined from high resolution bathymetry and used to determine the influence of spatial sediment variability on bypassing rates. The influence of waves, tides, wave tide interactions and headland topography on headland bypassing are also quantified. An existing parameterisation is tested and novel terms proposed to account for variable bathymetry and sediment coverage.

1.2.4 Chapter 5

This chapter presents a synthesis of the key findings of the thesis relative to the aims stated here and their context within the wider literature. Conclusions are summarised and presented at the end.

2 The Impact of Waves and Tides on Residual Sand Transport on a Sediment-poor, Energetic and Macrotidal Continental Shelf

The work in this chapter is published in:

King, E. V., Conley, D. C., Masselink, G., Leonardi, N., McCarroll, R. J., & Scott, T. (2019). The impact of waves and tides on residual sand transport on a sediment-poor, energetic, and macrotidal continental shelf. *Journal of Geophysical Research: Oceans*, 124, 4974 – 5002. https://doi.org/10.1029/2018JC014861

The work in this chapter was conceived and conducted by Erin King, with supervisory support from Professor Daniel Conley, Professor Gerd Masselink and Dr Nicoletta Leonardi, and with comments and discussion from Dr Robert McCarroll and Dr Tim Scott during preparation of the manuscript for publication.

The work in this chapter addresses the following thesis aims:

(i) Advancing our understanding and quantification of the impact of waves, tides and their interactions on net sand transport;

(ii) Understanding how net sand transport varies across the continental shelf and how that relates to observed sediment distributions and bed morphology.

Key Points:

- Median waves enhance tidal sand transport vectors, whereas extreme waves can dominate sand transport and sometimes induce full-reversals.
- A new continental shelf classification is presented based on wave-, tide- and non-linear wave-tide interaction dominance of sand transport.
- Non-linear wave-tide interactions are a dominant or sub-dominant contributor to sand transport in extreme conditions and cannot be ignored.

Chapter Abstract

The energetic, macrotidal shelf off South West England was used to investigate the influence of different tide and wave conditions and their interactions on regional sand transport patterns using a coupled hydrodynamic, wave and sediment transport model. Residual currents and sediment transport patterns are important for the transport and distribution of littoral and shelf-sea sediments, morphological evolution of the coastal and inner continental shelf zones and coastal planning. Waves heavily influence sand transport across this macrotidal environment. Median (50% exceedance) waves enhance transport in the tidal direction. Extreme (1% exceedance) waves can reverse the dominant transport path, shift the dominant transport phase from flood to ebb, and activate sand transport below 120m depth. Wave-tide interactions (encompassing radiation stresses, Stoke's drift, enhanced bottom-friction and bed shear stress, refraction, current-induced Doppler shift and wave-blocking) significantly and non-linearly enhance sand transport, determined by differencing transport between coupled, wave-only and tide-only simulations. A new continental shelf classification scheme is presented based on sand transport magnitude due to wave-forcing, tide-forcing and non-linear wave-tide interactions. Classification changes between different wave/ tide conditions have implications for sand transport direction and distribution across the shelf. Non-linear interactions dominate sand transport during extreme waves at spring tides across most of this macrotidal shelf. At neap tides, non-linear interactions drive a significant proportion of sand transport under median and extreme waves despite negligible tide-induced transport. This emphasises the critical need to consider wave-tide interactions when considering sand transport in energetic environments globally, where previously tides alone or uncoupled waves have been considered.

2.1 Introduction

Residual flow and sediment transport patterns have important implications for the transport and distribution of littoral and shelf sea sediments, and for morphological evolution of the coastal and inner continental shelf zones (Lin & Falconer, 2001; Lewis et al., 2015; Leonardi & Plater, 2017). Shelf sediments are susceptible to wave-driven resuspension and net transport by residual tidal currents and wave asymmetry due to wave shoaling. Net sand transport paths are susceptible to wave action, and can reverse direction during extreme wave events (Pattiaratchi & Collins, 1988). Understanding residual flow patterns and the effect of waves is important for understanding regional sediment transport pathways and is relevant for coastal zone management.

Many previous modelling efforts focus on residual tidal circulation, ignoring surface wave effects on regional sediment transport and morphological evolution. Residual currents are generated by non-linear advection of momentum, density gradients, bottom friction nonlinearities, wind stress and nonlinearities in the volume continuity equation related to Stokes drift (Zimmerman, 1978; Uncles, 1982, 2010). Pingree and Griffiths (1979) modelled tide-induced bed shear stress around the British Isles qualitatively matching mean and maximum bed shear stress vectors to sand transport paths described by Stride (1963). Recently, Leonardi & Plater (2017) focus on tidally-induced morphodynamic equilibrium of the South East UK coastline and potential long-term morphological evolution.

However, surface waves increase bed shear stress, enhancing sediment resuspension and enabling (enhancing) suspended sediment transport by weak (strong) tidal currents. Interactions between water level variations, combined steady tidal and wave-driven oscillatory flows, and the bed influence suspended and bedload sediment transport (Harris & Collins, 1991; van der Molen, 2002; Porter-Smith et al., 2004; van Rijn, 2007a, 2007b; Damen et al., 2018). For equivalent current magnitudes, wave induced bed shear stresses are larger than for tidal currents due to the thinner wave boundary layer (Nielsen, 1992). Wave-current interactions non-linearly enhance the bed shear stress and apparent roughness due to the interaction between wave and current bottom boundary layers (Kemp & Simons, 1982, 1983; Klopman, 1994; Umeyama, 2005). The relative incident wave angle to the steady flow influences the vertical current profile and variation in

apparent bed roughness, demonstrated by analytical and numerical models (Grant & Madsen, 1979, 1986; Fredsøe, 1984; Olabarrieta et al., 2010; Tambroni et al., 2015). With significant positive trends observed in global 99th percentile wave heights from 1991-2008 in buoy and altimeter data (Young et al., 2011), and upward trends in storminess across central, western and northern Europe (Donal et al., 2011; Castelle et al., 2018), understanding the effect of waves on shelf sediment transport is potentially of increasing importance to coastal communities.

Studies of shelf-scale sediment transport are considering wave-tide coupling more regularly (Dietrich et al., 2011; Hashemi et al., 2014; Moriarty et al., 2014; Xu et al., 2016; Zhang et al., 2016), however, coupled modelling systems are more computationally expensive. A number of studies consider uncoupled tides and waves as an approximation, ignoring wave-tide interactions (e.g., van der Molen, 2002; Porter-Smith et al., 2004; Neill et al., 2010; Xing et al., 2012; Bricheno et al., 2015). Evidence of wave impacts have been observed across the South West UK continental shelf to depths of 150m indicating wave-tide interactions must be considered when considering regional sand transport pathways (Channon & Hamilton, 1976; Reynaud et al., 1999; Thompson et al., 2019); however, the extent of wave influences on sediment transport across the continental shelf, including the influence of waves on regional sand transport pathways and the relative impact of wave-tide interactions, is not fully understood.

A challenge in understanding regional sand transport patterns is the spatial and temporal limitations of observational campaigns to capture flow patterns at sufficient resolution and time scales, and their susceptibility to local effects (Stride & Belderson, 1990). This results in uncertainties in regional-scale residual circulations and uncertainty regarding the relative importance of different processes such as surface waves, wind and baroclinic effects. Modelling can overcome spatial and temporal limitations provided sufficient observational data is available for calibration and validation.

The South West UK presents ideal conditions for examining the effect of waves and tides on sand transport due to its macro tidal regime and highly energetic waves. This chapter aims to determine under what conditions waves, tides and their interactions exert an important influence on regional sand transport pathways. Specifically, the following objectives will be investigated: (i) Categorisation of the

spatially varying contributions of waves and tides to potential sand transport using a validated coupled hydrodynamic, sediment transport and wave model, with applications for other exposed, macrotidal coastlines. (ii) Comparison of potential sand transport pathways, major partings and convergences to known sediment size distributions and observed bedforms to verify the potential sand transport approach. (iii) Understanding of the conditions where waves change or reverse sand transport pathways relative to tides alone. (iv) Quantification of the contribution and importance of non-linear wave-tide interactions to potential sand transport in a macrotidal environment.

2.2 Study Area

The South West UK peninsula, situated on the Northwest European Continental Shelf, comprises several distinct regions with different hydrodynamic/ wave regimes (Figure 2.1). The Approaches extend from the western boundary in the Celtic Sea to a border with the Bristol Channel (northeast) and English Channel (southeast). The North Coast stretches from Hartland Point to Land's End. The Bristol Channel extends from its mouth (spanning Hartland Point to Pembroke) to the upper reaches of the Severn Estuary. The South Coast extends east into the English Channel from Land's End.

2.2.1 Hydrodynamics

The Bristol Channel experiences the second-largest tidal range globally (mean spring tidal range (MSTR) >12m in the Upper Severn) due to amplification of the dominant M2 and quarter-wave resonances of the M4 and MS4 tides (Taylor, 1921; Fong & Heaps, 1978; Uncles, 1984). Maximum currents in the Upper Bristol Channel exceed 2.5ms^{-1}, with currents approaching 1ms^{-1} in bays (Collins et al., 1979; Uncles, 1984, 2010; Xia et al., 2010). Resonance contributes to large tidal amplitudes shelf-wide, with a North Coast MSTR exceeding 5m (>7m at Hartland Point; Uncles, 2010). Peak currents in the Approaches reaching 0.9ms^{-1} rework sediments year-round (Carruthers, 1963; Heathershaw et al. 1987; Reynaud et al. 1999; Thompson et al., 2019). The South Coast has a lower MSTR (4–5m), whilst a degenerate amphidromic point, complex bathymetry, coastal configuration and non-linear effects in the equations of motion cause a lower MSTR (2–3m) and double low water at

Weymouth (Pingree & Maddock, 1977; Uncles, 2010). The region experiences pronounced spring-neap variability, with much weaker neap currents (Pattiaratchi & Collins, 1988; Uncles, 2010; Thompson et al., 2019). A northeast residual current flows along the North Coast, with a weak, variable residual in the Approaches (Pingree & Le Cann, 1989). Non-linear advection of momentum dominates the residual in the Bristol Channel (Uncles, 1982; Holt et al., 2001).

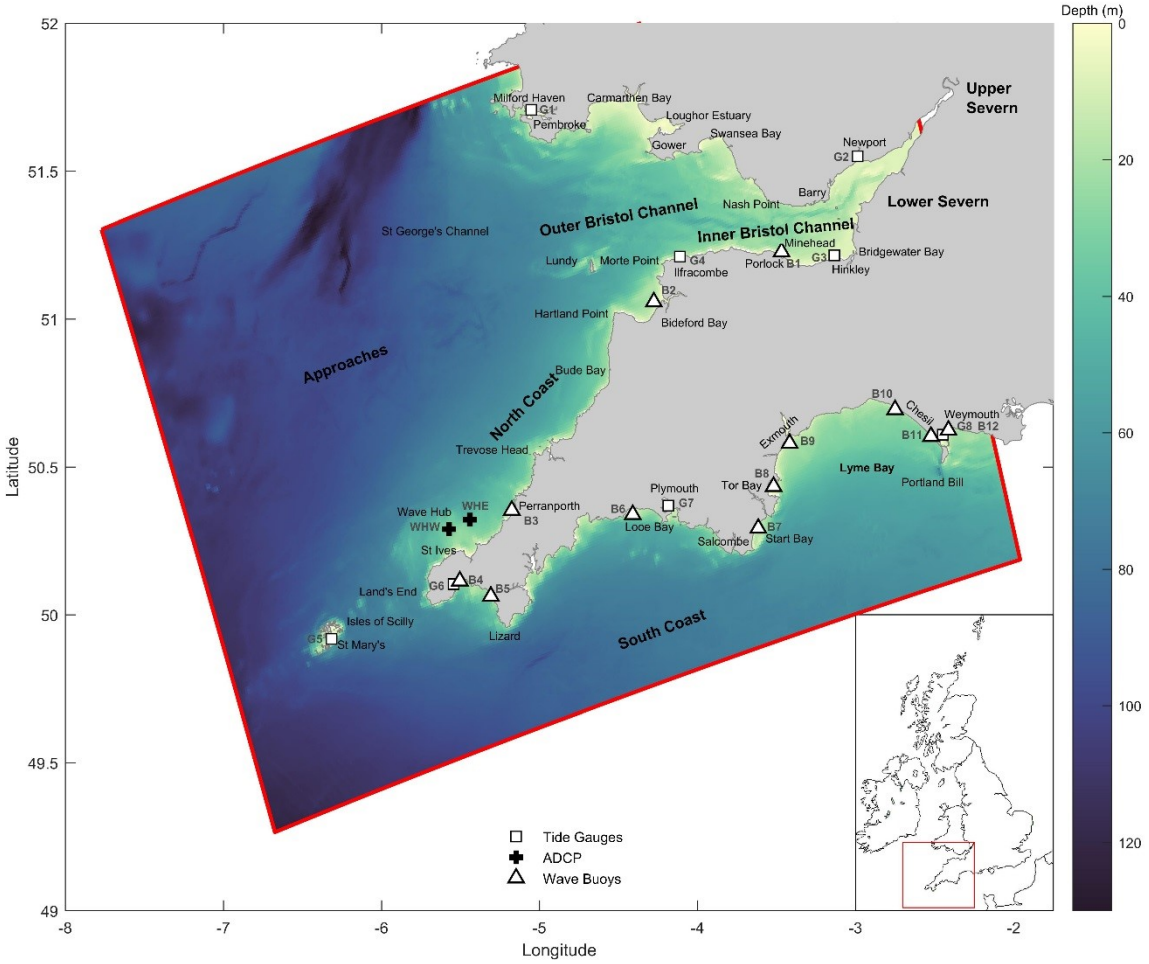

Figure 2.1: Map of the South West UK continental shelf area considered in this study. Regions are designated as the "Approaches", "Bristol Channel", "North Coast", and "South Coast". The Bristol Channel is further subdivided into "Outer/ Inner Bristol Channel", and "Lower Severn". The model domain is shown with model bathymetry, open boundaries (red lines) and validation locations: ADCP deployments (+), wave buoys (Δ) and tide gauges (□).

2.2.2 Waves

The region is exposed to Atlantic waves with potential fetch lengths of 6000km (Collins, 1987). The 1% exceedance H_s at Sevenstones (off Land's End) from 2008-2014 was 5.9m and nearshore winter storm H_s along the North Coast can often exceed 6m (Scott et al., 2016b). Mean H_s near the shelf break ~2m, reducing to ~1.5m and below in the Bristol Channel (Pattiaratchi & Collins, 1988; Reynaud et al., 1999; Bricheno et al., 2015). H_s and T_p increase during winter (October – March). Peak near-bed orbital velocities are caused by storm swell with typical storm durations of 24 hours, and can approach 1 ms^{-1} below 100m depth, exceeding critical sand resuspension thresholds (Hadley, 1964; Draper, 1967; Pattiaratchi & Collins, 1988; Reynaud et al., 1999; Thompson et al., 2019). Valiente et al. (2019a) show sheetflow conditions may occur around 30-40 m depth under extreme storm conditions. The region has been subject to a significant increase in extreme (99th percentile) H_s of 1% per annum, among the largest increases observed globally, and an increase in winter H_s and interannual variability associated with the North Atlantic Oscillation (NAO) and West European Pressure Anomaly (WEPA) indexes (Young et al., 2011; Castelle et al., 2017, 2018). Positive WEPA values result in higher wave heights south of 52°N and increased storm clustering (Hanley & Caballero, 2012; Scott et al., 2016b; Castelle et al., 2017).

2.2.3 Sand transport

The presence of a Bristol Channel bed load parting has been debated (Stride & Belderson, 1990, 1991; Harris & Collins, 1991), and uncertainty remains regarding its nature (McLaren et al., 1993; Lewis et al., 2015). Weak convergences and partings are present on the South Coast (Pingree & Griffiths, 1979). Modelling indicates northeast residual sand transport along the North Coast (Pingree & Griffiths, 1979; Holt et al., 2001; Uncles, 2010). Physical sediment characteristics are more important than biological factors for determining bed stability in the Celtic Sea (Thompson et al., 2019). Ward et al. (2015) show regional bed shear stress patterns at 1.1km resolution. This and aforementioned modelling studies focus on tide-induced bed shear stress, neglecting surface waves.

Observations indicate waves can strongly influence residual sand transport magnitude and direction, including full directional reversals (Collins, 1987;

Pattiaratchi & Collins, 1988; Reynaud et al., 1999; Lewis et al., 2015). Beach response in this region to extreme waves is well documented (Masselink et al., 2015; Scott et al., 2016b; Burvingt et al., 2017). There remains a need to place these observations into regional context, examining the influence of waves on sand transport pathways considering different wave and tidal conditions. Regional-scale residual currents, net sand transport, and the impacts of different wave conditions are not yet described for the Celtic Sea at high resolution.

2.3 Methods

2.3.1 Numerical model

A depth-averaged hydrodynamic, sediment transport and morphological model coupled to a SWAN third-generation spectral wave model was created based on Delft3D for the region shown in Figure 2.1. A model schematic is also shown in Figure 2.2. Depth-integrated hydrodynamics are calculated using the unsteady shallow-water equations, following the Boussinesq approximation with the vertical momentum equation reduced to the hydrostatic pressure relation, assuming vertical accelerations are small relative to gravitational acceleration (Lesser et al., 2004). This study considers conditions typical of winter, where stratification is weak with little near-bed effect (Holt et al., 2001). Consequently, depth-integrated hydrodynamics were considered adequate in line with previous modelling approaches in the region (Pingree & Griffiths, 1980; Uncles, 1982, 2010; Pingree & Le Cann, 1989; Holt et al., 2001; Xia et al., 2010; Bricheno et al., 2015; Lyddon et al., 2018). The effect of secondary flow generation due to a rotating current field on the depth-integrated flow is included by addition of a correction term to the depth averaged momentum equations, assuming a logarithmic velocity profile, where spiral motion intensity is described by a depth averaged advection-diffusion equation (Kalkwijk & Booij, 1986; Deltares, 2014). Delft3D uses SWAN, packaged as Delft3D-WAVE, a third-generation phase-averaged wave model based on fully spectral representation of the action balance equation, accounting for wave-current interaction through radiation stress, refraction, wind generation, whitecapping, non-linear wave-wave interactions, bottom dissipation and depth-induced breaking

(Booij et al., 1999). More details on wave-tide interactions in Delft3D are presented in section 2.3.2.

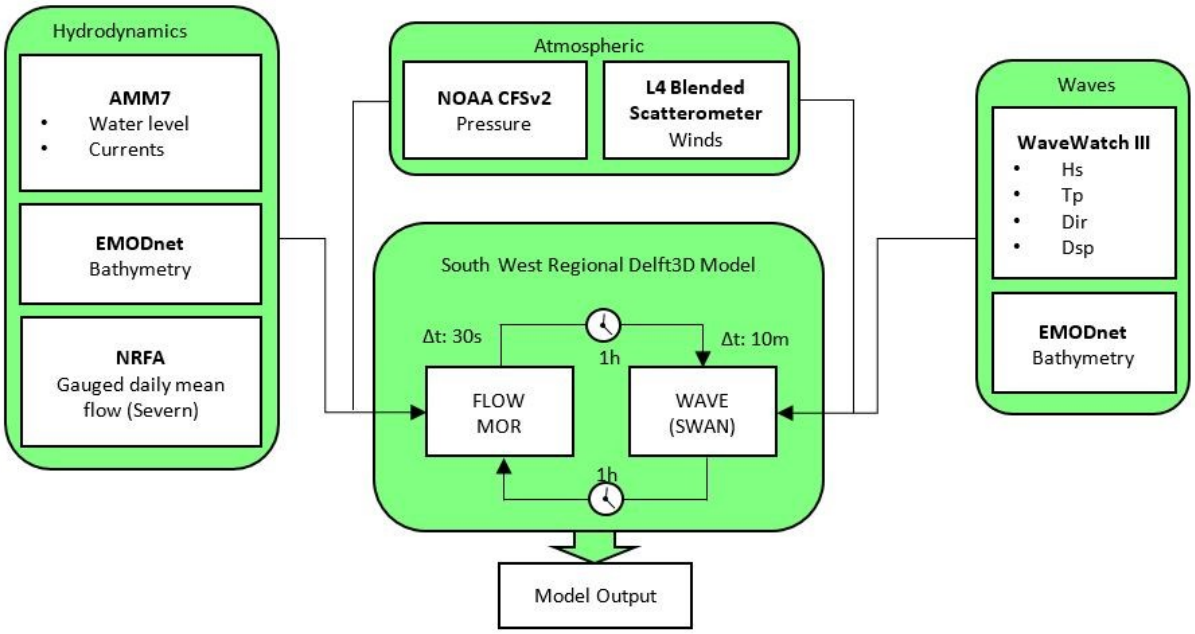

Figure 2.2: Model schematic diagram showing the integration of different modules and wave coupling.

Holt et al. (2017) indicate a resolution of 1.5km is necessary to be eddy resolving over ~70% of the coastal ocean areas globally, and 1.5km was considered sufficient for resolving the internal Rossby radius on the Northwest European shelf in the development of the operational AMM15 hydrodynamic model (Graham et al. 2018). A hydrodynamic resolution of 1 km was used in this study, on a curvilinear, spherical coordinate grid. This represents an eddy permitting grid resolution, suitable to resolve mesoscale eddies at the length scale of the baroclinic Rossby radius (2-5km on the shelf; Holt & Proctor, 2008), although eddies at the smaller end of this scale will not be fully resolved. Depths were averaged from 1/8′ resolution EMODnet digital bathymetry (EMODnet Bathymetry Consortium, 2016), corrected to Mean Sea Level 2000 (MSL2000) using the Vertical Offshore Reference Frame (Turner et al., 2010).

The hydrodynamic model has four water level boundaries and one discharge boundary at the Severn. Water level data were interpolated at 7km intervals across the boundaries from the Atlantic Margin Model (FOAM-AMM7; O'Dea et al., 2012; McConnell et al., 2017). Boundary conditions were then linearly interpolated between these 7km intervals at the intermediate boundary nodes by the model. This

interpolation can generate unrealistic flows adjacent to the open boundary. Consequently, data within 20 grid cells of each open boundary were excluded from the analysis. Boundaries were located far enough away from the South West peninsula in order that this did not influence the model results in the region of interest. Variations in the Severn discharge rate had little influence on modelled results; therefore, a representative average 100 m^3s^{-1} discharge was applied. The hydrodynamic time step was 30 seconds. Spatially variable winds were interpolated linearly from 0.25° resolution satellite scatterometer blended 6-hourly mean wind fields retrieved from the Copernicus Marine Service (Bentamy & Fillon, 2012). Spatially variable atmospheric pressure was interpolated linearly from the 0.5° resolution Climate Forecast System Version 2 (CFSv2) model (Saha et al., 2014).

The wave model overlapped the hydrodynamic domain at 1.5km resolution. Depth and wind forcing were assigned in the same manner as the hydrodynamic model. The wave model was forced with parametric boundary conditions (H_s, T_p, direction, directional spreading) interpolated from the UK Met Office Wave Watch III continental shelf model (Saulter, 2017) at 8km intervals along four open boundaries. The Severn boundary was closed. The wave domain extended slightly past the hydrodynamic domain in order to avoid hydrodynamic boundaries effects influencing the wave boundaries. The wave time step was 10 minutes. Waves were two-way coupled to the hydrodynamics with a 1hr communication time step, passing wave forces based on energy dissipation rate, bed shear stresses, Stokes drift and orbital bottom velocity and receiving water levels, depth-averaged velocities and updated bathymetry (Elias et al., 2012).

Bed-load and suspended-load sand transport rates were calculated using the TRANSPOR2004 formulation (van Rijn 2007a, b) with an essentially unlimited sediment depth for 330μm grain size, similar to measured grain sizes along the North Coast and Bristol Channel (Channon & Hamilton, 1976; Pattiaratchi & Collins, 1988; Lewis et al., 2015; Prodger et al., 2017). A single grain size was important for comparisons of potential sand transport between regions with different hydrodynamic and morphological characteristics. In reality, grain size becomes progressively finer moving north through the Approaches. The Bristol Channel shows pronounced local variability with grain sizes ranging from mud and fine sand in low-energy embayments to gravel and erosion-resistant substrate in high-energy

locations (Channon & Hamilton, 1976; Collins, 1987; Pattiaratchi & Collins, 1988; Ward et al., 2015; Thompson et al., 2019). Bed morphology was updated every hydrodynamic time step. Chapter 3 examines the influence of grain size on sand transport at the shelf scale in more detail.

2.3.2 Wave-tide interactions

Delft3D has been previously used in a depth-averaged form in studies of wave-current interactions and sediment transport on the inner continental shelf (Hansen et al., 2013; Hopkins et al., 2015; Ridderinkhof et al., 2016; Luijendijk et al., 2017). Wave-current interactions are parametrised in the depth-averaged implementation of Delft3D. Wave-induced set-up and long-shore currents, forced by wave-induced momentum flux due to radiation stress gradients, are approximated using the wave energy dissipation rate method of Dingemans et al. (1987). Wave induced mass flux due to Stokes drift is represented as the integration of the Stoke's drift velocity components over the total wave-averaged water depth. SWAN accounts for depth and current-induced wave refraction, wave-blocking by flow and current-induced Doppler shift. The effect of a mean current on the wave energy dissipation due to bottom friction is not taken into account in SWAN due to large potential errors in estimating the bottom roughness length (Booij et al., 1999).

Enhancement of the bed shear stress under combined waves and currents is implemented in Delft3D following the method of Soulsby et al. (1993). The current-related bed shear stress τ_c is:

$$\tau_c = \frac{g\rho_0 U|U|}{C_D^2} \tag{2.1}$$

and the wave-related bed shear stress is:

$$|\tau_w| = \frac{1}{2}\rho_0 f_w U_{orb}^2 \tag{2.2}$$

where f_w is a wave-related friction factor, U_{orb} is the bottom orbital velocity, U is the depth averaged velocity, ρ_0 is the density of seawater, g is gravitational acceleration and C_D is the drag coefficient. The wave-related friction factor takes the form:

$$f_w = \begin{cases} 0.00251 \exp\left[5.21\left(\frac{U_{orb}}{\omega k_s}\right)^{-0.19}\right] & \text{for} \frac{U_{orb}}{\omega k_s} > \frac{\pi}{2}, \\ 0.3 & \text{for} \frac{U_{orb}}{\omega k_s} \leq \frac{\pi}{2} \end{cases} \quad (2.3)$$

where ω is the apparent (Doppler-shifted) frequency, k_s is the Nikuradse roughness length, and the bottom orbital velocity is:

$$U_{orb} = \frac{1}{4}\sqrt{\pi}\frac{H_{rms}\omega}{\sinh(kh)} \quad (2.4)$$

Time-mean bed shear stress τ_m and maximum bed shear stress τ_{max} are then determined using three dimensionless parameters X, Y, and Z:

$$X = \frac{\tau_c}{\tau_c + \tau_w}, \quad (2.5)$$

$$Y = \frac{\tau_m}{\tau_c + \tau_w}, \quad (2.6)$$

$$Z = \frac{\tau_{max}}{\tau_c + \tau_w}, \quad (2.7)$$

The parameters Y and Z are related to X by the following equations:

$$Y = X[1 + bX^p(1 - X)^q] \quad (2.8)$$

$$Z = 1 + aX^m(1 - X)^n \quad (2.9)$$

where a, b, p, q, m and n are coefficients fitted by Soulsby et al. (1993) to various wave-induced shear stress formulations, which are available in Delft3D and are chosen during calibration. The total bed shear stress is corrected for Stokes drift U_S:

$$\tau_b = \frac{|\tau_m|}{|U|}(U - U_S) \quad (2.10)$$

The TRANSPOR2004 sediment transport formulation (van Rijn, 2007a,b) computes four sediment transport contributions: current- and wave- related suspended load and current- and wave-related bedload. The current related suspended transport is the product of the depth averaged concentration and current velocity, including the effects of wave-stirring on the sediment load (van Rijn, 2007b). The reference concentration is calculated using the method of van Rijn et al. (2000) for a single sediment fraction:

$$c_a = f_{SUS}0.015\rho_s\frac{d_{50}(\tau_\alpha)^{1.5}}{a(D_*)^{0.3}} \quad (2.11)$$

where ρ_s is the sediment density, d_{50} is the median particle diameter, D_* is the dimensionless particle diameter, a is van Rijn's reference height, τ_α is the non-

dimensional bed-shear stress including the effects of currents and waves and f_{SUS} is a user defined tuning parameter set to 1.4 in accordance with Grunnet et al. (2004). The instantaneous bedload transport rate is:

$$q_{b,t} = 0.5\rho_s d_{50} D_*^{-0.3} \left(\frac{\tau'_b}{\rho_0}\right)^{0.5} \left[\frac{\tau'_b - \tau_{b,cr}}{\tau_{b,cr}}\right] \tag{2.12}$$

in which τ'_b is the instantaneous grain-related bed shear stress due to combined currents and waves (for a full derivation see vanRijn, 2007a, their Equation 10), and $\tau_{b,cr}$ is the critical bed shear stress. The x and y components of the total bedload transport are then obtained by integrating the instantaneous bedload transport rate over the wave period T:

$$q_{b,x} = \left(\frac{1}{T}\right) \int \frac{v_b}{(u_b^2 + v_b^2)^{0.5}} q_{b,t} dt + q_{s,w} \cos(\phi) \tag{2.13}$$

$$q_{b,y} = \left(\frac{1}{T}\right) \int \frac{v_b}{(u_b^2 + v_b^2)^{0.5}} q_{b,t} dt + q_{s,w} \sin(\phi) \tag{2.14}$$

where u_b and v_b are instantaneous near bed velocity components due to the combined action of currents and waves, determined from the depth, wave height and wave period using the semi-empirical method of Isobe & Horikawa (1982; for more details on the calculation of wave-related bedload transport see van Rijn & Walstra, 2004; van Rijn, 2007a,b,c; van Rijn et al., 2011). ϕ is the angle between the wave propagation direction and the x-axis of the computational grid. The current-related bedload transport components are:

$$q_{b,c,x} = \left(\frac{1}{T}\right) \int \frac{u_{b,c}}{(u_b^2 + v_b^2)^{0.5}} q_{b,t} dt \tag{2.15}$$

$$q_{b,c,y} = \left(\frac{1}{T}\right) \int \frac{v_{b,c}}{(u_b^2 + v_b^2)^{0.5}} q_{b,t} dt \tag{2.16}$$

where $u_{b,c}$ and $v_{b,c}$ are the instantaneous current-related velocity components. The wave-related bedload transport components are then determined from the difference between the total transport and the current-related transport:

$$q_{b,w,x} = q_{b,x} - q_{b,c,x} \tag{2.17}$$

$$q_{b,c,y} = q_{b,y} - q_{b,c,y} \tag{2.18}$$

An additional transport component is generated due to asymmetric wave orbital motion within about 0.5m of the bed, which is included in the bedload transport vector. This wave-related suspended transport is modelled as:

$$q_{s,w,x} = 0.1\left(\frac{U_{\delta,for}^4 - U_{\delta,back}^4}{U_{\delta,for}^3 + U_{\delta,back}^3} + u_\delta\right) L_T \cos(\phi) \quad (2.19)$$

$$q_{s,w,y} = 0.1\left(\frac{U_{\delta,for}^4 - U_{\delta,back}^4}{U_{\delta,for}^3 + U_{\delta,back}^3} + u_\delta\right) L_T \sin(\phi) \quad (2.20)$$

in which $U_{\delta,for}$ and $U_{\delta,back}$ are the forward and backward directed peak orbital velocities based on significant wave height computed using a modification of the method of Isobe and Horikawa (1982; see van Rijn & Walstra, 2004), u_δ is the wave induced streaming velocity near the bed and L_T is the approximated suspended sediment load. The final bedload transport components are the sum of the corrected current and wave related components:

$$Q_{b,x} = f_{BED}(q_{b,c,x}) + f_{BEDW}(q_{b,w,x}) + f_{SUSW}(q_{s,w,x}) \quad (2.21)$$

$$Q_{b,y} = f_{BED}(q_{b,c,y}) + f_{BEDW}(q_{b,w,y}) + f_{SUSW}(q_{s,w,y}) \quad (2.22)$$

where f_{BED}, f_{BEDW} and f_{SUSW} are tuning parameters set to 0.8, 0.3 and 0.3 respectively, in accordance with Grunnet et al. (2004) (see also: van Rijn et al., 2004; McCarroll et al., 2018).

As this study considers depth-integrated computations, some effects of wave-current interactions are not represented. The effects of wave dissipation are applied in a depth-integrated manner, whereas for a 3D simulation, wave breaking and whitecapping would be represented at the free-surface and bottom friction would apply at the bed layer. Additional turbulence production due to wave breaking and bottom friction is parameterised by inclusion in the horizontal eddy viscosity and diffusivity coefficients. The implications of this are discussed in section 2.5.

2.3.3 Calibration

Calibration was conducted over a 62-day simulation period from 1st December 2013 to 1st February 2014 by varying the spatially uniform bed roughness coefficients, dimensionless wind drag coefficient and wave-induced bottom stress formulations. This covered the energetic winter 2013/14 period that saw the strongest storms to affect the region in >50 years (Masselink et al., 2015, 2016; Scott et al., 2016b). Model performance was assessed using an aggregation of skill metrics (R^2, bias, Willmott skill (WIA), Brier skill (BSS), and mean absolute error (MAE) for residuals) against observed tide elevations, depth-averaged currents and wave parameters from networks of tide gauges, ADCP deployments and wave buoys (Figure 2.1).

Qualitative sediment transport rates and directions were compared with previous observations and modelling results, and observed bedform asymmetries.

The skill metrics are outlined below. Bias is given by:

$$BIAS = \frac{\sum_{i=1}^{n}(P_i - O_i)}{n} \tag{2.23}$$

where P_i is the model prediction, O_i is the observed value and n is the number of points for comparison. Willmott skill, *WIA*, (Willmott et al., 2012) is given by:

$$WIA = \begin{cases} 1 - \dfrac{\sum_{i=1}^{n}|P_i - O_i|}{2\sum_{i=1}^{n}|O_i - \bar{O}|}, when \\ \sum_{i=1}^{n}|P_i - O_i| \leq 2\sum_{i=1}^{n}|O_i - \bar{O}| \\ \dfrac{2\sum_{i=1}^{n}|O_i - \bar{O}|}{\sum_{i=1}^{n}|P_i - O_i|} - 1, when \\ \sum_{i=1}^{n}|P_i - O_i| > 2\sum_{i=1}^{n}|O_i - \bar{O}| \end{cases}, \tag{2.24}$$

Where $\bar{P}$ and $\bar{O}$ are the predicted and observed mean, respectively. The score *WIA* ranges from -1 to 1 and indicates the summed magnitudes of the differences between the modelled and observed deviations about the observed mean, relative to the summed magnitudes for the perfect model, $P_i = O_i$ (Willmott et al., 2012). Values > 0 indicate the sum of the error-magnitudes is less than the magnitudes of the observed deviations (by half for *WIA* = 0.5).

Brier skill (BSS) is is determined following Davidson et al., (2010; see also: Murphy & Epstein, 1989; Sutherland et al., 2004) by:

$$BSS = 1 - \frac{\langle(|P_i - O_i| - \epsilon)^2\rangle}{\langle(|F_i - O_i|)^2\rangle} \tag{2.25}$$

Where F_i represents the i^{th} value interpolated from a linear fit to the observation data and ε is the observation error. Observation errors used were 0.1 m for H_s, 1 s for T_p, 5° for direction and 0.02 ms^{-1} for currents, in accordance with McCarroll et

al., (2018). Angle brackets represent the time mean. Values of 0–0.3 are considered poor, 0.3–0.6 reasonable, 0.6–0.8 good and >0.8 excellent.

Mean absolute error (Willmott & Matsuura, 2005) is given by:

$$MAE = \frac{\sum_{i=1}^{n}(|P_i - O_i|)}{n} \tag{2.26}$$

Metrics were calculated for the unfiltered time series, and two residual time series with the tidal signal removed by methods described in Brown et al. (2012): harmonic analysis using U-Tide (Codiga, 2011) and low-pass filtering using a 2-way recursive Chebyshev-II filter with pass band ≥30h, stop-band ≤26h, allowable pass-band ripple magnitude of 3dB, and stop-band attenuation of 30dB (allowing periods ≥30h to pass, attenuating periods ≤26h). The best performing calibration run was selected based on the run that scored best for the majority of the metrics considered. The default SWAN parameters and the Fredsøe (1984) bed shear stress formulation performed best, as used in studies of sediment dynamics in combined energetic tide and wave environments elsewhere (Ridderinkhof et al., 2016; Verschelling et al., 2017; Herrling & Winter, 2018). A minimum wind drag coefficient of 0.002 was selected. The Manning formulation for the drag coefficient was selected, which takes the form:

$$C_D = \frac{\sqrt[6]{h}}{n} \tag{2.27}$$

where h is the total water depth. The calibrated roughness coefficient n was 0.0275. Section 2.3.4 presents the full validation, including the calibration period.

2.3.4 Model Performance

2.3.4.1 Water levels

Validation was performed over a 9-month period from September 2013 to June 2014. Water levels were compared at hourly intervals using the nearest grid node to each gauge. The harmonic tide was subtracted from the total signal to give the harmonic residual elevation and a low-pass residual was determined through filtering, isolating long period residual elevations and removing semi-diurnal and diurnal signals. Two comparisons are shown in Figure 2.3: a representative site (Ilfracombe) and the worst performing site (Weymouth). Statistics for all sites are presented in Table 2.1.

Water levels were simulated with excellent skill (BSS > 0.8) across the domain at all gauges apart from Weymouth (G8, Figure 2.1). The model did not simulate the double-low water at Weymouth due to the proximity of this gauge to the boundary and because the model domain does not encompass the degenerate amphidromic system to the east. Despite this, high water was simulated well, as shown in the scatter plot (Figure 2.3 - right). Bias in the low-pass residuals reflects the water level bias, tending towards slight underestimation with an overall bias of -13cm. MAE (not shown for unfiltered signals) is 20cm overall, reflected in the harmonic residual (19cm).

2.3.4.2 Currents

Two ADCP deployments at the WaveHub on the North Coast were used for validation (WHE, WHW, Figure 2.1; Lopez et al., 2016). Instantaneous velocity profiles were de-spiked by the method of Mori et al. (2007), depth-integrated and hourly-averaged for comparison. Model data were linearly interpolated to the ADCP locations. Comparison was conducted for periods of continuous ADCP data and gaps were not filled. Comparisons are shown for the tidal and residual signals in the same manner as water levels in Figure 2.3.

Currents were simulated with good skill at both deployments (Table 2.1) with an eastward bias of 3cms^{-1} and northward bias of 2cms^{-1}, and MAE (not shown) of 9cms^{-1} and 5cms^{-1} respectively, reflected in the residual currents by low-pass filtering (bias) and harmonic analysis (MAE). WHW predictions have greater spread about the perfect model than WHE, reflected in a lower R^2. Depth-averaged residuals tend towards overestimation by several cms^{-1}, greater during storm events. Considering that ADCP measurements closer to the surface than 10% of the water depth can not be used due to sidelobe contamination (Marmorino & Hallock, 2001), this result is considered very good.

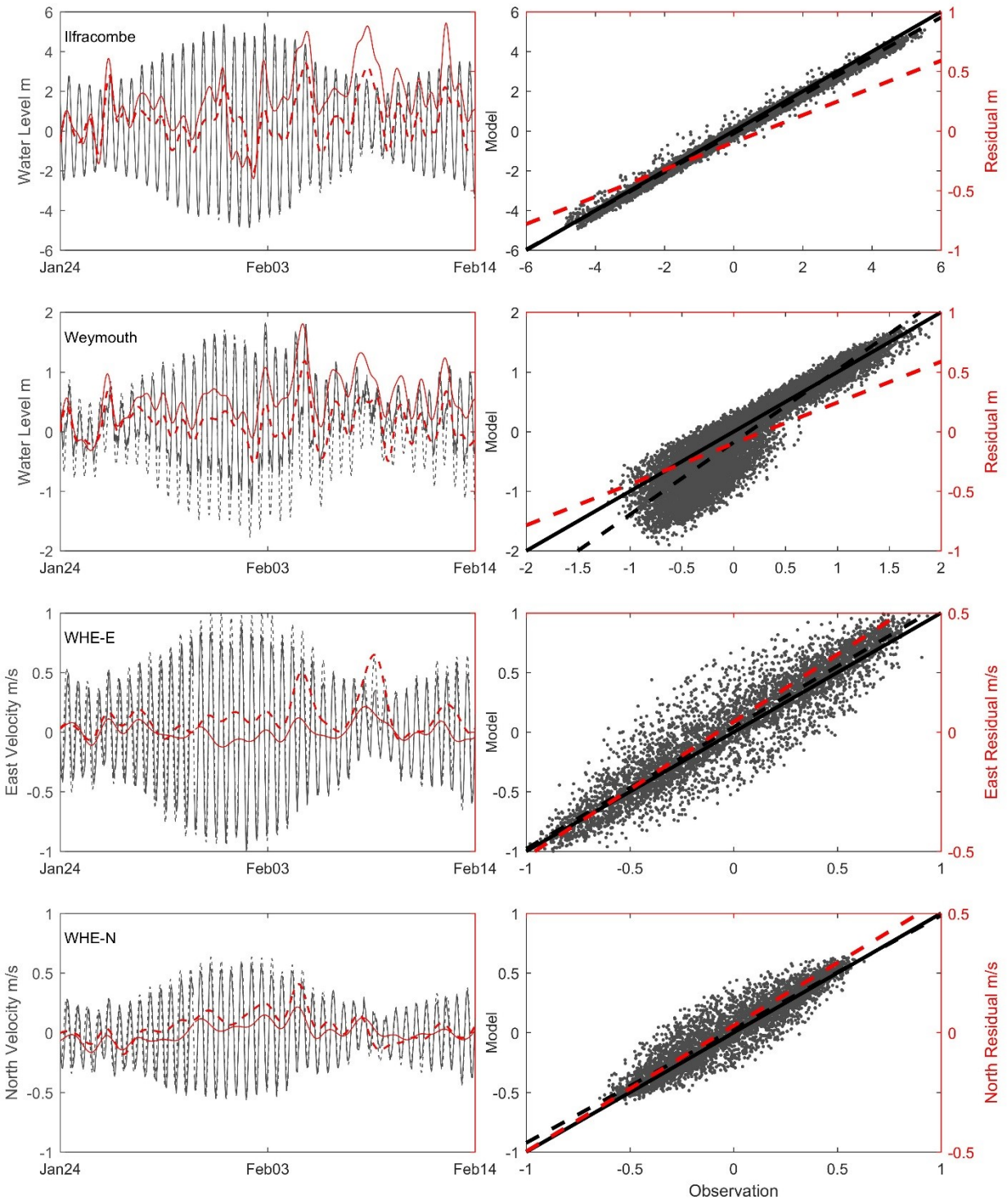

Figure 2.3: Model (dashed) versus observation (solid) comparisons for water levels (top half) and depth-averaged velocities (bottom half) for a period of energetic storms. The tidal signal (grey) and residual signal (red) are shown, with residuals presented from the low-pass filtering method only to reduce complexity. Velocities from the Wave Hub East deployment are presented, separated into east and north components. Scatter plots (right column) show the modelled parameters versus the observations for the full 9-month dataset. The 1:1 line of the perfect model (solid) and the trend line of the modelled parameters versus the observations (dashed) are shown for the tidal (grey) and residual (red) signals.

2.3.4.3 Waves

Comparisons of wave parameters for Bideford (B2) and Start Bay (B7) are presented in Figure 2.4 with statistics presented in Table 2.1. Bideford is representative of performance at exposed sites such as the North Coast (B2-3), Chesil (B10-11) and Looe Bay (B6). Exposed sites show excellent skill when compared to the buoy data for H_s. Start Bay is representative of sites with smaller wave heights due to sheltering. The model captures the bi-modal (southerly/ easterly) wave climate. Considerable scatter in observed wave directions is apparent for H_s < 1m (light blue) where buoy measurements are less reliable. Eliminating times where H_s < 1m improves model skill for direction. Locations with a majority H_s < 1m tended to be sheltered due to the shape of the coastline (e.g. B7: Start Bay, B8: Tor Bay; Figure 2.1), or the presence of features such as islands (e.g. B6: Looe Bay; Figure 2.1). The model tends to over-predict H_s in sheltered locations when the 1.5km resolution cannot resolve small-scale coastal features. In these locations, sheltering features such as headlands, islands and sand banks that affect the wave climate at the buoy may not be well resolved. These effects are localised close to shore, and as this study is interested in regional scale sand transport patterns, are not expected to impact the results. The model simulates H_s and direction with excellent skill overall, and T_p with reasonable skill. Overall biases are 23cm, 1.1s and -3° for H_s, T_p (Hs>1m) and direction (Hs>1m) respectively, with MAE (not shown) of 30cm, 2.2s and 11.7°.

The majority of Brier scores (47/54) indicate reasonable or better performance (and 38/54 indicate good or excellent). Areas with poor skill are explained by either proximity to the model boundary and highly site specific tidal characteristics (Weymouth), or a lower number of wave observations for H_s > 1m for comparison. This testifies to the suitability of this model for reproducing the wave and tidal characteristics of this region.

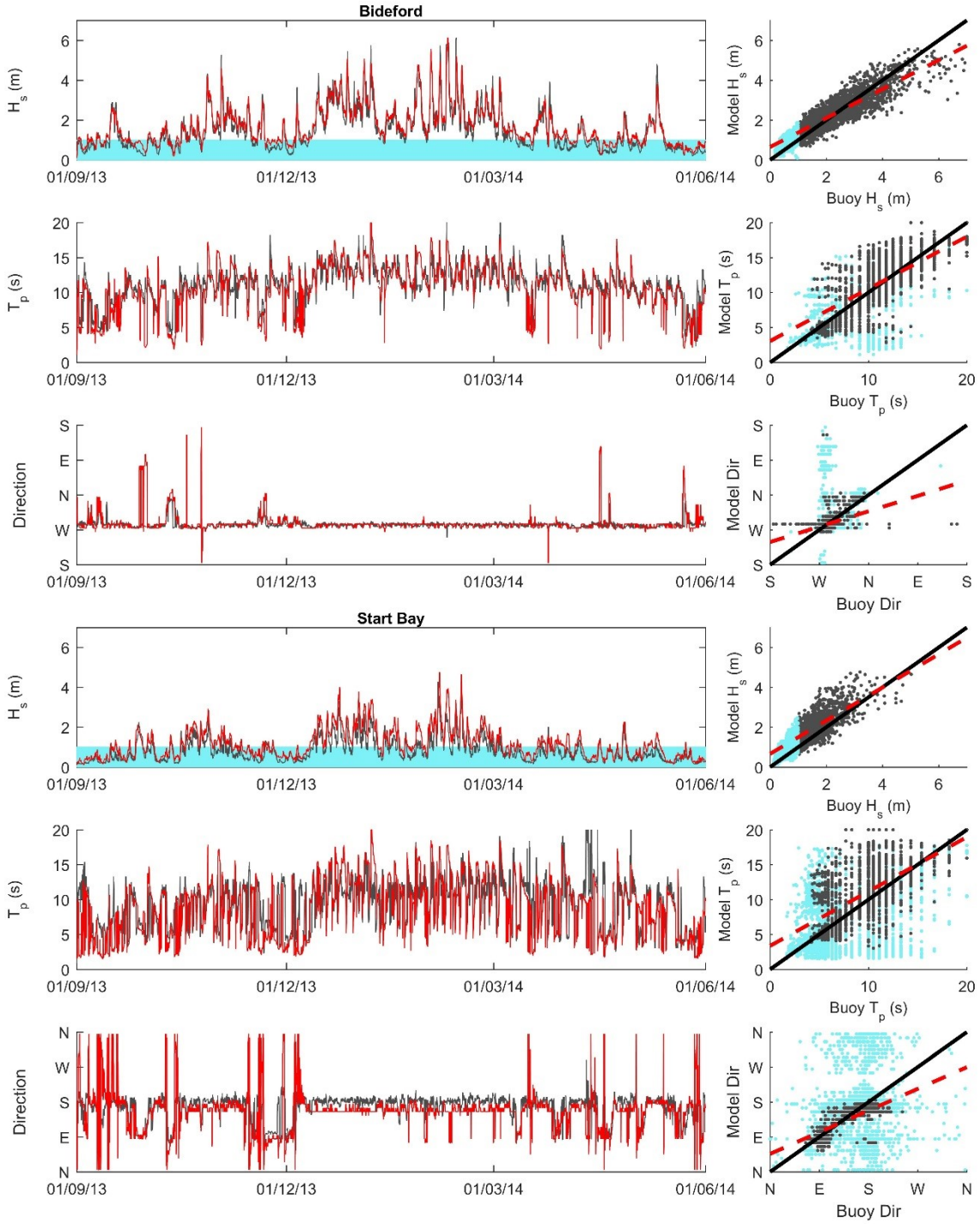

Figure 2.4: Model (red) versus observation (grey) comparisons for wave parameters at Bideford and Start Bay for the full 9 month validation period. The region for H_s < 1m is shaded blue. XY plots on the right show the modelled versus the observed wave parameters. Data where observed significant wave height < 1m are shaded blue. Observation time series have been median filtered over 6 hours for clarity due to considerable scatter in the wave buoy observations; however, validation and the XY plots were performed on the unfiltered data. The 1:1 line of the perfect model and the trend line of the modelled parameters versus the observations are shown. The trend line excludes data where the observed H_s was < 1m.

Table 2.1

Model Validation Statistics for Tidal Elevations, Currents, and Waves, including Residuals from Two Filtering Methods.

Water levels (m)													
		Unfiltered Signal				Low-Pass Residual				Harmonic Residual			
Location	N	R^2	BIAS	WIA	BSS	R^2	BIAS	WIA	MAE	R^2	BIAS	WIA	MAE
G1	13104	0.99	-0.18	0.94	**0.99**	0.80	-0.18	0.46	0.18	0.35	-0.04	0.57	0.17
G2	13104	0.99	-0.02	0.96	**0.99**	0.81	-0.02	0.76	0.09	0.57	-0.06	0.67	0.23
G3	13104	0.995	-0.12	0.96	**0.99**	0.78	-0.12	0.61	0.13	0.27	-0.04	0.56	0.26
G4	13104	0.996	-0.13	0.96	**0.99**	0.74	-0.13	0.58	0.14	0.32	-0.03	0.58	0.20
G5	13104	0.99	-0.17	0.92	**0.97**	0.51	-0.17	0.34	0.18	0.38	0.00	0.56	0.13
G6	13104	0.99	-0.12	0.94	**0.98**	0.69	-0.12	0.53	0.13	0.38	-0.02	0.58	0.13
G7	13104	0.99	-0.16	0.91	**0.96**	0.71	-0.16	0.45	0.16	0.50	-0.03	0.61	0.13
G8	13104	0.86	-0.14	0.75	0.22	0.71	-0.14	0.47	0.15	0.16	-0.01	0.11	0.24
ALL	104832	0.99	-0.13	0.94	**0.99**	0.68	-0.13	0.54	0.15	0.31	-0.03	0.56	0.19
Currents (ms^{-1})													
		Unfiltered Signal				Low-Pass Residual				Harmonic Residual			
Location	N	R^2	BIAS	WIA	BSS	R^2	BIAS	WIA	MAE	R^2	BIAS	WIA	MAE
WHE-E	2811	0.95	0.03	0.89	**0.85**	0.53	0.03	0.09	0.04	0.28	0.01	0.46	0.04
WHE-N	2811	0.93	0.01	0.87	**0.60**	0.43	0.01	0.18	0.01	0.30	0.01	0.53	0.02
WHW-E	5794	0.86	0.03	0.82	**0.74**	0.51	0.03	0.12	0.03	0.03	0.002	0.50	0.11
WHW-N	5794	0.86	0.02	0.83	**0.72**	0.49	0.02	0.17	0.03	0.05	0.004	0.51	0.07
ALL-E	8605	0.88	0.03	0.84	**0.76**	0.53	0.03	0.22	0.03	0.04	0.002	0.50	0.09
ALL-N	8605	0.86	0.02	0.84	**0.68**	0.46	0.02	0.17	0.02	0.06	0.005	0.51	0.05
Waves													
		Hs (m)				Tp (Hs > 1m) (s)					Dir (Hs > 1m) (°)		
Location	N	R^2	BIAS	WIA	BSS	N	R^2	BIAS	WIA	BSS	R^2	BIAS	WIA	BSS
B1	6553	0.74	0.11	0.68	**0.96**	856	0.17	-0.25	0.04	-2.86	0.73	5.99	0.74	**0.72**
B2	6553	0.87	0.15	0.80	**0.93**	3799	0.53	0.11	0.64	**0.83**	0.14	0.80	0.52	**0.69**
B3	6553	0.92	0.12	0.88	**0.97**	4285	0.68	-0.29	0.74	**0.89**	0.38	14.10	0.28	**0.73**
B4	6553	0.87	0.42	0.65	**0.68**	2055	0.28	2.98	0.31	*0.54*	0.16	-7.84	-0.06	*0.58*
B5	6553	0.82	0.39	0.78	**0.73**	3333	0.36	0.82	0.58	**0.71**	0.18	-5.64	0.49	*0.59*
B6	6553	0.89	0.28	0.77	**0.90**	3041	0.29	2.37	0.45	*0.47*	0.30	-12.70	0.22	*0.55*
B7	6553	0.80	0.32	0.66	**0.80**	2000	0.36	1.31	0.51	0.14	0.64	-17.25	0.53	**0.62**
B8	6553	0.62	0.17	0.66	**0.75**	373	0.20	0.23	0.09	-1.11	0.33	-9.02	0.57	0.29
B9	6553	0.79	0.24	0.66	**0.83**	1201	0.25	1.40	0.41	-0.19	0.53	-3.14	0.66	**0.60**
B10	6553	0.88	0.11	0.83	**0.95**	2870	0.32	1.30	0.57	*0.30*	0.31	-5.82	0.41	**0.69**
B11	6553	0.87	0.13	0.83	**0.94**	3174	0.32	1.39	0.58	*0.34*	0.27	-4.90	0.76	**0.92**
B12	6553	0.78	0.28	0.62	**0.62**	963	0.21	2.43	0.30	0.11	0.40	-4.52	0.54	*0.54*
ALL	78636	0.86	0.23	0.78	**0.90**	27950	0.38	1.07	0.62	*0.53*	0.91	-2.98	0.85	**0.84**

Note. Brier skill (BSS) scores are coded for excellent and good (bold), reasonable (italic) and poor (underlined) model skill. For residual water elevations and depth-averaged currents, the mean absolute error is presented instead of Brier skill. See Figure 2.1 for locations.

2.3.4.4 Sand transport

Tide-only bedload transport vectors were compared with observed sand waves from UKHO single beam bathymetry south of Carmarthen Bay (Figure 2.5). Depths along two transects bisecting the sand waves were extracted, referenced to mean sea level (MSL2000). Sand wave asymmetry is a common indicator of sand wave migration in the direction of the steeper face (Knaapen, 2005). Observed sand wave asymmetry (Figure 2.5b-c) and crest orientation qualitatively match predicted spring tide bedload transport vectors, suggesting migration of these waves is controlled by spring tide hydrodynamics. Sand transport magnitude and direction south of the Gower during extreme westerly waves at neaps (~45 $gcm^{-1}s^{-1}$ to the northeast) matches bedload transport rates calculated under similar conditions by Pattiaratchi & Collins (1988) (48 $gcm^{-1}s^{-1}$ to the northeast) from near-bed current meter data. These observations lend confidence to model predictions of potential sand transport, offering a means of validating modelled sand transport in the absence of direct measurements.

Model sensitivity to peak period was tested over extreme waves at springs (details of simulated scenarios is given in Section 2.3.5 and Figure A1 – see Appendix A). The magnitude of the peak period was varied by the model bias ($\pm$1.1s). Across most of the domain this resulted in a reduction of sand transport rates within 20% of the tested reference scenario, and was unlikely to impact the qualitative results presented in this paper (Figure A2).

This study considers potential transport with a homogeneous medium sand bed. The sediment Folk classification for this region is shown in Figure 2.5(d), from the British Geological Survey product DiGSBS250K, with sand classes shown in shades of yellow (Folk, R. L., 1954). Much of this region is comprised of sand or gravelly sand. A comparison between modelled sand transport results from the simulated scenarios and observed grain sizes is discussed in Section 2.5.

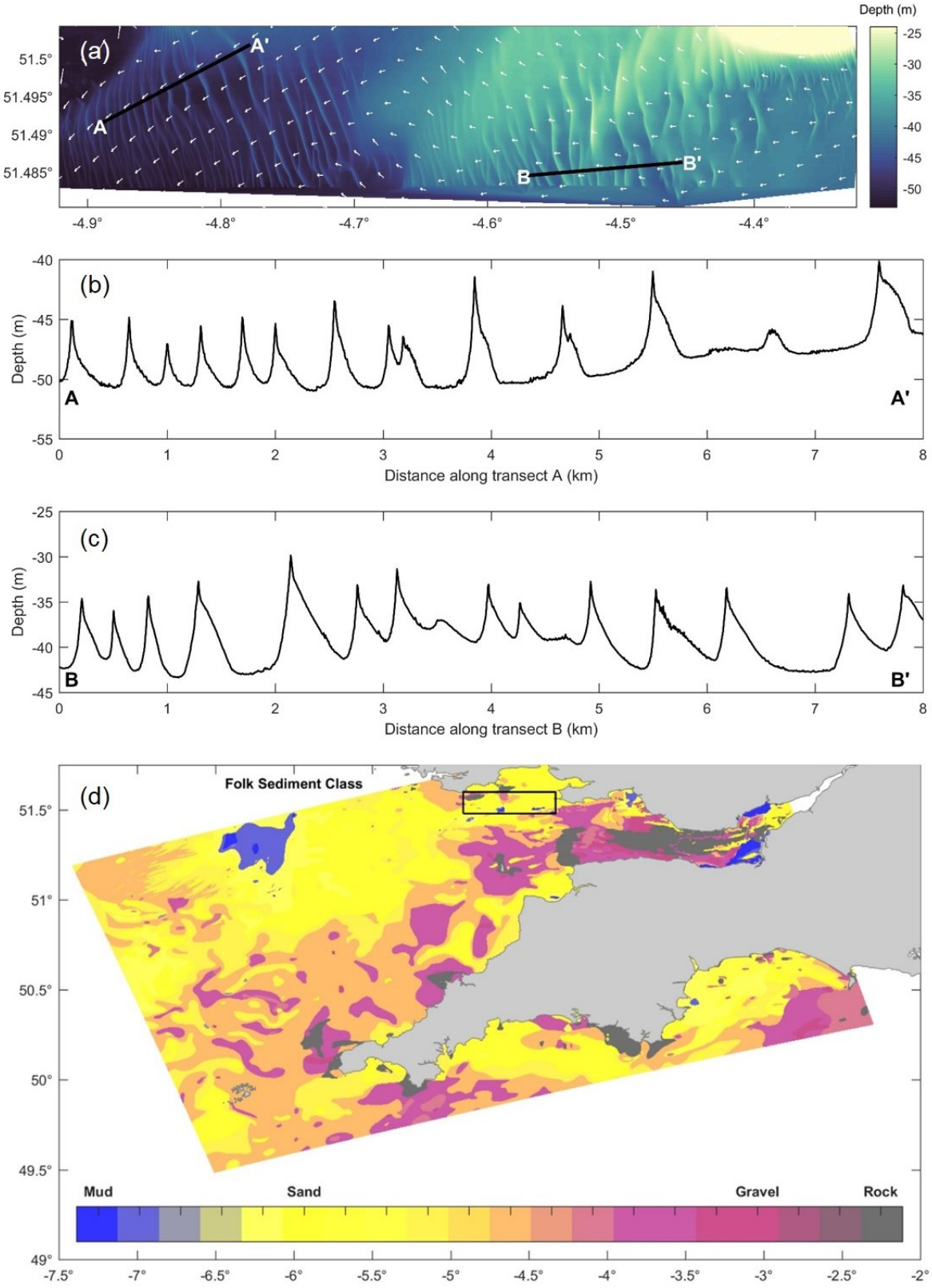

Figure 2.5: (a-c) Observed sand waves from UK Civil Hydrography Programme single-beam bathymetry (UKHO). Predicted spring tide net bed load transport vectors indicate direction only. Transects show sand wave asymmetry indicating bedform migration aligned with the model prediction. (d) Folk sediment class (Folk, R. L., 1954) obtained from British Geological Survey product DiGSBS250K. All classes are included, broadly grouped into mud, sand, gravel or rock.

2.3.5 Simulated scenarios

The inter-dependent relationship between marginal probability distributions of offshore H_s and T_p from four years of WWIII data (2013–2016) on the most south-western and deepest extent of the domain boundary was modelled following a copula approach outlined in Genest & Favre (2007). H_s and T_p were respectively fitted with generalised extreme value and rician marginal distributions (the best fitting distributions using the Akaike Information Criterion), with their joint-probability distribution described by a Gumbel copula (Figure A1a-b).

An extreme (1% exceedance) offshore H_s of 9m is predicted, corresponding to a nearshore H_s of ~6m on the North Coast, matching observed extreme wave heights reported in Scott et al. (2016) of 5.9m at Sevenstones (off Land's End). Two joint-probability $H_s \cap Tp$ exceedance conditions were selected: median $H_s \cap Tp_{50\%}$ (2m, 10.5s) and extreme $H_s \cap Tp_{1\%}$ (9m, 18s). Two directions were selected from the modal wave directions at the same location (Figure A1c), west (270°) and west-northwest (292.5°), resulting in four simulated wave conditions (Figure A1d). Wind was not included, therefore only swell was simulated. Peak orbital velocities in the region are induced by swell waves (Draper, 1967).

Simulations were performed over a full spring-neap tidal cycle with seven days of model spin-up time. Tidal forcing was generated by subtracting the harmonic residual elevation at each boundary node, leaving only the astronomic tide for a period of a full 14.72 day spring-neap cycle (31st January to 16th February 2014). Four consecutive spring tides and four consecutive neap tides were extracted from the cycle and averaged for analysis (Figure A1e).

Additionally, a tide-only simulation and wave-only simulation were performed. The wave-only simulation was coupled to the hydrodynamic module without any hydrodynamic forcing at the open boundaries, to simulate the individual effect of waves on sand transport in the absence of tidal currents, and therefore quantify the wave driven sand transport component. These were then used to determine the contribution of non-linear wave-current interactions.

2.4 Results

Depth-averaged velocity was integrated over springs, neaps and a full spring-neap cycle for the tide-only simulation (Figure 2.6). The residual (mean) current distribution qualitatively matches results published elsewhere (Pingree & Griffiths, 1980; Uncles, 1982, 2010; Holt et al., 2001; Bricheno et al., 2015). The South Coast exhibits an ebb-dominated residual broadly to the southwest, flood and ebb dominance being defined by the half of the tidal cycle contributing most to the residual. The North Coast has a progressively weakening north-eastward residual, interrupted by large headland-enclosed embayments. Large embayments exhibit residual flow into the embayment with return flow at the sides, e.g. Carmarthen Bay, St Ives Bay and Bideford Bay. A ~10cm/s ebb-dominated residual flows through St George's Channel to the southwest before rotating west out of the domain. The Bristol Channel's deep central channel is ebb-dominated, with residual westward flow. The spring-neap residual (Figure 2.6c) is dominated by the spring tide signal (Figure 2.6a) over the North Coast, Bristol Channel and Approaches.; however, for the South Coast it is dominated by a stronger ebb-dominant neap signal (Figure 2.6b). The Isles of Scilly interrupt the residual around the tip of the South West Peninsula with a strong (circa 20 cm/s) clockwise circulation around the archipelago resulting from a flood-dominant north and ebb-dominant south shore.

Headland associated eddies are present west of Portland Bill, Salcombe and The Lizard with smaller eddies present in the lee of smaller headlands (e.g. along the North Coast). The clockwise spring-tide eddy west of Portland Bill drives a south-eastward coastal residual past Chesil. Residual eddies at the margins of the Bristol Channel are associated with linear sandbanks, such as Scarweather Sands south of Swansea Bay. The largest magnitude residuals are off headlands at Hartland Point, Trevose Head, Perranporth, Start Point, Lizard Point, Portland Bill and Morte Point. During springs, a divergence emerges south of Salcombe, and a convergence south of Exmouth. The intervening region is flood-dominant during springs and ebb dominant at neaps. Coastal residuals are largest during springs.

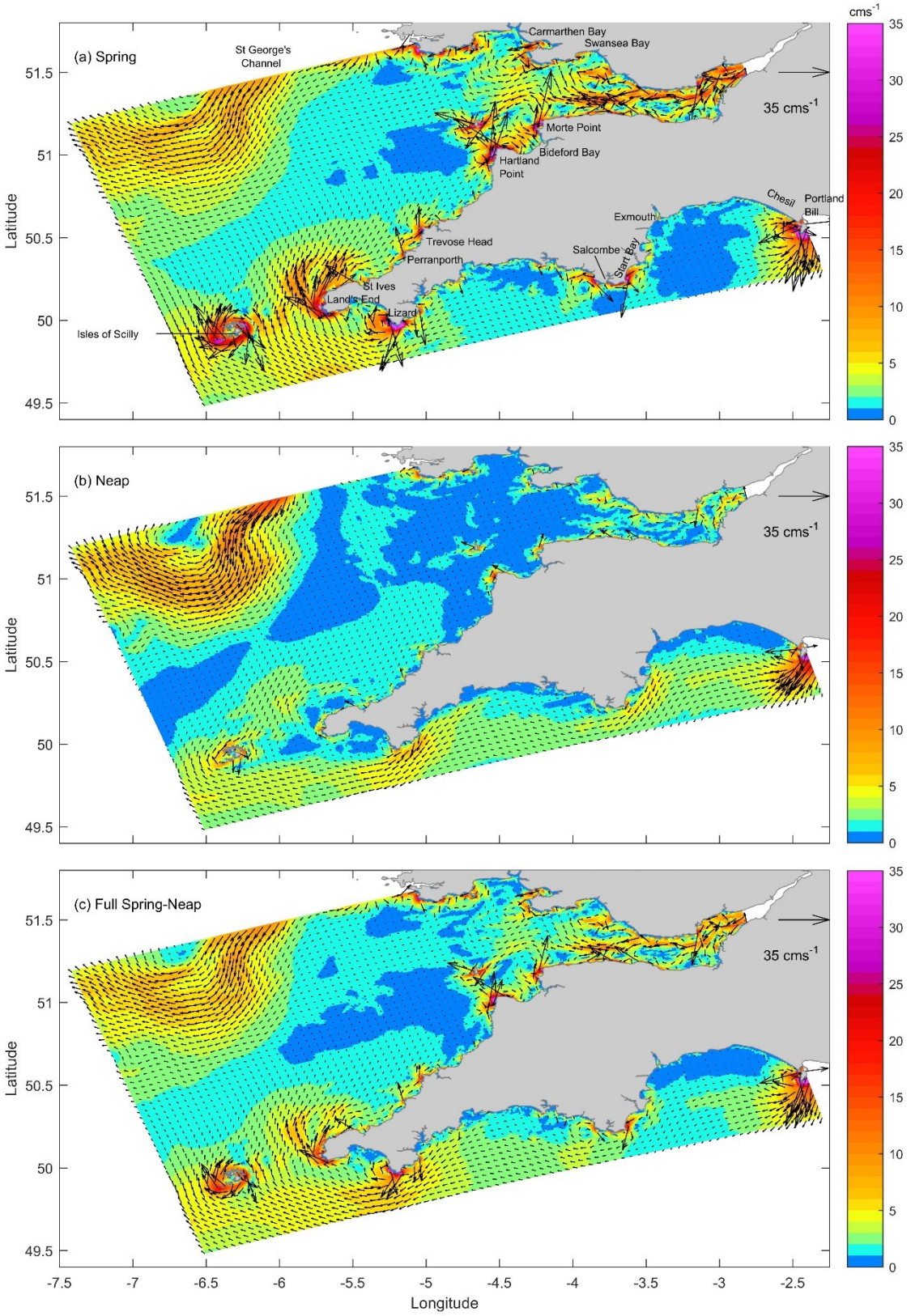

Figure 2.6: Mean current over spring tides (a), neap tides (b) and a full spring-neap tidal cycle (c). Vectors are shown every 4km for clarity. Values are presented in cm/s.

Strong spring-neap differences are present in tidal bed shear stress (Figure 2.7a-b) with spring values up to 15 N/m^2 in the Bristol Channel and off headlands, and values at neaps less than 1 N/m^2 across the domain apart from the Bristol Channel (up to 3 N/m^2). Tides exert a greater relative influence on bed shear stress in the Bristol Channel than the Approaches. Tidal bed shear stress is greater in regions of strong topographic curvature, such as large promontories where tidal currents are greatest.

Results are shown for WNW waves (292.5°). During median waves ($Hs \cap Tp_{50\%}$; Figure 2.7c-d), bed shear stress increases by a factor of two across much of the domain, with similar spatial distribution to tidal bed shear stress. Maximum bed shear stress over a tidal cycle during extreme conditions ($Hs \cap Tp_{1\%}$; Figure 2.7e-f) increases by over an order of magnitude versus tide-only maximum stress along the North Coast and Approaches, and a factor of three in the Bristol Channel. The greatest bed shear stresses are off headlands, with magnitudes >40 N/m^2 at North Coast headlands during extreme forcing. Changing wave direction between WNW and west had little effect on the bed shear stress distribution.

The position of the Bristol Channel shear stress parting is sensitive to incident wave climate and tidal state. The divergence is seen between Porlock and Nash Point at springs for tide-only forcing (Figure 2.7a). At neaps, the tidal divergence shifts up channel to a (less distinct) line between Barry and Bridgewater Bay (Figure 2.7b). Median waves (Figure 2.7c-d) shift the whole divergence slightly eastwards at springs, and the southern part westwards at neaps. Extreme waves shift the bedload parting westward to a line west of Porlock, unaffected by tide state (Figure 2.7e-f). A weak tidal divergence extends south of Salcombe (South Coast) during springs, with convergence south of Exmouth. These are not present during neaps or under wave forcing.

Sand transport maps (Figure 2.8) show net sand transport per tidal cycle for tide-only and coupled wave+tide conditions for WNW waves. Both wave directions simulated result in similar spatial distributions of sand transport, although a slightly greater magnitude is predicted in the Bristol Channel and South Coast for westerly waves with notably greater wave influence in embayments of the northern Bristol Channel.

Significant tide-only net sand transport (Figure 2.8a-b) is isolated to spring tides and areas of the strongest tidal currents, such as the Bristol Channel and around large promontories at neaps. The North Coast has northeast net sand transport during springs, rotating anticlockwise and decreasing in magnitude moving offshore into the Approaches. The Bristol Channel has a bedload parting near Porlock with large potential net sand transports adjacent to the divergence directed up (down) channel to the east (west) of the divergence, interrupted by local deviations into the centre of large embayments. Other locations with large transport magnitudes are off headlands with low magnitudes in embayments. Transport vectors are directed east into the sand-rich Loughor Estuary on the east side of Carmarthen Bay. A divergence is present south of Salcombe, with a convergence south of Exmouth, matching maximum bed shear stress vectors. The Isles of Scilly has a clockwise tide-only sand transport circulation around the archipelago.

The superposition of median waves ($Hs \cap Tp_{50\%}$, Figure 2.8c-d) results in similar spatial patterns of sand transport to tides alone, generally enhancing tidal sand transport in shallow water with little influence in deeper areas where the waves have a smaller effect on the bed. The North Coast net northeast sand transport is disrupted, shifting anticlockwise towards the offshore with greater magnitude closer to shore. Sand transport in the Bristol Channel embayments increases by an order of magnitude. Net sand transport is directed out of Carmarthen Bay, indicating a direction shift versus the low-magnitude tide-only case. Sheltering of the South Coast from westerly and WNW waves by large promontories (Lizard Point, Start Point) combined with a lower tidal range results in distinct regions of minimal tidal and wave forced sand transport within the large scale south-facing embayments (e.g. Lyme Bay).

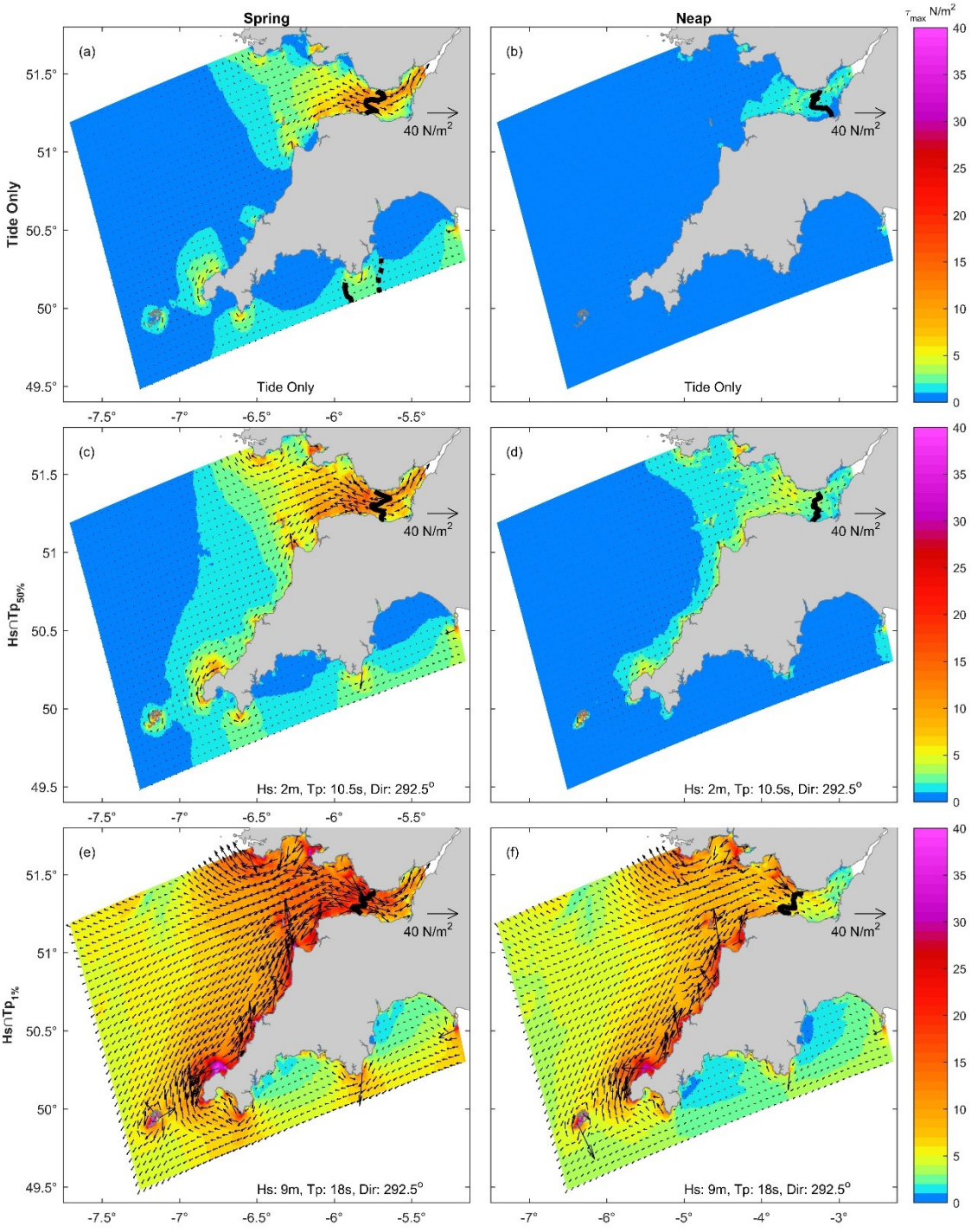

Figure 2.7: Maximum bed shear stress over a spring (left) and neap (right) tidal cycle for the tide-only (top), 50% exceedance (middle) and 1% exceedance wave condition (bottom). Vectors are shown every 6km for clarity. Solid black lines indicate the Bristol Channel and South Coast partings, the dashed line indicates a South Coast convergence zone. Wave conditions are annotated at the bottom of each plot.

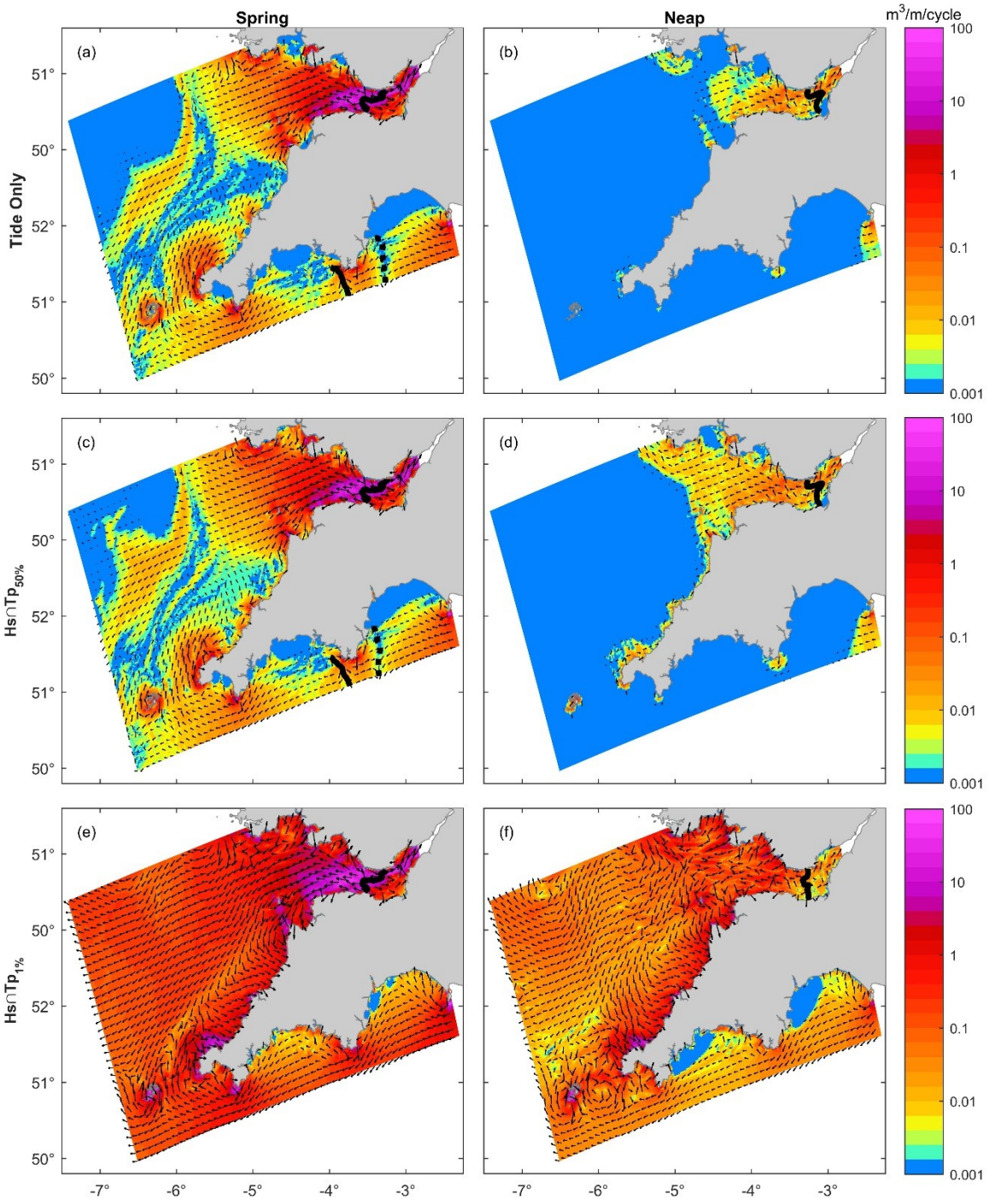

Figure 2.8: Cumulative sand transport for spring and neap tides and tide-only, median ($H_s \cap T_{p50\%}$) and extreme ($H_s \cap T_{p1\%}$) forcing conditions. Sand transport was averaged over four consecutive spring/ neap tidal cycles. Values below 0.00016m^3/m/cycle have been removed based on the lower transport rates presented in the transport formulation validation in van Rijn (2007b). Vectors have been thinned to 6km for clarity. The Bristol Channel and South Coast sand transport partings are shown with black lines. The dashed line represents an area of convergent sand transport.

Extreme superimposed waves ($H_s \cap T_{p1\%}$, Figure 2.8e-f) increase sand transport by an order of magnitude across the Approaches at springs, with greater impact closer to shore. These waves mobilise medium sand at all depths across the domain. The exposed North Coast is impacted most, where tidally immobile sands in shallow water embayments are fully exposed to the incident waves and net sand transport increases by a factor >100 out to 60m depth in areas where tidal net sand transport is low. This indicates the potential for widespread mobilisation of tidally immobile sand deposits during high-energy wave events. Within the Bristol Channel, the impact of waves on sand transport is significantly smaller, as waves propagating up-channel are attenuated due to bottom friction. Although the South Coast is relatively protected from west/ WNW waves due to sheltering provided by Lizard Point (Figure 2.1), increases in transport magnitude of factor ~25 are extensive offshore, decreasing to the east.

To highlight the relative influence of waves, tides and wave-tide interactions on sand transport magnitude, bar graphs of net sand transport per tidal cycle spatially averaged over 5m depth bins are presented (Figure 2.9). The domain was split into the Approaches, Bristol Channel and South Coast to highlight the effect of different hydrodynamic regimes and wave exposures (macrotidal versus mesotidal; exposed versus sheltered). The Isles of Scilly were excluded from the Approaches due to their distinct sand transport regime around the archipelago, which dominated the shallowest depth bins (0-15m).

In the Approaches (Figure 2.9a-b), net sand transport during extreme waves increases by an order of magnitude versus tides alone, and all depths are activated, with sand transport occurring in regions of negligible tidal sand transport. Tide-only sand transport switches off during neaps across the Approaches and little sand transport occurs during median waves at neaps, isolated to the shallowest bins. In the Bristol Channel (Figure 2.9c-d) tides dominate net sand transport during springs <30m depth for all conditions. Median waves have little relative effect at all depths. In deeper waters near the channel mouth, waves dominate net sand transport during high-energy conditions as tide-only sand transport diminishes. Similar to the Approaches, tidal net sand transport in the Bristol Channel is very low during neaps, and waves dominate during high-energy conditions.

The South Coast is relatively sheltered from waves from the west/west-northwest, resulting in relatively low wave-forced sand transport magnitudes, especially in the lee of large promontories such as Start Point and Lizard Point (Figure 2.8). Westerly/WNW wave forcing at the south and east boundaries is atypical for the South Coast (e.g. see the bimodal wave climate at Start Bay; Figure 2.4). Further consideration of Southerly and Easterly wave events would be beneficial when considering wave impacts on sand transport along this coastline. Refraction of westerly/ WNW waves results in sand transport across all depths and exposure of the east side of large embayments to wave forcing (e.g. Lizard Point-Start Point/ Lyme Bay), with sheltering of the west side. Peaks at 10-15m and 25-30m result from enhanced sand transport off Lizard Point, Start point and Portland Bill. Note that these are spatial averages, and considerable local variability was observed (Figure 2.8); however, they serve to highlight and quantify the broad spatial trends in net sand transport.

Wave-only net sand transport is shown for extreme WNW waves (light blue bars - Figure 2.9). Tide-only (dark grey) and wave-only transport is not equal to coupled wave+tide transport (dark blue). In the Bristol Channel, tides exert a greater influence than waves on sand transport and stronger tidal currents are able to transport wave-mobilised sand, despite low wave-only transport magnitudes. The non-linear effect of waves+tides accounts for a significant proportion of net sand transport during extreme conditions, dominating sand transport in the deep central channel where wave-only and tide-only transport magnitudes are low. Waves exert a greater influence than tides on the exposed North Coast during extreme conditions. During median conditions, tide and wave driven sand transports have similar magnitude. Non-linear interactions are dominant for depths >30m. At neaps, waves dominate sand transport with significant sand transport occurring only in shallow water for median waves, negligible tide-only sand transport, and smaller contributions from non-linear wave-tide interactions.

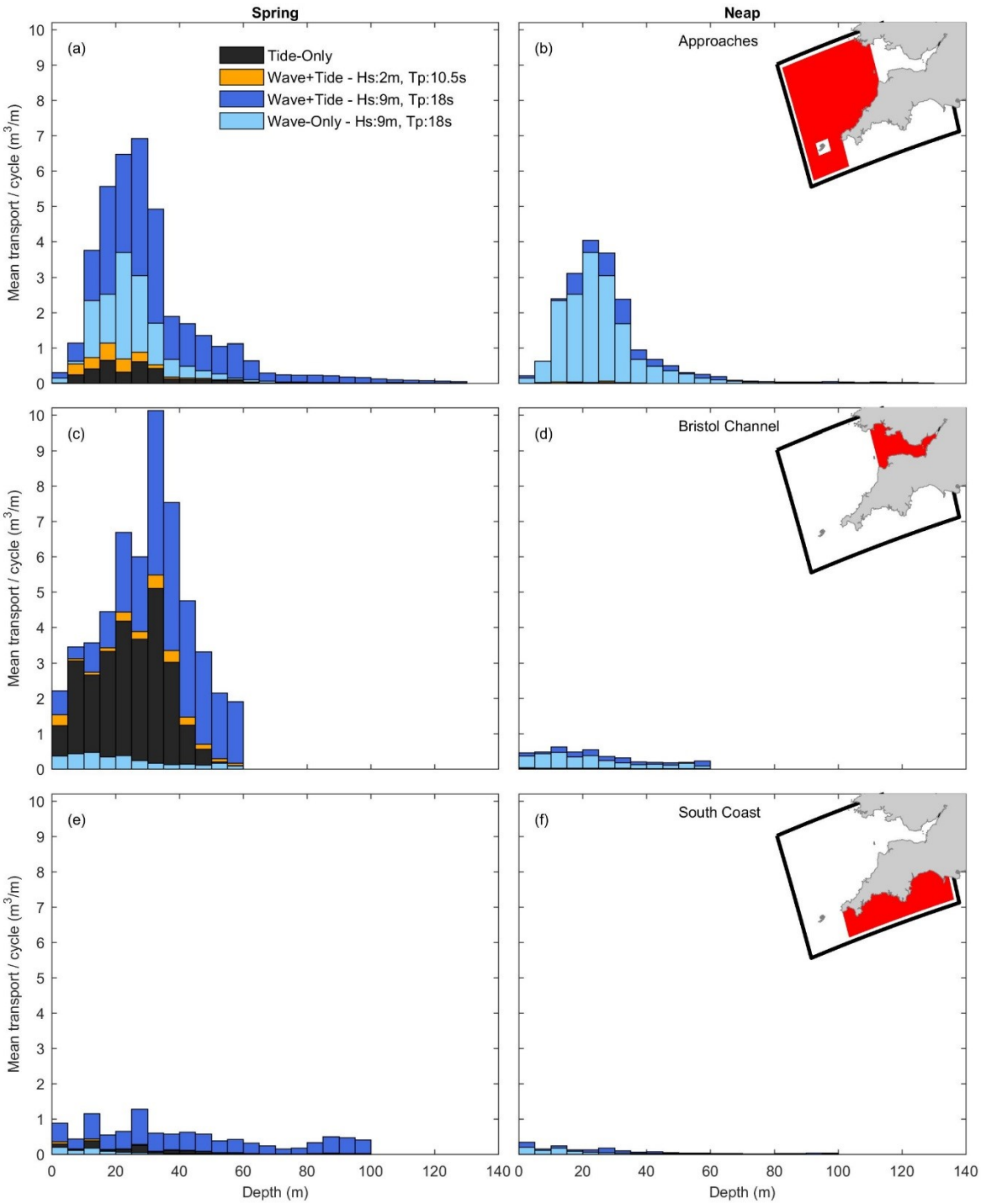

Figure 2.9: Sand transport integrated over 5m depth bands for the Approaches (a-b), Bristol Channel (c-d) and South Coast (e-f), for tide-only, wave-only and wave+tide conditions. Heights of the bars represent the spatial mean sand transport magnitude per tidal cycle over that depth band. The wave conditions shown are for WNW waves (292.5°). Wave direction had a small effect on the magnitude however the distribution remained the same for Westerly and WNW waves.

2.5 Discussion

This paper has presented residual tidal circulation, maximum bed shear stress and sand transport rates for extreme and median wave conditions and spring and neap tides on a macrotidal exposed coast. A calibrated and validated coupled hydrodynamic and wave numerical model of the South West UK was used.

2.5.1 Comparison with observed bedforms, grain size distributions and literature

This study considers potential sand transport using a homogeneous medium sand bed. Further research integrating different sediment classes taken from observed size distributions could enable an assessment of the relative influence of tidal currents and waves on sediment transport paths for different sediment classes and the creation of an accurate regionalisation for this area and a regional sediment budget based on realistic sediment availability. Much of the bed in this region is sand/ gravelly sand, although areas of gravel, rock and mud are present (Figure 2.5). Areas of gravel or rock correspond to strong potential sand transports predicted in the tide-only scenario, while areas of mud correspond to areas with very weak or negligible potential tidal sand transport.

In the Bristol Channel, a bedload parting zone is predicted (Figures 6 & 7), in agreement with previously published literature (Pingree & Griffiths, 1979), and supporting the bedload parting model argued by Stride & Belderson (1991). The region of the predicted divergences in the Bristol Channel coincides with rock and coarse sediment classes observed (Figure 2.5d) and erosional zones reported by McLaren et al. (1993), lending further support to the prediction. The Bristol Channel bedload parting zone is variable with the tidal state. During springs, the position of the bedload parting in sand transport extends between Porlock and Barry for all wave conditions. During neaps, the bedload parting moves up-channel reflecting the shift in the divergence of max bed shear stress (Figure 2.7). The presence of gravel barriers, such as observed at Porlock (Jennings et al., 1998; Orford & Jennings, 1998) matches the observation of Anthony (2002) that bedload parting of sand exposes gravel banks enhancing shoreward gravel reworking by storm waves and contributing to the formation of gravel barriers. These observations complement the observed sand wave morphology (Figure 2.5a-c), further supporting the

predictions of this model. Further work at this scale could examine hydrodynamic and wave controls on regional sand wave morphology and behaviour (e.g. Campmans et al., 2018a,b; Damen et al., 2018).

Seaward residual currents occur in the deeper main channel of the Bristol Channel, matching lower-resolution model results from Uncles (1982), partly driven by localised lowering of mean sea level at the seaward boundary relative to the Severn mouth. Return flow occurs in areas of low or negative gradients in tidal energy, such as embayments. A progressive tidal wave drives a progressively weakening northeast residual along the North Coast towards the Bristol Channel, matching modelled residuals published elsewhere at much lower resolution (Pingree & Le Cann, 1989; Holt et al., 2001). This drives a progressively weakening northeast net sand transport, interrupted close to shore by several embayments, reaching insignificant levels near Bude Bay indicating sand transport in this area is wave-dominated, in agreement with coastal management reports (Welshby & Motyka, 1989; Motyka & Brampton, 1993). Residual circulation is enhanced in regions of strong topographic curvature such as headlands, around Land's End and islands such as Lundy and the Isles of Scilly. Consequently, these areas exhibit stronger tidal influence on potential sand transport.

Headlands are associated with tidal residual eddies with convergent sand transport, some matching the locations of well-known sand banks, such as Skerries Bank near Start Point (Pingree & Maddock, 1979). Convergence at these locations is enhanced during extreme waves. Headlands act as a focal point for tidal and wave energy, resulting in enhanced bed shear stresses and resuspension of sediments in these regions of higher residual currents and consequently the greatest potential sand transport rates (although in reality this will be limited by sediment availability) (Uncles, 1982, 2010; Carter et al., 1990; Draper et al., 2013). Median waves enhance sand transport off headland tips in the tidal transport direction, whereas extreme waves can dominate sand transport direction, potentially causing a full-reversal. This indicates open coast, macrotidal, exposed, headland-bound embayments such as those along the North Coast are likely headland bypassing candidates, and the directionality of this process likely depends upon the incident wave height and direction (Klein, et al., 2010; Goodwin et al., 2013; Vieira da Silva et al., 2016; McCarroll et al., 2018). Valiente et al. (2019a) observed significant sediment

transport beyond the depth of many headland cross-shore extents, challenging the notion of embayments being closed sediment cells. Higher resolution modelling is required to examine the contribution of headland and embayment morphologic controls on headland sand bypassing during different conditions on a wider range of headland-bound embayments.

2.5.2 Wave-induced changes in sand transport direction

Changes in net sand transport direction are evident between extreme wave, median wave and tide-only conditions. These changes are presented in Figure 2.10, comparing both wave conditions with the tide-only prediction by subtracting the wave+tide from the tide-only transport directions. Little change in direction is observed at neap tide for median waves. Hydrodynamic and wave parameters and sand transport timeseries for example points I-VI are shown in supplementary Figures S2-7. Large direction changes are present offshore in the Approaches during springs, associated with variations in the weak tide-only transport direction (subplot I; Figure A3). A reversal in transport direction is predicted for outer Carmarthen Bay (subplot II; Figure A4) during median versus extreme waves, with net sand transport directed out of the embayment for median waves. Tide-only sand transport is weak here. Ebb asymmetry in current magnitude (strongest on the ebb) results in ebb asymmetry in bed shear stress and ebb dominant sand transport for median waves. During extreme forcing, bed shear stress is modulated by water level, with a sustained increase over low water and a peak for waves propagating with the current (flood). Combined with a longer flood duration, this results in flood dominated net sand transport for extreme waves.

At St Ives Bay, sand transport around the west headland reverses from sand leaving to entering the bay (subplot IV; Figure A6). Tide-only and median wave depth-averaged velocity is ebb-asymmetric, with equal flood and ebb durations, driving ebb-dominated sand transport. Under extreme waves the currents become flood-asymmetric with a longer flood duration due to the tidal flood direction aligning with the modal wave directions at this site, driving flood-dominated sand transport. Changes in sand transport direction around headlands could have significant implications for adjacent beach response to extreme storms. Beaches on the west of St Ives Bay accreted during the extreme 2013/14 winter storms when other North Coast beaches experienced net erosion (Burvingt et al., 2017). The west side of St

Ives Bay is an area of convergence during extreme waves and divergence during tides-only. Offshore from the North Coast sand transport vectors shift clockwise towards the shore under extreme waves, contrasting the median wave case (subplot III; Figure A5). Extreme wave spring sand transport vectors match closely those for neaps, where tide-only sand transport is effectively switched off, indicating this shift results from wave-dominance of sand transport.

The South Coast experiences a sand transport reversal south of Start Point under extreme waves, as the region of flood-dominated sand transport becomes ebb-dominant (subplot V; Figure A7). Tidal currents have flood-asymmetry driving flood dominated tidal and median wave sand transport. Tidal currents and elevations are in phase at this location, resulting in enhanced bed shear stress at low water (peak ebb) under wave forcing. The effect is greatest for extreme waves, driving a shift to ebb-dominant sand transport. Porter-Smith et al. (2004) found swell waves were most effective at mobilising sediments at low water, and water level variation must be considered when estimating sand transport in combined wave and tidal flows.

Extreme waves cause sand transport reversals in the margins of the outer Bristol Channel at neaps (subplot VI; Figure A8). Pattiaratchi & Collins (1988) reported this reversal for similar conditions observed at a point south of the Gower peninsula, shown here to be part of a broader directional trend of wave-dominated, up-channel directed transport during high-energy conditions at neaps. Currents at this location are ebb-asymmetric resulting in ebb-asymmetry of bed shear stress for tides and median waves driving ebb-dominant sand transport. Under extreme waves, bed shear stress is modulated by water level with a sustained increase over low water. Enhanced wave impact at low water shifts net sand transport direction in the up-channel direction of wave propagation for low ebb-velocities, resulting in a shorter period of ebb than flood transport. Additionally the sand transport magnitude is higher with waves following the current (flood) than opposing (ebb).

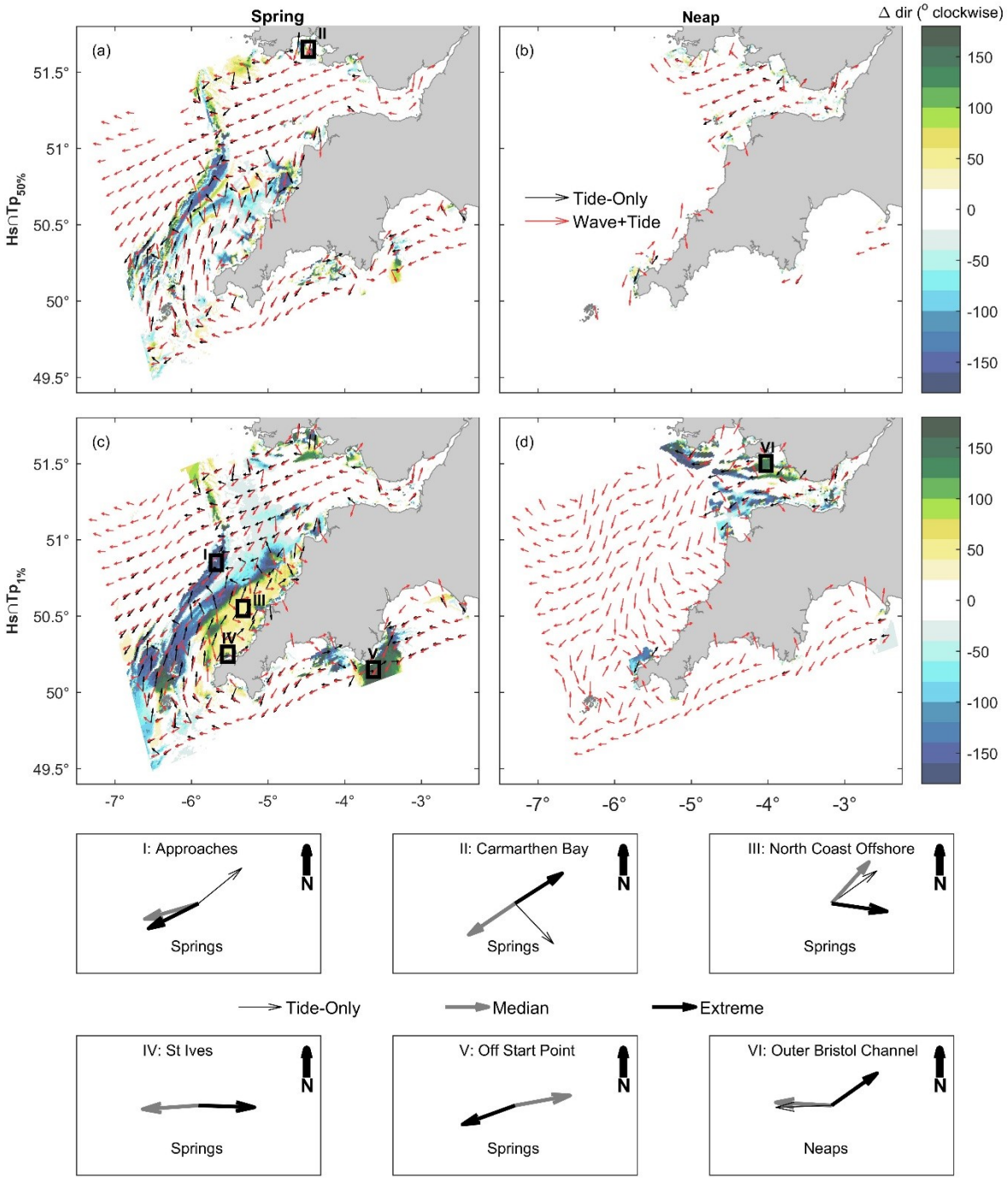

Figure 2.10: Changes in sand transport direction relative to the tide-only simulation for WNW wave forcing. Vectors represent net sand transport direction only. Red (black) arrows represent wave+tide (tide-only) forced sand transport direction. Areas of interest are marked and their sand transport directions shown in subplots I-VI. Bold arrows in I-VI represent wave forced transport with grey indicating median, black indicating extreme waves+tides; thin black arrows are tide-only.

2.5.3 Classification of wave-tide dominance

Net sand transport magnitude per tidal cycle for the tide-only, wave-only and wave+tide simulations was used to determine the contribution from non-linear wave-tide interactions, NL:

$$NL = WT - W - T \tag{2.28}$$

Where WT, W and T are the combined wave+tide, wave-only and tide-only net sand transport magnitudes respectively. Two ratios were used to determine firstly the relative influence of waves (including non-linear wave-tide interactions) versus tides, and secondly the relative contribution of non-linear wave-tide interactions versus waves alone. These ratios are:

$$R1 = T:(W + NL), \tag{2.29}$$

$$R2 = W:NL \tag{2.30}$$

Increasing (decreasing) values of R1 indicate increasing tide (wave) dominance of sand transport. Regions with $R1 > 3$ were classified as "Tide-dominated", T. Further subdivision of regions where $R1 < 3$ was made using $R2$. Increasing values of R2 indicate increasing dominance of the wave-only contribution to net sand transport, while decreasing values indicate increasing non-linear interaction dominance. Regions where $R1 < 1/3$ and $R2 > 3$ were classified as "Wave-dominated", W. Regions where $R1$ & $R2 < 1/3$ were classified as "Non-linear Dominated", NL. The full classification is shown in Figure 2.11. Sub-divisions are shown for intermediate ratios in the form "A(b)" where A indicates the dominant forcing and (b) indicates the sub-dominant forcing. For example, W(t) indicates wave dominant sand transport with a sub-dominant tidal contribution. Regions where $1/3 < R1$ & $R2 < 3$ were classified as "Mixed". From here on, wave-dominance refers to "Wave-dominated" regions, indicating wave-only sand transport is the major contribution to net sand transport per tidal cycle.

For median waves (Figure 2.11a-b), tides are dominant across much of the region except where tide-only sand transport is low and non-linear wave-tide interactions become either a sub-dominant or dominant forcing. Median wave dominance at springs is isolated to shallow waters in North Coast embayments where tide-only sand transport is very low. Median wave dominance at neaps becomes more extensive along the North Coast, Isles of Scilly and inner Carmarthen Bay where tide-only sand transport is negligible. At neaps, tide dominance is restricted mainly to

the Upper Bristol Channel and off major promontories. Non-linear interactions become dominant or sub-dominant in the Outer Bristol Channel where tide-only sand transport is weaker.

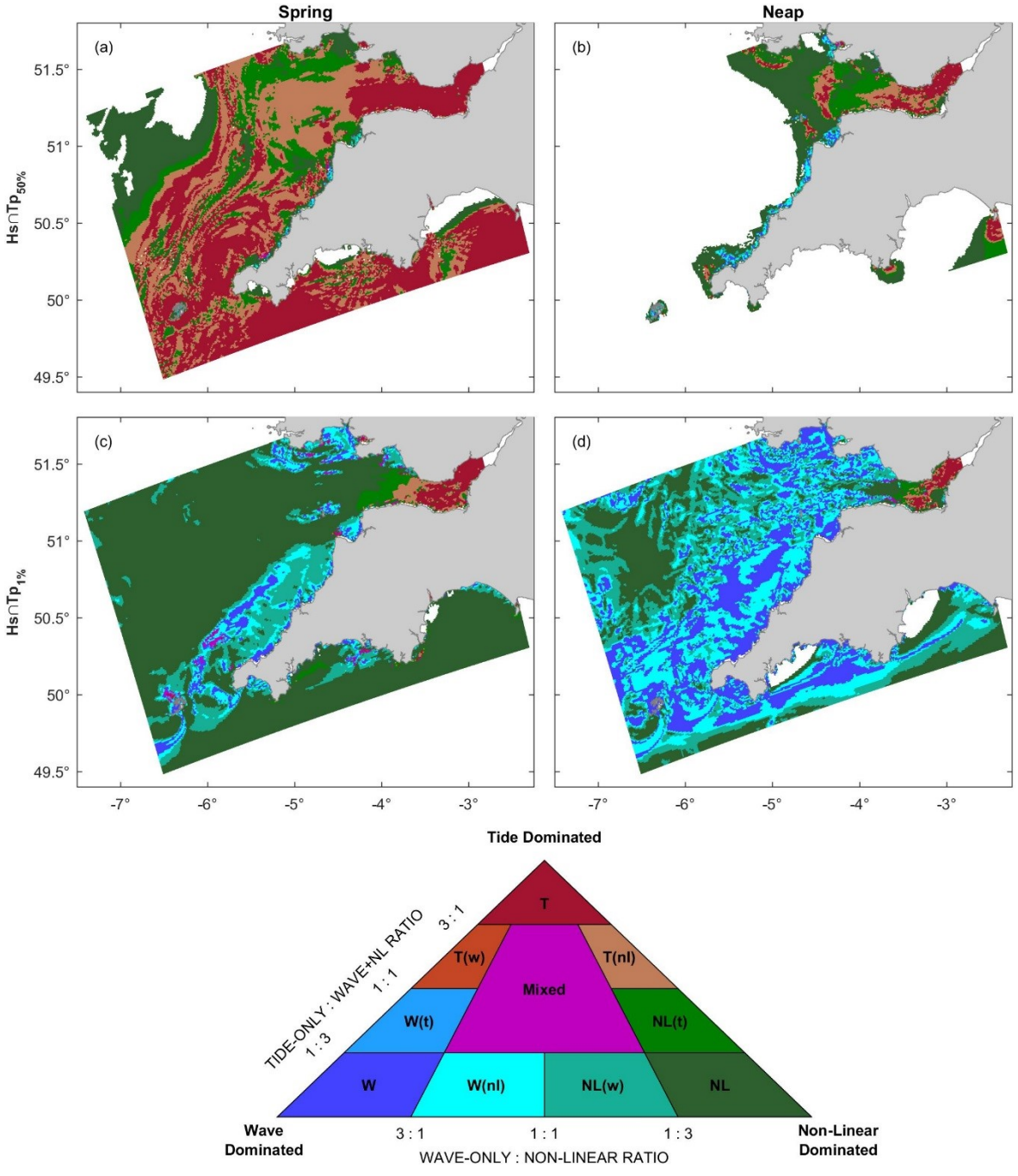

Figure 2.11: Wave-tide dominance classification of the South West UK during different wave and tide exceedance conditions for the modal wave direction (292.5°), accounting for the relative influence of non-linear wave-tide interactions. Based on potential net sand transport magnitude per tidal cycle. Areas where wave+tide sand transport was < 0.00016m^3/m/cycle have been removed based on the transport formulation validation in van Rijn (2007b).

Tides are dominant up-channel of the upper Bristol Channel at springs, and up-channel of the Lower Severn at neaps for all wave conditions, due to wave attenuation and tidal flow constriction as it progresses up-channel resulting in larger tidal currents. These are the only regions that remain tide-dominated under all conditions. Under extreme waves at springs (neaps), the Outer Bristol Channel becomes non-linear (wave) dominated. The spatial pattern of transition to wave-dominance under extreme waves at neaps in the Outer Bristol Channel (Figure 2.11b,d) matches the pattern of sand transport reversals seen in Figure 2.10(d) and observed by Pattiaratchi & Collins (1988), supporting the assertion of wave-dominance in this area under these conditions.

The exposed North Coast becomes wave-dominated under extreme waves (Figure 2.11c-d). Other areas of wave-dominance are large embayments (e.g. Carmarthen Bay) and exposed areas of the South Coast. Propagation of WNW waves to the west-facing stretches of the South Coast is evident in the pattern of wave/ non-linear dominance at neaps (Figure 2.11d). At neaps, extreme waves are dominant across much of the region, with a sub-dominant non-linear interaction contribution. This is in agreement with predictions that waves cause significant additional net sand transport by enhancing transport in shallower, exposed regions where the tide-only contribution is small (van der Molen, 2002).

Non-linear wave-tide interactions become the dominant forcing mechanism for sand transport across most of this macrotidal environment during 1% exceedance waves at springs (Figure 2.11c), contrasting wave-dominance at neaps (Figure 2.11d). At neaps, non-linear interactions significantly contribute to net sand transport, as shown in Figures 8 and 11(b,d). This emphasises the need for a fully coupled wave and hydrodynamic model for studies of sand transport paths in macro- and meso-tidal environments exposed to extreme incident waves. The non-linear effect of the interaction between waves and tides can significantly enhance sand transport beyond transport calculated for waves and tides in isolation.

This model considers depth-averaged hydrodynamics. Accordingly, some three-dimensional effects are parameterised, such as secondary flow generation by rotating current fields, or turbulence generation by breaking waves and enhanced bottom friction. Other processes are modelled in a depth-integrated manner, such

as the energy dissipation due to wave-breaking, whitecapping and bottom friction. To investigate the potential impact of this on the results and classification scheme presented, a number of unvalidated 3D tests were conducted for the same scenarios using 10 terrain-following sigma layers and a $k - \epsilon$ turbulence scheme.

The impact of the addition of sigma layers was mainly to enhance the tide-only and wave-only net transport magnitude, with a larger relative increase in potential wave-related sand transport offshore in waters deeper than 60m where net transport magnitudes are small (Figure A9). Offshore, low net transport regions shifted from purely non-linear dominated NL to non-linear dominated with a wave contribution NL(w) for extreme waves at springs, with wider spread wave-dominance along the North Coast. There was more wave dominance for extreme waves at neaps, although the tide-dominated region in the upper Bristol Channel remained unchanged. Qualitatively, the spatial pattern of net sand transport remained the same, and the direction changes presented in Figure 2.10 were predominantly unchanged except for where weak tide-only sand transport was enhanced in the 3D simulation. Non-linear interactions remained dominant or subdominant across most of the domain during extreme wave forcing, supporting the conclusions presented here.

This classification has potential to be applied in other shelf areas; however, this currently requires a coupled hydrodynamic, wave and sediment transport model. Chapter 3 presents a predictive relationship for this classification based on readily available tide and wave data. Many regions globally experience high wave and tidal energy. Harris and Coleman (1998) estimate swell waves were able to mobilise 0.1mm quartz sand over 41.6% of the earth's continental shelves over 3-years. Waves dominate sediment transport in areas of the New Zealand and Australian shelves (Carter & Heath, 1975; Porter-Smith et al., 2004; Hale et al., 2014; Moriarty et al., 2014). Wave-current interactions are significant drivers of sediment resuspension on the Northwest Iberian shelf (Zhang et al., 2016). The Northwest European shelf experiences high tidal and high wave energy, which is enhanced by wave-current interactions in areas of strong tidal currents (Hashemi & Neill, 2014). Sand transport on the UK east coast was designated as tide-dominated by van der Molen (2002), ignoring wave-current interactions. However, the results of this study suggest wave-tide interactions can have a significant impact on net sand

transport even for median waves. This classification scheme should be tested in similar environments globally to test for wave-, tide- or non-linear interaction dominance of sediment transport.

2.6 Conclusions

- A Delft3D numerical model was used to investigate the relative influence of tidal and wave forcing on potential sand transport in an energetic, exposed, macrotidal environment. The South West UK was used as a test site with a uniform medium sand bed allowing direct comparison between different regions. Waves were forced with median (50% exceedance) and extreme (1% exceedance) wave scenarios from two modal directions at spring and neap tides. Tide-only, wave-only and fully coupled scenarios were simulated for all forcing combinations.

- Bedload transport directions match observed sand wave asymmetry and orientations for tides-only and previously published observations under energetic waves. Regions of the greatest potential sand transport or major divergence correspond to observed coarse sediment classes. These observations indicate a potential sand transport approach can give indications of sediment transport pathways, divergences and likely size distributions in the absence of detailed observations.

- Sand transport across this macrotidal environment is heavily influenced by waves. The greatest influence is in areas fully exposed to the incident wave forcing. Extreme waves increase potential sand transport by over an order of magnitude, and are capable of mobilising medium sand below 100m depth.

- Waves can strongly influence sand transport direction. Median waves predominantly enhance sand transport in the tidal direction, whereas extreme waves are able to induce directional shifts and full-reversals.

- Tidal forcing is more important around headlands and islands, and in regions where constriction of the tidal wave produces strong tidal currents. Elsewhere, tidal forcing is significant only at springs, and is effectively switched off during neaps except under extreme waves.

- A new classification scheme was created for the region in terms of tide-only, wave-only or non-linear wave-tide interaction dominance of net sand transport with potential for application elsewhere.

- During median waves at springs the whole region is tide-dominated apart from where tidal sand transport is weakest. Wave dominance is restricted to shallow embayments fully exposed to the incident waves.

- Wave-tide interactions (encompassing radiation stresses, stokes drift, enhanced bottom friction, enhanced bed shear stress, current and depth-induced wave refraction, Doppler shift and wave-blocking) non-linearly enhance net sand transport. These processes are dominant or sub-dominant across most of the region during extreme waves for all tide conditions, and during median waves at neaps, apart from where the tidal constriction and wave attenuation are greatest. This implies a critical need to consider the impact of wave-tide interactions on regional sand transport patterns on energetic, exposed continental shelves globally.

3 Predicting dominance of sand transport by waves, tides and their interactions on sandy continental shelves

The work in this chapter is accepted for publication in:

King, E. V., Conley, D. C., Masselink, G. & Leonardi, N. (2021). Predicting dominance of sand transport by waves, tides and their interactions on sandy continental shelves. *Journal of Geophysical Research: Oceans*, 126, e2021JC017200. https://doi.org/10.1029/2021JC017200

The work in this chapter was conceived and conducted by Erin King, with supervisory support from Professor Daniel Conley, Professor Gerd Masselink and Dr Nicoletta Leonardi

The work in this chapter addresses the following thesis aims:

(i) Advancing our understanding and quantification of the impact of waves, tides and their interactions on net sand transport;

(ii) Understanding how net sand transport varies across the continental shelf and how that relates to observed sediment distributions and bed morphology.

.

Key Points:

- Dominant forcing mode and magnitude of net sand transport is predictable from readily available data using a k-Nearest Neighbour algorithm.

- Sand waves increase in length and asymmetry, and decrease in height, for increasing wave-dominance under extreme conditions.

- Over an average year, meso-macrotidal areas are tide-dominated, while shallow, finer grained, microtidal regions are wave-dominated.

Chapter Abstract

Waves and tidal currents resuspend and transport shelf sediments, influencing sediment distributions and bedform morphology with implications for various topics including benthic habitats, marine operations, and marine spatial planning. Shelf-scale assessments of wave-tide-dominance of sand transport tend not to fully include wave-tide interactions (WTI), which non-linearly enhance bed shear stress and apparent roughness, change the current profile, modulate wave forcing, and can dominate net sand transport. Assessment of the relative contribution of WTI to net sand transport requires computationally/ labour intensive coupled numerical modelling, making comparison between regions or climate conditions challenging. Using the Northwest European Shelf, we show the dominant forcing mode and potential magnitude of net sand transport is predictable from readily available, uncoupled wave, tide and morphological data in a computationally efficient manner using a k-Nearest Neighbour algorithm. Shelf areas exhibit different dominant forcing modes for similar wave exceedance conditions, relating to differences in depth, grain size, tide range, and wave exposure. WTI dominate across most areas in energetic combined conditions. Over a statistically representative year, meso-macrotidal areas exhibit tide-dominance, while shallow, finer grained, amphidromic regions show wave-dominance, with WTI dominating extensively >30m depth. Seabed morphology is strongly affected by sediment transport mode, and sand wave geometry varies significantly between predicted dominance classes with increased length and asymmetry, and decreased height, for increasing wave-dominance. This approach efficiently indicates where simple non-interactive wave and tide processes may be sufficient for modelling sediment transport, and enables efficient inter-regional comparisons and sensitivity testing to changing climate conditions with applications globally.

3.1 Introduction

Residual (net) sediment transport patterns influence the transport and fate of continental shelf sediments, influencing sediment distributions and morphological evolution (Stride, 1963; Pingree & Griffiths, 1979; Pingree & Le Cann, 1989; Harris & Collins, 1991; van der Molen, 2002; Xu et al., 2016; Zhang et al., 2016; Leonardi & Plater, 2017; King et al., 2019). Waves and tidal currents result in resuspension and transport of shelf sediments (Pattiaratchi & Collins, 1988; Thompson et al., 2019), influencing sand wave morphology (Damen et al., 2018; Wang et al., 2019) with implications for marine spatial planning of pipelines and cables for windfarms and offshore renewable energy (Németh et al., 2003; Roetert et al., 2017; Cheng et al., 2020), dispersal of contaminants (e.g. dredge disposal; Cieślikiewicz et al., 2018; Uncles et al., 2020), and the fate of shoreface nourishments (Luijendijk et al., 2017). Shear stresses and sand transport driven by tides and waves influence benthic communities through disturbance, whilst also acting as a vector for recolonization (Hall, 1994; Levin, 1995; Dernie et al., 2003; Reiss et al., 2010; Harris, 2014; Aldridge et al., 2015; Bricheno et al., 2015). The relative impact of wave and tidal forcing influences sand wave morphology and migration rates (Van Dijk & Kleinhans, 2005; Campmans et al., 2018a,b; Damen et al., 2018), causing potential disturbance and affecting the distribution of benthic communities (Harris, 2014; Damveld et al., 2018, 2020). Predictive habitat suitability modelling requires an understanding of physical disturbance regimes and knowledge of the dominant drivers of sand transport at the shelf scale is important (Harris, 2014).

Assessments of the relative impact of waves and tidal currents on the bed across sandy continental shelves have been conducted. Bricheno et al. (2015) map the relative impact of tides and storm events at the bed across the NW European Shelf over a 10-year period. South West exposed coasts and shallow water areas were found to be most at risk from large waves and thus are most likely to show wave-dominated transport, and modelling suggests the maximum benthic force is wave-dominated (Bricheno et al, 2015). The detailed distribution of physical disturbance shows a complex relationship between depth, tidal stress, wave fetch and grain size, with large uncertainty (Aldridge et al., 2015). Porter-Smith et al. (2004) classify the Australian continental shelf based on sediment threshold of motion exceedance from tidal currents and swell waves with classes ranging through waves-only, wave-

dominated, mixed, tide-dominated and tide-only. Van der Molen (2002) considers the relative impact of waves, winds and tides on sand transport in the Southern North Sea. However, at present, shelf scale analyses of dominant forcing modes for sand transport do not consider wave-tide interactions. Wave-tide interactions (WTI) non-linearly enhance bed shear stress and apparent roughness due to interaction between wave and tidal bottom boundary layers, influence the vertical current profile and modulate wave forcing through tidal elevation changes (Grant & Madsen, 1979, 1986; Kemp & Simmons, 1982, 1983; Fredsøe, 1984; Nielsen, 1992; Klopman, 1994; Umeyama, 2005; Olabarrieta et al., 2010; Hopkins et al., 2015; Tambroni et al., 2015).

Boundary layer processes dominated by WTI are fundamentally different from those dominated by either waves or tides, and WTI can dominate net sand transport across large areas of the shelf over a tidal cycle (King et al., 2019). Analyses excluding WTI may underestimate net sand transport under combined wave and tide conditions where WTI can dominate. A classification scheme was proposed by King et al. (2019) for net sand transport per tidal cycle to account for contributions of waves, tides and WTI (accounting for radiation stresses, Stoke's drift, enhanced bottom-friction and bed shear stress, refraction, current-induced Doppler shift, tidal modulation of wave heights and wave blocking); however, this currently requires computationally expensive coupled numerical modelling to assess. A computationally efficient method to assess the dominant sand transport mode and magnitude will enable efficient inter-regional comparison of the role of waves, tides and WTI on sand transport at scale and under varied or changing climate forcing. This enables efficient assessment of where simple non-interactive wave and tide processes may be sufficient to model sediment transport, particularly relevant where application of a model or parameterisation is predicated on dominance of waves (e.g., parameterisations of headland bypassing; King et al., 2021; McCarroll et al., 2021b), or tides (e.g., models of sand wave morphological evolution in tide-dominated environments; Besio et al., 2007). It also enables efficient assessment of the role of combined wave and tidal processes on seafloor morphology, such as by comparing dominant processes with observed sand wave geometries (e.g., Damen et al., 2017, 2018). It is therefore beneficial to develop a means to quickly assess the dominant sand transport mode on sandy continental shelves without the need for computationally expensive numerical modelling.

This study aims to apply a data driven method to predict the dominant sand transport drivers and sand transport magnitude on sandy continental shelves using the classification scheme of King et al., (2019). This will allow assessment of the importance of WTI to sand transport on sandy continental shelves with a computationally efficient method versus fully coupled hydrodynamic modelling. To achieve this aim we will pursue the following objectives: (i) determine a list of readily available environmental and morphological variables with predictive capacity for the dominant sand transport mode and order of magnitude; (ii) use results of sand transport rates obtained through a validated numerical model to train a k-Nearest Neighbour classifier for dominant sand transport class and order of magnitude; (iii) collate environmental and morphological predictors across a sandy continental shelf with highly varied environmental conditions; and (iv) use the trained kNN classifier to assess the dominant transport mode and sand transport magnitude across the shelf.

3.2 Methods

3.2.1 Study region

The Northwest European continental shelf (Figure 3.1) was selected for this study due to a combination of ready availability of environmental and morphological variables at the shelf scale (O'Dea et al., 2012; Graham et al., 2018; Wilson et al., 2018; Tonani et al., 2019; Tonani & Saulter, 2020), a highly varied tidal regime ranging from macrotidal to microtidal (Pingree & Griffiths, 1979), a varied wave climate ranging from regions exposed to a potential 7000km fetch dominated by long-period swell waves (e.g., Celtic Shelf; Draper, 1967; Collins, 1987; Scott et al., 2016b) to regions sheltered from the Atlantic swell and dominated by wind-waves (e.g., Netherlands Shelf; van der Molen, 2002). This continental shelf has a predominantly sand bed with median sand fraction grain size ranging from fine to coarse sand (Figure 3.1b, c; Wilson et al., 2018). The shelf area has a wealth of literature examining environmental drivers of benthic disturbance (Aldridge et al., 2015; Bricheno et al., 2015; Thompson et al., 2019), sand transport (Pingree & Griffiths, 1979; Harris & Coleman, 1998; van der Molen, 2002; Uncles, 2010; Leonardi & Plater, 2017; King et al., 2019) and bedform morphodynamics (Ward et

al., 2015; Damen et al., 2018; Cheng et al., 2020). These factors make this an ideal region to examine the performance of a method for predicting the dominant driver of sand transport at the shelf scale.

Previous modelling work by King et al. (2019) simulated net sand transport per tidal cycle across a macro-mesotidal section of the Celtic Shelf (Figure 3.1a) using Delft3D (Booij et al., 1999; Lesser et al., 2004) in a depth-averaged mode using the sand transport formulation of Van Rijn (2007a, b). Delft3D in a depth-averaged mode has previously been used successfully to simulate sand transport processes including WTI on the inner shelf (Hansen et al., 2013; Hopkins et al., 2015; Ridderinkhof et al., 2016; Luijendijk et al., 2017; McCarroll et al., 2018; King et al., 2019). Simulations were performed for spring and neap tides and median and extreme (1% exceedance) waves from two modal directions with all possible combinations of these forcings, including their absence, to allow isolation of individual wave, tide and WTI components. King et al., (2019) derived a classification scheme for categorising the dominant sand transport mode between wave, tide and WTI dominance of sand transport (Section 3.2.2). From these simulations, it is possible to extract sand transport dominance class, net sand transport magnitude and the corresponding environmental variables for use in a predictive model.

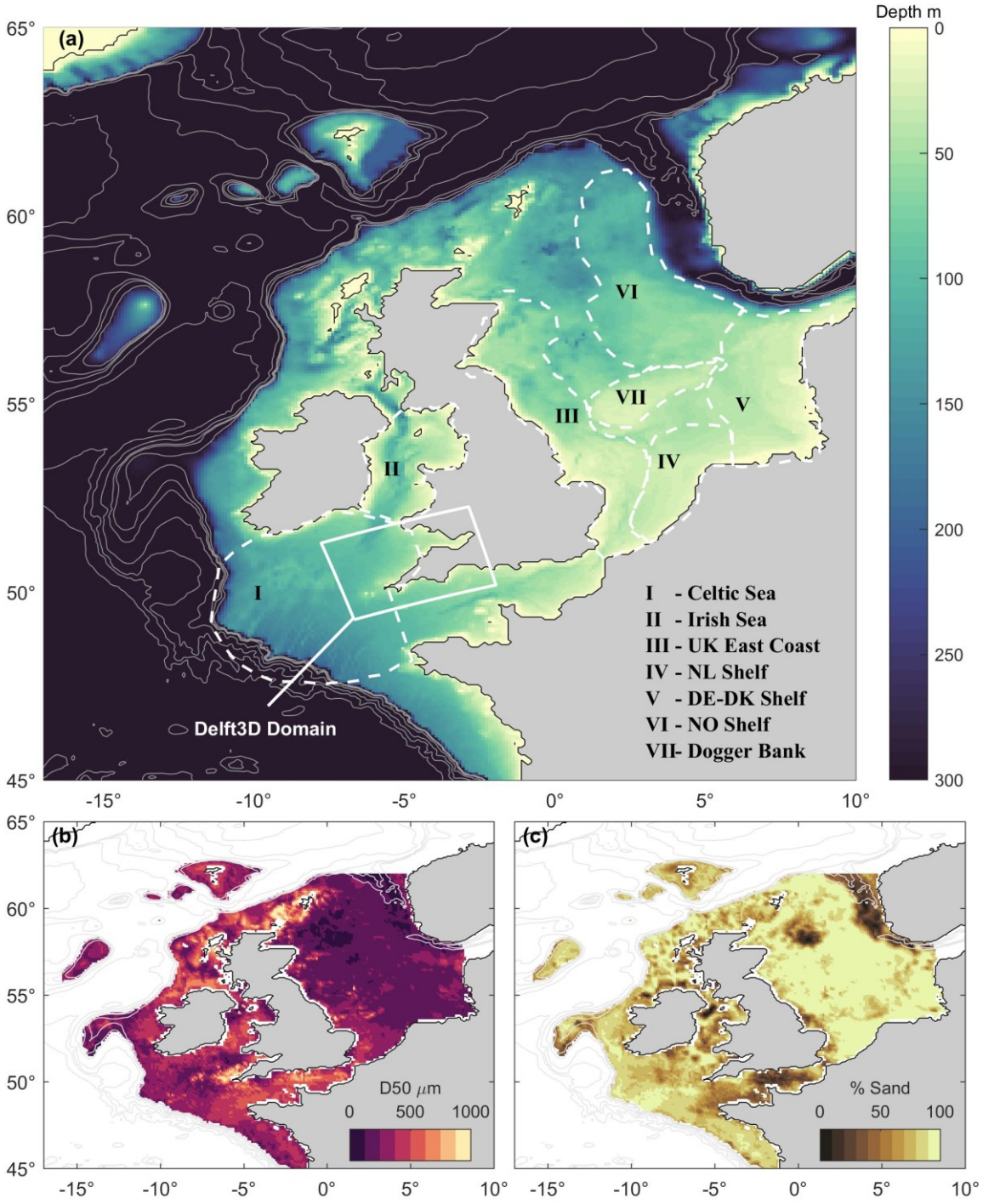

Figure 3.1: Maps of (a) depth, (b) median sand fraction grain size and (c) sand as a percentage of available sediment for the Northwest European Continental Shelf. Depths are taken from the FOAM-AMM7 model, whilst sediment characteristics are taken from Wilson et al. (2018). Selected shelf areas for later comparison are indicated and named in (a). The extent of the model domain of King et al. (2019) is also indicated. UK – United Kingdom; NL – Netherlands; DE-DK – Germany-Denmark; NO – Norway.

3.2.2 Classification scheme

The classification scheme of King et al. (2019) categorises sand transport between wave-dominated, tide-dominated and non-linear-dominated, where non-linear refers to non-linear WTI (Figure 3.2). Classes are determined by two ratios:

$$R1 = Q_T : (Q_W + Q_N), \quad (3.1)$$

$$R2 = Q_W : Q_N \quad (3.2)$$

$$Q_N = Q_{ALL} - Q_T - Q_W \quad (3.3)$$

Where $R1$ represents the ratio of tide-only net sand transport magnitude (Q_T) to the combined wave-only net transport magnitude (Q_W) and the component attributed to non-linear WTI (Q_N). This determines the relative influence of waves (including non-linear interactions) versus tides, determined by subtracting the tidal component from the combined wave+tide net transport magnitude (Q_{ALL}). Ratio $R2$ represents the relative contribution on non-linear interactions (Q_N) versus waves alone (Q_W). This allows the contribution of tides, waves and wave-tide interactions to be quantified, visualised and compared. This classification scheme considers net sand transport per tidal cycle, and the class can change under different combinations of wave and tidal forcing. Classification changes under different conditions qualitatively matched modelled shifts in sand transport direction (Pattiaratchi & Collins, 1988; King et al., 2019), supporting the predicted shift in the dominant mode of net sand transport.

This classification scheme results in three dominant modes of net sand transport (wave-dominated, W, tide-dominated, T, and non-linear dominated, N), where the respective forcing is responsible for at least 75% of the net sand transport magnitude. When the dominant class is responsible for >50% of net sand transport, but <75%, a subdominant class is defined (noted using lowercase letters). At present, this scheme requires results from coupled and uncoupled numerical simulations of net sand transport to calculate. The following section will examine kNN as a classification prediction method, based on defined predictor variables, which we will apply to this classification scheme (Section 3.2.3).

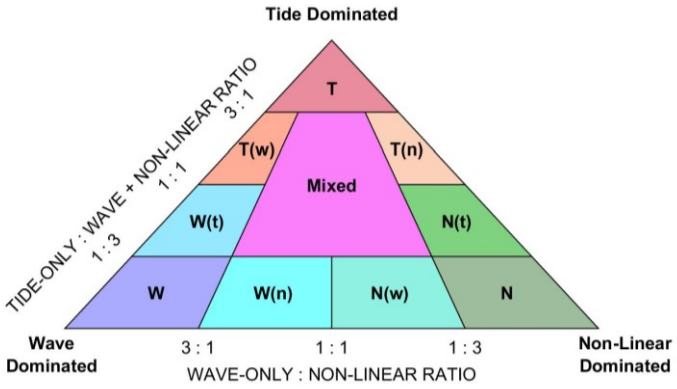

Figure 3.2: Classification scheme for sand transport dominant forcing proposed by King et al. (2019).

3.2.3 K-Nearest Neighbour (kNN)

Machine learning algorithms are being increasingly used in the geosciences (Kanevski et al., 2009; Lary et al., 2016). The kNN algorithm has been employed for prediction of seafloor properties in the geosciences including seafloor total organic carbon (Lee et al., 2019), isochore thickness (Lee et al., 2020) and sediment accumulation rates (Restreppo et al., 2020). Other applications of machine learning algorithms in the geosciences include predictions of seafloor sediment porosity (Martin et al., 2015) and seafloor fluid expulsion anomalies (Phrampus et al., 2020). The kNN algorithm is one of the simplest machine learning algorithms, and can be used in geospatial classification prediction (Kanevski et al., 2009). The algorithm works on the principle that areas with similar conditions are likely to share the same class.

The kNN algorithm requires a predictand (the variable or class we want to predict) and a set of defined predictors (variables we have measured or estimated). The algorithm is trained on the predictor data associated with known values of the predictand. The algorithm is then used to predict unseen data where the predictand is unknown by calculating the distance to the "k" nearest neighbours in parameter space to the new data, where "k" is the number of nearest points the algorithm uses for its calculation. The implementation used in this study is included in the MATLAB Statistics and Machine Learning Toolbox (MathWorks, 2020). The predicted class is the class with the minimum estimated cost, determined as a function of the probability that the new data comes from a particular class and the expected cost of misclassification for each observation. Numerous search methods exist for

determining the nearest neighbours for use in the algorithm. In this study a *K*d-tree is used to perform the nearest neighbour search, saving computation time as only a subset of the distances to points need to be calculated. Distances were calculated using a city-block distance metric with k = 7, as this provided optimal accuracy whilst minimising the value of k to avoid smoothing the data.

Model performance was determined using five-fold cross-validation of the training dataset. This entails splitting the dataset into five equal parts, and iteratively training the model on four of five parts, whilst validating using the fifth part by calculating the percentage of observations which were classified correctly, changing the validation fifth each time. The final model accuracy is an average of the five cross-validation scores. This method mitigates the likelihood of overfitting (Kanevski et al., 2009; Lee et al., 2019).

The choice of predictors is motivated by data availability, physical relevance to the prediction of net sand transport forcing mode and magnitude, as well as predictive value of each potential predictor. To assess the value of individual predictors, each predictor was tested in isolation to predict the class and order of magnitude of the net sand transport. The accuracy of each predictor was then compared with the predictive accuracy of an array of random numbers, to test whether predictors had greater predictive value than random noise. The selection of predictors, including their predictive accuracy, is described below (Section 3.2.4).

3.2.4 Environmental Predictors

Environmental predictors across the NW European Shelf used in this study are shown in Table 3.1a, including their sources and resolution (spatial, temporal) where applicable. Selection criteria were data availability, spatio-temporal resolution and predictive value. With these data sources defined, the model scenarios conducted to generate training data are included in Table 3.1b, including the range of the parameters used. Modelled scenarios were conducted as described in King et al. (2019), calculating net sand transport for wave-only, tide-only and wave+tide forcing over springs and neaps at 1-km resolution for an approx. 350 x 240 km region of the Celtic shelf with variable wave exposure and meso-megatidal regime. A full model description and validation is also presented therein. Additional scenarios were conducted in addition to those described in King et al. (2019) to

include more intermediate wave conditions and a range of grain sizes. Mixed size fractions (e.g., sand-gravel mixtures) were not considered, and this is discussed in section 3.4.2. Dominant transport classes were calculated as in Figure 3.2, and order of magnitude of net sand transport was determined from the coupled wave+tide simulations. Predictors for training were determined from the uncoupled simulations to ensure WTI were not included in the predictor variables, replicating the uncoupled nature of the shelf-scale models.

An example of the relationship between tide range TR, maximum tidal current speed U_{max}, relative wave height H_s/h and the sand transport dominance classes of King et al. (2019) is shown in Figure 3.3. The modelled TR and U_{max} are shown as a function of H_s/h with class indicated by colour (Figure 3.3a, b). Tide-dominated areas exhibit low wave heights and stronger tidal currents and a greater tidal range, whilst wave-dominated areas are the inverse. Non-linear dominated areas occupy the mixed energy section of the parameter space. A three-predictor kNN classifier is shown in Figure 3.3c, indicating the classification boundaries for relative to the three predictors: new data falling within this parameter space will be classified accordingly. This is a simplified classifier for 3D visualisation, whereas the final classifier has eight dimensions (see Table 3.2).

Table 3.1

(a) Environmental predictors across the NW European Shelf; (b) Environmental predictors and scenarios used in Delft3D simulations to generate training data.

(a) Environmental predictors across the NW European Shelf

Predictor Name	Symbol	Units	Source	Spatial resolution	Temporal Resolution	Interpolation	Processing
Significant wave height	H_s	m	Tonani & Saulter (2020)	1.5 km	1 hour	Interpolated to 7km grid	Mean H_s per tidal cycle
Peak period	T_p	s	As H_s	1.5 km	1 hour	Interpolated to 7km grid	Mean T_p per tidal cycle
Power	P	W	As H_s	1.5 km	1 hour	Interpolated to 7km grid	Mean P per tidal cycle
Depth⁺	h	m	O'Dea et al. (2012)	7 km	-	Converted to MSL2000	-
Relative wave height	H_s/h	-	As H_s and h	7km	1 hour	-	Mean Hs/h per tidal cycle
Tide range	TR	m	Graham et al. (2018); O'Dea et al. (2012)	7 km	1 hour	-	Determined per tidal cycle
Max tidal current	U_{max}	ms^{-1}	As TR	7 km	1 hour	-	Determined per tidal cycle
Angle between waves and currents	θ	Deg	As H_s and TR	7 km	1 hour	-	Mean wave direction and max tidal current direction
Median grain size	D_{50}	µm	Wilson et al. (2018)	0.125°	-	Interpolated to 7km grid	-

(b) Modelled scenarios for training

Scenario	$H_s \cap T_p$ joint exceedance probability	H_s min, median, max (m)	T_p min, median, max (s)	Tide condition	TR min, median, max (m)	U_{max} min, median, max (ms^{-1})	D_{50} (µm)	№ data
1	1%	0.2, 7.1, 8.5	5.9, 17.6, 19.0	Springs	1.8, 3.0, 7.8	0.03, 0.7, 3.6	125	44861
2*	1%	0.2, 7.1, 8.5	5.9, 17.6, 19.0	Springs	1.8, 3.0, 7.8	0.03, 0.7, 3.6	330	44683
3	1%	0.2, 7.1, 8.5	5.9, 17.6, 19.0	Springs	1.8, 3.0, 7.8	0.03, 0.7, 3.6	750	43582
4	1%	0.2, 7.1, 8.5	5.9, 17.6, 19.0	Neaps	0.6, 1.2, 4.2	0.02, 0.3, 1.5	125	44566
5*	1%	0.2, 7.1, 8.5	5.9, 17.6, 19.0	Neaps	0.6, 1.2, 4.2	0.02, 0.3, 1.5	330	43652
6	1%	0.2, 7.1, 8.5	5.9, 17.6, 19.0	Neaps	0.6, 1.2, 4.2	0.02, 0.3, 1.5	750	39972
7	10%	0.1, 4.1, 4.8	5.0, 14.9, 15.4	Springs	1.8, 3.0, 7.8	0.03, 0.7, 3.6	125	44577
8	10%	0.1, 4.1, 4.8	5.0, 14.9, 15.4	Springs	1.8, 3.0, 7.8	0.03, 0.7, 3.6	330	44272
9	10%	0.1, 4.1, 4.8	5.0, 14.9, 15.4	Springs	1.8, 3.0, 7.8	0.03, 0.7, 3.6	750	41709
10	10%	0.1, 4.1, 4.8	5.0, 14.9, 15.4	Neaps	0.6, 1.2, 4.2	0.02, 0.3, 1.5	125	41885
11	10%	0.1, 4.1, 4.8	5.0, 14.9, 15.4	Neaps	0.6, 1.2, 4.2	0.02, 0.3, 1.5	330	39175
12	10%	0.1, 4.1, 4.8	5.0, 14.9, 15.4	Neaps	0.6, 1.2, 4.2	0.02, 0.3, 1.5	750	16637
13	50%	0.1, 1.9, 2.1	3.4,10.5,10.8	Springs	1.8, 3.0, 7.8	0.03, 0.7, 3.6	125	43380
14*	50%	0.1, 1.9, 2.1	3.4,10.5,10.8	Springs	1.8, 3.0, 7.8	0.03, 0.7, 3.6	330	41224
15	50%	0.1, 1.9, 2.1	3.4,10.5,10.8	Springs	1.8, 3.0, 7.8	0.03, 0.7, 3.6	750	30842
16	50%	0.1, 1.9, 2.1	3.4,10.5,10.8	Neaps	0.6, 1.2, 4.2	0.02, 0.3, 1.5	125	13415
17*	50%	0.1, 1.9, 2.1	3.4,10.5,10.8	Neaps	0.6, 1.2, 4.2	0.02, 0.3, 1.5	330	10274
18	50%	0.1, 1.9, 2.1	3.4,10.5,10.8	Neaps	0.6, 1.2, 4.2	0.02, 0.3, 1.5	750	5265
Summary:	**1% – 50%**	**0.1 – 8.5**	**3.4 – 19.0**	**Springs – Neaps**	**0.6 – 7.8**	**0.02 – 3.6**	**125 – 750**	**633972**

Note: ⁺ Depth used as a predictor combined in H_s/h.

* Scenarios described in King et al. (2019).

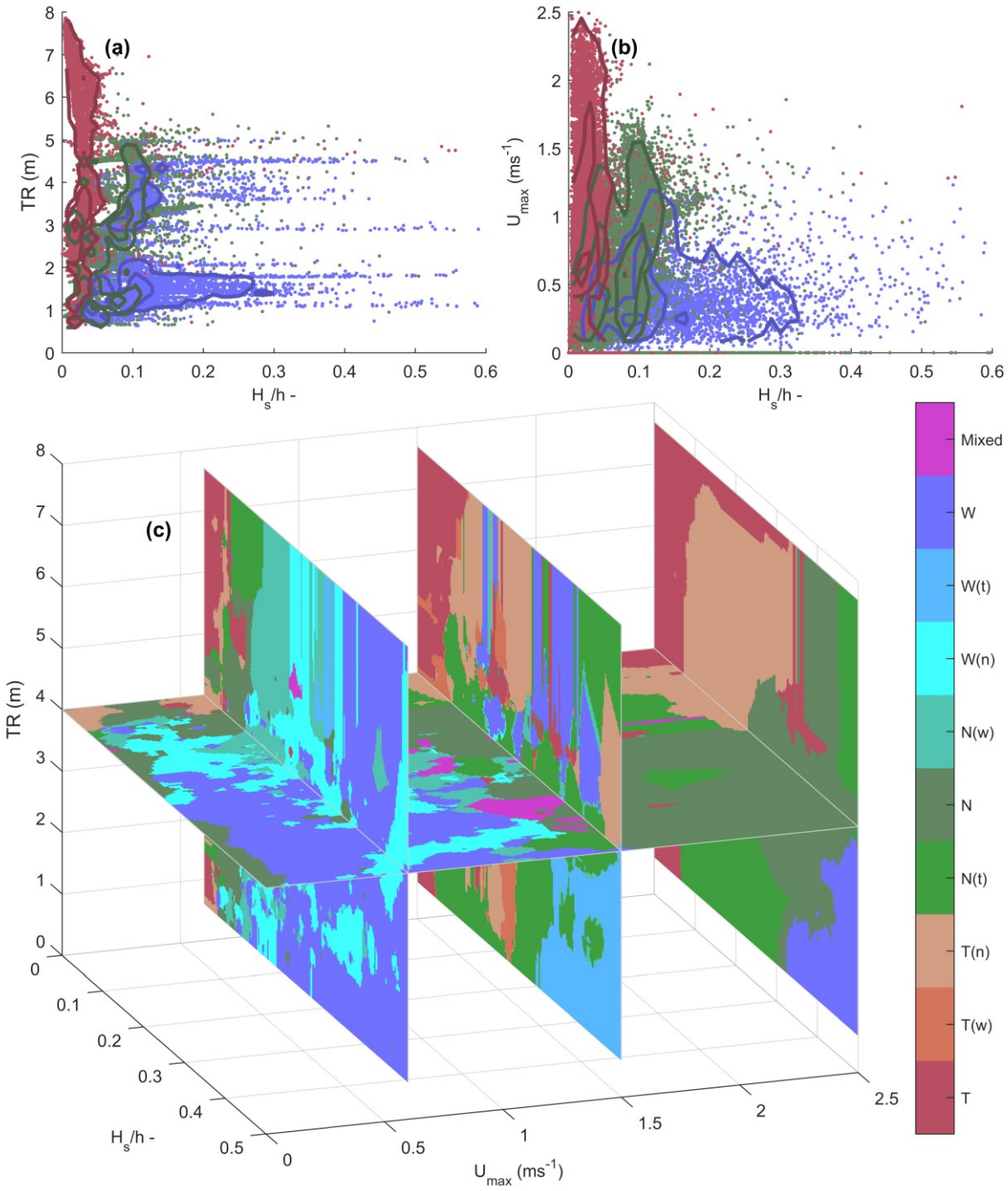

Figure 3.3: For illustrative purposes only - Relation of classes to predictor variables: (a, b) Modelled tide range *TR* and maximum tidal current speed U_{max} as a function of relative wave height H_s/h, data are coloured as per their associated dominance class (King et al., 2019), contours are shown to indicate point density for each class. Only data in the three primary classes are shown for simplicity (tide-dominated, wave-dominate and non-linear-dominated); (c) Example of classification boundaries for a simple 3D k-NN classifier using tide range, maximum current speed and relative wave height. New data falling within the 3D parameter space are classified accordingly. The actual classifier has 8 dimensions, and this should be viewed as a simplified example only.

Each of the eight predictors in Table 3.1 was tested in isolation and compared with classifications predicted by an array of random numbers to determine its predictive value. For a predictor to be accepted, it needed to have an accuracy greater than that of the random array, as in Lee et al. (2019). The predictive accuracy of each predictor is shown in Table 3.2 for the dominance class and order of magnitude. The only variable with a lower predictive value than random noise in isolation was median grain size D_{50} (test 9). To further test D_{50}, accuracy of the k-NN prediction was tested alongside the other predictors with and without D_{50} (tests 10 and 12) and also with and without the random array (tests 10 and 11). It was found that in conjunction with the other predictors, D_{50} provided a greater improvement in accuracy (class - 21.1%, magnitude - 46.3%) than the random array (class - 12.3%, magnitude - 9.1%), and was vital for an accurate prediction of the dominant class and order of magnitude (Table 3.2), therefore D_{50} was included as a predictor. Final predictive accuracy was 81.9% for class and 90.8% for magnitude, and most misclassified data were only out by one class.

Table 3.2

(a) Predictive accuracy of environmental predictors compared with calculated dominance classes and order of magnitudes from model data. Accuracy is determined from 5-fold cross-validation of the training dataset, and is calculated for a random number array (test 1), individual predictors (tests 2 – 9), and the combined predictors to further test D_{50} (tests 10 – 12). The accuracy of the final kNN prediction with all predictors is shown (test 12).

Test Number	Variable(s)	Symbol	Accuracy: Dominant class (King et al., 2019) % correct	Accuracy: Order of magnitude (OOM) % correct	Difference relative to random array for Class %	Difference relative to random array for OOM %
1	**Random array**	***Rnd***	**30.2**	**27.2**	**-**	**-**
2	Significant wave height	H_s	58.3	42.3	+28.1	+15.1
3	Peak period	T_p	49.2	27.4	+19.0	+0.2
4	Power	P	58.5	42.3	+28.3	+15.1
5	Relative wave height	H_s/h	58.2	42.1	+28.0	+14.9
6	Tide range	TR	49.1	28.7	+18.9	+1.5
7	Max tidal current	U_{max}	49.0	28.7	+18.8	+1.5
8	Angle between waves and currents	θ	43.0	35.1	+12.8	+7.9
9	Median grain size	D_{50}	9.4	24.5	-20.8	-2.7
10	All – D_{50} and Rnd	-	60.8	44.5	+30.6	+17.3
11	As 10 + Rnd	-	73.1	53.6	+42.9 (+12.3)*	+26.4 (+9.1)*
12	**As 10 + D_{50}**	**-**	**81.9**	**90.8**	**+51.7 (+21.1)***	**+63.6 (+46.3)***

*Difference relative to test number 10.

Tidal predictors (tide range *TR*, maximum current speed U_{max}) are shown across the NW European shelf in Figure 3.4a-d for springs and neaps. A distribution of *TR* over a statistically representative year is shown in Figure 3.4e-f at two locations marked with triangles in subplots a-b. The distribution of *TR* was calculated across each node the NW European shelf area over 1 year. Areas below the shelf break were excluded from analysis as they were below the maximum depth in the training data. Similarly, wave predictors are shown in Figure 3.5a-d. These predictors are shown for 1% and 50% joint exceedance of H_s and T_p, as determined from a fitted joint probability gumbel copula distribution (Genest & Favre, 2007) at each node across the domain over 1 year, using generalised extreme value and gamma marginal distributions for H_s and T_p respectively. Wave direction was taken as the mean wave direction over the year. Wave heights are in agreement with wave conditions for similar exceedances modelled by Bricheno et al. (2015). Depth was taken from the AMM7 model for calculation of H_s/h, whilst grain size was determined from the synthetic map created by Wilson et al. (2018; Figure 3.1). All variables were resampled where necessary to the AMM7 model grid at 7km resolution. The fitted distributions of tide range (e.g., Figure 3.4e, f) and joint H_s and T_p (e.g. Figure 3.5e, f) enable the generation of tide and wave forcing data for a statistically representative year, assuming wave and tide condition are independent, keeping water depth and grain size constant and using the mean wave direction and maximum tidal current direction as an indicator of the direction difference between waves and the tidal major axis.

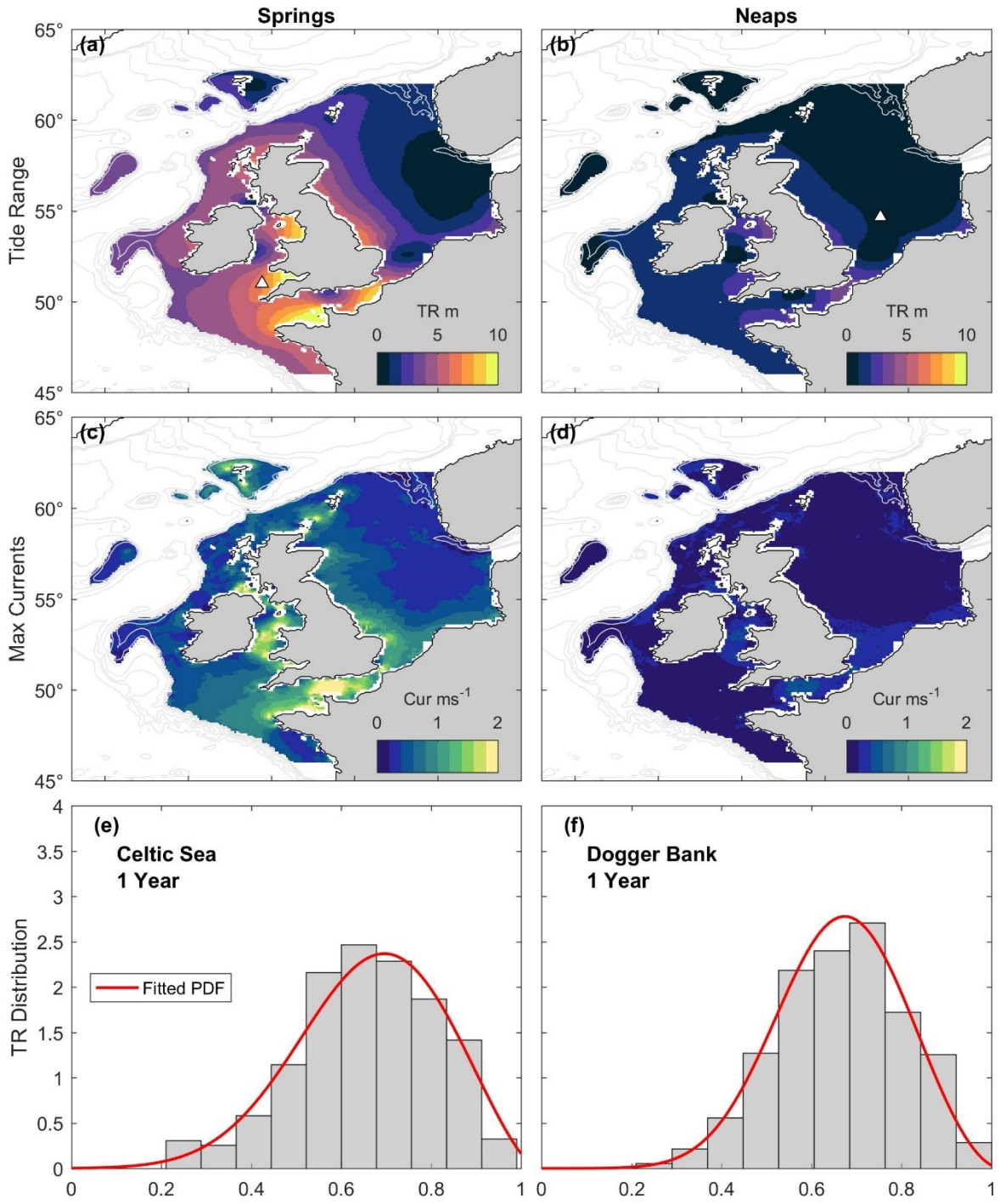

Figure 3.4: Maps of representative tide conditions across the NW European Shelf. Histograms show distributions of tide range (*TR*) normalised by the maximum tide range over 1 year for two locations indicated by white triangles in subplots (a) and (b) for their respective columns. Fitted probability distribution functions are shown (red curves).

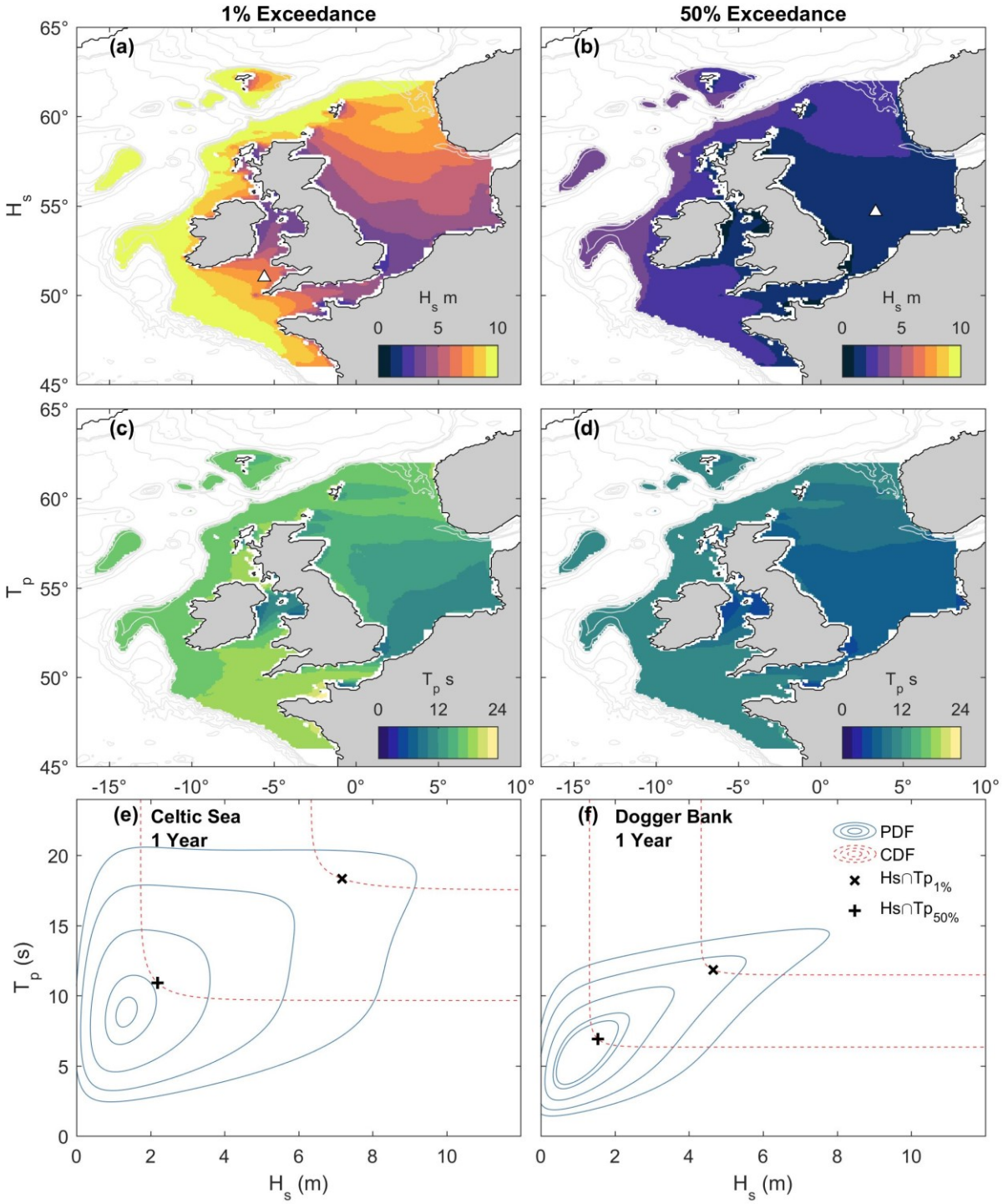

Figure 3.5: Maps of representative wave statistics. (a – b) Significant wave height H_s for 1% exceedance and 50% exceedance probability. (c – d) Peak period T_p for 1% exceedance and 50% exceedance probability. (e – f) Joint probability distribution function (blue) and cumulative distribution function (red dashed) contours for two locations over 1 year. Selected H_s and T_p for the 1% and 50% exceedance probability are indicated by a + and x respectively, taken at the point on the CDF contour with the maximum probability density interpolated from the PDF. The locations used for subplots (e) and (f) are indicated by white triangles in subplots (a) and (b) respectively.

3.3 Results

In this section we present the results of the kNN classification across the NW European shelf for different environmental conditions, and examine the influence of different conditions on the shelf areas presented in Figure 3.1a. We go on to present the determination of the dominant sand transport class and order of magnitude over a statistically representative year.

3.3.1 Environmental forcing controls on sand transport across the shelf

Results from the kNN prediction for different environmental forcing conditions are presented as maps in Figure 3.6. The dominant class, indicating the dominant driver of sand transport, and the potential order of magnitude of net sand transport are presented for spring (Figure 3.6a,b,e,f) and neap (Figure 3.6c,d,g,h) tides under median (50% exceedance; Figure 3.6a,b,c,d) and extreme (1% exceedance; Figure 3.6e,f,g,h) wave forcing as characterised for each node on the shelf area (see Figures 4 & 5). Regions greater than 140 metres depth are excluded to avoid extrapolation, as these exceed the largest depth in the training model and are deep enough that wave impacts are likely to be minimal.

Coastal areas around the UK are generally tide-dominated at spring tides and median wave forcing, with the second largest predicted order of magnitude of potential net sand transport (Figure 3.6a, b), exceeded only by the extreme waves at spring tide conditions (Figure6e, f). This includes large areas of the meso-macrotidal Celtic shelf, UK East Coast and the Irish Sea. Deeper areas of the shelf tended to show dominance of non-linear interactions, with net transport several orders of magnitude lower. Only microtidal, shallow, wave-exposed areas such as Dogger Bank and the DE-DK Shelf show wave-dominance in these conditions. The lowest magnitudes are found for median waves at neaps, where only the shallow, exposed areas of the NL and DE-DK Shelves show elevated net sand transport driven by waves (Figure6c, d). Sand transport is effectively switched off for most other shelf areas under these low energy conditions.

In the highest energy conditions with extreme waves at springs, macro-meso tidal areas show dominance of WTI, whilst waves dominate sand transport in the Eastern North Sea where tidal currents are weaker (Figure 3.6e, f). Sand transport is dominated by waves across this shelf area during extreme waves at neaps, with the

greatest magnitudes in finer grained, shallow and wave-exposed areas of the NL and DE-DK Shelves in the Eastern North Sea (Figure 3.6g, h). This is despite these areas having lower wave energy at this exceedance than more swell exposed regions (e.g., Celtic Shelf), indicating the importance of grain-size and water depth as controls. The next section explores the influence of environmental forcing conditions in more detail for the different shelf areas.

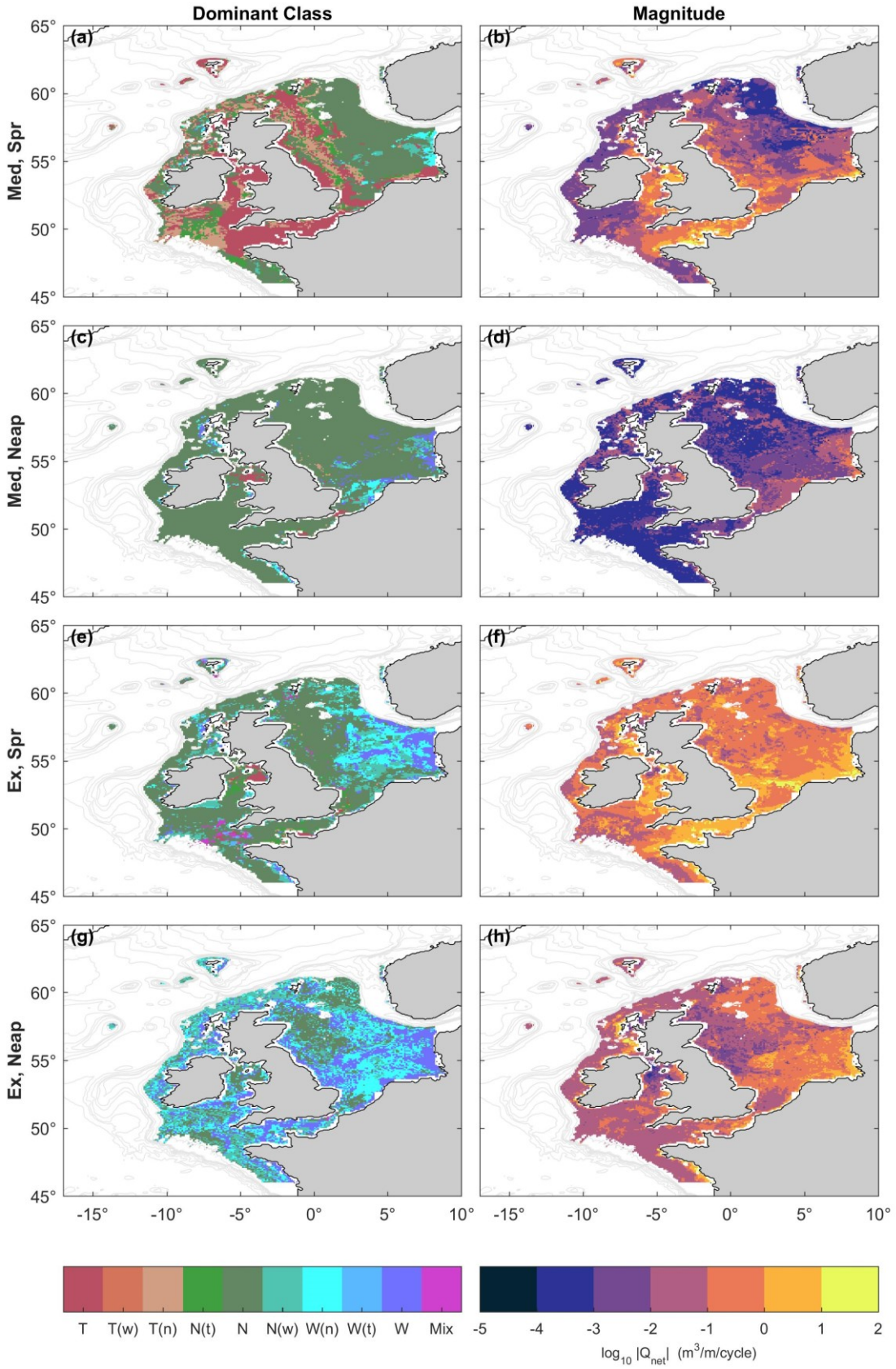

Figure 3.6: Results from the KNN predictions for different conditions presented as maps, including dominant transport mode classification (left column) and order of magnitude (right column). Colours on the right column are on a logarithmic scale. Extreme (1% exceedance; Ex) and median (50% exceedance; Med) wave forcing is shown at springs (Spr) and neaps (Neap).

3.3.2 Environmental forcing controls on sand transport for shelf sub-areas

A sensitivity analysis for different shelf areas was conducted by changing the environmental forcing conditions, including tidal condition, wave exceedance and grain size, and calculating the average class across each shelf area. To determine an average class, the kNN-predicted classification for each node within the designated region (Figure 3.1a) was converted to a representative pair of ratios R1 and R2 (Equations 3.1 & 3.2; Figure 3.2). Values of R1 and R2 were taken as the centre value of each classification bin, whilst end values (e.g., for R1 > 3 in tide-dominated conditions) were assumed to be dominant by a factor 6 in their respective direction (e.g., R1 = 6 for tide-dominated transport). The mean R1 and R2 of all nodes within each region was calculated, weighted by the predicted net transport magnitude. These results are presented in Figure 3.7.

The same wave and tidal forcing conditions are presented as shown in Figure 3.6. Symbols are placed within the classification triangle according to the regional mean R1 and R2 for that forcing condition. The influence of grain size variation is shown in Figure 3.7b. This is an indication of the variability in the response throughout the region arising from the spatial variability of grain size (D_{50}). The dominant class was calculated for the median, 2.5th and 97.5th centiles of D_{50} through each region. Sand transport was more tidally dominated for finer grain sizes, due to easier resuspension. For clarity, the results for the other regions are shown for the median D_{50} through that region, with an indication of the variability in grain size shown on a scale.

Environmental forcing conditions are the primary control on the dominant net sand transport mode, with grain size moderating this. Different shelf areas exhibit different responses to changing forcing. Shelf areas adjacent to the UK (Irish Sea, Celtic Sea & UK-East Coast) are tidally dominated for median wave forcing at spring tides, whilst the NL Shelf and DE-DK Shelf show a significant tidal influence. Dogger Bank and the microtidal area of the NO Shelf have relatively low tidal net sand transport magnitudes ($Q_{net} \lesssim 0.01$ m^{3}m^{-1}cycle^{-1}; Figure 3.6b) and are classified as non-linear dominated. Under median waves at neaps, tidal sand transport is low across the shelf and non-linear interactions drive the sand transport that does occur. For extreme waves at springs, sand transport in most areas is dominated by WTI with the exception of the DE-DK Shelf which is wave dominated with a subdominant

impact from WTI. Under extreme waves at neaps, most areas shift to wave dominated sand transport. The macrotidal Celtic Sea and the relatively sheltered Irish Sea retain a sub-dominant contribution from WTI in these conditions. The next step is to determine which forces drive net sand transport over a statistically representative year, and the order of magnitude of that sand transport, taking the full annual distribution of waves and tides into account.

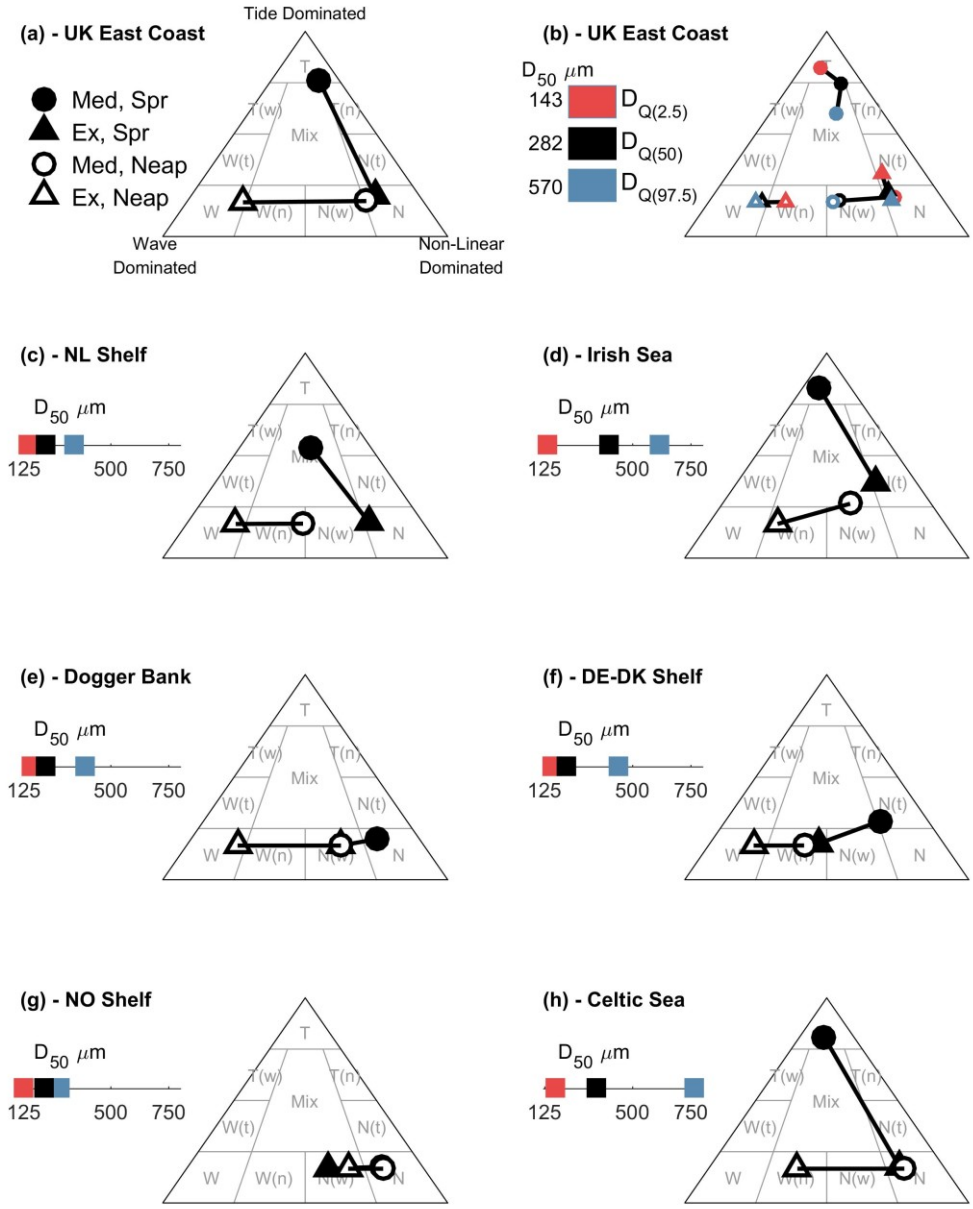

Figure 3.7: Sensitivity analysis for different shelf areas under changing environmental forcing conditions. "Ex" denotes 1% exceedance "Extreme" wave forcing, "Med" denotes 50% exceedance "Median" wave forcing. $D_{Q(N)}$ denotes the Nth quantile of the sediment D_{50} diameter as distributed through the specified region. (b) The influence of grain size on the predicted classification for the UK East Coast region. Red and blue symbols indicate the class for the 2.5th and 97.5th centiles D_{50} in the region, respectively. Other shelf areas show the class for the median D_{50} in these regions. The 2.5th, 50th and 97.5th centile D_{50} values are indicated on linear scales next to the classification triangle for each region.

3.3.3 Dominance and magnitude of net sand transport over a year

Using the fitted tide range distribution (e.g. Figure 3.4e, f), and the fitted copula joint probability distribution for significant wave height and peak period (e.g. Figure 3.5e, f) for each node across the shelf, it was possible to generate tide and wave forcing data for a statistically representative year of semi-diurnal tidal cycles. By assuming independence between wave condition and tide condition, keeping water depth and grain size constant, and using the mean wave direction and tidal maximum current direction, it was possible to tabulate a representative set of predictors over a statistically representative year. These were then used to determine a classification and order of magnitude for each tidal cycle. The sum of the order of magnitude over the statistically representative year gives a sense of the magnitude of potential net sand transport across the shelf over one year, whilst the classification for each node was determined as the class for which the maximum net sand transport occurred over the year. Results are shown in Figure 3.8.

Net sand transport ranges from approx. 10 $m^3m^{-1}y^{-1}$ in deeper, microtidal areas of the NO Shelf, to up to 10000 $m^3m^{-1}y^{-1}$ in more wave-exposed areas of the DE-DK Shelf and the macrotidal areas of the south west English Channel. Much of the shelf surrounding the UK is tidally dominated, whilst deeper areas of the shelf, including much of the Celtic Sea and NO Shelf, are dominated by non-linear WTI. Shallow, fine grained areas of Dogger Bank and the DE-DK shelf are dominated by wave driven sand-transport, reflecting the lower tidal velocities across these regions. The NL Shelf is also dominated by non-linear WTI, reflecting stronger tidal currents and coarser grain size than Dogger Bank and the DE-DK Shelf (Figures 1b & 4). This does not consider wind driven net sand transport, nor the influence of sand-mud or sand-gravel mixtures. Areas with very low fractions of sand (Figure 3.1c) are included in these figures, and therefore these results should be considered potential net sand transport magnitude assuming continual availability of sand at the bed. These points are discussed in detail in section 3.4.2. In addition, a comparison to observed sand wave morphology is made in the Discussion (Section 3.4.1).

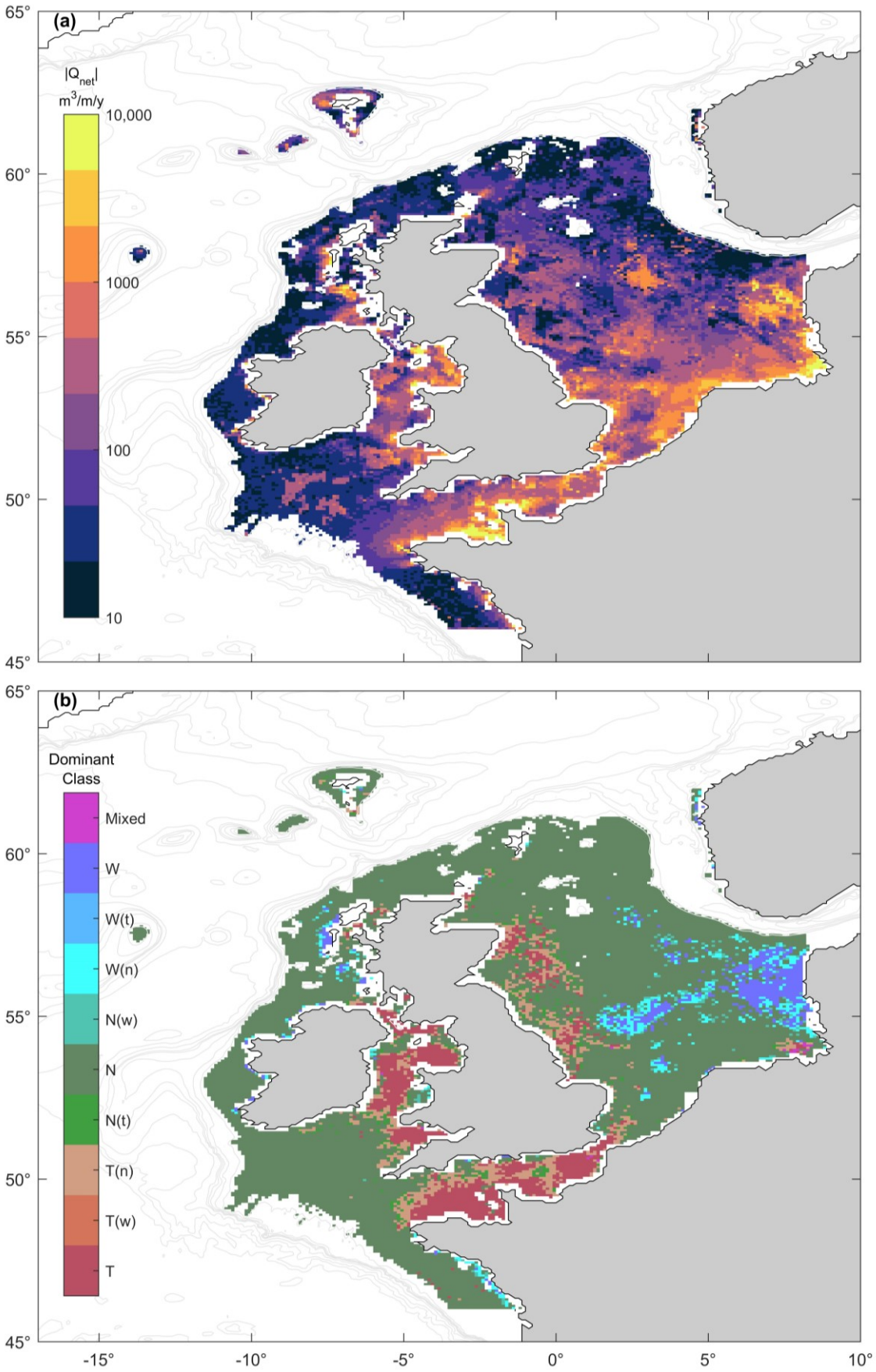

Figure 3.8: Dominant net sand transport classification and order of magnitude integrated over a statistically representative year using forcing conditions taken from the wave exceedance joint-probability distributions and tidal range probability distributions.

3.4 Discussion

The magnitude of net sand transport and relative dominance of waves, tides and their non-linear interactions was predicted for the Northwest European Continental Shelf using a kNN approach trained on extensive numerical modelling data on the Celtic Shelf area using a coupled hydrodynamic, wave and sand transport model (King et al., 2019). This shelf area has a highly varied tidal climate ranging from micro- to mega-tidal, varying degrees of wave exposure and a highly energetic wave climate (Harris & Coleman, 1998). These factors result in a varied parameter space with which to test the application of this kNN classification approach whilst generating insights into the dynamics of sand transport across this shelf.

The dominance of waves on the DE-DK Shelf and Dogger Bank, and dominance of tides along the UK East Coast predicted here is in agreement with modelling of wave, wind and tidal sand transport in the North Sea (van der Molen, 2002), lending confidence to the predictions of the kNN model. This paper builds upon previous work by considering the influence of WTI, indicating that non-linear wave-tide interaction dominates along the Dutch Shelf and deeper areas of the Celtic Sea and the Norwegian Shelf. Here, WTI includes radiation stresses, Stoke's drift, enhanced bottom-friction and bed shear stress, refraction, current-induced Doppler shift and wave-blocking. See Section 2.3.2 for more detail on the representation of wave effects, including WTI, in the calculation of sand transport rates in this study. This paper also presents a computationally efficient method for estimating the dominant processes influencing net sand transport, and its magnitude, for different environmental forcing conditions using readily available data. In the next section we examine a potential application of this method to look at the influence of environmental forcing parameters on sand wave morphology. We then discuss other applications, limitations and future work that arises from this.

3.4.1 Comparison with sand wave morphology

Modelling of sand wave dynamics is important for offshore renewable energy industrial activities and studies have been conducted to understand their dynamics in the Dutch North Sea and elsewhere (Van Oyen et al., 2011; van Santen et al., 2011; Roetert et al., 2017; Damen et al., 2018; Wang et al., 2019; Cheng et al., 2020). Tidal sand waves are also habitat to benthic species whose spatial distribution is

dependent upon sand wave morphology, with feedback effects on sand wave evolution (Damveld et al., 2018, 2020).

Surface waves affect sand wave growth, wave length and migration, reducing sand wave height and increase wave length (Campmans et al., 2018a,b). Damen et al. (2018) examined sand waves on the NL Shelf, finding weaker than expected correlation of sand wave height with H_s possibly due to the interdependent and opposite acting correlations between H_s, water depth and sand wave height (Houthuys et al., 1994; Van Dijk & Kleinhans, 2005; Campmans et al., 2018a,b). They find that it is more reliable to consider the impact of the waves at the bed, for example using the Shields parameter.

Tidal currents are known to positively correlate with spatial frequency (van Santen et al., 2011; Damen et al., 2018). Damen et al. (2018) find weak correlation between tidal currents and sand wave height. It is important to consider the level of suspended sediment transport as a control on sand wave length and height (Borsje et al., 2014; Damen et al., 2018). This could be a future application of this kNN method, to predict the balance between suspended and bedload sand transport under variable forcing conditions.

Here, we utilise same trained kNN classifier as presented earlier to predict the dominant transport mode across the same region considered by Damen et al. (2018). Where possible, predictor data used were taken from the dataset of Damen et al. (2017). These included 1% exceedance H_s, M2 current amplitude (in lieu of the maximum tidal current) and grain size D_{50}. Tide range, current mean direction and wave mean direction were interpolated from the shelf-scale predictors used earlier, and T_P was interpolated from the 1% exceedance T_p (Figure 3.5c). The predicted transport class was determined at 1km resolution at the same locations as the data presented in Damen et al. (2018) and this is presented in Figure 3.9a. Under these conditions we predict dominance of non-linear WTI in the southeast of the sand wave field, moving to wave-dominance in the northwest.

The height, wave length and asymmetry of the sand waves was binned for each classification and compared between classes (Figure 3.9b-d). This resulted in comparison of 9161 data points each representing sand wave characteristics over a $1km^2$ area. Results suggest sand wave height is lowest in wave-dominated regions, and larger in regions dominated by non-linear WTI. Similarly, wave length and

asymmetry appear to increase with an increase in wave-dominance. The statistical dissimilarity of the sand wave populations in each class was tested using the Kolmogorov-Smirnov (KS) test. Distributions of sand wave characteristics were found to be unique between classes at the 95% confidence level. A second one-sided KS test was performed to test the hypotheses that sand wave height decreases moving from non-linear interaction dominated to wave-dominated sand transport, and that wave length and asymmetry increase. These hypotheses were found to be true at the 95% confidence level, and P-values are included in Figure 3.9e-g.

These results are in agreement with previous research into wave and tidal influences on sand wave height, wave length and asymmetry (Campmans et al., 2018a,b; Damen et al., 2018), lending confidence to the results of the kNN prediction and indicating WTI may play a significant role influencing sand wave morphology, and this classification scheme has a predictive power for sand wave morphology on sandy continental shelves. This prediction is based on the most energetic wave and tidal conditions. The annual classification determined in Figure 3.8 indicates this region is dominated by non-linear WTI on an annual scale, suggesting that the more energetic conditions play a significant role in controlling sand wave morphology, with increased wave-dominance under storm conditions limiting sand wave heights.

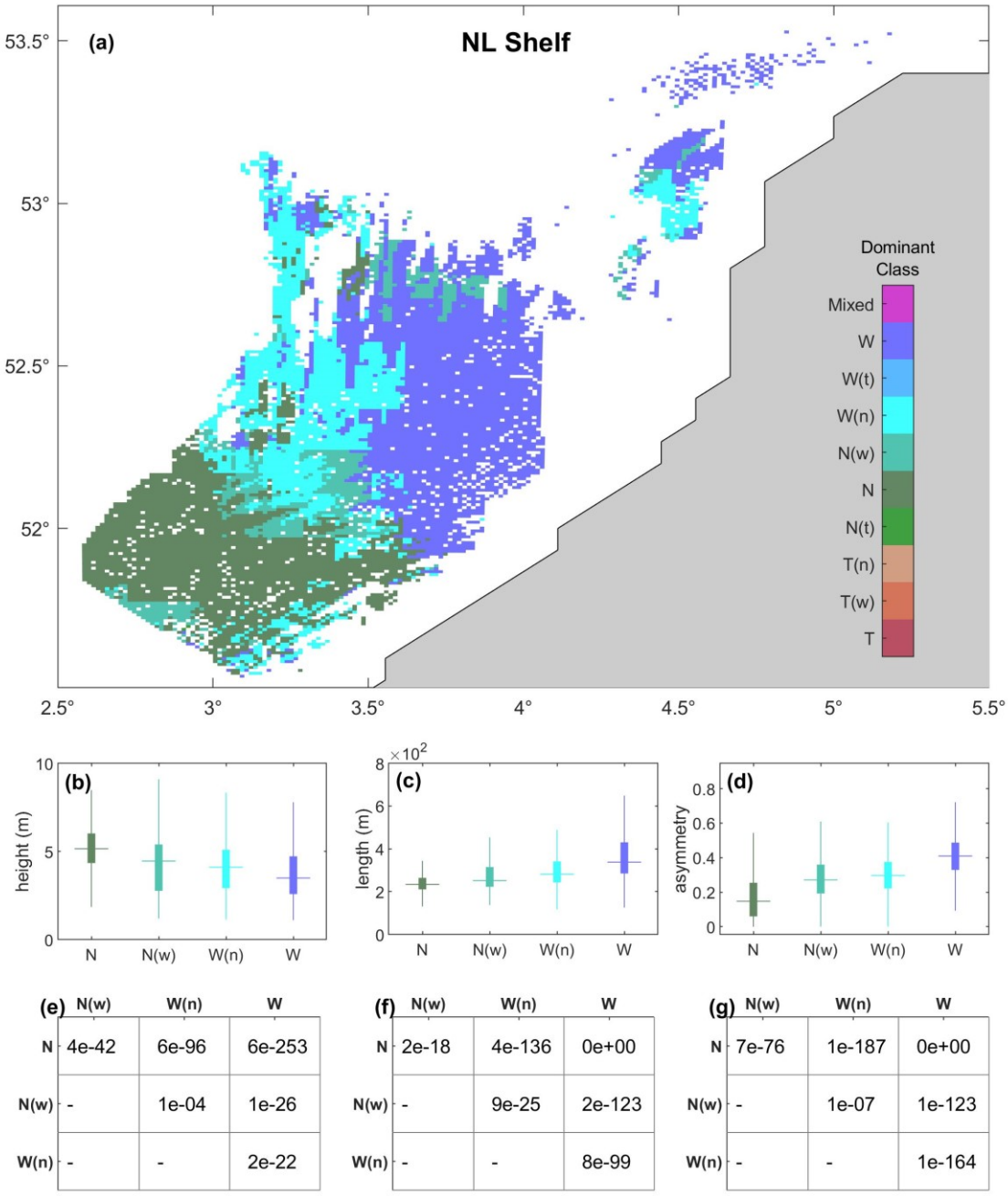

(e)

	N(w)	W(n)	W
N	4e-42	6e-96	6e-253
N(w)	-	1e-04	1e-26
W(n)	-	-	2e-22

(f)

	N(w)	W(n)	W
N	2e-18	4e-136	0e+00
N(w)	-	9e-25	2e-123
W(n)	-	-	8e-99

(g)

	N(w)	W(n)	W
N	7e-76	1e-187	0e+00
N(w)	-	1e-07	1e-123
W(n)	-	-	1e-164

Figure 3.9: Application of classification prediction to sand wave physical characteristics averaged per square km (Damen et al., 2017). (a) Sand transport dominant class across the NL Shelf determined with a mix of data from Damen et al. (2017) and other predictors as described earlier, interpolated to each square km (1 pixel = 1 km^2). (b-d) Box plots showing sand wave height, wave length and spatial frequency respectively for each dominant class. Plots indicate median, 25th and 75th percentiles and whiskers indicate 1.5 times the IQR beyond the 75th or 25th percentile. (e-g) P-values from a 2-sample, 1-sided Kolmogorov-Smirnov test, testing if data are significantly lower in magnitude in more wave-dominated conditions (height, spatial frequency – e,g), or greater in magnitude in the more wave-dominated condition (wave length – f) at the 95% confidence level.

3.4.2 Assumptions, limitations and future work

In this study we show that the magnitude of net sand transport and the relative contribution from waves, tides and non-linear WTI is amenable to estimation using readily available wave and tidal data utilising a kNN classification prediction approach. The kNN method itself does not account for the physical relationships between predictors and the resultant classification, relying instead on the associations between predictors and classifications in the parameter space. This implies the trained classifier will only be representative of the physical processes represented in the training data. The trained classifier cannot therefore be used to extrapolate outside the range and physics represented in the data used to train it, however it can be applied in other regions. Here we discuss the processes represented in the model used to generate the training data, and the implications of those not represented.

Data used to train this kNN predictor were generated by a well validated numerical model of coupled hydrodynamics, waves and sand transport (King et al., 2019). The range of each predictor in the training data is shown in Table 3.1. Sand transport rates are determined using the formulation of van Rijn (2007a,b), therefore the predictor is representative of the physics included therein (see Section 2.3.2 for discussion of the physics included in this formulation with an emphasis on representation of wave-tide interactions). Importantly, baroclinic and wind-driven currents are not included in the training model. This paper considers processes at the shelf scale, and due to the resolution of the forcing variables it should be considered to represent an estimate of the dominant sand transport processes on the continental shelf, and does not consider processes landward of the shoreface (approx. 15m) (e.g., Héquette et al., 2008; Hamon-Kerivel et al., 2020).

Important wind speed events can interact constructively or destructively with tidal currents to influence sand transport rates, depending on the relative angle of wind driven currents to the tidal current direction (Héquette et al., 2008). Wind driven currents are weak on the Celtic Shelf (Pingree & Le Cann, 1989), and wind driven residual currents across the NW European Shelf are likely to be most significant at neaps when tidal currents are weakest (Pingree & Griffiths, 1980), with the strongest wind driven residuals present in the Southern North Sea. Van der molen (2002) discusses wind driven sand transport relative to tides and wind waves in the

Southern North Sea, finding wind-driven flows contribute significantly to net sand transport where tidal currents are small, alongside wave driven currents. The areas defined by van der Molen (2002) as storm dominant (winds + waves) qualitatively agree with the wave-dominated areas of the NL Shelf under energetic wave and tidal forcing presented in Figure 3.9. Their tide-dominated area corresponds to the non-linear wave-tide interaction dominated part of the shelf, and it is noted that wave-tide interaction is not fully represented in their modelling. Whilst wind-driven circulations are beyond the scope of this study, this kNN method could be extended using a coupled training model to isolate the relative influence of wind-driven circulations on net sand transport and incorporate these into the classification.

Baroclinic circulations are not considered in this study either. Van Leeuwen et al. (2015) classify the North Sea by stratification regime. The regions of greatest net sand transport predicted here correspond qualitatively with areas either permanently mixed or intermittently stratified conditions, with seasonally stratified conditions affecting the deeper, microtidal areas of the North Sea which are predicted to have a lower magnitude of net sand transport. In winter, the NW European shelf area considered in this study is well mixed whilst areas such as the UK East Coast, the NL Shelf, the DE-DK Shelf and English Channel tend to remain well mixed or show weak stratification through spring, summer and autumn (Holt et al., 2010), and therefore baroclinic effects are not expected to influence significantly the prediction of this model in these regions.

An additional limitation is that this study only considers a pure sand bed, whereas sand-mud and sand-gravel mixtures affect sand resuspension (McCarron et al., 2019; Thompson et al., 2019). Graded sediment transport resulting from heterogeneous, bimodal sand distributions may also affect the wave length of sand waves (Van Oyen & Blondeaux, 2009). In sand-gravel mixtures, the hiding-exposure effect increases the critical shear stress required to mobilise the sand fraction, its effect becoming more significant for mixtures of >10% gravel (McCarron et al., 2019). Much of the North Sea sediment is comprised of > 90% sand (Figure 3.1c), and this effect is most likely to impact predictions on shelf areas with a higher coarse grain size fraction such as the Celtic Sea. Whilst we also do not consider biological effects on sediment resuspension, Thompson et al. (2019) show physical sediment characteristics to be more significant than biological factors in controlling bed

stability. The purpose of this kNN classification method is to be applicable with readily available hydrodynamic and morphological data, therefore consideration of non-uniform grain size distributions, the effect of mixed sand-mud or sand-gravel substrates, and biological effects would necessarily add complexity to the predictive model and therefore limit its use by introducing a data requirement which may not be readily available to coastal practitioners. The method could be extended to include the effects of mixed grain size fractions in future.

The benefit of this method is to enable a rapid assessment of the dominant processes affecting net sand transport, and its magnitude, without the need for a computationally expensive numerical model. We show that the classification scheme of King et al. (2019) has predictive value for sand wave morphology on the NL Shelf, as a further application of this method. Whilst this paper considers shelf-scale processes, this classification scheme can be applied to other sand transport processes in the nearshore, such as headland bypassing (King et al, 2021). The computational efficiency of this method relative to running a coupled wave-tide numerical model enables quick assessment to be made of the influence of changing environmental conditions such as upward trends in storminess across central, western and northern Europe (Donal et al., 2011; Castelle et al., 2018) on the magnitude and dominant forces driving the net transport of sand on sandy continental shelves, with potential applications globally.

3.5 Conclusions

In this paper we apply a data driven method to predict the dominant sand transport drivers and magnitude across a sandy continental shelf. We use k-Nearest Neighbour classification prediction trained with data from coupled hydrodynamic, wave and sediment transport modelling on a subdomain of the shelf to predict sand transport magnitude and mode across the entire shelf, using readily available wave, tide and morphological data. Key findings of this paper include:

- The relative dominance of waves, tides and non-linear wave-tide interactions (WTI) in the net transport of sand over a tidal cycle, as well as net sand transport magnitude, are amenable to prediction using readily available environmental predictors. These are: significant wave height, peak period, mean wave direction, wave power, tide range, maximum tidal current speed and direction, water depth and median grain size.
- Wave and tidal conditions are primary controls on net sand transport mode and magnitude, whilst grain size is a secondary control.
- Different shelf areas exhibit different dominant drivers of net sand transport for similar exceedance conditions, relating to differences in water depth, grain size, tide range and wave exposure between regions.
- Most shelf areas are tide-dominated or show significant tidal influence on net sand transport for median waves at springs. For extreme waves at springs, most areas show dominance of the non-linear effects of wave-tide interactions. At neaps, with median waves, sand transport is very low across the shelf, driven by wave-tide interaction where it does occur. Extreme waves at neaps result in wave-dominated sand transport in most areas of the shelf, whilst wave-tide interactions influence sand transport in deeper or macrotidal regions.
- Sand transport magnitude and dominance was predicted for a statistically representative year based on distributions of tide range and H_s-T_p joint-probability calculated across the shelf. Potential net sand transport shows tidal dominance in meso-macrotidal waters around the UK, wave-dominance on Dogger Bank and the German/ Denmark Shelf, and dominance of WTI on the Netherlands shelf and in deeper areas of the North Sea and Celtic Sea.

- The kNN prediction was applied at higher resolution to the Netherlands shelf area, and classes for energetic conditions (1% exceedance waves at spring tide) compared with sand wave morphology across the region with data obtained from Damen et al. (2017). Sand wave height is shown to significantly (95% confidence) reduce with greater wave-dominance, while sand wave length and asymmetry significantly increase. Sand wave morphologic parameters were significantly different between predicted classes at the 95% confidence level.
- This paper presents a computationally efficient method to determine an initial estimate of the dominant driving forces and magnitude of net sand transport on sandy continental shelves, enabling efficient large-scale comparison between different regions and testing of the influence of changing environmental forcing on net sand transport with applications globally.

4 Wave, tide and topographical controls on headland sand bypassing

The work in this chapter is accepted for publication in:

King, E. V., Conley, D. C., Masselink, G., Leonardi, N., McCarroll, R. J., Scott, T., & Valiente, N. G. (2021). Wave, Tide and Topographical Controls on Headland Sand Bypassing. *Journal of Geophysical Research: Oceans*, 126, e2020JC017053. https://doi.org/10.1029/2020JC017053

The work in this chapter was conceived and conducted by Erin King, with supervisory support from Professor Daniel Conley, Professor Gerd Masselink and Dr Nicoletta Leonardi, and with comments and discussion on the analysis and drafted manuscript by Dr Robert McCarroll, Dr Tim Scott and Dr Nieves Valiente during the publication process.

The work in this chapter addresses the following thesis aims:

(i) Advancing our understanding and quantification of the impact of waves, tides and their interactions on net sand transport;

(iii) Furthering our understanding of the extent, drivers and predictability of headland bypassing on embayed coastlines.

Key Points:

- Headland bypassing is potentially widespread on energetic embayed coasts.
- Bypassing can be predicted for realistic morphology and sand coverage; key parameters are headland extent, surf zone width and toe depth.
- Tides are a secondary control on bypassing rate under energetic waves. Wave-current interactions can dominate bypassing for median waves.

Chapter Abstract

Embayed beaches separated by irregular rocky headlands represent 50% of global shorelines. Quantification of inputs and outflows via headland bypassing is necessary for evaluating long-term coastal change. Bypassing rates are predictable for idealised headland morphologies; however, it remains to test the predictability for realistic morphologies, and to quantify the influence of variable morphology, sediment availability, tides and wave-tide interactions. Here we show that headland bypassing rates can be predicted for wave-dominated conditions, and depend upon headland cross-shore length normalised by surf zone width, headland toe depth and spatial sediment coverage. Numerically modelled bypassing rates are quantified for 29 headlands under variable wave, tide and sediment conditions along 75km of macrotidal, embayed coast. Bypassing along the North Coast of Cornwall is predominantly wave-driven and nearly ubiquitous under energetic waves. Tidal elevations modulate bypassing rates, with greatest impact at lower wave energies. Tidal currents mainly influence bypassing through wave-current interactions, which can dominate bypassing in median wave conditions. Limited sand availability off the headland apex can reduce bypassing by an order of magnitude. Bypassing rates are minimal when cross-shore length > 5 surf zone widths. Headland toe depth is an important secondary control, moderating wave impacts off the headland apex. Parameterisations were tested against modelled bypassing rates, and new terms are proposed to include headland toe depth and sand coverage. Wave-forced bypassing rates are predicted with mean absolute error within a factor of 4.6. This work demonstrates wave-dominated headland bypassing is amenable to parameterisation and highlights the extent to which headland bypassing occurs with implications for embayed coasts worldwide.

4.1 Introduction

Embayed beaches separated by irregular rocky headlands represent around 50% of the world's shoreline and are important zones ecologically and commercially (Short & Masselink, 1999). Accurate determination of sediment budgets is necessary for prediction of coastal change over long timescales in these zones. It has been recognised that the traditional view of embayed beaches as closed littoral cells is not accurate for many embayments, where sediment can enter and exit the system via headland bypassing (Goodwin et al., 2013; Duarte et al., 2014; Vieira da Silva et al., 2016, 2018; Ribeiro et al., 2017; Valiente et al., 2019a, b).

Headland bypassing is defined as the process of sand transport around headlands, which act as obstructions to longshore sediment transport, forced by wave, tide and wind action (Evans, 1943; Vieira da Silva et al., 2016, 2018; Valiente et al., 2019a). Headland bypassing can be an important contribution to longshore sediment transport and hence influence coastal sediment budgets and management plans (Thom et al., 2018). Investigations of circulation and bypassing around engineering structures and inlets have been conducted (FitzGerald et al., 2000; Acworth & Lawson, 2012; Ab Razak et al., 2013; Scott et al., 2016a) whilst more recently studies have focussed on sand bypassing natural headlands (Goodwin et al., 2013; Duarte et al., 2014; George et al., 2015; Vieira da Silva et al., 2016, 2018; Ribeiro et al., 2017; McCarroll et al., 2018; Valiente et al., 2020). Recent modelling works demonstrate bypassing rates are predictable for individual headlands (McCarroll et al., 2018; Valiente et al., 2020) and idealised headland morphologies (George et al., 2019; McCarroll et al., 2021b), however it remains to test this predictability using a range of real headland morphologies, and to examine the influence of embayment morphology, sediment availability and tidal effects on sand bypassing rates.

Embayment morphology is an important control on embayment circulation. Embayment morphology is an important control on embayment circulation, which influences the longshore and cross-shore transport of sediments. Circulation is influenced by embayment length, cross-shore headland extent and surf zone width, incident wave height, incident wave angle, tide state and local bathymetry (e.g. Castelle et al., 2016; McCarroll et al., 2016, 2018; Mouragues et al., 2020; Scott et al., 2016a). Embayment cellular circulation can involve one or two headland attached cellular rip currents, or a single cellular rip current at the centre of the embayment

(Castelle et al., 2016). These rips are often referred to as 'mega-rips' (Akan et al., 2020; McCarroll et al., 2016, 2018; Short, 1985), and are associated with high-energy conditions with major storm events thought to be an important driving force of headland-attached rip bypassing (Short & Masselink, 1999). Embayment length is important in determining the flushing of the surf zone via headland rips with wider embayments allowing greater development of longshore drift in oblique wave conditions, resulting in stronger flushing at the downwave headland (Castelle & Coco, 2013). Goodwin et al. (2013) observed sensitivity of the cross-embayment sand transport pathway downdrift of a headland to the dominant wave direction, and switching between cross-embayment and nearshore transport modes dependent upon incident wave modality and directional power. In addition to the influence of embayment morphology on intra-embayment circulation pathways, it is necessary to consider the influence of headland morphology on the potential for inter-embayment sand transport via headland bypassing.

Headland morphology is an important control on headland bypassing (McCarroll et al., 2019; Wiggins et al., 2019; McCarroll et al., 2021b). It is key to quantify headland and embayment morphometric parameters in order to examine their influence on headland bypassing. Such measurements are non-trivial due to the fractal nature of rocky coastlines (Mandelbrot, 1967; Burrough, 1981). Embayment morphometric parameters have been quantified in studies of embayment circulation and rip channel morphology (Short & Masselink, 1999; Castelle & Coco, 2012), whilst Fellowes et al. (2019) quantify a range of embayment morphometric parameters and use these to produce a morphometric classification. Recommendations are made in McCarroll et al. (2021b) for a method to calculate headland morphometric parameters for use in headland bypassing predictions. George et al. (2015) classify headlands into eight classes based on geomorphic and bathymetric parameters, finding headland perimeter, apex sharpness and bathymetric expression to be most important for controlling headland bypassing under wave forcing. Of these headland classes, it was suggested only one acts as a barrier to sand transport under all conditions, indicating the potential ubiquity of headland sand bypassing. These efforts give a basis from which to derive headland and embayment morphometric parameters for the purpose of predicting headland bypassing rates.

Prediction of headland bypassing has become a recent focus of research on this topic. The classification and method presented by George et al. (2015) can be used to indicate likelihood of headland bypassing and bypassing direction under wave forcing, but does not give an indication of bypassing magnitude. Predictions of bypassing magnitude were initially proposed by McCarroll et al. (2018), where a headland-specific parameter was conceived based upon modelled daily sand bypassing of a macrotidal headland. George et al. (2019) found that bypassing is controlled by wave angle, headland size and grain size. Valiente et al. (2020) show that headland bypassing of multiple headlands is predictable as a function of offshore wave power, although this requires a computationally expensive numerical model to first calibrate a polynomial to each headland. By modelling headland bypassing of a large number of synthetic headlands, McCarroll et al. (2021b) demonstrated that headland bypassing Q_b can be parameterised as an initial approximation as a function of headland cross-shore extent X_{head} and surf zone width X_{surf}:

$$Q_{b\_Orig} = Q_0 \cdot e^{-\left(\frac{X_{head}}{X_{surf}}\right)^2}, \tag{4.1}$$

Where the unconstrained open coast longshore sediment flux Q_0 is estimated using van Rijn (2014):

$$Q_0 = 0.00018 \cdot K \cdot g^{0.5} \cdot \tan(\beta)^{0.4} \cdot D_{50}^{-0.6} \cdot H_{s,b}^{3.1} \cdot \sin(2\alpha_b), \tag{4.2}$$

In which K is a proxy for wave period where K is 1.5 for swell waves and 1 for wind waves, g is gravitational acceleration, $\tan(\beta)$ is beach slope, D_{50} is median grain size, $H_{s,b}$ is breaking wave height and α_b is breaking wave angle relative to shore-normal. This parameterisation has the benefit of being calculable without use of computationally expensive numerical techniques. However, there are important limitations to be addressed to support application of this parameterisation to embayed coasts in realistic settings.

It remains to test the current headland bypassing parameterisation of McCarroll et al. (2021b) on a range of realistic headland morphologies. Additionally, circulation and bypassing can be influenced by embayment morphology and nearby headlands (Scott et al., 2016a; McCarroll, et al., 2018, 2021b), sediment availability off the headland toe (George et al., 2019) and headland underwater bathymetric

expression (George et al., 2015; McCarroll et al., 2021b). The influences of bathymetric expression and sediment spatial variability in sand bypassing rates are yet to be quantified. Waves are the primary driver of headland sand bypassing based on observation and modelling studies (Goodwin et al., 2013; Vieira da Silva et al., 2018; McCarroll et al., 2018; George et al., 2019); however, tidal elevations and tidal currents play a secondary role (McCarroll et al., 2018, 2021b). Costa et al. (2019) indicate non-linear interaction between waves and tides can increase bypassing by an order of magnitude relative to tides-alone. A recent review of the major controls on headland bypassing is given by Klein et al. (2020). Uncertainty remains as to the influence of these variables and how they relate to headland bypassing in a manner which could be included in bypassing parameterisations, which we aim to address in this study.

This paper aims to test the applicability of existing headland bypassing parameterisations against realistic headland morphologies, and to expand the parameterisations to include the influence of headland underwater expression, sediment availability and embayment morphology. We also aim to quantify the impact of tides and non-linear wave-tide interactions on headland bypassing rates. The North Coast of Cornwall presents ideal conditions for this investigation, with a wide variety of embayed beaches separated by irregular and varied rocky headlands, energetic waves, spatially variable sand coverage and macrotidal regime (King et al., 2019). We quantify headland and embayment morphologies and sediment spatial variability across this region and determine sand bypassing rates under various physical forcing conditions using a validated coupled hydrodynamic, wave and sediment transport model. The following objectives are addressed: (i) testing the performance of the parameterisation as presented in McCarroll et al. (2021b) against realistic headland morphologies, and suggesting improvements; and (ii) examining the impact of tidal currents and wave-current interactions on headland bypassing relative to wave-only forcing.

4.2 Study area

The North Coast of Cornwall is situated in the South West United Kingdom, on the Northwest European Continental Shelf (Figure 4.1). Resonant effects contribute to large tidal amplitudes over the whole Celtic shelf, with a mean spring tide range (MSTR) in the study area of circa 5m in the Southwest and increasing to >7m at Hartland Point (Uncles, 2010). Modelled regional scale bed shear stresses, tidal residual currents and sand transport pathways indicate residual sand transport towards the northeast along this coastline, progressively weakening as it moves up coast (Pingree & Griffiths, 1979; Holt et al., 2001; Uncles, 2010; King et al., 2019). Strong tidal currents (around 1.5 ms^{-1} at springs) drive a net residual current of up to 15 cms^{-1} towards the northeast immediately adjacent to large coastal promontories. This residual is broken up by multiple headland-bound embayments, resulting in areas of low residual tidal transport close to shore. In combined wave and tide conditions, sand transport is wave-dominated for median waves in these areas where tidal forcing is weakest and is wave-dominated across the whole North Coast under extreme waves (King et al., 2019), although as the modelling of King et al. (2019) was conducted at 1 km resolution, higher resolution modelling is required to resolve individual embayment circulations.

A 75-km stretch of this coast was selected for this study (Figure 4.1). This section of coastline is comprised of embayed beaches separated by irregular rocky headlands (29 embayments were selected for this study). Beaches in the study area are comprised of medium quartz sand (Prodger et al., 2016). These embayments comprise a wide range of wave exposures, embayment lengths, degrees of embaymentisation and headland morphologies. This coast is directly exposed to the Atlantic, bringing waves with potential fetch lengths of 6000km (Collins, 1987). Winter storm H_s at nearshore wave buoys along the North Coast can exceed 6m (Scott et al., 2016b). Average H_s based on a 10-year hindcast of WAM is ~1.5m along this section of coast, with H_s of ~2m further offshore (Bricheno et al., 2015; King et al., 2019). The wave climate in the region has experienced an increase in extreme (99th percentile) H_s of up to 1% per annum between 1985 and 2008, and has also experienced an increase in winter wave height and interannual variability (Young et al., 2011; Castelle et al., 2018).

The large tidal range, high degree of wave exposure and diversity of headland and embayment morphologies make this a suitable site for an investigation into the impacts of different environmental and morphological forcing conditions on potential headland bypassing.

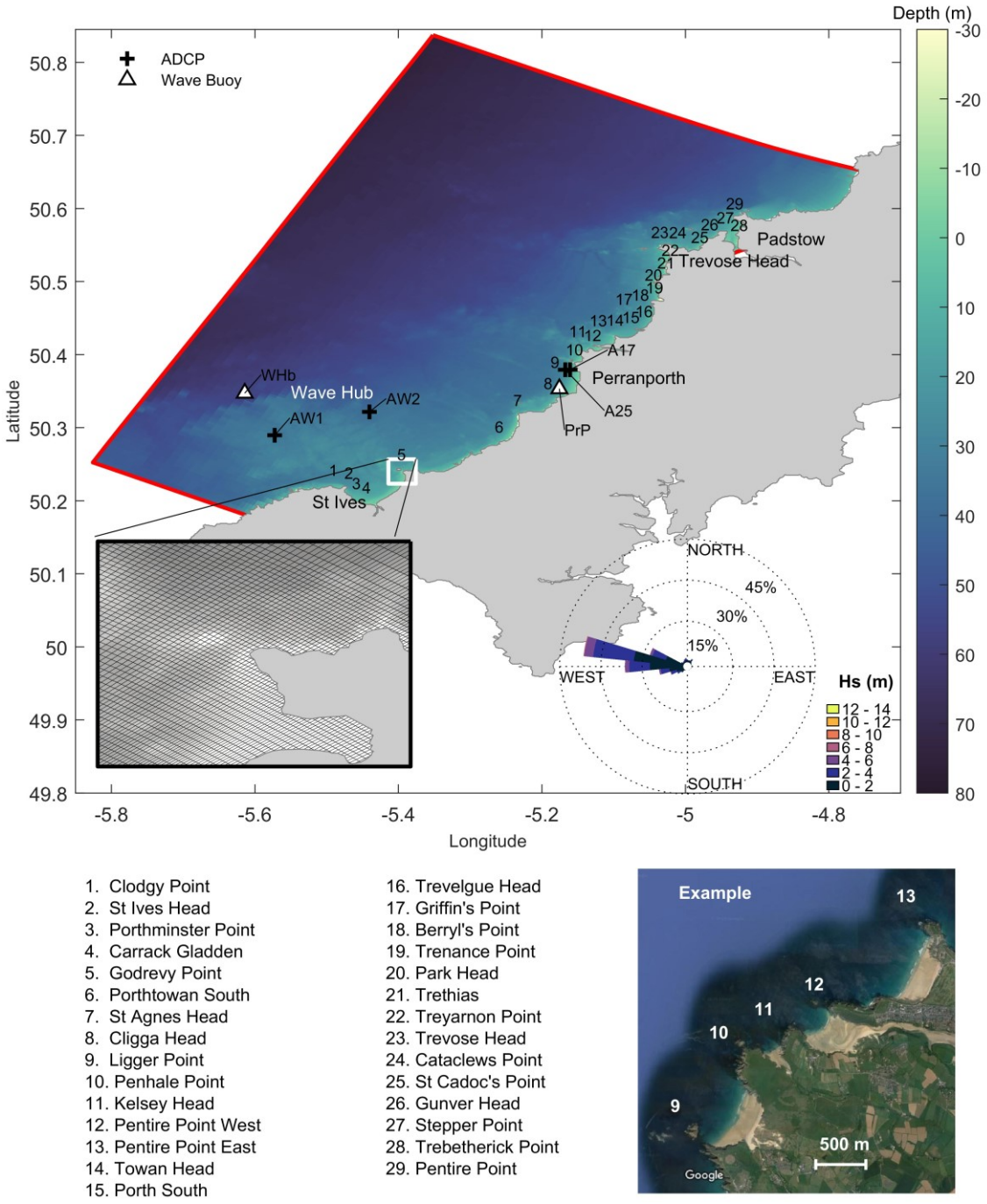

1. Clodgy Point
2. St Ives Head
3. Porthminster Point
4. Carrack Gladden
5. Godrevy Point
6. Porthtowan South
7. St Agnes Head
8. Cligga Head
9. Ligger Point
10. Penhale Point
11. Kelsey Head
12. Pentire Point West
13. Pentire Point East
14. Towan Head
15. Porth South
16. Trevelgue Head
17. Griffin's Point
18. Berryl's Point
19. Trenance Point
20. Park Head
21. Trethias
22. Treyarnon Point
23. Trevose Head
24. Cataclews Point
25. St Cadoc's Point
26. Gunver Head
27. Stepper Point
28. Trebetherick Point
29. Pentire Point

Figure 4.1: Map of the North Coast of Cornwall as represented within the model domain, showing the wave computational grid and bathymetry. The inset around Godrevy Point shows the computational grid as an example of the localised grid refinement around headlands. Headlands are numbered from southwest to northeast as indicated, and their names are included below the map. Other locations of reference are annotated. ADCP deployments (+) and wave buoy locations (Δ) are marked, alongside their name as referred to in the text. Open model boundaries are marked with a solid red line. A wave rose of the wave climate at the Wave Hub between 01-June-2015 and 31-May-2018 is inset bottom-right, showing principle wave directions. An example aerial image of headlands 9-13 is included for reference (bottom right). For the purpose of this study, upcoast is defined as towards the northeast (increasing headland number).

4.3 Methods

4.3.1 Numerical model

The process-based numerical model Delft 3D was used to model the North Coast (Figure 4.1). The FLOW hydrodynamic module was 2-way coupled to a SWAN third-generation spectral wave model packaged as Delft3D WAVE with an identical grid. Three-dimensional hydrodynamics are calculated using the unsteady shallow-water equations, following the Boussinesq approximation with the vertical momentum equation reduced to the hydrostatic pressure relation, assuming that vertical accelerations are small relative to gravitational acceleration (Lesser et al., 2004). The contribution of 3D turbulent eddies is modelled using a k-ε turbulence model. SWAN, packaged as Delft3D-WAVE, is a third-generation phase-averaged wave model based on fully spectral representation of the action balance equation, accounting for wave-current interaction through radiation stress, refraction, wind generation, whitecapping, nonlinear wave-wave interactions, bottom dissipation, and depth-induced breaking (Booij et al., 1999).

The North Coast model was one-way nested within a regional fully coupled hydrodynamic, wave and sand transport model validated and presented in King et al. (2019). Grid resolution of the North Coast model was circa 50m in the vicinity of headlands, and the model was run in 3D hydrodynamic mode with 10 sigma-levels in the vertical to allow resolution of 3D effects such as wave dissipation at the surface due to breaking and whitecapping, and dissipation at the bed due to bottom friction, in order to best reproduce wave-induced mass flux and undertow (van Rijn et al., 2004; Deltares, 2014). A horizontal resolution of 50 m was selected as a balance between resolving high resolution circulations around headlands and computational efficiency, and only headlands that were well resolved at this resolution were selected for analysis. The WAVE grid was extended two grid cells out from the FLOW grid. Bathymetry was derived from merged high-resolution multibeam data from the UK Hydrographic Office and lidar data Plymouth Coastal Observatory, corrected to Mean Sea Level 2000 datum using the Vertical Offshore Reference Frame (Turner et al., 2010) and merged with coarser EMODnet bathymetry offshore (EMODnet Bathymetry Consortium, 2016; Figure 4.1). Bathymetry at the boundaries matched the bathymetry of the regional forcing

model. High-resolution bathymetry was assigned to the grid using spatial averaging, while lower resolution EMODnet bathymetry was assigned to the grid using triangular interpolation. A uniform grain size of 330μm (Prodger et al., 2017) throughout the domain was used, allowing cross-comparison of different embayments. In reality, this is likely to underestimate potential sand bypassing in areas with finer sediments.

The hydrodynamic model has water level boundary conditions at the offshore and northeast boundaries and one velocity boundary to the south-west. Several boundary configurations were tested for the hydrodynamic model, and this combination of forcing types provided the best agreement with observations during calibration. Boundaries were situated far from the headlands of interest. Boundary conditions were linearly interpolated from the regional model, which was itself one-way nested within the Atlantic Margin Model (FOAM-AMM7; O'Dea et al., 2012; McConnell et al., 2017). The hydrodynamic time-step was 12 s. Wind fields were interpolated linearly from 0.25° resolution scatterometer blended 6-hourly mean wind fields retrieved from the Copernicus Marine Service (Bentamy & Fillon, 2012). Atmospheric pressure was interpolated linearly to the model grid from the 0.5° resolution Climate Forecast System version 2 model (Saha et al., 2014).

The wave model was forced with parametric boundary conditions (H_s, T_p, direction, directional spreading) linearly interpolated from the regional model at 1km resolution at the open boundaries. For calibration and validation the regional model in turn was forced by the UK Met Office Wave Watch III continental shelf model (King, 2019; Saulter, 2017). The wave model was simulated in non-stationary mode, with a time-step of 10 minutes, and a coupling interval between WAVE and FLOW of 1 hour, where wave forces are passed based on energy dissipation rate radiation stresses, bed shear stresses, Stokes drift and bottom orbital velocity, and receiving water levels and velocities. The wave model had a directional resolution of 5° (72 bins over a full circle) and 24 frequency bins between 0.05 and 1 Hz.

4.3.2 Sediments

Simulations were conducted under two bed composition scenarios: (i) a spatially uniform sediment coverage, to enable comparison of bypassing rates between different headlands; and (ii) a realistic sediment spatial coverage to highlight the role of sediment spatial availability on bypassing. Variability in grain size was not considered in this study. This is discussed in Section 4.5.2.

A uniform grain size of 330μm (Prodger et al., 2017) was used throughout the domain, allowing cross-comparison of different embayments. Whilst this enables isolation of the controls of headland morphology on bypassing rates, it means absolute bypassing rates reported here will likely be underestimated in embayments with finer sediments, such as Padstow to the northeast (Figure 1; Prodger et al., 2016; Oyedotun, 2020). The influence of different grain sizes on bypassing around an individual headland is covered by McCarroll et al., (2021b; see also George et al., 2019; Klein et al., 2020). In the parameterisation of headland bypassing (equation 1; McCarroll et al., 2021b), grain size is an input to the calculation of unconstrained longshore flux (equation 2; van Rijn, 2014). Modelled sand transport rates were calculated using the TRANSPOR2004 formulation of Van Rijn et al. (2004; see also van Rijn, 2007a, b). The TRANSPOR2004 sediment transport formulation computes sediment transport contributions of suspended and bed load transport for both currents and waves, including their interactions. Enhancement of bed shear stress under currents and waves is accounted for in Delft3D following the method of Soulsby et al. (1993).

4.3.2.1 Spatially variable sediment distributions

To model the influence of spatial variability in sand coverage it is necessary to determine what locations in the domain are covered with sand or are exposed rock or gravel. Maps of spatial sediment classes available in the region such as the British Geological Survey product DiGBS250K are coarse, and unsuitable for modelling at the resolution required by this study. Consequently, an alternative method to determine sediment spatial variability was developed. High-resolution (2m) UKHO bathymetry was used for this purpose. These data cover all embayments in this study. The bathymetry was resampled to 10m resolution for reasons of computational efficiency (Figure 4.2a). A 100m median filter was applied to generate a smoothed surface. This surface was subtracted from the resampled

bathymetry (Figure 4.2b). The standard deviation of this surface was calculated over the same 100m square window, and the maximum of this standard deviation was calculated over this window (Figure 4.2c). This highlighted regions of rock across the domain. Polygonal areas of sediment in each embayment were then selected by eye roughly following the 0.2m threshold (Figure 4.2d).

This method assumes areas of sediment are vertically smoother than rock over a 100m window. Some sediment features were highlighted as rock due to their large vertical expression (such as large sand waves west of St Ives). These were identifiable due to their linear, repeating pattern, and included in the sediment polygons. Perranporth has a sand-gravel transition at circa -26m ODN (Valiente et al., 2019a). This was identifiable in the data as a border with elevated maximum standard deviation and was used to define the offshore sand polygon boundary. Similar borders elsewhere were also used for this purpose. The purpose of this was not to determine the exact spatial extent of sediment across this region, as this would require a more detailed observational campaign to determine sediment physical characteristics and spatial extent. Rather, the method was used as a means of generating an approximate sediment distribution to test the effect of a realistic pattern of sediment spatial coverage on headland bypassing rates *versus* a uniform, homogeneous sand bed. As such, this method was considered sufficient for the purpose of this study.

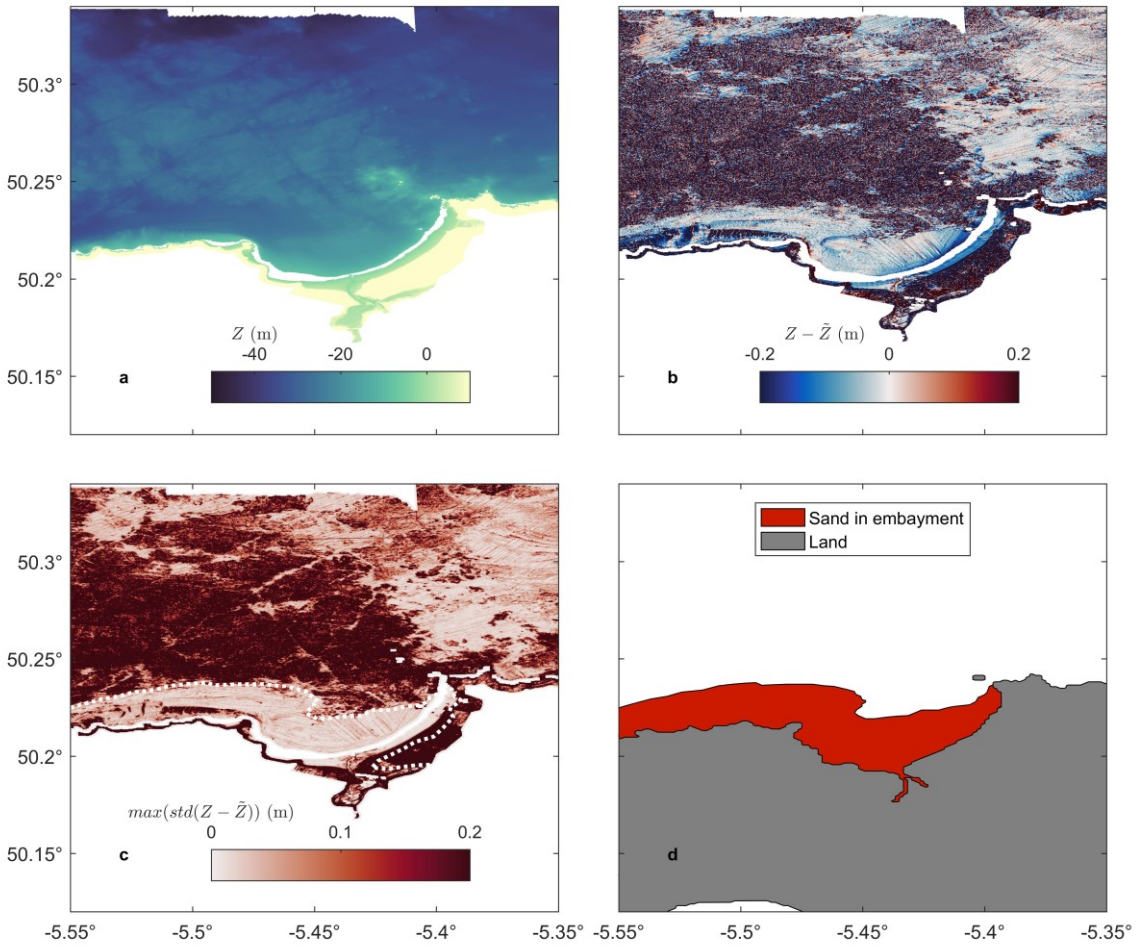

Figure 4.2: Sediment availability determination: example from St Ives Bay. (a) 10m resampled UKHO bathymetry. (b) The difference surface once a 100m window median filtered surface was subtracted from (a). (c) Maximum standard deviation of (b) over the same 100m window. Areas of high vertical variability are assumed to generally correspond to rock offshore. The selected sand-rock boundary is indicated with a white dashed line, corresponding to roughly the 0.2m contour offshore. (d) Polygons of spatial sand extent in embayments of interest, determined by eye from (c), also indicating areas of land.

4.3.3 Calibration and validation

Numerical model calibration was performed using ADCP data at the Wave Hub, and wave buoy data at Perranporth (AW1/2 & PrP; Figure 4.1) over a 32-day window between 23/12/2013 and 24/01/2014, including three large storm events. Hydrodynamics were calibrated for bottom friction and bed shear stress formulations, and roughness coefficient. The Manning bottom friction formulation with a uniform roughness coefficient of 0.0275 performed best, as well as the Fredsøe (1984) bed shear stress formulation. Waves were calibrated for whitecapping formulations, bed friction formulations and bed friction coefficients. Calibration of these had a significant impact on wave model skill, with the default combination overestimating H_s at Perranporth. The best performing combination was the formulation of Komen et al. (1984) for whitecapping, Madsen et al. (1988) for bed friction, with a bed friction coefficient of 0.05. A full list of model formulations and parameters is included in Appendix B.

Validation of the model was performed for waves using wave buoys at Perranporth and Wave Hub, and for currents using ADCP derived currents offshore of the North headland of Perranporth (Figure 4.3; For locations, see Figure 4.1). Validation was performed over a 92-day period from 2016/06/01 to 2016/09/01 including an energetic event of 20th August. Time series in Figure 4.3 show a subset of the validation period for clarity. The tidal current axis is predominantly north-south oriented at the deployment sites, with very low east-west velocity components; therefore, only northward velocity components are shown in Figure 4.3. East-west components are validated and their skill metrics shown in Table 4.1.

Scatter plots in Figure 4.3 show all 2016 comparison data from which model skill was determined. Validation skill metrics are shown in Table 4.1. Skill was assessed using the following metrics: R^2, *BIAS*, mean absolute error *MAE*, Willmott Index of Agreement *WIA* and Brier Skill Score *BSS* (calculated as per Davidson et al., 2010). Equations for these metrics are included in Appendix C. Values of $BSS \geq 0.8$ were considered excellent, ≥ 0.6 considered good, ≥ 0.3 considered reasonable, and < 0.3 considered poor.

Validation of velocity components was performed for both the depth-integrated and near-bed velocities to assess model skill through the water column (relevant to suspended load transport) and near the bed (relevant to bed shear stress and

sediment resuspension). In general, the model has good or excellent skill for both depth-integrated and near-bed instantaneous and residual (low-pass filtered) northward velocity components. The lowest performing residual northward velocity skill is the near-bed velocity at A17, which has "reasonable" skill. Eastward velocity components at both ADCP deployments were very small, which resulted in lower Brier Skill and R^2 metrics. A more informative metric at these sites is *WIA*: with $-0.09 \leq WIA \leq 0.56$ indicating the sum of the model error magnitudes is roughly equal to or less than the sum of the observed variability in the ADCP data, by half for a value of 0.5. The *MAE* for all velocity comparisons does not exceed 5 cms^{-1}.

The model has excellent skill for H_s and good skill for T_p. There is a slight northward bias in wave direction (~7° across all observations, increasing to ~14° at the Perranporth buoy). The *WIA* for wave direction indicates modelled errors are within the magnitude of observed variability about the mean direction ($0.07 \leq WIA \leq 0.35$).

Validation of sand transport rates is impossible due to a lack of observation data. McCarroll et al. (2018) applied sediment transport settings from the literature to model headland sand-bypassing at Perranporth (Figure 4.1). King et al. (2019) used observed bedform asymmetry in high resolution bathymetric survey data and sand transport rates reported in the literature to validate their results, and found these settings performed adequately. The TRANSPOR2004 formulation (van Rijn 2007a, b) has been used successfully in other sand transport and headland bypassing studies (Grunnet et al., 2004; Luijendijk et al., 2017; McCarroll et al., 2018; Valiente et al., 2020). Accordingly, the settings included in Appendix B were used in this study.

Overall, good or excellent skill across most comparisons, and in particular, generally good or excellent skill predicting near-bed velocity components off the northern headland of Perranporth, indicates the suitability of this model to investigate sand transport at the coastal scale and headland bypassing.

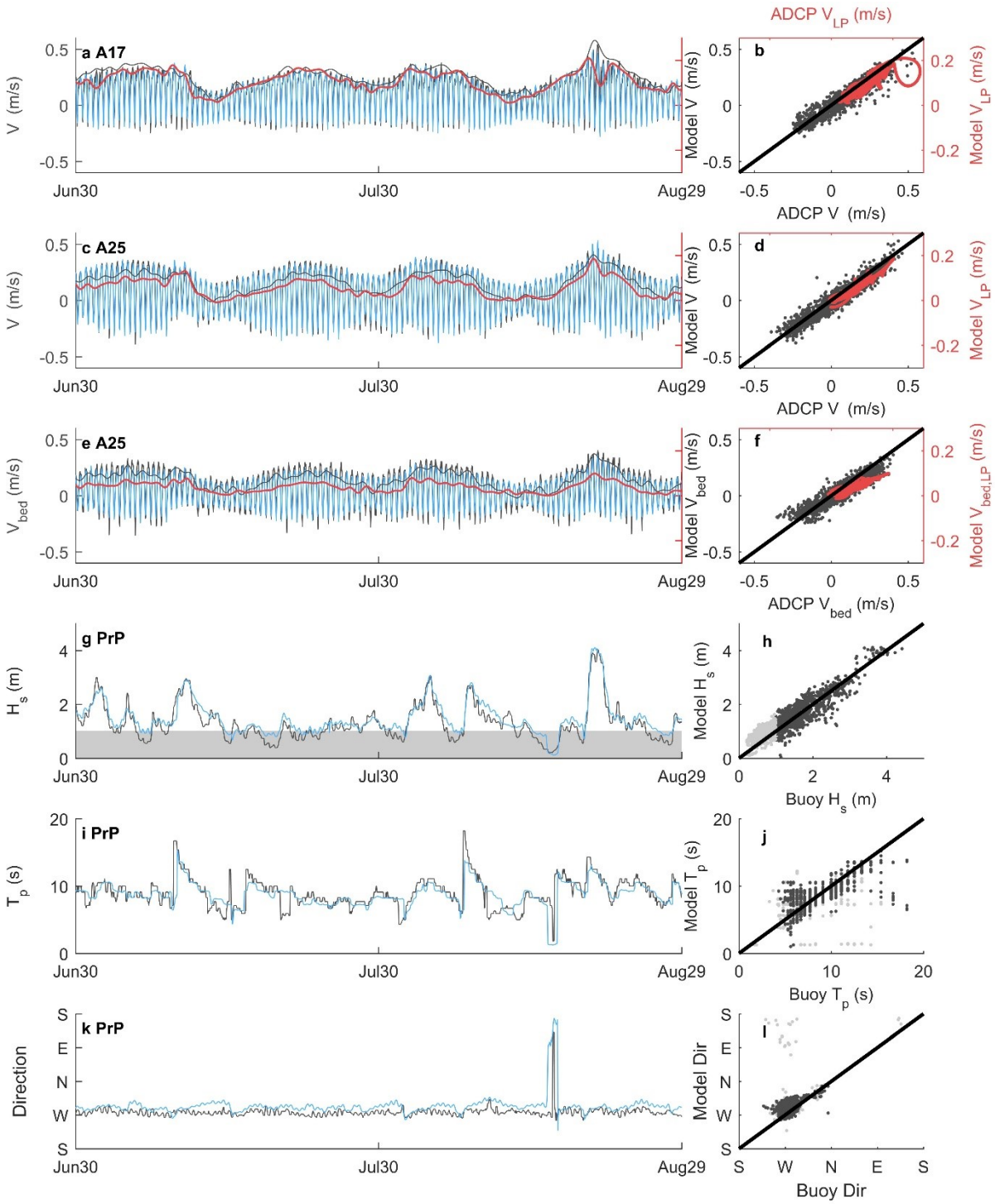

Figure 4.3: Validation time series and scatter plots. Observed time series are dark grey, modelled time series are blue. Where residual (low-pass) time series are shown, observations are dark grey and model data are red. Dark grey points in the scatter plots are hourly unfiltered data of model vs observation, red data are low-pass filtered data. (a-d) Depth-averaged northward velocity components from the Perranporth ADCP deployments A17 and A25. (e, f) Near bed northward velocity components at ADCP deployment A25. (g, h) Significant wave height at the Perranporth wave buoy. Data for H_s < 1m are highlighted in light grey here and in subsequent scatter plots. (I, j) Spectral peak wave period at the Perranporth wave buoy. (k, l) Mean wave direction at the Perranporth wave buoy. Wave buoy data are median filtered for clarity.

Table 4.1

Model Validation Statistics for Currents and Waves, including Residuals from Low-Pass Filtering.

Currents (ms^{-1})												
	Unfiltered Signal						Low-Pass Residual					
Location	N	R^2	BIAS	MAE	WIA	BSS	N	R^2	BIAS	MAE	WIA	BSS
A17-E	2208	0.04	3e-3	0.02	0.30	0.08	2208	0.02	2e-3	0.01	0.29	0.22
A17-N	2208	0.88	-0.01	0.03	0.83	**0.92**	2208	0.71	-0.01	0.02	0.69	**0.75**
A17-E (bed)	2208	0.01	-2e-3	0.02	0.31	0.09	2208	3e-3	-3e-3	0.01	0.14	-0.02
A17-N (bed)	2208	0.82	-0.02	0.04	0.75	**0.84**	2208	0.60	-0.02	0.02	0.55	*0.53*
A25-E	1538	0.06	-0.02	0.04	0.47	0.09	1538	3e-4	-0.02	0.02	-5e-3	-0.66
A25-N	1538	0.93	-0.02	0.04	0.87	**0.96**	1538	0.90	-0.02	0.02	0.71	**0.91**
A25-E (bed)	1538	0.05	-0.02	0.04	0.46	0.06	1538	0.01	-0.02	0.02	-0.09	-0.99
A25-N (bed)	1538	0.88	-0.02	0.05	0.81	**0.91**	1538	0.82	-0.02	0.03	0.61	**0.83**
ALL-E	3746	0.04	-0.01	0.03	0.48	0.16	3746	0.21	-0.01	0.01	0.56	*0.33*
ALL-N	3746	0.92	-0.02	0.03	0.85	**0.94**	3746	0.84	-0.02	0.02	0.72	**0.84**
ALL-E (bed)	3746	0.03	-0.01	0.03	0.43	0.10	3746	0.08	-0.01	0.02	0.39	-0.08
ALL-N (bed)	3746	0.85	-0.02	0.04	0.78	**0.88**	3746	0.73	-0.02	0.02	0.60	**0.66**

Waves														
	H_s (m)					T_p (H_s > 1m) (s)					*Dir* (H_s > 1m) (°)			
Location	N	R^2	BIAS	WIA	BSS	N	R^2	BIAS	WIA	BSS	R^2	BIAS	WIA	MAE
WHb	2168	0.86	0.32	0.66	**0.78**	1634	0.51	-0.14	0.70	**0.71**	0.01*	2.12	0.35	13.81
PrP	2207	0.83	0.14	0.74	**0.88**	1372	0.49	-0.12	0.70	**0.72**	0.26*	13.84	0.10	15.06
ALL	4375	0.87	0.24	0.71	**0.84**	3008	0.58	-0.15	0.73	**0.76**	0.04*	7.34	0.07	13.50

Note. Brier skill scores are coded for excellent and good (bold), reasonable (italic) and poor (underlined) model skill. Eastward and Northward velocity components are denoted by "-E" and "-N" respectively. Near-bed currents are denoted by "(bed)".

* Circular correlation coefficient for directional data.

4.3.4 Simulated scenarios

The wave climate was characterised near the offshore boundary using wave buoy data from the Wave Hub (Figure 4.1) over three years from 01-June-2015 to 31-May-2018. A Gumbel copula was fitted to the data for H_s and T_p to describe the joint probability distribution with H_s and T_p represented by gamma and rician marginal distributions respectively, following the method described in Genest & Favre (2007; Figure 4.4). Marginal distributions were selected based on optimal performance minimising the Akaike Information Criterion. Joint $H_s \cap T_p$ conditions were selected from this distribution for exceedance probabilities of .50, .05 and.0014, the latter representing 12-hour exceedance. These predicted exceedances are in agreement with values for the region presented in the literature (Bricheno et al., 2015; Scott et al., 2016b; King et al., 2019). Three modal wave directions were selected (Figure 4.4). Peak orbital velocities in the region are induced by swell wave action (Draper, 1967) and, consequently, scenarios presented here beyond calibration and validation exclude wind forcing.

Wave-only, tide-only and coupled wave-tide scenarios were conducted. Wave-only scenarios were conducted for two water levels corresponding approximately to spring high water (SHW) and spring low water (SLW) to give maximum variability in tidal elevations tested. Tidal scenarios were conducted over a spring-neap cycle and times where water levels were at Spring High or Spring Low were extracted for analysis. Velocities at these times ranged from 0.02 – 1 ms^{-1}. All scenarios were simulated for a uniform homogeneous sand bed and for the spatially variable sand distribution demonstrated in Figure 4.2. This resulted in a total of 56 scenarios for analysis.

Sand transport components were rotated to their along-shore and cross-shore components along each apex transect (Figure 4.5) and these components were integrated from the headland apex to the maximum depth of transport (DoT; Valiente et al., 2019a) as a measure of instantaneous headland bypassing rate Q_b (m^3s^{-1}). Headlands have both an up-coast and down-coast transect defined by the beach orientation adjacent to each side of the headland (see Section 4.3.5). Bypassing was defined as positive up-coast (generally towards the northeast). Where bypassing rates at the two transects were divergent, bypassing was set to zero. There were no cases of convergent transport in the modelled bypassing rates.

Sand transport rates lower than the range of validation presented in van Rijn (2007b) were set to zero prior to integration (0.00016 $m^3/m/tidal\ cycle$).

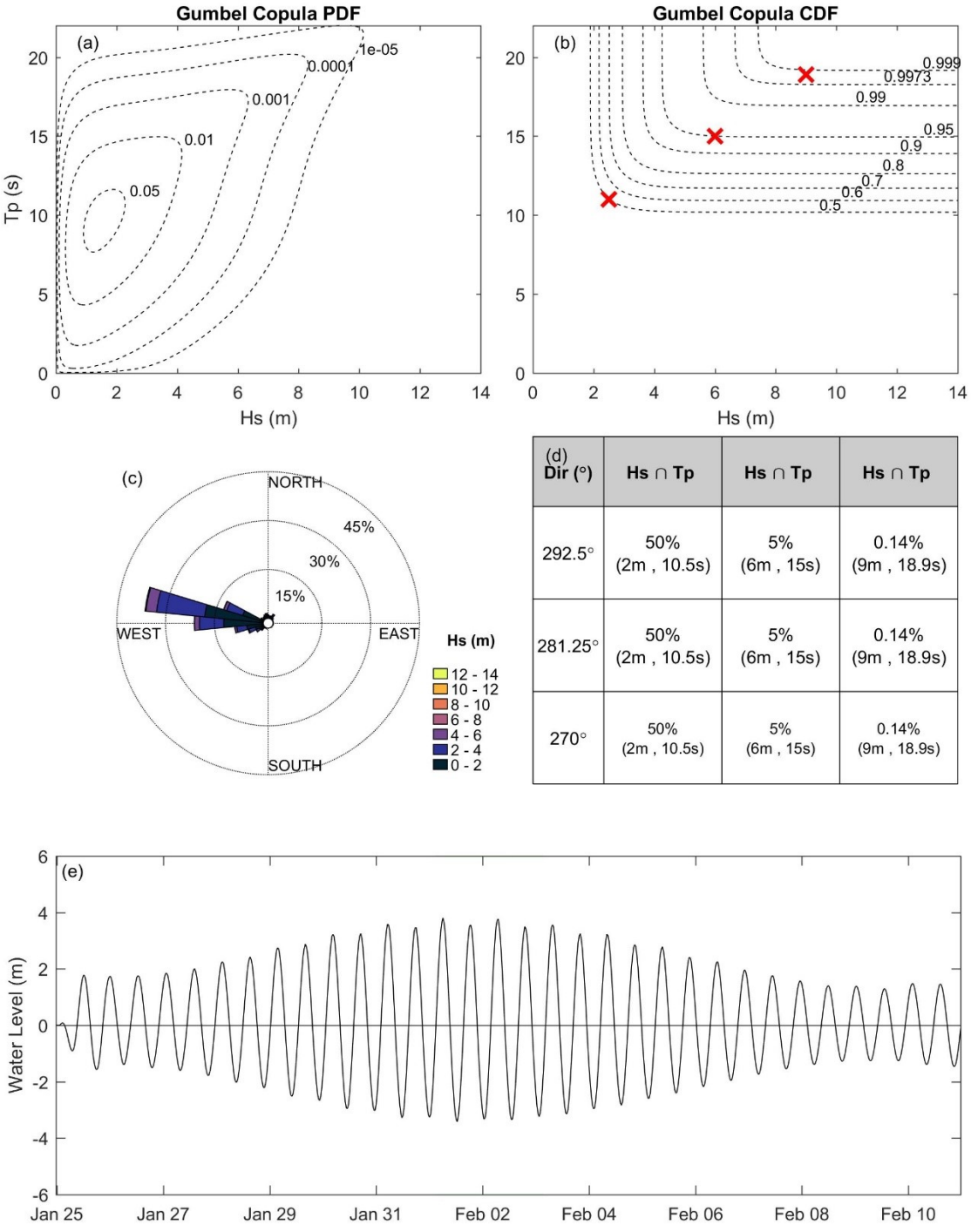

(d)

Dir (°)	Hs ∩ Tp	Hs ∩ Tp	Hs ∩ Tp
292.5°	50% (2m , 10.5s)	5% (6m , 15s)	0.14% (9m , 18.9s)
281.25°	50% (2m , 10.5s)	5% (6m , 15s)	0.14% (9m , 18.9s)
270°	50% (2m , 10.5s)	5% (6m , 15s)	0.14% (9m , 18.9s)

Figure 4.4: Wave climate characterisation used to select conditions for simulation. (a) Gumbel copula PDF representing the joint probability density of H_s and T_p. (b) Gumbel copula CDF representing the cumulative joint probability of H_s and T_p from which conditions were selected (red crosses). (c) Wave rose showing three modal wave directions from West to West-northwest. (d) Wave conditions selected for simulations. (e) Example tidal signal from Perranporth during the tide-only simulation. The first 7 days were used as model spin-up.

Wave-only scenarios were run for 72 hours, and sand transport was averaged over the final 24 hours. In tidal scenarios, times of spring high and low water were defined as when the median water level across each transect was > + 3m or < - 3m relative to mean sea level (MSL2000 datum) respectively. Tide range increases towards the northeast; therefore, the number of points satisfying this criteria increased moving up-coast. Bypassing rates were averaged over all times where the water level was within the SHW or SLW depth bin at each headland.

4.3.5 Quantifying morphometric and environmental parameters

Headland and embayment morphometric and environmental parameters were selected for their relevance to existing headland bypassing parameterisation efforts (McCarroll et al., 2019; 2021b), or for exploratory purposes. Parameters relevant to the calculation of uninhibited longshore transport (van Rijn, 2014; Equation 2) and the blocking potential of a headland (McCarroll et al., 2021b; Equation 1) described in this section include headland cross-shore length X_{head}, surf zone width X_{surf}, breaking wave height $H_{s,b}$, breaking wave angle relative to shore-normal α_b and beach slope β. Exploratory morphometric parameters include headland toe depth Z_{toe} and beach length L_b. Parameters related to spatially variable sediment coverage were explored, including the relative coverage of sediment adjacent to the headland R_{sed} and the cross-shore extent of sediment coverage X_{sed}.

In this study, morphometric parameters were calculated using bathymetry as interpolated to the model grid, to ensure relation to the bathymetry used by the model in the calculation of model hydrodynamics, wave propagation and sand transport. Headland morphology is measured in relation to the waterline around the headland for the water level under consideration, resulting in an apparent morphology that varies over a tidal cycle. Morphology of the headland is considered on the up-wave side, between the beach and the headland apex, defined as the furthest point of the headland cross-shore perpendicular to the water line on the beach. Thus, headland morphology down-wave of the apex is not considered. Headland and embayment morphometric parameters used are depicted in Figure 4.5.

The apparent headland cross-shore extent X_{head} for a certain water level is measured perpendicular to the orientation of the waterline on the up-wave beach adjacent to

the headland (McCarroll et al., 2021b). For very small beach lengths, where determination of the beach orientation at the resolution of the model was subject to greatest error, the orientation was determined from either the adjacent bay or the general orientation of that stretch of coastline.

Surf zone width X_{surf} is measured perpendicular to the beach waterline adjacent to the headland (Figure 4.5), from the beach waterline to the edge of the outer surf zone. For the purpose of this study, this was defined as the point at which the fraction of wave energy dissipation due to breaking reached 5%. This was derived from the model. Breaking wave height $H_{s,b}$ and direction at breaking α_b were then interpolated from the model at this point. Beach slope was also determined along this transect from the waterline to the DoT, taken from Valiente et al. (2019a).

Depth off the headland toe Z_{toe} was determined 50m offshore of the headland apex along the apex transect, between the water line at the headland apex and the bed level at 50 m horizontally along this transect. The point 50m offshore relates to model resolution which aimed to be $\lesssim$ 50m around the headlands. Therefore, this point was chosen as the first wet grid node off the headland apex. This was nondimensionalised across all headlands by dividing by 50m to give the slope of the headland toe m_t:

$$m_t = \frac{Z_{toe}}{50\ m}, \tag{3}$$

Beach length L_b was calculated between the two headland faces using the point of intersection between the headland face and the beach along the water line (Fellowes et al., 2019), defined at the point where the water level contour diverges offshore from the general orientation beach.

Sediment coverage was considered between the headland adjacent transect and the headland apex transect. This adjacent transect was taken at 100m from the headland intersection with the beach, or at the midpoint of the beach if L_b < 200m. Exploratory parameters included the cross-shore sediment extent X_{sed} and the area of sediment coverage adjacent to the headland A_{sed}. This was used to determine the ratio R_{sed} defined as:

$$R_{sed} = \frac{A_{sed}}{A_{DoT}}, \quad (4)$$

Where A_{DoT} is the total area between the adjacent and apex transects, bounded by the headland face and DoT.

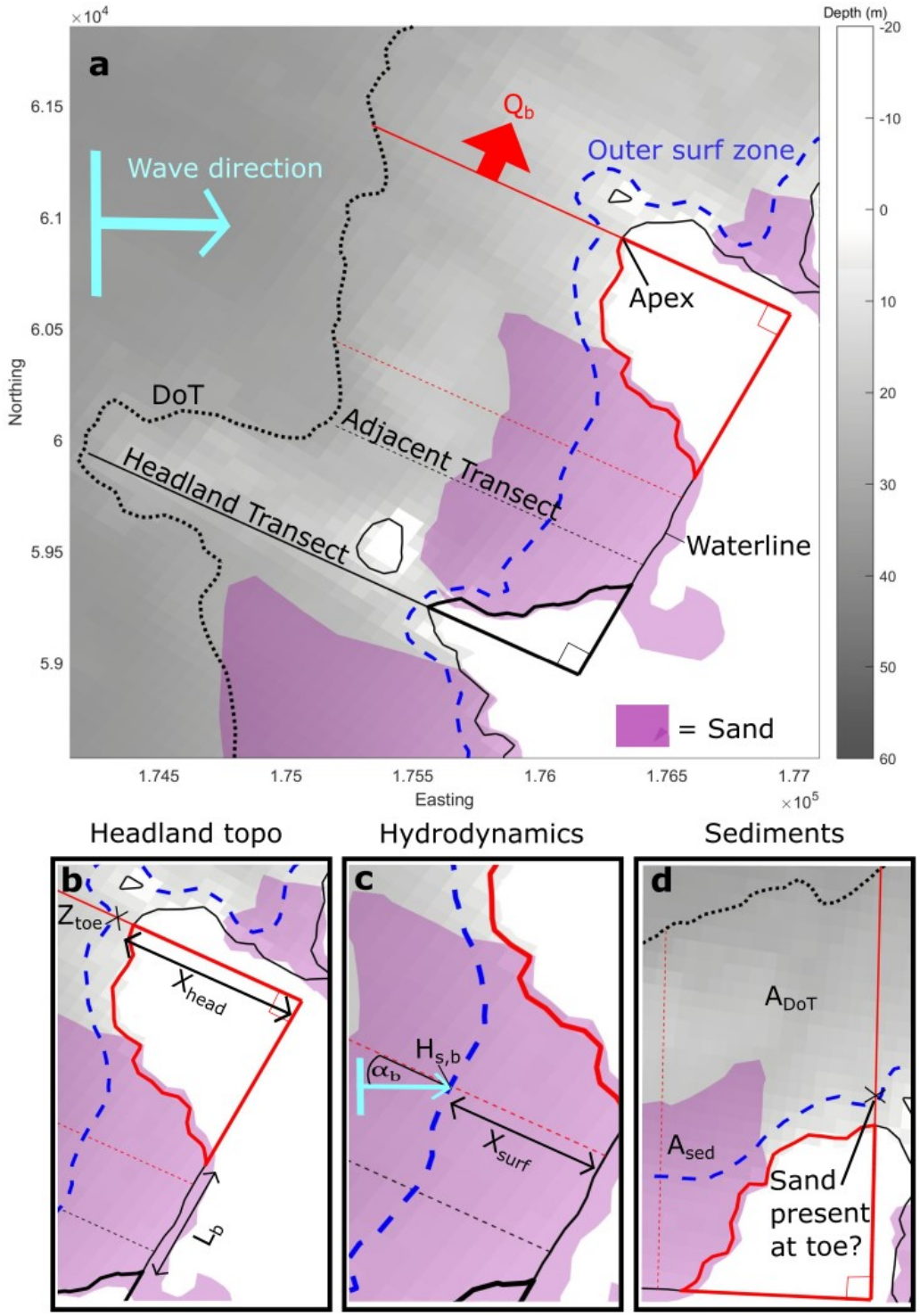

Figure 4.5: Example schematic of morphological and environmental parameters at Holywell Bay at spring high water. (a) Schematisation of the embayment with headland apex transects (solid line) and adjacent beach transects (dashed line) coloured by their respective headland. Other features shown include incident wave direction (light-blue arrow), maximum Depth of Transport (thick black dotted line), outer surf zone (blue dashed line), sand cover (purple shading), and sand bypassing rate Q_b (red arrow). (b) Headland topographical parameters including cross-shore headland length X_{head}, beach length L_b, and headland toe depth Z_{toe}. (c) Hydrodynamic parameters including breaking wave angle α_b relative to shore normal, breaking wave height $H_{s,b}$, and surf zone width X_{surf}. (d) Sediment parameters including sand coverage area adjacent to headland A_{sed}, total area between headland and maximum depth of transport A_{DoT}, and "is sediment present at the headland toe?" In all subplots, bathymetry is indicated in grayscale where sediment is not present.

4.4 Results

4.4.1 Headland and embayment morphology

Selected quantified morphological parameters are displayed in Figure 4.6 for each headland (a, c, e and g) with summary statistics shown using boxplots in (b, d, f and h). Parameters were quantified for upcoast and downcoast apparent morphologies for spring high and low water (SHW and SLW, respectively). For the purpose of this study, upcoast is defined as towards the northeast (increasing headland number). Headland morphology varies widely along this coast, and some headlands (4, 15, 16 & 22) cease to be apparent headlands at SLW, when the water line recedes beyond the headland apex. Headland cross-shore extent X_{head} (a, b) was seen to vary between circa 40 m and 1800 m, and increase by around a factor 2 between SLW and SHW. X_{head}, defined relative to the waterline on the beach and at the headland apex (Figure 4.5), tended to be smaller upcoast than downcoast which may predispose this coastline towards upcoast bypassing. Toe depth Z_{toe} (c, d) varied between circa 0.5 m and 17 m, and was fairly constant between up and downcoast morphologies, whilst increasing between SLW and SHW by circa 3 – 4 m. Beach length L_b (e, f) varied between circa 50 m to 7500 m, and decreased between SLW and SHW by around 1/3 on average. Sediment coverage R_{sed} (g, h) was distributed between full sediment coverage to the DoT and circa 1 % coverage, and was similarly distributed between water levels and up and downcoast aspects. The wide range of morphologies represented here indicates the suitability of this region for testing the parameterisation of headland bypassing rates.

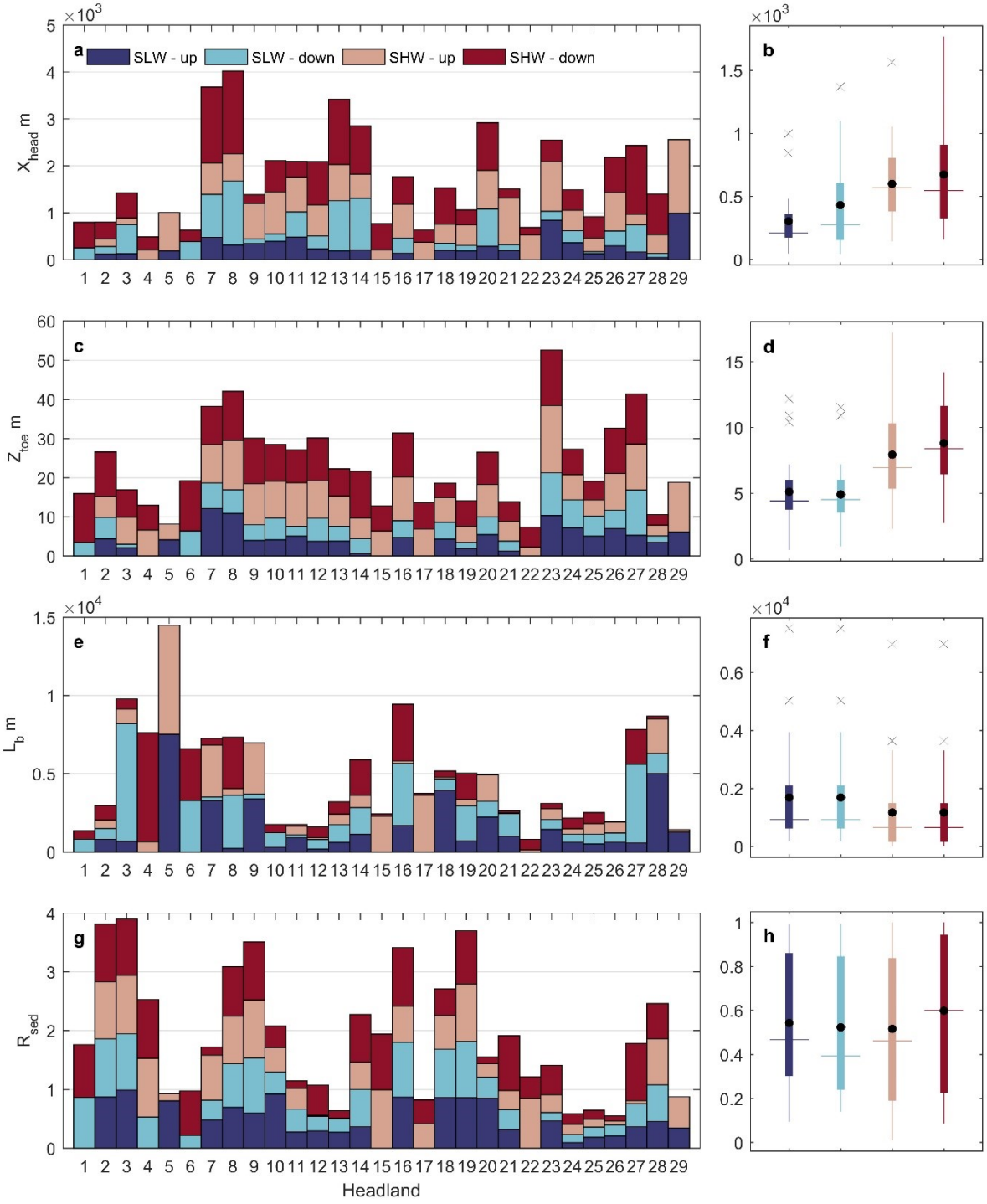

Figure 4.6: Summary figure of headland and bay morphological parameters including: headland cross-shore length X_{head}, headland toe depth Z_{toe}, beach length L_b and sediment ratio R_{sed}. Stacked bar graphs (a, c, e, g) show parameter values per headland for spring high water (SHW) and spring low water (SLW), and for the upcoast orientation (up) and downcoast orientation (down). Values are represented by the individual block lengths. Box plots (b, d, f, h) show summary statistics for each water level and headland orientation. The main body of the boxes span the 25th and 75th percentiles, the horizontal bar shows the median, the mean is shown (black dots), whiskers span up to 1.5 × inter quartile range, and outliers are shown (black crosses).

4.4.2 Headland bypassing

Headland bypassing was active across ~93% (27/29) of headlands for at least one wave condition under wave-only forcing. Only two headlands (5 – Godrevy Point & 23 – Trevose Head) were closed to wave-forced bypassing under all tested conditions. Headland bypassing was blocked for at least one incident wave direction for 41.4% (12/29) of headlands under median (50% exceedance) waves, for 27.6% (8/29) of headlands under large (5% exceedance) waves, and 24.1% (7/29) of headlands for extreme (12 hour exceedance) waves. More headlands exhibited upcoast bypassing than downcoast for the tested conditions. In this section we quantify the influence of wave conditions, headland bathymetric expression, sediment spatial availability and tides. We test the performance of the parameterisation of McCarroll et al (2021b), and suggest improvements to account for bathymetric expression and non-uniform sediment coverage.

This section is subdivided into four parts: (1) starting with uniform sediment availability and wave-only forcing scenarios, we examine the influence of wave conditions and tidal elevations on bypassing rates; (2) we test the performance of the parameterisation of McCarroll et al. (2021b; Equation 4.1), and examine the effect of headland bathymetric expression (toe depth); (3) we compare uniform and non-uniform sediment scenarios under wave-only forcing; and (4), we quantify the impact of tidal currents for uniform and non-uniform sediments, including wave-current interactions.

4.4.2.1 Effect of wave condition and tidal elevation

Bypassing rates for wave-only scenarios are shown in Figure 4.7a-c. Sequential headlands with positive bypassing rates indicate a potential wave-forced upcoast sand transport pathway, while sequential negative bypass rates indicate a potential downcoast transport pathway. Headlands with zero net bypassing (including cases with divergent transport) under all conditions (5, 23) are considered closed to wave-forced sand bypassing. Data for different tidal elevations are differentiated with solid and dashed lines for SHW and SLW respectively. Beyond headlands 1 and 29, model resolution decreases gradually towards the lateral boundaries. While the model resolution at these headlands is adequate, the full embayments on the outside of each of these headlands are not fully resolved (including the next headland along the coast). For this reason, bypassing into the region of interest at headlands 1 and

29 is excluded from analysis. Bypassing out of the region of interest at these headlands is not affected by this, and is included here.

The impact of tidal elevation on headland bypassing rates was independent of wave direction (Figure 4.7a-c). The median impact of tidal elevation changes was greatest during median wave conditions, where in some cases bypassing was activated only at SLW. In other cases, bypassing direction changed between SHW and SLW, mainly for median wave conditions. The impact of changing water levels decreases as wave height increases (Figure 4.7d). For median waves, bypassing at SLW has a median increase in magnitude of circa 4 × relative to SHW, whereas this is reduced to circa 2.5 × for large waves and circa 1.5 × for extreme waves. When determining the mean increase in bypassing rate between SHW and SLW, large outliers were excluded for cases where SHW bypassing rates were very low (Q_b < 10^{-4} m^3s^{-1}), which affected median wave conditions. The mean increase in bypassing at SLW was around a factor of 2 relative to SHW. This relative change is driven by changes to apparent headland morphology at different water levels.

Bypassing rates were strongly dependent upon the cross-shore headland extent relative to surf zone width (Figure7e), in agreement with prior literature on headlands and groynes (Scott et al., 2016a; McCarroll et al., 2021b). There was very little bypassing for $X_{head} > 5\ X_{surf}$ under all conditions, and for $X_{head} > 3\ X_{surf}$ except where $\sin(2\alpha_b)$ was high indicating oblique wave angles conducive to strong longshore transport. With a couple of exceptions, cases where bypassing was totally blocked fell within the region of $X_{head} > 5\ X_{surf}$. Most model results where bypassing was active in this region of $X_{head} > 5\ X_{surf}$ indicated very low bypassing rates of circa 10^{-5} and 10^{-4} m^3s^{-1}, or approximately 1 – 10 m^3day^{-1}.

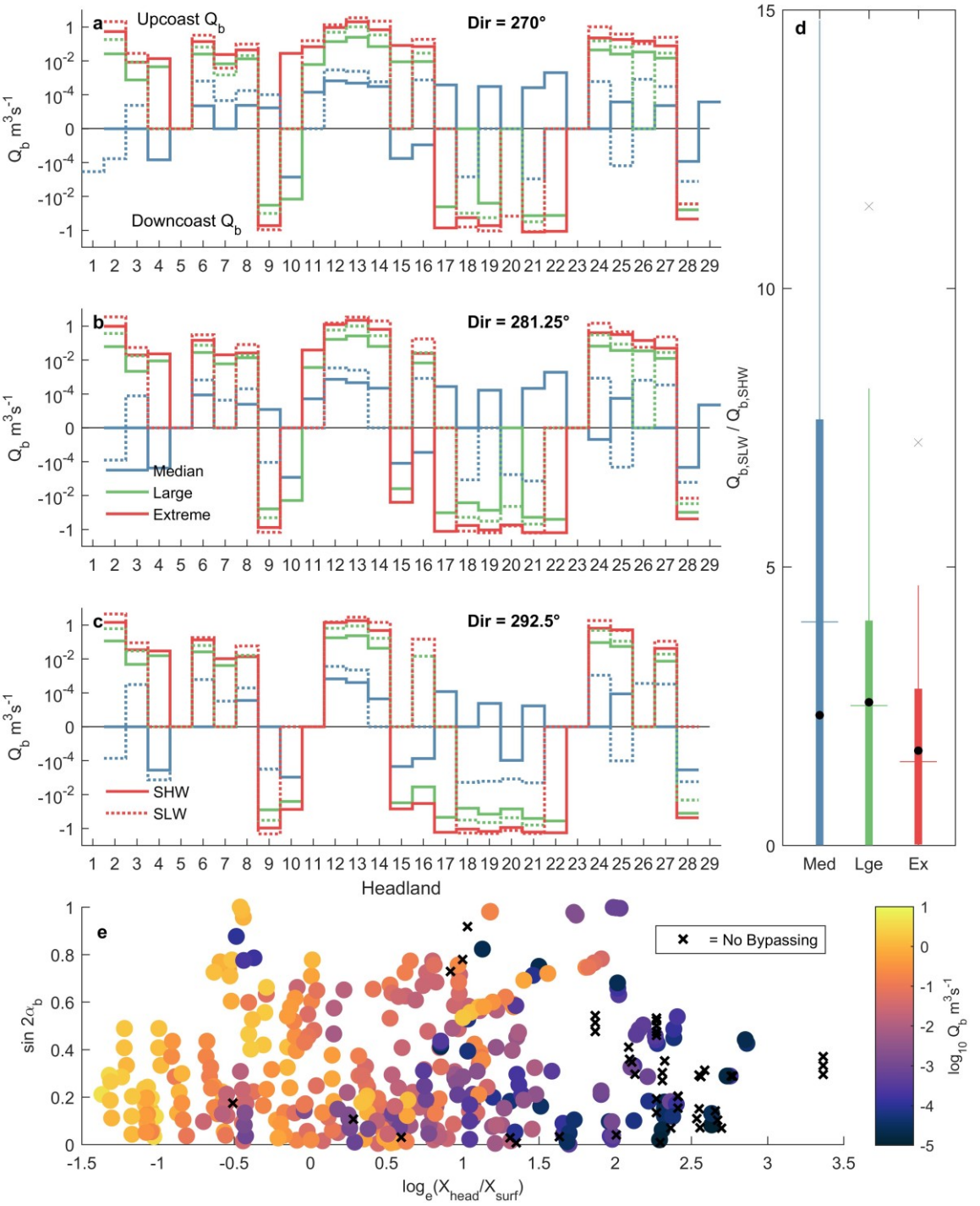

Figure 4.7: The influence of different wave conditions, wave direction and tidal elevation on headland bypassing rates for a uniform sand bed without tidal currents. (a-c) sand bypassing rates per each headland for median (blue), large (green) and extreme (red) wave conditions at spring high (solid) and low (dotted) water, and waves from (a) 270°, (b) 281.25° and (c) 292.5°. Y axes are a $\log_{10}$ scale. Positive (negative) values are indicative of upcoast (downcoast) bypassing. (d) Boxplots summarising the ratio of bypassing rates at spring low vs high water with median (horizontal line), mean (black dot) and whiskers indicating $1.5 \times IQR$. (e) Scatter diagram illustrating effect of wave breaking angle and surf zone width on bypassing rates using $\sin(2\alpha_b)$ and $\log_e(X_{head}/X_{surf})$. Colours show bypassing magnitude on a $\log_{10}$ scale. Crosses denote cases with no bypassing.

4.4.2.2 Parameterisation and the influence of bathymetry

The parameterisation of McCarroll et al., (2021b), based on idealised isolated headlands with uniform bathymetric expression and uniform sediment availability (Equations 4.1 & 4.2), was tested against the bypassing rates shown in Figure 4.7. These bypassing rates represent the most idealised conditions in this study, with uniform sediment availability and no tidal currents. Therefore, the primary differences in these data relative to the idealised conditions of McCarroll et al., (2021b) are the bathymetric expression of the headland below the water line and the proximity of adjacent headlands.

A comparison of the modelled headland bypassing rates versus the parameterisation in Equation 4.1 is shown in Figure 4.8a. This includes bypassing rates from all wave scenarios and water levels. Headland X_{head} was calculated separately for SHW and SLW, therefore this also represents the ability of the parameterisation to handle variability in tidal elevation. The original formulation greatly underestimates bypassing rates for the median wave conditions. A relatively minor alteration of the formulation of Equation 4.1 results in an improved fit to the bypassing rates predicted by the Delft3D model (Figure 4.8b), by changing the power in the exponent from 2 to 0.5 (Equation 4.5), effectively adjusting the slope of the exponential curve. This alteration mainly influences predictions in low-magnitude bypassing conditions where $X_{head} >> X_{surf}$, and its implications are discussed in Section 4.5. For $X_{head} < 0.5\ X_{surf}$ the parameterised bypassing rate was set to Q_0 (McCarroll et al., 2021b).

$$Q_{b\_Adj} = Q_0 \cdot e^{-\left(\frac{X_{head}}{X_{surf}}\right)^{0.5}}, \tag{4.5}$$

There remains spread about the ideal fit 1:1 line with a MAE of a factor 4.3 and RMSE of a factor 6.5. This spread was hypothesised to be due to the influence of the variable bathymetric expression of the headlands and variable embayment morphology. A number of bathymetric and embayment morphological parameters were tested, including the bathymetric slope ratio of George et al. (2015), the beach length, headland separation, the degree of embaymentisation of Fellowes et al. (2019), headland longshore extent and headland toe depth in the form of m_t (Equation 4.4). Ultimately, the only parameter with a clear relationship to the

deviation of the headland bypassing rates from the idealised solution was m_t (Figure 4.8c). An exponential term was fitted of the form:

$$Q_{b\_Toe} = Q_{b\_Adj} \cdot e^{a-\frac{1}{(m_t-b)^2}}, \tag{4.6}$$

Where a and b were calibration parameters. The best fit was found for a = 3.5 and b = 0.7, shown in Figure 4.8d. This improved the MAE of the parameter to a factor 3.5 and RMSE to a factor 5.2.

Bypassing directions were generally predicted correctly as a function of breaking wave direction relative to shore normal. The percentage of scenarios where bypassing was predicted correctly is shown in Figure 4.8e (grey bars) for each headland. Where there was no bypassing under any conditions, no bars are shown. Coloured bars with negative percentages indicate the percentage of scenarios where bypassing direction was wrongly predicted. The colours indicate the wave conditions where bypassing direction was predicted wrongly. For over half of headlands that had at least one bypassing direction wrongly predicted, the direction was wrong for median wave, low bypassing conditions or for only one or two scenarios. Six headlands had bypassing direction wrongly predicted for over 50% of cases. These are discussed in section 4.5.

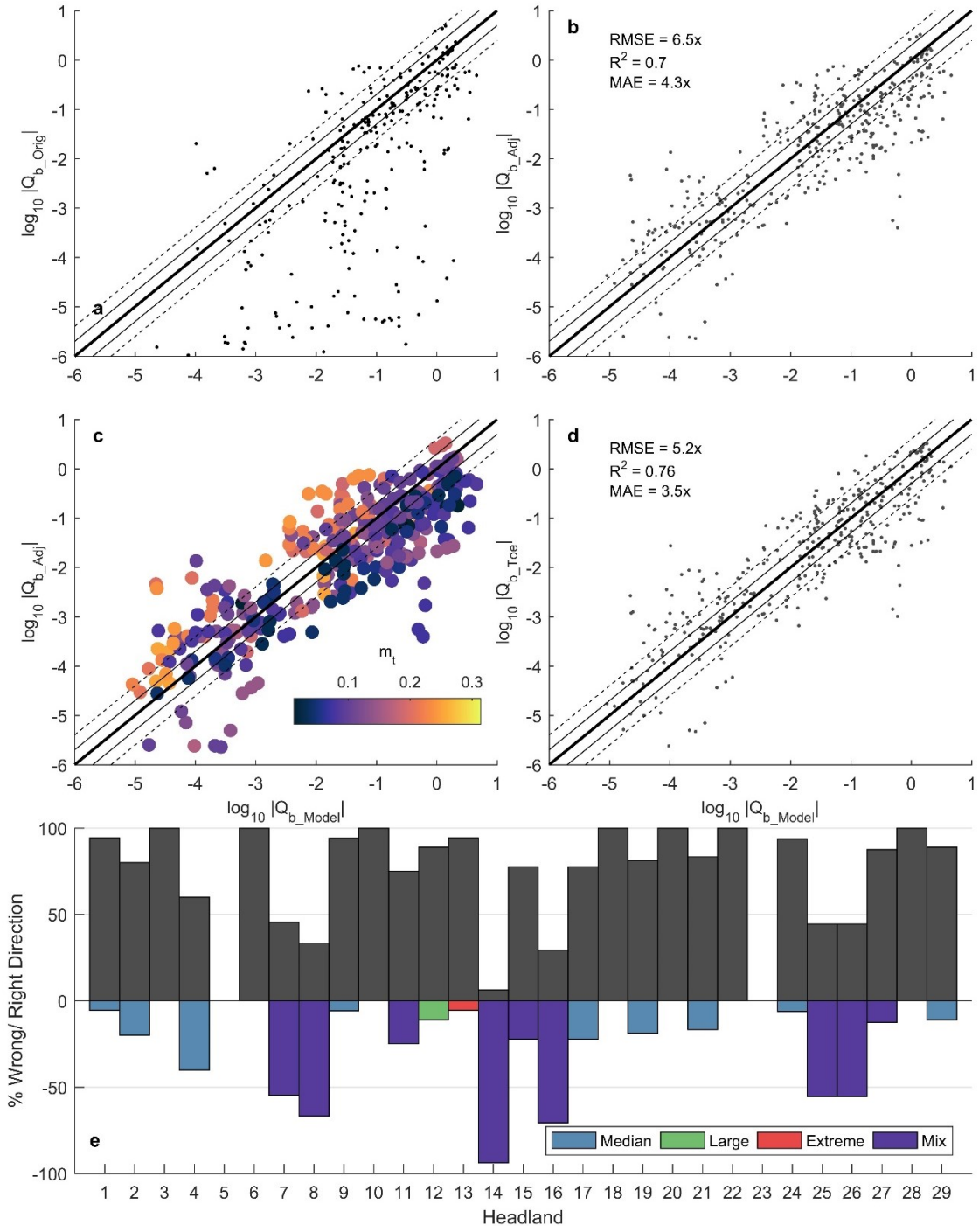

Figure 4.8: Comparison of headland bypassing parameterisations against the predictions of the Delft3D model. (a) The parameterisation of McCarroll et al. (2021b), without adjustment (Q_{b_Orig}), there are 135 outliers (N = 402) where Q_{b_Orig} predicted near zero bypassing. (b) The parameterisation of McCarroll et al. (2021b), adjusted to better fit these data (Q_{b_Adj}). Statistics are shown, calculated using the log-transformed data and converted into factor errors where relevant (e.g. 5.2x represents a factor of 5.2). The 1:1 line for a perfect model is shown in black (thick line), a factor 2 deviation from the perfect model is shown with thin black lines, and a factor 4 with dashed black lines. (c) The parameterisation as in (b) with colours representing the m_t parameter. (d) The parameterisation as in (b) with an additional term to account for variable depth off the headland toe via m_t (Q_{b_Toe}). (e) Percentage of scenarios where sand bypassing direction was correctly predicted (grey bars), or incorrectly predicted (coloured bars). Colours represent the wave conditions where bypassing direction was wrongly predicted. No bars are shown where no bypassing occurred, and percentages were calculated relative to the number of cases where bypassing occurred.

4.4.2.3 The effect of spatially variable sediment coverage

The impact of introducing spatially variable sediments was determined for each headland using the ratio:

$$\frac{\Delta Q_{b\_Sed}}{Q_{b\_Uni}} = \frac{Q_{b\_Sed} - Q_{b\_Uni}}{Q_{b\_Uni}}, \tag{4.7}$$

Where Q_{b_Sed} represents bypassing for the non-uniform sediment coverage scenarios, and Q_{b_Uni} represents bypassing for the uniform sediment scenarios. Results are presented in Figure 4.9a. The main impact of introducing a realistic sediment spatial coverage was that bypassing rates were generally reduced, or bypassing ceased altogether (ratio = -1). There was only one headland (headland 6; Figure 4.9a) where bypassing direction was predicted to change (ratio < -1) between the uniform and spatially variable sediment scenarios. This occurred for median waves and a low bypassing magnitude.

Eight headlands exhibited an activation of net bypassing in the case of non-uniformly distributed sediment for at least one wave condition, and a further five exhibited an increase in net bypassing rate, although this tended to be relatively small, never more than a factor 2 (ratio = 1). In these cases, gross transport along the apex transect was greater for uniform sediments, however net bypassing was low or zero/ divergent. This was due to a relatively large magnitude divergent transport off the headland toe in the uniform sediment scenario which opposed alongshore transport past the headland further offshore, resulting in zero or low net bypassing for uniform sediment coverage. This nearshore transport divergence was of a much lower magnitude when sediment was unavailable for resuspension off the headland toe, and bypassing further offshore in the suspended load dominated (example: headland 11 - Figure 4.9d, e).

Two conditions were determined that were indicative of where a sediment availability parameter should be applied. Firstly, if $X_{head} < 1.5\ X_{surf}$ then bypassing was approximately equal to the uniform sediment availability case and a sediment availability parameter need not be applied. Likewise, if sediment is available off the headland toe (in this case tested at 100 m from the headland toe) then bypassing can be approximated using the uniform sediment parameterisation and the

sediment parameter need not be applied. These conditions account for the headlands with zero or very small relative change in Figure 4.9a.

For cases where these conditions indicate a change in bypassing rate due to sediment availability, a number of parameters were tested for influence on bypassing rates, including: cross-shore extent of sediment adjacent to the headland, sediment coverage ratio R_{sed}, X_{head}, Z_{toe}, headland alongshore length and headland perimeter length. No parameters indicated a clear correlation with changes in bypassing rates predicted by the model. A uniform reduction of an order of magnitude performed best when applied to Q_{b_Toe} (Equation 4.6).

$$Q_{b\_Sed} = 0.1 \times Q_{b\_Toe}$$
$$\text{for: } \frac{X_{head}}{X_{surf}} > 1.5 \text{ \& No sediment at headland toe,} \quad (4.8)$$

When applying the criteria discussed above with this parameter, the MAE for all headlands under the spatially variable sediment scenarios was reduced from a factor of 5.5 to a factor of 4.6 (Figure 4.9b, c). This indicates the parameters applied thus far are able to capture the order of magnitude of wave-forced instantaneous headland bypassing for different headland morphologies, at different tidal elevations, and for spatially variable sediments with an overall R^2 of 0.66. While an order of magnitude reduction under these conditions improves the overall skill of the parameterisation when all headlands are considered together, skill decreased for some individual headlands. This was associated mainly with two headlands (12 & 24). Both of these headlands are highly asymmetric, with a shallower angle intersecting the beach on the side exposed to the dominant wave forcing, presenting less of a barrier to bypassing. The parameterisation consistently underestimated bypassing rates at these headlands during energetic wave events. This is discussed further in Section 4.5.1. This parameterisation does not consider limited sediment depth off the headland toe, which is likely to further limit potential bypassing where only a thin veneer of sediment is available at the toe. This is discussed in Section 4.5.2. It remains to test the influence of tidal currents on bypassing rates, which we address in the following section.

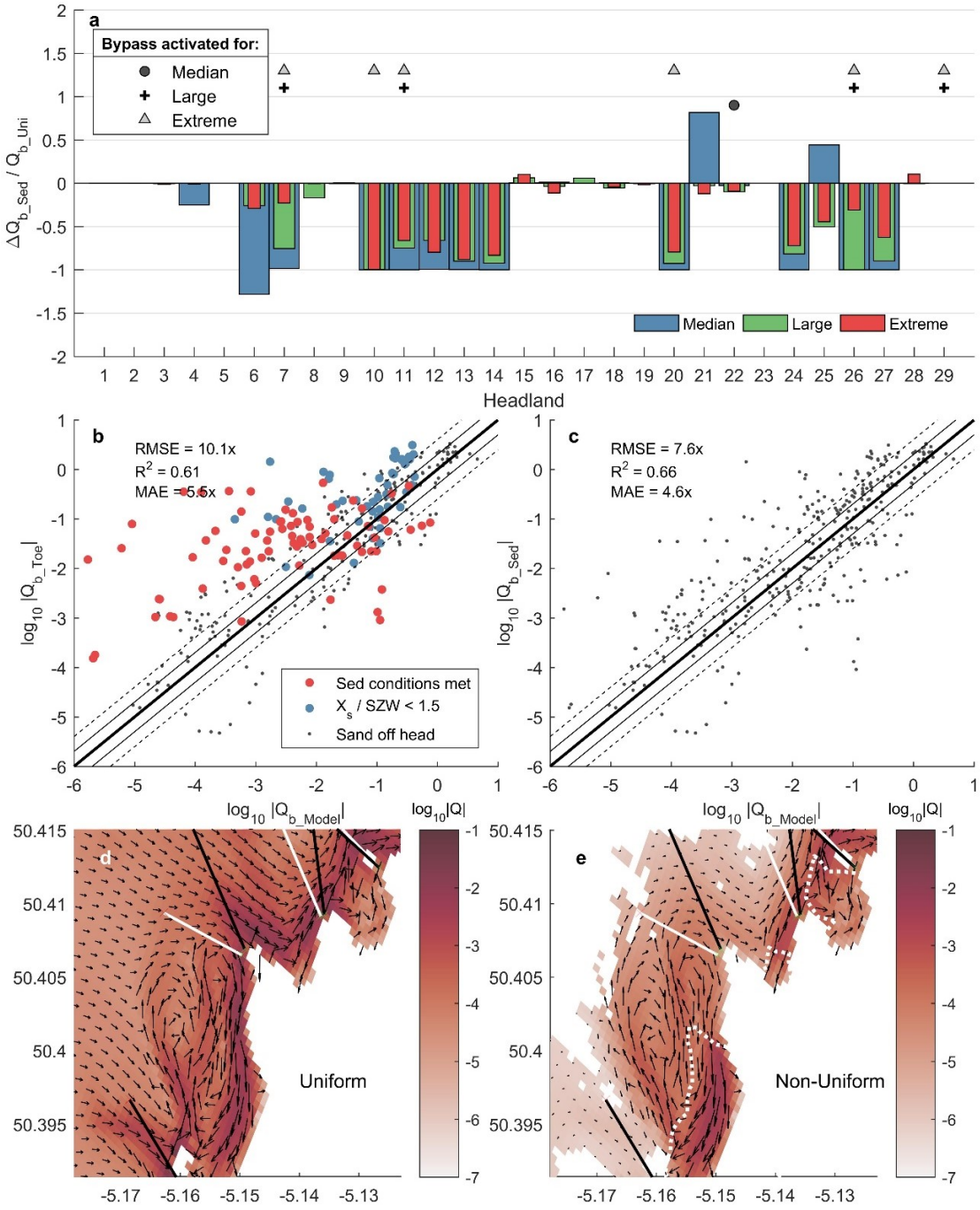

Figure 4.9: The effect of sediment availability of sand bypassing rates, and comparisons of headland bypassing parameterisations against the predictions of the Delft3D model. (a) The difference between bypassing rates for limited versus uniform sediment availability ($\Delta Q_{b\_Sed} = Q_{b\_Sed} - Q_{b\_Uni}$), relative to the magnitude of bypassing for uniform sediments (Q_{b_Uni}), for each headland. Bars are coloured for each wave condition. Bar values were averaged over all wave directions. Symbols indicate wave conditions where net bypassing was activated in Q_{b_Sed} but not in Q_{b_Uni} for at least one wave direction. (b) The parameterisation Q_{b_Toe} versus the Delft3D model. Statistics are shown, calculated using the log-transformed data and converted into factor errors where relevant. Colours indicate data where sediment was absent from the headland toe. Blue data indicate cases where $X_{head} / X_{surf} < 1.5$. (c) The parameterisation of (b) with an added term to account for limited sediment availability. (d, e) Example headland (11 - Kelsey Head) where net bypassing was divergent for uniform sediments but upcoast for non-uniform sediments, with sand transport magnitude and vectors shown. Colours and vectors are log-scaled. The condition shown is extreme waves from 292.5° at SHW. Dashed white lines in (e) indicate the offshore limit of sand coverage.

4.4.2.4 Tidal currents and wave-current interactions

To quantify the influence of tidal currents and wave-current interactions on headland bypassing, scenarios described above were repeated with the inclusion of tidal currents, including all wave conditions, and with uniform/ non-uniform sediment coverage. Tide-only scenarios were also conducted. Here, wave-current interactions refers to the combined influence of radiation stresses, Stoke's drift, enhanced bottom-friction and bed shear stress, enhanced turbulence due to wave dissipation in the bottom wave boundary layer, current-induced wave refraction, current-induced Doppler shift, and wave blocking on headland bypassing rates (Booij et al., 1999; Dingemans et al., 1987; Soulsby et al., 1993; van Rijn, 2007a,b). Tidal currents at the times of SHW and SLW extracted for processing ranged between 0.02 and 1 ms^{-1} in magnitude off the headland apexes, with greater magnitude off larger promontories. Whilst these were not the peak ebb and flood currents, they represent a large range of velocities for the assessment of the impact of tidal currents on instantaneous bypass rates. Bypass rates were averaged over all times of SHW or SLW respectively. Example results are presented in Figure 4.10 (a-d) for the modal wave direction (281.25°) and at SLW (when bypassing rates tended to be larger). The same figure showing bypassing at SHW is provided in Appendix Figure A10.

Tidally-driven bypassing, in the absence of wave forcing, had a maximum magnitude of circa 10^{-3} m^3s^{-1} across SHW and SLW in the case of uniform sediments (Figure 4.10a,b). The greatest bypassing magnitude for uniform sediments was off Trevose Head (headland 23), the largest promontory in the domain. This is driven by resuspension and transport of sediments off the headland apex by the amplified currents. When realistic sand coverage is considered, there is no sediment present off the apex of Trevose head and tide-only bypassing there is negligible for non-uniform sediments (Figure 4.10c,d). Tide-driven bypassing directions sometimes opposed the wave-driven bypassing. In this case, for median waves (Figure 4.10a), bypassing under combined wave-tide forcing tended to follow the tide-driven bypassing direction, indicating that median waves act to enhance sand transport in the tidal direction. For extreme waves (Figure 4.10b), bypassing direction rarely changed between wave-only and wave-tide scenarios (headland 15 at SHW only), and there was generally only a minor enhancement of bypassing magnitudes

relative to wave-only scenarios. In some cases (headlands 20 (SHW) and 26) bypassing was switched off with the addition of tidal forcing.

Tide-driven bypassing was greatly reduced when non-uniform sediment coverages were included (Figure 4.10c-d). Bypassing was switched off across most headlands, and only active for seven headlands in total between SHW and SLW (1, 2, 10, 14, 21, 23 & 27). In these cases, bypassing was generally downcoast (with the exception of 10 and 21 at SLW) and of very low magnitude. The greatest magnitude was for headlands 1 and 2 at SHW, which indicated tidally driven sand transport out of St Ives Bay to the west, in agreement with transport directions reported in King et al., (2019). Regardless of low tide-only bypassing rates, tidal currents were able to induce reversals in the median wave bypassing directions (Figure 4.10c) indicating that wave-current interactions are important during median waves, even when tide-only bypassing may be negligible.

This is indicated in the relative change bar plots for uniform sediments (Figure 4.10e) and non-uniform sediments (Figure 4.10f). Here, relative differences were averaged over the SHW and SLW scenarios and all wave directions. The largest relative differences tended to be for median waves (blue bars). There was also a widespread activation of bypassing under the wave-tide forcing when wave-only bypassing was nil, particularly for median and large waves.

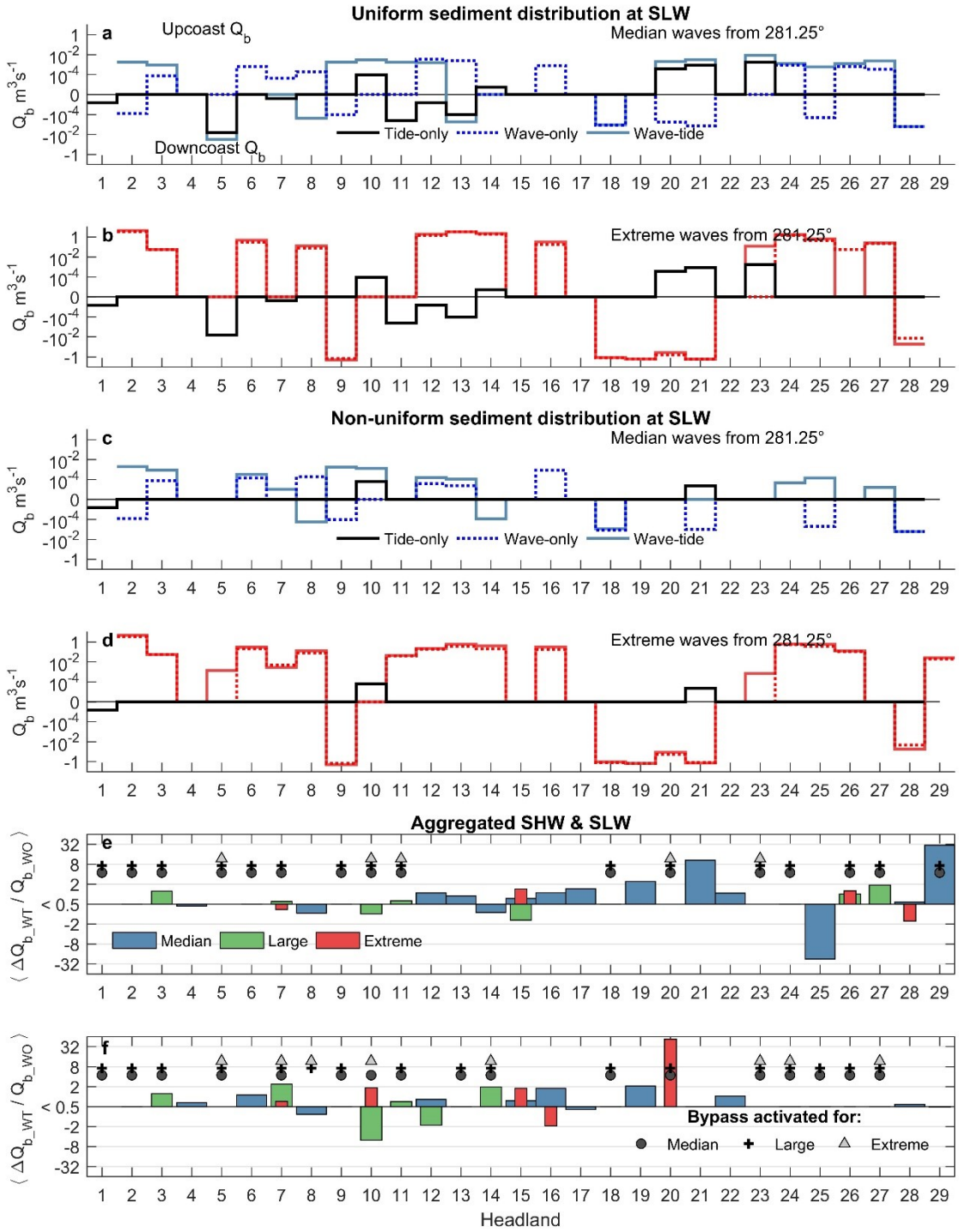

Figure 4.10: Comparison between tide-only, wave-only and wave-tide bypassing rates, for waves from the modal wave direction 281.25°. Instantaneous bypassing rates are presented for median and extreme waves for uniform sediments (a, b respectively) and non-uniform sediments (c, d respectively) for tide-only (black solid line), wave-only (coloured solid line) and wave-tide (coloured dashed line). Positive values represent upcoast bypassing, and downcoast bypassing for negative values. Values are for each headland. (e, f) Relative differences for uniform sediments (e) and non-uniform sediments (f) per headland. Values are an average over all water levels and wave directions. Bars are coloured for each wave condition. Symbols indicate wave conditions where bypassing was activated by wave-tide forcing Q_{b_WT} but not by wave only forcing Q_{b_WO} for at least one condition. The y-scale increases in $\log_2$ increments.

To quantify the relative impact of waves, tides and their non-linear interactions, bypassing rates were used to determine their wave-tide dominance classification as per King et al., (2019). This indicates whether the dominant driver of sand transport is tidal forcing (T), wave forcing (W) or the non-linear interactions between the waves and tides (N) using two ratios:

$$R1 = T : (W + N), \tag{4.9}$$

$$R2 = W : N, \tag{4.10}$$

Where W represents wave-only bypassing rate, T represents tide-only bypassing rate and N represents the contribution of non-linear wave-current interactions to bypassing, calculated as:

$$N = WT - (W + T), \tag{4.11}$$

Where WT is the bypass rate under coupled wave-tide forcing. Bypassing rates in these formulations represent vector quantities (up- or downcoast). Results of the classification over all scenarios are presented in Figure 4.11. Lower-case letters indicate a sub-dominant contribution from the denoted forcing mechanism. There was no appreciable difference between wave directions, therefore all directions were aggregated to calculate the percentage of data in each class for each scenario wave scenario (columns) and waver level (rows). Median waves exhibit non-linear wave-tide interaction dominance of bypassing rates under all scenarios for the majority of headlands. At SLW around 10% of headlands shift from non-linear dominated to wave-dominated under median waves, reflecting greater wave impacts at low water. The relative influence of tides under these waves is greatest at SHW, mainly manifested as a subdominant tidal contribution, denoted by a lower-case “t” (e.g. Nt). This reduces to < 5 % of data at SLW.

Dominant forcing shifts towards wave-dominance as the wave exceedance increases (median → large → extreme). For large and extreme waves, the majority of bypassing is wave-dominated in this macrotidal environment at both SHW and SLW. For these waves and uniform sediments there is a secondary, tide-dominated mode

of sand transport for ~ 18 % of data at SLW (Figure 4.11 e – f). This occurs where wave-only bypassing was weak or negligible, for example at headland 23. This signal is much reduced, or negligible, for non-uniform sediment coverages (Figure 4.11g – l), reflecting the much reduced tidally driven bypassing when sediment is not available off large headland promontories. For extreme waves and non-uniform sediments (Figure 4.11i, l), wave-current interactions have a greatest impact at SLW, shifting the class of bypassing from W to Wn for around 30 % of the data.

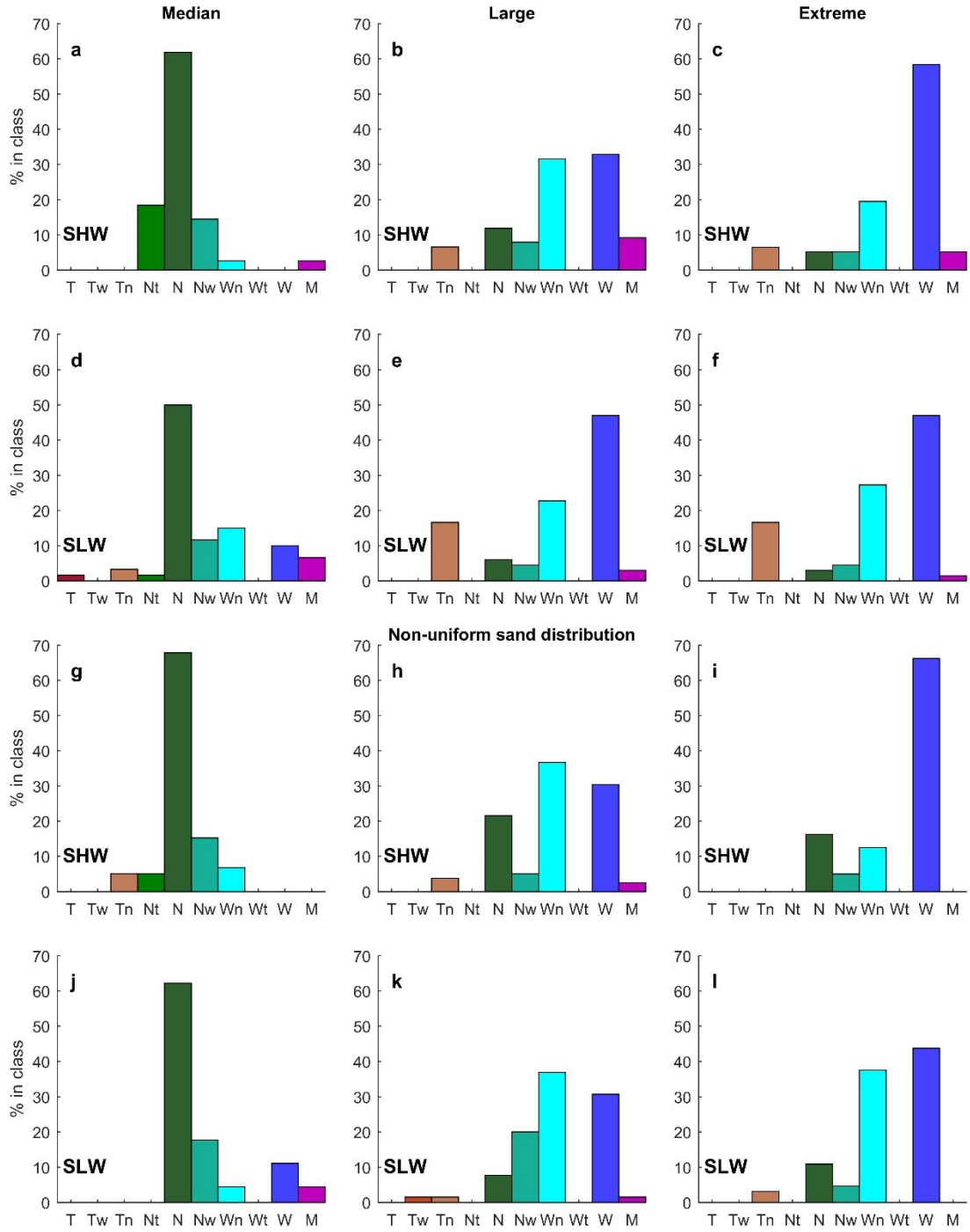

Figure 4.11: Wave-tide dominance classification as per King et al. (2019a). Classifications range from tide-dominate ("T" – red) through dominance of non-linear wave-tide interactions ("N" – green) to wave-dominated ("W" – blue), and mixed ("M" – purple). Lower-case letters denote a subdominant contribution from the denoted process. Data for all three wave directions were aggregated into median (50% exceedance, column 1), large (5% exceedance) and extreme (12h exceedance) wave conditions for simplicity. Classifications are shown for uniform (a – f) and non-uniform (g – l) sediment coverage. Water levels are denoted by SHW and SLW for spring high and low water respectfully.

4.5 Discussion

This paper tested the influence of wave, tide and morphological controls on instantaneous headland sand bypassing using a coupled wave-tide numerical model, and tested the performance of an existing parameterisation when applied to realistic headland morphologies and sediment coverage, making recommendations for additional terms to improve model performance. We discuss connectivity between embayments via headland bypassing along this stretch of coast in the context of previous work in this region and globally (Section 4.5.1). We then discuss the assumptions and limitations of the proposed bypassing parameterisation (Section 4.5.2), before outlining practical considerations for the application of a headland bypassing parameter with recommendations for further research (Section 4.5.3).

4.5.1 Headland bypassing on embayed coastlines

Prior studies on headland bypassing that consider wave and tidal forcing have established that bypassing is generally a wave-dominated process (McCarroll et al., 2018; Vieira da Silva et al., 2018; George et al., 2019; Valiente et al., 2019a; 2020); however, the non-linear effects between waves and tidal forcing can be a major contributor to headland bypassing rates (Costa et al., 2019; Klein et al., 2020; McCarroll et al., 2018; Valiente et al., 2019a). Results presented here suggest that, in macrotidal environments, bypassing during energetic events (deep water $H_s \geq 6$ m) is wave-dominated; however, during median wave events (deep water $H_s = 2$ m) bypassing rates are dominated by non-linear wave-current interactions between waves and tidal velocities, with waves enhancing bypassing in the tidal direction and activation of sand transport when tide-only bypassing is negligible.

Non-uniform sediment availability reduces tide-only bypassing when sand is not available adjacent to the headland apex, where tidal currents are amplified (King et al., 2019). Bypassing in these situations was in the suspended load. Tides have a greatest impact for median waves: tidal elevations modulate bypassing by a factor of 4 between SHW and SLW because of modulation of headland cross-shore length, whilst the impact of currents is generally not more than a factor of 2 for non-uniform sand coverage, matching the minor tidal control reported by Valiente et al. (2020). The primary control on bypassing rates is the cross-shore length of the headland

relative to surf zone width, and low bypassing rates for X_{head} / X_{surf} > 3 matches McCarroll et al. (2021b).

Reduced depth off the headland toe increases headland bypassing rates following the relationship in Equation 4.6. McCarroll et al. (2021b) report an increase in bypassing magnitude of a factor 1.5 for headlands with sub-aqueous ridges of around 1 to 3 m prominence, resulting from increased orbital velocities at the bed off the headland. Equation 4.6 predicts this, as a decrease in depth off the headland toe of circa 2 m for depths between 3 and 10 m results in an increase in bypassing of a factor between 1.3 and 1.8. This acts as an additional term to the parameterisation (Equations 4.5 & 4.6).

The parameterisation of the form of Equations 4.1 and 4.5 had previously been shown to apply for an isolated headland with uniform offshore bathymetry, sediments and wave-only forcing (McCarroll et al., 2021b). The alteration of the exponent between Equations 4.1 and 4.5 reduces the rate of decay of the bypassing parameter as headlands extend beyond the surf zone (X_{head} / X_{surf} > 1). This implies, for realistic headland morphologies and bathymetric expressions, headland bypassing occurs for greater relative headland cross-shore extents than predicted through idealised scenarios with a linear shoreface gradient.

We show that with this minor adaptation, and the addition of terms for variable headland toe depth (Equation 4.6) and sediment availability (Equation 4.8), instantaneous headland bypassing is amenable to parameterisation along stretches of coastline with realistic morphologies and spatial variability in sand coverage. The final parameterisation, when X_{head} > 1.5 X_{surf} and there is no sand at the headland toe, is:

$$Q_{b\_Sed} = 0.1 \times Q_0 \cdot e^{-\left(\frac{X_{head}}{X_{surf}}\right)^{0.5}} \cdot e^{3.5-\frac{1}{(m_t-0.7)^2}}, \quad (4.12)$$

Else if X_{head} ≤ 1.5 X_{surf} or there is sand at the headland toe:

$$Q_{b\_Sed} = Q_0 \cdot e^{-\left(\frac{X_{head}}{X_{surf}}\right)^{0.5}} \cdot e^{3.5-\frac{1}{(m_t-0.7)^2}}, \quad (4.13)$$

Where Q_0 is the uninhibited longshore transport formulation of van Rijn (2014):

$$Q_0 = 0.00018 \cdot K \cdot g^{0.5} \cdot \tan(\beta)^{0.4} \cdot D_{50}^{-0.6} \cdot H_{s,b}^{3.1} \cdot \sin(2\alpha_b), \quad (4.14)$$

This parameterisation is able to reproduce modelled bypassing rates with a MAE of a factor of 4.6, which suggests it is possible to predict the magnitude of instantaneous bypassing rates with some confidence and accuracy. The order of magnitude reduction associated with Q_{b_Sed} improves parametrisation skill overall, however it was associated with a reduced skill for two headlands with a shallow angle of intersection with the beach on the exposed side to the dominant wave forcing. For these headlands, predicted bypass rates were underestimated. Headland orientation can promote unidirectional bypassing, with the angle between the headland and the adjacent shoreline altering the nature of the barrier to longshore transport presented by the headland (Wiggins et al., 2019; McCarroll et al., 2019). The influence of this, combined with limited sediment availability both spatially and in terms of sediment depth, are areas that warrant further focused research.

Bypassing directions were mainly predicted correctly using the breaking wave angle relative to shore normal, but with exceptions. Of all cases, 77 % of directions were predicted correctly. Of the 23% of directions predicted incorrectly, 43 % were for median wave, low bypassing conditions, and the remainder were associated mostly with six headlands. These cases were associated with bypassing offshore in the opposite direction to the prediction and either divergent transport nearshore of the headland apex, or opposing bypassing nearshore in the predicted direction. Offshore transport was driven by strong embayment cellular circulation and deflection rips from the downwave headland driving alongshore flow offshore past the upwave headland (e.g. headland 14), or activation of sand transport off the headland apex where sand was available at the headland toe (e.g. headland 7).

Valiente et al. (2019b) suggested the concept of a 'river of sand' linking embayments along this stretch of coast through headland bypassing, based on observations of inter- and sub-tidal volumetric changes in response to environmental forcing at Perranporth. Bypassing magnitude and directions at Perranporth (headland 9) and the adjacent bays (headlands 7 - 11) match predictions published previously, with northward bypassing during median wave conditions and southward bypassing for energetic wave forcing at Perranporth (McCarroll et al., 2018; Valiente et al., 2020).

This lends confidence to the predictions of this model. Results presented here indicate widespread linkages between the embayments along this coastline, with only two headlands (5 - Godrevy Point & 23 - Trevose Head) predominantly blocking longshore sand transport. This suggests that headland bypassing has the potential to be ubiquitous along exposed embayed coastlines globally.

4.5.2 Assumptions and limitations

The parameterisation terms presented in Equations 4.2, 4.5, 4.6, and 4.8 have been tested against a wide range of headland and bay morphologies, wave forcing conditions and tidal elevations. This parameterisation accurately predicts instantaneous bypassing magnitude in wave-dominated conditions. This study considers instantaneous bypassing rates, without considering morphology change and limited sediment depth. Whilst we do not consider different grain sizes here, grain size is accounted for in Equation 4.2, and its effects on bypassing rates are covered by McCarroll et al. (2021b).

Morphology was kept constant to avoid feedback effects over the course of a simulation, keeping bed morphology constant and not considering limited sediment depth, enabling averaging over time under consistent forcing conditions for analysis. This enabled a constant morphology to be quantified and morphological controls such as headland toe depth to be determined. Thus, the results presented here do not account for cases where strong beach rotation drives accumulation of sediment against the downwave headland which facilitates bypassing (Wiggins et al., 2019), or where limited sediment depth constrains potential bypassing magnitude. Thus, results presented here might be considered an upper limit for a given bed morphology and spatial sediment coverage.

The parameterisation does not account for tidal currents and their interactions with waves, or wind driven currents. Vieira da Silva et al. (2018) found that waves drove sand bypassing at a rate two orders of magnitude greater than wind-driven currents. Our results suggest that bypassing is wave-dominated during energetic events, even in a macrotidal environment; however, wave-current interactions are dominant for median wave conditions. Thus, we recommend caution when applying the parameter for median waves in macrotidal environments as wave-current interactions can be dominant. The parameterisation accounts for varying tidal

elevation through changes to the apparent headland morphology (changes to X_{head} and Z_{toe}). As this parameterisation has been optimised for headlands on this coastline, it remains to test the applicability of this parameter on other coastlines with different wave and tide regimes, and this presents an avenue for further research.

There is a scarcity of observations of headland bypassing rates. Observations during low energy conditions have been made by tracer experiment (Duarte et al., 2014) and sand trapping (Vieira da Silva et al., 2016). In other cases, volumetric changes have been used to infer bypassing (Klein et al., 2010; McCarroll et al., 2019; Valiente et al., 2019b; Wiggins et al., 2019). Thus, bypassing rates presented here could not be validated directly, and validation relied upon validation of current velocities, including near-bed velocities, and comparison of bypassing magnitudes to those reported elsewhere using different models (McCarroll et al., 2018, 2021b; Valiente et al., 2020), whilst using transport formulae and settings used elsewhere under similar conditions (van Rijn, 2007a, b; Luijendijk et al., 2017; McCarroll et al., 2018; King et al., 2019). Thus, absolute bypassing magnitudes presented here should be considered exploratory in nature.

Whilst the parameterisation on which this work builds (McCarroll et al., 2021b; Equation 1) is based on idealised headland morphologies, and is thus not optimised to any single location, the additional parameterisation terms applied in this study for headland toe depth and sediment coverage should be considered optimised for the North Coast of Cornwall, UK. Further work is required to examine the applicability of these terms to other coastlines. Testing of this parameterisation in regions with contrasting tidal and wave conditions (e.g., microtidal, wind-sea dominated; Vieira da Silva et al., 2018), varied headland, embayment and nearshore morphologies (Duarte et al., 2014; George et al., 2015), and different sediment characteristics (e.g., gravel; Wiggins et al., 2019; McCarroll et al., 2019, 2021b) would support the development and generalisation of the parameters developed here.

4.5.3 Implications for coastal modelling

In this section, we summarise the key considerations arising from this research with implications for those modelling long-term shoreline change. Figure 4.12 summarises the key findings relating to instantaneous headland bypassing on embayed coastlines.

The results of this study are of particular interest to those engaged in development and application of long-term hybrid shoreline models, where the parameterisation of headland bypassing enables efficient computation of bypassing magnitude for a large number of conditions. Many of these models do not directly incorporate headland bypassing (e.g., Toimil et al., 2017; Vitousek et al., 2017; Robinet et al., 2018, 2020; Antolinez et al., 2019). The one-line longshore transport model of Roelvink et al. (2020) includes a parameterisation of headland bypassing, however this approach is for a simple groyne without consideration of more complex factors present in realistic headlands such as variable sediment coverage. For an approach that robustly deals with bypassing, it is necessary to include computationally intensive process based components to estimate sediment transport (e.g., MIKE ST-SM by DHI; Drønen et al., 2011; Kristensen et al., 2012). Therefore, development of bypassing parameterisations is of direct benefit to these efforts, and the parametric approach described in this paper could be incorporated into any of the above mentioned hybrid approaches. In applying the parameterisation presented in this paper, the following should be considered:

1. Quantifying morphometric parameters:
    a. For pocket beaches where it is difficult to determine the beach orientation, or beach orientation is highly oblique to the orientation of the adjacent coastlines up and downcoast, it is recommended to take the orientation of the nearest adjacent stretch of open beach or the general orientation of the coastline.
    b. Headland transects and morphology should be determined as described in McCarroll et al. (2021b; their section 5) with the addition of toe depth along the apex transect (50 m from the headland toe) as shown in Figure 4.5/ Figure 4.12d.

c. It should be determined if sediment is present at the headland toe, for example from high-resolution bathymetry using the method described in Section 4.3.2.1 (Figure 4.2).
d. Repeat the process for beaches adjacent on the up- and downcoast headland aspects, giving an upcoast and downcoast morphology (Figure 4.5).

2. Wave forcing:
    a. A method for transformation of waves from offshore to the breakpoint is presented in McCarroll et al., (2021b) using linear wave theory and van Rijn (2014).
3. Unconstrained longshore flux:
    a. An estimate of unconstrained flux alongshore Q_0, can be determined using van Rijn (2014); Equation 4.2/ 4.14.
4. Wave-forced bypassing estimation:
    a. Using Equations 4.12/ 4.13, an estimation of wave forced bypassing can be determined for a given stretch of coast. These should be applied bearing the following points in mind:
    b. For $X_{head} > 5\ X_{surf}$, bypassing can be assumed to be very low or negligible (Figure 4.12a);
    c. Equation 4.13 applies to all other cases, determining the constraint on longshore flux due to the headland (Figure 4.12b);
    d. For $X_{head} < 0.5\ X_{surf}$, the unconstrained longshore flux should be applied (Equation 4.2/ 4.14), and the headland assumed to not block bypassing (Figure 4.12c);
    e. Equation 4.12 applies instead of Equation 4.13 only when sediment is not available off the headland apex, and $X_{head} > 1.5\ X_{surf}$ (Figure 4.12e).

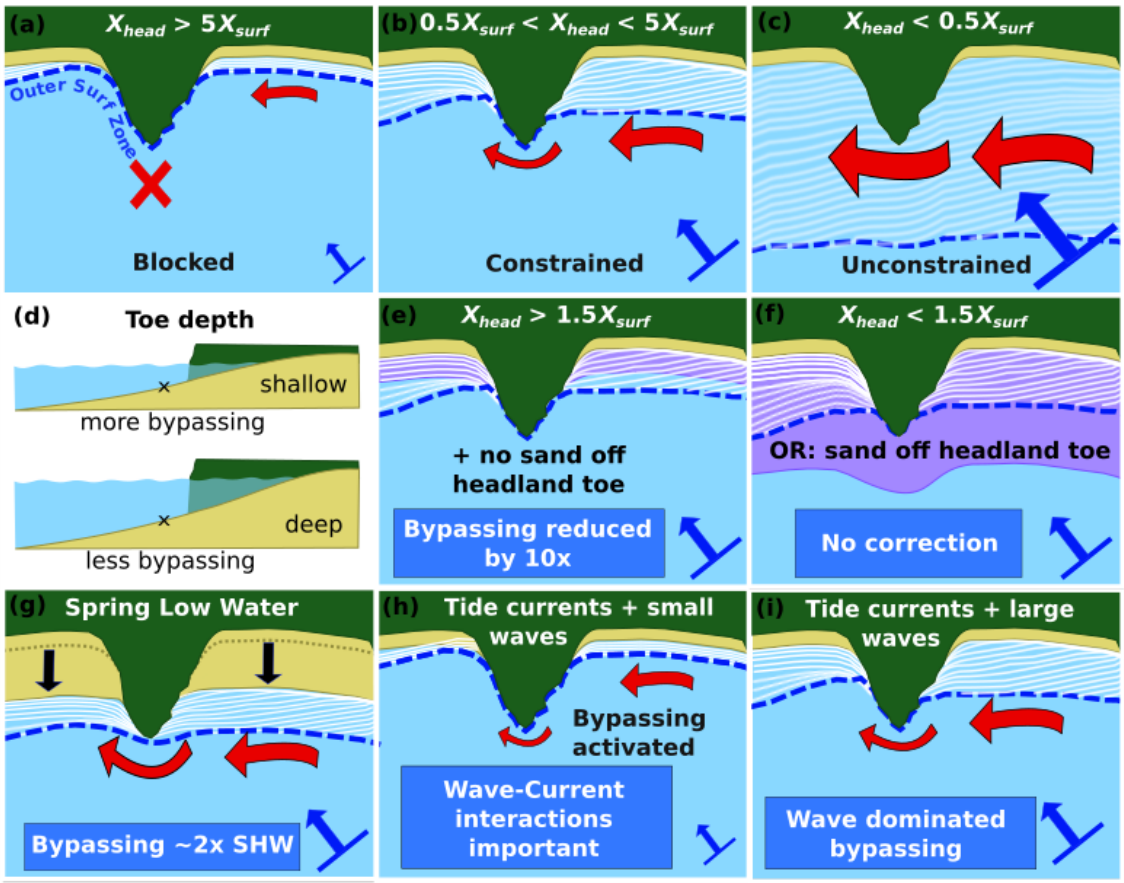

Figure 4.12: Summary schematic cartoon indicating key findings related to instantaneous headland bypassing. Non-erodible headlands and hinterland is shown in Green, sandy beaches are yellow and seawater is blue. Red arrows show simplified sand transport pathways for indicative purposes, scaled to show increasing and decreasing magnitude of net sand transport. Blue arrows indicate wave power and direction. The blue dashed line indicates the outer limit of the surf zone (white lines indicate of wave breaking). Purple polygons indicate subaqueous sand coverage (e, f).

In macrotidal environments and low wave energy, it may be prudent to assess the dominant transport mode to check the applicability of this parameter. The parameter may underestimate transport or predict bypassing in the wrong direction where wave-current interactions are important. This tended to be for low wave energy and spring tides in this macrotidal environment (King et al., 2019; Figure 4.12h). Variable sediment depth is not accounted for in this parameter, as discussed in Section 4.5.2. Understanding the role of spatially variable sediment depth in constraining headland bypassing rates needs to be addressed through further research. In this context, these results and this parameter may represent an upper estimate of potential bypassing rates.

To constrain the applicability of this parameter in cases where bypassing could be dominated by wave-current interactions, a means of determining the dominant sand

transport mode under specific wave and tide conditions without a computationally expensive numerical model could be of benefit. This would be an application and extension of the classification scheme of King et al., (2019). King et al. (2021) highlight potential for the prediction of wave-tide dominance of sand transport based on readily available predictors such as tide range, maximum current speed, significant wave height, peak period, direction and depth (Chapter 3).

4.6 Conclusions

A validated 3D numerical model (Delft3D) was developed for a 75 km stretch of macrotidal, exposed coastline to investigate environmental and morphological controls on headland sand bypassing. Three wave exceedance conditions were tested (50 %, 5 % and 12 hour) from three directions, with both uniform and variable sediments, with and without tidal currents. Headland morphology was generally asymmetric, suggesting a predisposition to bypassing towards the northeast along the North Coast of Cornwall. Key findings relating to headland bypassing are listed below:

- Bypassing is strongly dependent upon headland cross-shore extent relative to surf zone width. When cross-shore length exceeds five surf zone widths, bypassing is effectively negligible.
- Headland toe depth represents an important secondary control on bypassing magnitude, through moderation of wave impacts off the headland toe.
- Sediment spatial variability can reduce bypassing by several orders of magnitude depending on the relative coverage of sand adjacent to the headland, and reduces the effect of tidal currents relative to a uniform sand bed.
- Tidal elevations are a secondary control on bypassing during energetic wave events, and have a greater relative impact during median wave energy conditions. The impact of tidal elevations is largely through modifications of the apparent morphology of the headland and in this macrotidal environment modulates bypassing rates by a factor of 4 on average for median wave energy, and a roughly factor 2 for energetic waves.
- Tidal currents have a minor effect during energetic waves, however they have a greater impact for median wave energy conditions through non-linear

wave tide interactions. Wave-current interactions can dominate bypassing during median wave energy conditions at spring tides.

- An existing parameterisation based on an isolated headland with uniform offshore bathymetry was tested against bypassing with realistic embayment morphologies, and additional terms for headland toe depth and sediment availability were explored.
- Bypassing rates were predicted with mean absolute error of a factor 4.6. Generalised estimations of bypassing in realistic settings are entirely novel, therefore any predictor within an order of magnitude is highly useful. These results indicate wave-dominated bypassing is amenable to parameterisation in embayed settings.

5 Synthesis and conclusions

5.1 Key findings

This thesis aimed to advance our knowledge of the role of waves and tides on sand transport at coastal and shelf scales by: (i) advancing our understanding and quantification of the impact of waves, tides and their interactions on net sand transport; (ii) understanding how net sand transport varies across the continental shelf and how that relates to observed sediment distributions and bed morphology; and (iii) furthering our understanding of the extent, drivers and predictability of headland bypassing on embayed coastlines. These aims are addressed through a combination of numerical modelling, machine learning classification prediction and comparison with observed sediment distributions and bedform morphologies. In this chapter, the key findings of this research are discussed in the context of each of these aims in turn.

5.1.1 Understanding and quantification of Impact of waves, tides and WTI on net sand transport

A Delft3D numerical model of the South West UK was created to investigate the relative influence of tidal and wave forcing on potential sand transport in an energetic, exposed, macrotidal environment. In Chapter 2, the regional model of the South West UK was used to simulate net transport of medium quartz sand under median and extreme wave forcing and spring and neap tides. In Chapter 3, these results are expanded and used to train a kNN classifier to predict the dominant drivers and magnitude of net sand transport across the Northwest European continental shelf.

Waves are shown to heavily influence net sand transport pathways in energetic, macrotidal environments. Changes in sand transport direction are evident between tide-dominated and wave-dominated conditions across the South West UK shelf area, including within megatidal Bristol Channel. A shift in net sand transport direction in the outer Bristol Channel under extreme wave forcing matched closely results for a single point observed previously (Pattiaratchi & Collins, 1988). Shifts in transport direction under wave forcing can act as a source of sediments to large-scale embayments such as Swansea Bay or St Ives Bay where the tidal residual is

directed out of the bay, which may have implications for beach response to extreme storms (Burvingt et al., 2017). This is further demonstrated in Chapter 4, where potential for shifts in headland bypassing direction is demonstrated between wave-dominated conditions under high energy waves versus median wave conditions where median waves enhance transport by the tidal residual and wave tide interactions become important. Wave-tide interactions can also be important under extreme conditions where enhanced sediment transport at low water (e.g., Porter-Smith et al., 2004) can drive a shift between flood and ebb dominant sand transport (Section 2.5.2).

The individual contributions of waves, tides and non-linear wave tide interactions (WTI) are quantified and it is demonstrated in Section 2.4 that WTI can dominate net sand transport in combined energetic wave and tidal conditions, including where wave-only forced sand transport is minimal, which indicates conditions where swell waves act to enhance tidal sand transport (van der Molen, 2002). To assess the relative dominance of waves, tides and WTI on net sand transport, a novel classification scheme is proposed which accounts for the contributions of the tide-only, wave-only and WTI components of net sand transport (King et al., 2019). This classification scheme (Figure 2.11) is reiterated below for reference (Figure 5.1). Results indicate WTI to be a dominant or sub-dominant contributor to net sand transport across large areas of the shelf during extreme waves for all tide conditions, and during median waves at neaps, apart from where the tidal constriction and wave attenuation are greatest. Many previous studies of the dominant drivers of sediment resuspension and transport at the shelf scale do not fully consider the influence of WTI (van der Molen, 2002; Porter-Smith et al., 2004; Neill et al., 2010; Xing et al., 2012; Bricheno et al, 2015), however, these results imply WTI can be a critical component of net sand transport.

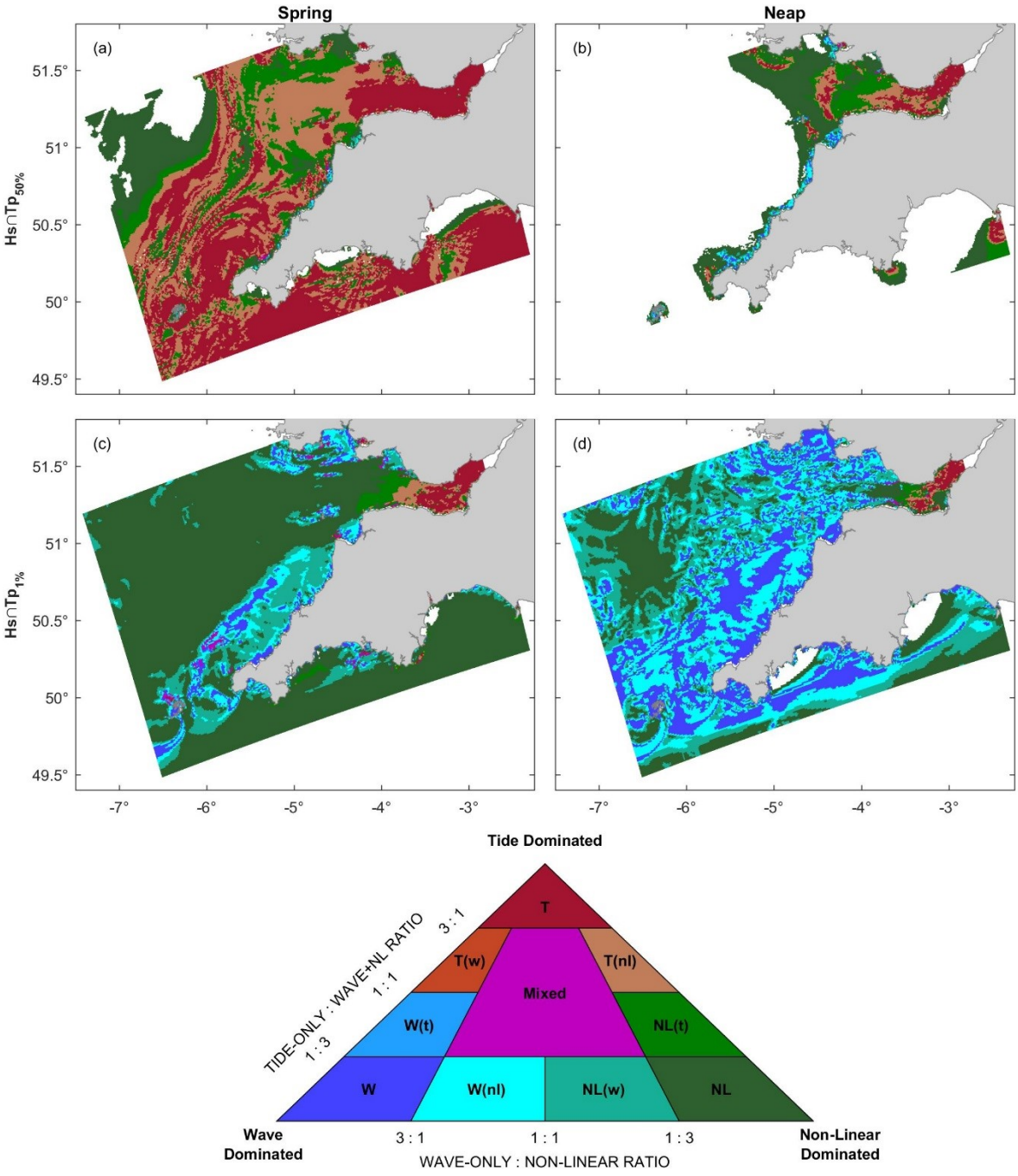

Figure 5.1: Wave-tide dominance classification of the South West UK during different wave and tide forcing, accounting for the relative influence of non-linear wave-tide interactions. Based on potential net sand transport magnitude per tidal cycle. Areas where wave+tide sand transport was < 0.00016m^3/m/cycle have been removed based on the transport formulation validation in van Rijn (2007b). This figure is reproduced from Figure 2.11 in Chapter 2.

A barrier to study of net sand transport including the influence of WTI at scale is the computational cost of numerical modelling at large scales and high resolutions. To address this, computationally efficient, data-driven methods were explored. A k-Nearest Neighbour classification algorithm was trained on uncoupled wave and tide modelling data, bathymetric data and sedimentological data, with modelled wave-tide dominance classifications and net sand transport magnitudes (Chapter 3; see also: Kanevski et al., 2009; Lary et al., 2016; Lee et al., 2019, 2020; Restreppo et al., 2020). This method was able to efficiently and accurately estimate the dominant mode and magnitude of net sand transport across the shelf using readily available data (O'Dea et al., 2012; Graham et al., 2018; Wilson et al., 2018; Tonani & Saulter, 2020) without the need for computationally expensive numerical modelling. This represents a novel application of kNN to shelf scale sediment transport studies with potential for application elsewhere.

Wave and tidal conditions are primary controls on net sand transport mode and magnitude, with grain size acting as a secondary control. The dominant drivers of net sand transport vary across the shelf reflecting differences in water depth, grain size, tide range, and wave exposure between regions (Harris & Coleman, 1988; Bricheno et al., 2015; Wilson et al., 2018). In high energy combined wave and tide conditions, WTI dominate across large areas of the shelf, whereas waves dominate in amphidromic regions with a microtidal regime, matching results of van der Molen (2002) for regions of the North Sea. At neaps, waves are dominant across the Northwest European shelf. Differences in grain-size and water depth are important controls on sand transport magnitude. These effects are discussed further in Section 5.1.2, where influences on sediment distribution and sand wave morphology are also discussed.

5.1.2 Variability of net sand transport and relation to sediments and bed morphology

Potential net sand transport of a uniform homogeneous sand bed shows major divergences and areas of amplified potential tidal sand transport which correspond to regions with the coarsest observed grain sizes in the British Geological Survey product DiGSBS250K. A major bedload parting is predicted in the Bristol Channel, matching conceptual models of sand transport in the Bristol Channel proposed previously (Pingree & Griffiths, 1979; Stride & Belderson, 1991) and corresponding to regions of observed rock and gravel classes (Folk, 1954), erosional zones (McLaren et al., 1993), and gravel barriers (Jennings et al., 1998; Orford & Jennings, 1998), suggesting bedload parting of sand exposes coarser grain sizes (Anthony, 2002). Convergences associated with tidal residual eddies driven by flow past large coastal promontories matches known sand banks (e.g., Skerries Bank; Pingree & Maddock, 1979). Headlands also focus tidal energy and the area immediately offshore of large headland apexes shows enhanced resuspension and residual currents with the greatest potential sand transport rates (Section 2.4). Many of the largest of these headlands, such as Trevose Head or Godrevy Point (Figure 4.1) are consequently stripped of sand off the headland toe (e.g., Figure 4.2).

When considering spatially variable grain sizes, median grain size becomes an important moderating control on net sand transport magnitude, and the dominant forces driving sand transport. In Section 3.3.3 the dominant drivers and magnitude of net sand transport over a statistically representative year is estimated using the kNN approach for the Northwest European Shelf with spatially variable grain sizes from Wilson et al., (2018). This is reiterated below in Figure 5.2 for ease of reference. Wave dominance on Dogger Bank and the German/ Danish shelf area (DE-DK Shelf; Figure 3.1) corresponds to the finer observed grain sizes and shallower depths, while coarser grained areas correspond to regions of greater WTI or tide dominance, indicating the links between grain size and net sand transport at the shelf scale and supporting results for the North Sea by van der Molen (2002) and links between tidal bed shear stress and grain size as modelled by Ward et al. (2015).

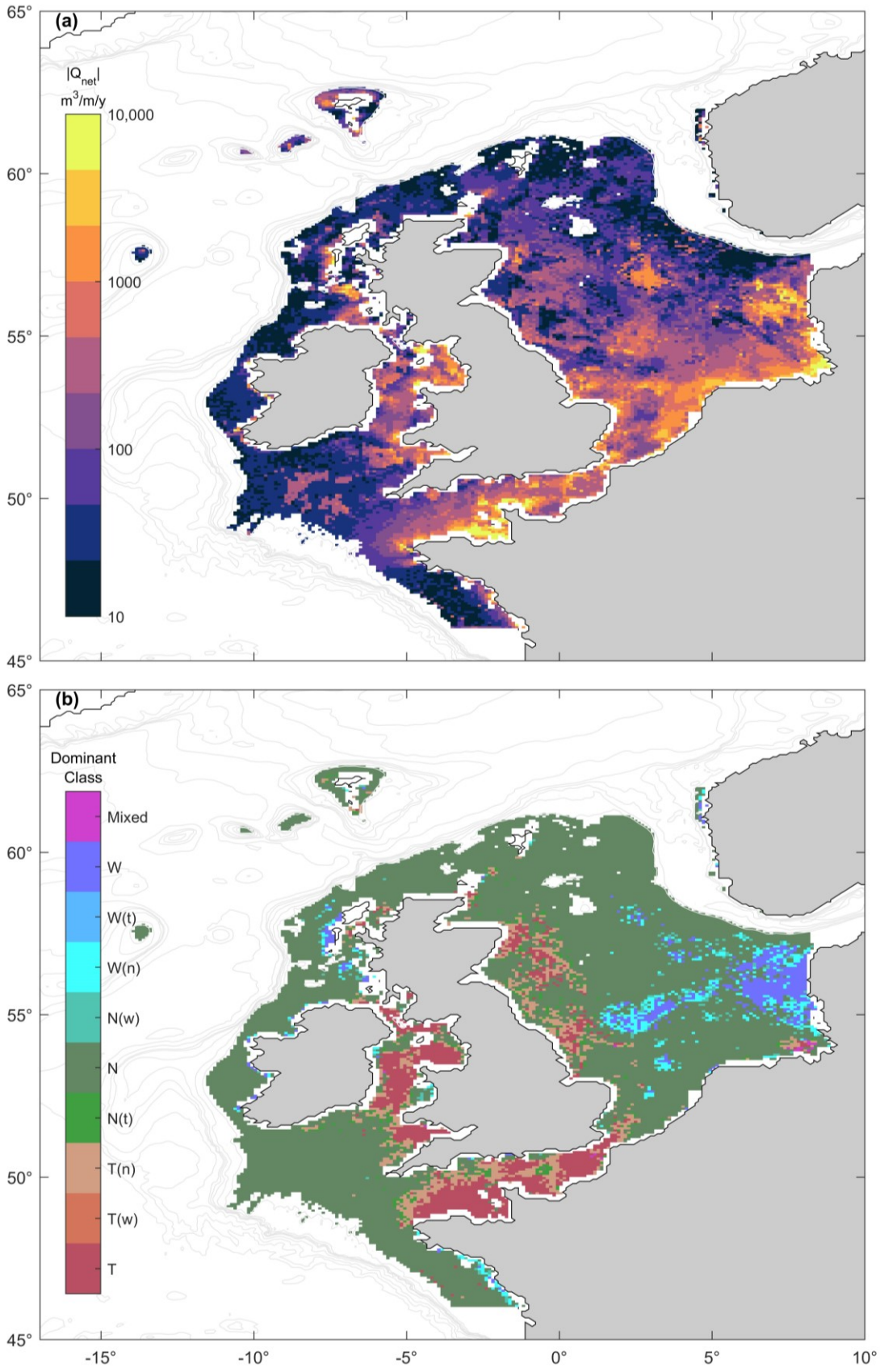

Figure 5.2: Dominant net sand transport classification and order of magnitude integrated over a statistically representative year using forcing conditions taken from the wave exceedance joint-probability distributions and tidal range probability distributions. This is reproduced from Figure 3.8 in Chapter 3.

Comparisons between predicted net sand transport pathways and observed bedform morphologies were made. The orientation of sand wave asymmetry, taken to be indicative of sand wave migration (Knaapen, 2005), matches predicted tidal bedload transport vectors south of Carmarthen Bay (Figure 2.5), lending confidence to the modelling results presented here. Understanding sand wave dynamics is important for offshore renewable energy, marine spatial planning of pipelines, and benthic habitat distribution and disturbance regimes (Van Dijk & Kleinhans, 2005; Van Oyen et al., 2011; van Santen et al., 2011; Harris, 2014; Roetert et al., 2017; Damen et al., 2018; Damveld et al., 2018, 2020; Campmans et al., 2018a, b; Wang et al., 2019; Cheng et al., 2020). We use the trained kNN classifier to predict the dominant transport mode for 1% exceedance waves and spring tides across the Netherlands shelf area using environmental data at 1km resolution from Damen et al., (2017, 2018). Sand wave height is found to significantly decrease, while wavelength and asymmetry significantly increase, for increasing wave dominance (versus WTI) during extreme waves (95% confidence level; Figure 3.9). These results support previous research into environmental controls on sand wave morphology (Campmans et al., 2018a, b; Damen et al., 2018) and indicate that sand wave morphology is significantly moderated by the degree of wave dominance during extreme (1% exceedance) events.

5.1.3 Extent, drivers and predictability of headland bypassing

Headland bypassing rates were simulated for 29 headlands over a 75km stretch of rocky, embayed coastline using a validated 3D hydrodynamic model with coupled waves and sediment transport (Chapter 4). Headland topography was quantified relative to the water line for the up- and downcoast headland aspects, at spring high and spring low water. A method to estimate the spatial extent of sediment coverage was developed using high resolution bathymetry in the nearshore. Bypassing rates were simulated for three wave exceedance conditions (50%, 5% and 12 hour) at each water level, both including and excluding tidal currents, and with uniform and spatially variable sediment coverage. Results indicate bypassing is potentially

ubiquitous on embayed coastlines, with only two headlands blocking bypassing under all forcing conditions. Bypassing behaviour along this coast was compared to previous modelling studies in the same region, matching predictions published for Perranporth and the adjacent embayments (headlands 7 – 11, Figure 4.1; McCarroll et al., 2018, 2021b; Valiente et al., 2020), lending confidence to the model. The predictability of bypassing rates for realistic headland morphologies was tested using the parameterisation of McCarroll et al. (2021b).

It is established that headland bypassing is generally a wave-dominated process (McCarroll et al., 2018; Vieira da Silva et al., 2018; George et al., 2019; Valiente et al., 2020). Costa et al. (2019) find that wave-tide interactions can have a significant influence on bypassing rates, increasing bypassing by an order of magnitude relative to tides alone. This is supported by results presented in Chapter 4, which suggest bypassing in macrotidal environments is wave-dominated during energetic wave events, and dominated by wave-current interaction during median wave events, where waves enhance bypassing in the tidal direction. Tidal elevation change between spring high to spring low water increases bypassing rates by approximately a factor of 4 for median waves and a factor of 2 for energetic wave conditions, indicating greatest bypassing potential at spring low water. Tidal elevation changes alter the apparent subaqueous morphology of the headland, reducing headland cross-shore extent relative to the water line at the beach. McCarroll et al. (2021b) find bypassing is strongly dependent upon headland cross-shore length, X_{head}, relative to surf zone width, X_{surf}, supported by the findings of this study. Bypassing was effectively negligible for $X_{head} > 5\ X_{surf}$. The performance of a parameterisation based on the unconstrained longshore sand transport (van Rijn, 2014), X_{head} and X_{surf} proposed by McCarroll et al. (2021b) was tested against the highly varied headland morphologies along this coastline, and the influence of headland toe depth, Z_{toe}, and sediment spatial coverage were incorporated.

The parameterisation of McCarroll et al. (2021b; Equation 4.1) has been shown to perform well for an isolated headland with idealised bathymetric expression, uniform sediments, and wave-only forcing. When tested without alteration against modelled bypassing rates along this coastline, bypassing rates were predicted well for higher bypassing magnitudes, however the parameterisation largely under estimated lower bypassing magnitudes. For non-idealised headland topography and

bathymetric expression, bypassing occurs for greater ratios of X_{head} : X_{surf} than predicted through idealised scenarios with a linear shoreface gradient. Bypassing predictions were improved though minor adjustment of the decay rate of bypassing with increasing ratios of X_{head} : X_{surf}, and inclusion of a novel term to account for variable Z_{toe} (Equation 4.13). With these contributions, bypassing rates are predictable with MAE of a factor of 3.5 in wave-dominated conditions with uniform sediment coverage. Variable sediment coverage reduces bypassing magnitude by an order of magnitude when sediment is unavailable at the headland toe and $X_{head} > 1.5$ X_{surf}. Correcting for this, bypassing is predictable with MAE of a factor of 4.6 with non-uniform sediment coverage.

Headland bypassing behaviour and conditions for applying these parameters and corrections are summarised in Figure 5.3. This summary diagram focuses on representing inter-embayment headland bypassing magnitude, rather than intra-embayment sand transport pathways. For a detailed schematic of observed and inferred intra-embayment sand transport patterns in a similar environment see Valiente et al. (2020). These results indicate headland sand bypassing is amenable to parameterisation in embayed settings.

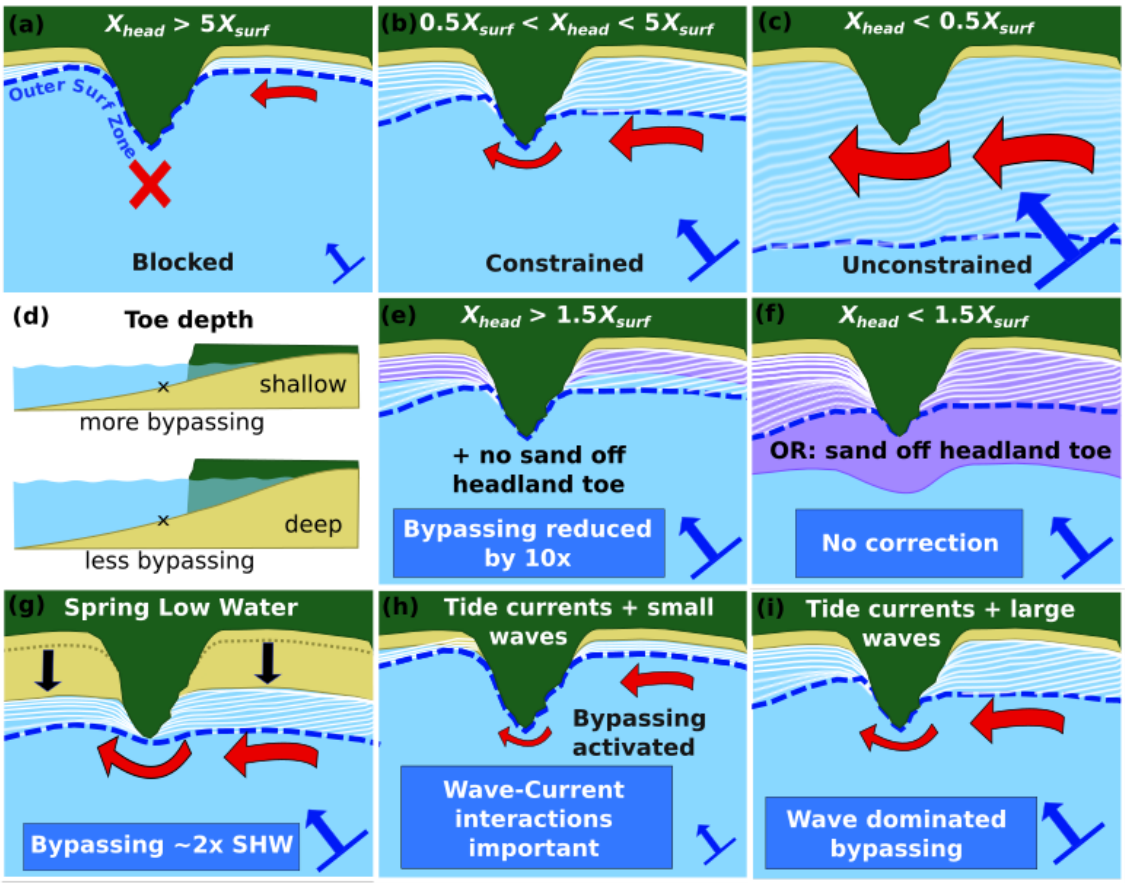

Figure 5.3: Summary schematic cartoon indicating key findings related to instantaneous headland bypassing. Non-erodible headlands and hinterland is shown in Green, sandy beaches are yellow and seawater is blue. Red arrows show simplified sand transport pathways for indicative purposes, scaled to show increasing and decreasing magnitude of net sand transport. Blue arrows indicate wave power and direction. The blue dashed line indicates the outer limit of the surf zone (white lines indicate of wave breaking). Purple polygons indicate subaqueous sand coverage (e, f). This figure is reproduced from Figure 4.12 in Chapter 4.

5.2 Limitations and areas for future research

Detailed discussion of the limitations of this research is made in sections 3.4.2 and 4.5.2. This section briefly summarises those limitations discussed and highlights future avenues for research that arise. Due to scarce observations of sand transport and headland bypassing under energetic conditions, validation of modelling conducted here relies upon validation against observed currents, bedform morphology, sediment distributions, and sand transport rates and directions from the literature (Folk, 1954; Pingree & Maddock, 1979; Pingree & Griffiths, 1979; Pattiaratchi & Collins, 1988; Stride & Belderson, 1991; McLaren et al., 1993; Jennings et al., 1998; Orford & Jennings, 1998; Anthony, 2002; Lopez et al., 2016; McCarroll et al., 2018, 2021b; Damen et al., 2018; Valiente et al., 2020). Delft3D has successfully been used to model the processes considered in this study at the shelf and coastal scale, and parameters for the TRANSPOR2004 formulation were obtained from studies in similar environments (Grunnet et al., 2004; van Rijn 2007a, b; Hansen et al., 2013; Hopkins et al., 2015; Ridderinkhof et al., 2016; Luijendijk et al., 2017; McCarroll et al., 2018; Valiente et al., 2020). As the methods developed here are applied to other regions, this will further constrain their limitations and shed light on the performance of the kNN predictions and headland bypassing parameterisation in other environments.

This study considers transport of sand from a homogeneous bed, however mixed sediments affect resuspension and transport of sediments (McCarron et al., 2019; Thompson et al., 2019). As much of the shelf area considered in this study is comprised of > 90% sand (Wilson et al., 2018), this is likely to have limited impact on the results of this study (McCarron et al., 2019). While inclusion of the effect of mixed sediment fractions would introduce a potentially restrictive data requirement for application of the kNN predictor and headland bypassing parameterisation, as further data becomes available and inclusion of the effects of mixed sediment fractions improves in numerical models, these effects could be incorporated. Whilst we do not consider different grain sizes in Chapter 4, grain size is included in Equation 4.2, and its effect on bypassing is covered by McCarroll et al. (2021b). Other sedimentological variables such as limited sediment depth, and morphological change are not considered in this study, and results presented here

represent an upper limit on potential sand transport rates. The impact of these variables present a future avenue for research.

The numerical modelling on which the results of Chapter 2 and 3 are based was conducted in a depth averaged mode. When considering wave-tide interactions in these sections, we consider radiation stresses, stokes drift, enhanced bottom friction, enhanced bed shear stress, current and depth-induced wave refraction, Doppler shift and wave-blocking (Section 2.3.2; Dingemans et al., 1987; Soulsby et al., 1993; Booij et al., 1999; Lesser et al., 2004; van Rijn, 2007a, b). Three dimensional effects in these sections are parameterised or depth integrated, including turbulence generation by wave breaking and enhanced bottom friction, and wave induced mass flux. The impact of these is shown to increase potential tide-only and wave-only sand transport, however WTI remain dominant or sub-dominant across most areas and the conclusions are unchanged.

Other potential forcing mechanisms for net sand transport such as wind and baroclinic density gradients are not considered in this study. Regions of greatest potential net sand transport corresponded to regions of permanently mixed or intermittently stratified hydrodynamics, and stratification remains weak in many parts of the shelf throughout the year and is not expected to significantly influence the results of this study (Holt et al., 2010; van Leeuwen et al., 2015). Wind driven currents are weak on the Celtic shelf while, in other regions on the NW European Shelf, wind driven currents are mainly significant at neaps or where tidal currents are small (Pingree & Griffiths, 1980; Pingree & Le Cann, 1989; van der Molen, 2002). The relative importance of winds or stratification could be incorporated to a similar classification as used here, and presents a potential future avenue for development and application of these methods.

The results, conclusions and limitations of the research presented in this thesis present opportunities for future works expanding on the approaches applied here. There remains a need to further test the sensitivity of the classification scheme and kNN classifications presented in Chapters 2 and 3 to different sediment transport formulations, numerical modelling systems and different shelf areas. This is also true of the headland bypassing parameterisations presented in Chapter 4, which are optimised for the North Coast of Cornwall, UK, and based on results from the same sediment transport formulation (van Rijn, 2007a, b). It would be beneficial to test

the sensitivity of the kNN classification and headland bypassing parameterisations to different sediment transport formulations, such as Bijker (1971), which was shown to perform well against sediment trapping measurements in a study of headland bypassing on the central coast of Santa Catarina state in Brazil (Vieira da Silva et al., 2016). Likewise, it would be of benefit to test sensitivity to different modelling systems beyond Delft3D and examine kNN classifier performance on different continental shelf areas with similar and contrasting hydrodynamic and wave regimes to identify limitations of these approaches and expand them. This would enable a more generally applicable classifier to be trained, and an assessment of the dominant driving forces of sediment transport on continental shelves to be made on a potentially global scale.

The headland bypassing parameterisation developed in Chapter 4 can be further expanded by testing performance on different coastlines to further generalise the expressions. Further work can be done to generalise the kNN approach and additional headland bypassing parameterisation terms presented here to a wider set of grain size conditions including silt and gravel. McCarroll et al., (2021b) find that an XBeach optimised version of the headland bypassing parameterisation is an effective predictor of bypassing volume when headland toe depth is incorporated. Future work could compare the additional bypassing terms developed here for sediment spatial coverage and toe depth with the performance of the parameterisation presented in McCarroll et al. (2021b) along the same gravel barrier system. Further development of the parameterisation could also include the effects of variable sediment depth and mixed sediments, which would benefit from sensitivity testing using idealised headland morphologies. The influence of tides on headland bypassing is quantified in Chapter 4, however further concentrated scenario testing is required, using a wide range of idealised headland morphologies, to model and isolate the effects of tides in a way that can be used to further develop the parameterisation of headland bypassing. With further development as described above, a generalised expression for headland bypassing on embayed coasts could be achieved.

5.3 Thesis Conclusions

This thesis applies a combination of numerical modelling, statistical methods such as machine learning classification prediction and copula joint probability modelling, and development of novel parameterisations to the problems of continental shelf sediment transport and headland sand bypassing on embayed coasts. New insights are contributed to our understanding of the dominant drivers of net sand transport at the shelf scale, its relation to shelf sediment distributions and bedform morphology, and the environmental and topographical controls on headland sand bypassing.

A novel classification scheme for the dominance of waves, tides and non-linear wave-tide interactions (WTI) on sand transport across the shelf is developed and applied to a macrotidal shelf region, showing consideration of WTI is essential in studies of sand transport in mixed energy environments (Chapter 2). The relative influence of waves, tides and WTI is shown to vary across the shelf, dependent upon variability in wave exposure, tidal regime, grain size and local bathymetry, with significant links to observed sand wave morphologies (Chapter 3). Headland bypassing is shown to be predictable under wave-dominated conditions, and dependent upon headland cross-shore length normalised by surf zone width, headland toe depth and spatial sediment coverage (Chapter 4). Key conclusions of this thesis are listed below.

Key conclusions:

- Sand transport in energetic, macrotidal environments can be heavily influenced by waves. Median (50% exceedance) waves enhance tidal sand transport vectors, whereas extreme (1% exceedance) waves can dominate sand transport, increasing potential sand transport by over an order of magnitude, mobilising medium sand below 100m depth, and potentially inducing full-reversals in the net transport direction.
- A new continental shelf classification is presented based on wave-, tide- and WTI dominance of net sand transport with potential for application elsewhere.

- The dominant forcing mode (classification) and magnitude of net sand transport is predictable from readily available data using a k-Nearest Neighbour algorithm.
- WTI (encompassing radiation stresses, stokes drift, enhanced bottom friction, enhanced bed shear stress, current and depth-induced wave refraction, Doppler shift and wave-blocking) non-linearly enhance net sand transport and are a dominant or sub-dominant contributor to net sand transport across large areas of the Northwest European shelf in extreme conditions.
- Over a statistically representative year, meso-macrotidal areas around the UK are tide-dominated, while shallow, finer grained, microtidal regions such as Dogger Bank and the German/ Denmark Shelf are wave-dominated. WTI dominate on the Netherlands shelf and in deeper areas of the North Sea and Celtic Sea.
- Sand wave morphology is significantly different between predicted classes at the 95% confidence level. Sand waves significantly increase in length and asymmetry, and decrease in height, for increasing wave-dominance under extreme conditions. This suggests increased wave-dominance under storm conditions play a significant role in controlling sand wave morphology.
- Headland bypassing is potentially widespread on energetic embayed coasts. Only two headlands on the North Coast of Cornwall presented a complete barrier to headland bypassing under all modelled conditions.
- Headland bypassing is generally a wave-dominated process. Tides are a secondary control on bypassing rate under energetic (> 5% exceedance) waves. Wave-current interactions can dominate bypassing for median waves at spring tide. Tidal elevations are a secondary control, having greatest impact during median waves, modulating bypassing rates by a factor of 4.
- Limitations in available sand due to variable sand spatial coverage can reduce headland bypassing by several orders of magnitude, and reduce the effect of tidal currents, when sand is unavailable off the headland toe.

- Headland cross-shore extent relative to surf zone width is a primary control, while toe depth represents an important secondary control by moderating wave impact at the headland toe.
- An existing parametrisation was further developed, and bypassing rates were predictable for realistic headland morphologies and sediment coverage, with MAE of a factor of 4.6. Key parameters are: unconstrained longshore sand flux, headland cross-shore length, surf zone width, toe depth, and sediment availability at the headland toe.

References

Ab Razak, M. S., Dastgheib, A. & Roelvink, D. (2013). Sand bypassing and shoreline evolution near coastal structure, comparing analytical solution and XBeach numerical modelling. *Journal of Coastal Research*, 65, 2083 – 2088. https://doi.org/10.2112/SI65-352.1

Acworth, C. & Lawson, S. (2012). The Tweed River entrance sand bypassing project, ten years of managing operations in a highly variable coastal system. Proceeding of the 20th NSW Coastal Conference 2012 Tweed Head, 1 – 23.

Akan, C., McWilliams, J. C. & Uchiyama, Y. (2020). Topographic and coastline influences on surf Eddies. *Ocean Modelling*, 147, 101565. https://doi.org/10.1016/j.ocemod.2019.101565

Aldridge, J. N., Parker, E. R., Bricheno, L. M., Green, S. L. & van der Molen, J. (2015). Assessment of the physical disturbance of the northern European Continental shelf seabed by waves and currents. Continental Shelf Research, 108, 121-140. https://doi.org/10.1016/j.csr.2015.03.004

Anthony, E. J. (2002). Long-term marine bedload segregation, and sandy versus gravelly Holocene shorelines in the eastern English Channel. *Marine Geology*, 187, 221-234. https://doi.org/10.1016/S0025-3227(02)00381-X

Antolínez, J. A., Méndez, F. J., Anderson, D., Ruggiero, P., & Kaminsky, G. M. (2019). Predicting Climate-Driven Coastlines With a Simple and Efficient Multiscale Model. *Journal of Geophysical Research: Earth Surface*, 124(6), 1596 – 1624. https://doi.org/10.1029/2018JF004790

Bentamy, A. & Fillon, D. C. (2012). Gridded surface wind fields from Metop/ASCAT measurements. *International Journal of Remote Sensing*, 33(6), 1729-1754. https://doi.org/10.1080/01431161.2011.600348

Besio, G., Blondeaux, P., Brocchini, M., Hulscher, S. J. M. H., Idier, D., Knaapen, M. A. F., Németh, A. A., Roos, P. C. & Vittori, G. (2008). The morphodynamics of tidal sand waves: A model overview. *Coastal Engineering*, 55(7-8), 657-670. https://doi.org/10.1016/j.coastaleng.2007.11.004

Booij, N., Holthuijsen, L. H. & Ris, R. C. (1999). A third-generation wave model for coastal regions 1. Model description and validation. *Journal of Geophysical Research: Oceans*, 104(C4), 7649-7666. https://doi.org/10.1029/98JC02622

Borsje, B. W., Kranenburg, W. M., Roos, P. C., Matthieu, J. & Hulscher, S. J. M. H. (2014). The role of suspended load transport in the occurrence of tidal sand waves, Journal of Geophysical Research: Earth Surface, 119, 701–716. https://doi.org/10.1002/2013JF002828

Bricheno, L. M., Wolf, J. & Aldridge, J. (2015). Distribution of natural disturbance due to wave and tidal bed currents around the UK. *Continental Shelf Research*, 109, 67-77. https://doi.org/10.1016/j.csr.2015.09.013

Brown, J. M., Bolaños, R., Howarth, M. J., Souza, A. J. (2012). Extracting sea level residual in tidally dominated estuarine environments. *Ocean Dynamics*, 62(7), 969-982. https://doi.org/10.1007/s10236-012-0543-7

Burrough, P. A. (1981). Fractal dimensions of landscapes and other environmental data. *Nature*, **294**, 240 – 241. https://doi.org/10.1038/294240a0

Burvingt, O., Masselink, G., Russell, P. & Scott, T. (2017). Classification of beach response to extreme storms. *Geomorphology*, 295, 722-737. https://doi.org/10.1016/j.geomorph.2017.07.022

Campmans, G. H. P., Roos, P. C., de Vriend, H. J. & Hulscher, S. J. M. H. (2018a). The influence of storms on sandwave evolution: A nonlinear idealized modeling approach. *Journal of Geophysical Research: Earth Surface*, 123, 2070-2086. https://doi.org/10.1029/2018JF004616

Campmans, G. H. P., Roos, P. C., Schrijen, E. P. W. J. & Hulscher, S. J. M. H. (2018b). Modeling wave and wind climate effects on tidal sandwave dynamics: A North Sea case study. *Estuarine, Coastal and Shelf Science*, 213, 137-147. https://doi.org/10.1016/j.ecss.2018.08.015

Carruthers, J. N. (1963). History, sandwaves and near-bed currents of La Chapelle Bank. *Nature*, 197, 942-946. https://doi.org/10.1038/197942a0

Carter L. & Heath R. A. (1975). Role of mean circulation, tides, and waves in the transport of bottom sediment on the New Zealand continental shelf. *New Zealand Journal of Marine and Freshwater Research*, 9:4, 423-448. https://doi.org/10.1080/00288330.1975.9515579

Carter, R. W. G., Jennings, S. C., & Orford, J. D. (1990). Headland erosion by waves. *Journal of Coastal Research*, 6(3), 517-529. http://www.jstor.org/stable/4297714

Castelle, B. & Coco, G. (2012). The morphodynamics of rip channels on embayed beaches. *Continental Shelf Research*, 43, 10 – 23. https://doi.org/10.1016/j.csr.2012.04.010

Castelle, B. & Coco, G. (2013). Surf zone flushing on embayed beaches. *Geophysical Research Letters*, 40, 2206 – 2210. https://doi.org/10.1002/grl.50485

Castelle, B., Dodet, G., Masselink, G. & Scott, T. (2017). A new climate index controlling winter wave activity along the Atlantic coast of Europe: The West Europe Pressure Anomaly. *Geophysical Research Letters*, 44, 1384-1392. https://doi.org/10.1002/2016GL072379

Castelle, B., Dodet, G., Masselink, G. & Scott, T. (2018). Increased winter-mean wave height, variability and periodicity in the North-East Atlantic over 1949-2017. *Geophysical Research Letters*, 45, 3586-3596. https://doi.org/10.1002/2017GL076884

Castelle, B., Scott, T., Brander, R. W. & McCarroll, R. J. (2016). Rip current types, circulation and hazard. *Earth-Science Reviews*, 163, 1 – 21. https://doi.org/10.1016/j.earscirev.2016.09.008

Channon, R. D., & Hamilton, D. (1976). Wave and tidal current sorting of shelf sediments southwest of England. *Sedimentology*, 23, 17-42. https://doi.org/10.1111/j.1365-3091.1976.tb00037.x

Cheng, C. H., Soetaert, K., & Borsje, B. W. (2020). Sediment Characteristics over Asymmetrical Tidal Sand Waves in the Dutch North Sea. *Journal of Marine Science and Engineering*, 8(6), 409. https://doi.org/10.3390/jmse8060409

Cieślikiewicz, W., Dudkowska, A., Gic-Grusza, G., & Jędrasik, J. (2018). Assessment of the potential for dredged material dispersal from dumping sites in the Gulf of Gdańsk. *Journal of Soils and Sediments*, 18, 3437–3447. https://doi.org/10.1007/s11368-018-2066-4

Codiga, D. L. (2011). Unified Tidal Analysis and Prediction Using the UTide Matlab Functions. URI/GSO Technical Report 2011-01, pp. 1-59. Graduate School of Oceanography, University of Rhode Island, Narragansett, RI. https://doi.org/10.13140/RG.2.1.3761.2008

Collins, M. B. (1987). Sediment transport in the Bristol Channel: A review. Proceedings of the Geologists' Association, 98(4), 367 – 383. https://doi.org/10.1016/S0016-7878(87)80076-7

Collins, M. B., Ferentinos, G. & Banner, F. T. (1979). The hydrodynamics and sedimentology of a high (tidal and wave) energy embayment (Swansea Bay, northern Bristol Channel). *Estuarine and Coastal Marine Science*, 8, 49-74. https://doi.org/10.1016/0302-3524(79)90105-1

Constanza, R., d'Arge, R., de Groot, R., Farber, S., Grasso, M., Hannon, B., Limburg, K., Naeem, S., O'Neill, R., Paruelo, J., Raskin, R. G. & Sutton, P. (1997). The value of the world's ecosystem services and natural capital. *Nature*, 387, 253 – 260. https://doi.org/10.1038/387253a0

Costa, W. L. L., Silveira, L. F. & Klein, A. H. F. (2019). Influence Of Wave Climate And Tidal Regime On Headland Bypassing - Study Case: Northern São Francisco Do Sul Island, Sc, Brazil. *Coastal Sediments 2019*, 488-501. https://doi.org/10.1142/9789811204487_0044

Damen, J. M., van Dijk, T. A. G. P., & Hulscher, S. J. M. H. (2017). Replication data for: Spatially varying environmental properties controlling observed sand wave morphology. *4TU*. https://doi.org/10.4121/uuid:0d7e016d-2182-46ea-bc19-cdfda5c20308

Damen, J. M., van Dijk, T. A. G. P., & Hulscher, S. J. M. H. (2018). Spatially Varying Environmental Properties Controlling Observed Sand Wave Morphology. Journal of Geophysical Research: Earth Surface, 123(2), 262–280. https://doi.org/10.1002/2017JF004322

Damveld, J. H., Borsje, B. W., Roos, P. & Hulscher, S. (2020). Biogeomorphology in the marine landscape: modelling the feedbacks between patches of the polychaete worm Lanice conchilega and tidal sand waves. *Earth Surface Processes and Landforms*, 45(11), 2572-2587. https://doi.org/10.1002/esp.4914

Damveld, J. H., van der Reijden, K. J., Cheng, C., Koop, L., Haaksma, L. R., Walsh, C. A. J., et al. (2018). Video transects reveal that tidal sand waves affect the spatial distribution of benthic organisms and sand ripples. *Geophysical Research Letters*, 45, 11,837– 11,846. https://doi.org/10.1029/2018GL079858

Davidson, M. A., Lewis, R. P. & Turner, I. L. (2010). Forecasting seasonal to multi-year shoreline change. *Coastal Engineering*, 57, 620–629. https://doi.org/10.1016/j.coastaleng.2010.02.001

de Haas, H., van Weering, T. C. E. & de Stigter, H. (2002). Organic carbon in shelf seas: sinks or sources, processes and products. *Continental Shelf Research*, 22 (5), 691 – 717. https://doi.org/10.1016/S0278-4343(01)00093-0

Deltares. (2014). Delft3D-FLOW, Simulation of multi-dimensional hydrodynamic flows and transport phenomena, including sediments. User Manual: Hydro-Morphodynamics. Version 3.15.34158. Delft, The Netherlands: Deltares.

Dernie, K. M., Kaiser, M. J. & Warwick, R. M. (2003). Recovery rates of benthic communities following physical disturbance. Journal of Animal Ecology, 72(6), 1043-1056. https://doi.org/10.1046/j.1365-2656.2003.00775.x

Dietrich, J. C., Zijlema, M., Westerink, J. J., Holthuijsen, L. H., Dawson, C., Luettich Jr, R. A., Jensen, R. E., Smith, J. M., Stelling, G. S. & Stone, G. W. (2011). Modeling hurricane waves and storm surge using integrally-coupled, scalable computations. *Coastal Engineering*, 58, 45-65. https://doi.org/10.1016/j.coastaleng.2010.08.001

Dingemans, M. W., Radder, A. C. & De Vriend, H. J. (1987). Computation of the driving forces of wave-induced currents. *Coastal Engineering*, 11, 539-563. https://doi.org/10.1016/0378-3839(87)90026-3

Donal, M. G., Renggli, D., Wild, S., Alexander, L. V., Leckebusch, G. C. & Ulbrich, U. (2011). Reanalysis suggests long-term upward trends in European storminess since 1871. *Geophysical Research Letters*, 38, L14703. https://doi.org/10.1029/2011GL047995

Draper, L. (1967). Wave activity at the sea bed around northwestern Europe. *Marine Geology*, 5(2), 133 – 140. https://doi.org/10.1016/0025-3227(67)90075-8

Draper, S., Borthwick, A. G. L. & Houlsby, G. T. (2013). Energy potential of a tidal fence deployed near a coastal headland. *Philosphical Transactions of the Royal Society A*, 371: 20120176. http://dx.doi.org/10.1098/rsta.2012.0176

Drønen, N., Kristensen, S., Taaning, M., Elfrink, B., & Deigaard, R. (2011). Long term modeling of shoreline response to coastal structures. In: *The Proceedings of the Coastal Sediments 2011: In 3 Volumes* (pp. 965 – 978). https://doi.org/10.1142/9789814355537_0073

Duarte, J., Taborda, R., Ribeiro, M., Cascalho, J., Silva, A. & Bosnic, I. (2014). Evidences of sediment bypassing at Nazaré headland revealed by a large scale sand tracer experiment. *Proceedings of the 3rd as Jornadas de Engenharia Hidrográica*, Lisboa, Portugal, 24–26 June 2014, 289 – 292. https://doi.org/10.1142/9789811204487_0230

Elias, E. P. L., Gelfenbaum, G. & Van der Westhuysen, A. J. (2012). Validation of a coupled wave-flow model in a high-energy setting: The mouth of the Columbia River. *Journal of Geophysical Research: Oceans*, 117, C09011. https://doi.org/10.1029/2012JC008105

EMODnet Bathymetry Consortium. (2016). EMODnet Digital Bathymetry (DTM 2016). EMODnet Bathymetry Consortium. https://doi.org/10.12770/c7b53704-999d-4721-b1a3-04ec60c87238

Evans, O. F. (1943). The relation of the action of waves and currents on headlands to the control of shore erosion by groins. *Proceedings of the Oklahoma Academy of Sciences*, 24, 9 – 13.

Fellowes, T. E., Villa-Concejo, A. & Gallop, S. L. (2019). Morphometric classification of swell-dominated embayed beaches. *Marine Geology*, 411, 78 – 87. https://doi.org/10.1016/j.margeo.2019.02.004

Fitzgerald, D. M., Kraus, N. C. & Hands, E. B. (2000). Natural Mechanisms of Sediment Bypassing at Tidal Inlets. CHETN-IV-30. U.S. Army Corps of Engineers, Vicksburg, MS. https://apps.dtic.mil/dtic/tr/fulltext/u2/a588774.pdf

Folk, R. L. (1954). The distinction between grain size and mineral composition in sedimentary rock nomenclature. *Journal of Geology*, 62(4), 344-359. www.jstor.org/stable/30065016

Fong, S. W., & Heaps, N. S. (1978). Note on quarter-wave tidal resonance in the Bristol Channel. (Institute of Oceanographic Sciences Report No. 6), 11 pp. UK. Institute of Oceanographic Sciences. https://eprints.soton.ac.uk/id/eprint/14346

Fredsøe, J. (1984). Turbulent boundary layer in wave-current motion. *Journal of Hydraulic Engineering*, 110(8), 1103-1120. https://doi.org/10.1061/(ASCE)0733-9429(1984)110:8(1103)

Genest, C. & Favre, A. C. (2007). Everything you always wanted to know about copula modeling but were afraid to ask. *Journal of Hydrologic Engineering*. 12(4), 347 – 368. https://doi.org/10.1061/(ASCE)1084-0699(2007)12:4(347)

George, D. A., Largier, J. L., Pasternack, G. B., Barnard, P. L., Storlazzi, C. D. & Erikson, L. H. (2019). Modelling sediment bypassing around idealized rocky headlands. *Journal of Marine Science and Engineering*, 7(40). https://doi.org/10.3390/jmse7020040

George, D. A., Largier, J. L., Storlazzi, C. D. & Barnard, P. L. (2015). Classification of rocky headlands in California with relevance to littoral cell boundary delineation. *Marine Geology*, 369, 137 – 152. https://doi.org/10.1016/j.margeo.2015.08.010

Goodwin, I. D., Freeman, R., Blackmore, K. (2013). An insight into headland sand bypassing and wave climate variability from shoreface bathymetric change at Byron Bay, New South Wales, Australia. Marine Geology, 341, 29 – 45. https://doi.org/10.1016/j.margeo.2013.05.005

Graham, J. A., O'Dea, E., Holt, J. T., Polton, J., Hewitt, H. T., Furner, R., et al. (2018). AMM15: a new high-resolution NEMO configuration for operational simulation of the European north-west shelf. *Geoscientific Model Development*, 11, 618-696. https://doi.org/10.5194/gmd-11-681-2018

Grant, W. D. & Madsen, O. S. (1979). Combined wave and current interaction with a rough bottom. *Journal of Geophysical Research: Oceans*, 84(C4), 1797-1808. https://doi.org/10.1029/JC084iC04p01797

Grant, W. D. & Madsen, O. S. (1986). The Continental-Shelf Bottom Boundary Layer. *Annual Review of Fluid Mechanics*, 18, 265-305. https://doi.org/10.1146/annurev.fl.18.010186.001405

Grunnet, N. M., Walstra, D. J. R. & Ruessink, B. G. (2004). Process-based modelling of a shoreface nourishment. *Coastal Engineering*, 51, 581–607. https://doi.org/10.1016/j.coastaleng.2004.07.016

Hadley, M. L. (1964). Wave-induced bottom currents in the Celtic Sea. *Marine Geology*, 2(1–2), 164–167. https://doi.org.10.1016/0025-3227(64)90033-7

Hale, R. P., Ogston, A. S., Walsh, J. P. & Orpin, A. R. (2014). Sediment transport and event deposition on the Waipaoa River Shelf, New Zealand. *Continental Shelf Research*, 86, 52-65. https://doi.org/10.1016/j.csr.2014.01.009

Hall, S.J. (1994) Physical disturbance and marine benthic communities: life in unconsolidated sediments. *Oceanography and Marine Biology: an Annual Review*, 32, 179–239. https://doi.org/10.2307/2404893

Hamon-Kerivel, K., Cooper, A., Jackson, D., Sedrati, M. & Pintado, E. G. (2020). Shoreface mesoscale morphodynamics: A review. *Earth Science Reviews*, 209, 103330. https://doi.org/10.1016/j.earscirev.2020.103330

Hanley, J. & Caballero, R. (2012). The role of large-scale atmospheric flow and Rossby wave breaking in the evolution of extreme windstorms over Europe. *Geophysical Research Letters*, 39, L21708. https://doi.org/10.1029/2012GL053408

Hansen, J. E., Elias, E., List, J. H., Erikson, L. H. & Barnard, P. L. (2013). Tidally influenced alongshore circulation at an inlet-adjacent shoreline. *Continental Shelf Research*, 56, 26-38. https://doi.org/10.1016/j.csr.2013.01.017

Harris, P. T. & Coleman, R. (1998). Estimating global shelf sediment mobility due to swell waves. *Marine Geology*, 150, 171-177. https://doi.org/10.1016/S0025-3227(98)00040-1

Harris, P. T. & Collins, M. B. (1991). Sand transport in the Bristol Channel: Bedload parting zone or mutually evasive transport pathways? *Marine Geology*, 101(1-4), 209–216. https://doi.org/10.1016/0025-3227(91)90072-C

Harris, P. T. (2014). Shelf and deep-sea sedimentary environments and physical benthic disturbance regimes: A review and synthesis. Marine Geology, 353, 169-184. https://doi.org/10.1016/j.margeo.2014.03.023

Harris, P. T., Macmillan-Lawler, M., Rupp, J. & Baker, E. K. (2014). Geomorphology of the ocean. *Marine Geology*, 352, 4 – 24. https://doi.org/10.1016/j.margeo.2014.01.011

Hashemi, M. R. & Neill, S. P. (2014). The role of tides in shelf-scale simulations of the wave energy resource. *Renewable Energy*, 69, 300-310. https://doi.org/10.1016/j.renene.2014.03.052

Hashemi, M. R., Neill, S. P. & Davies, A. G. (2014). A coupled tide-wave model for the NW European shelf seas. *Geophysical & Astrophysical Fluid Dynamics*, 109(3), 234-253. https://doi.org/10.1080/03091929.2014.944909

Heathershaw, A. D., New, A. L., & Edwards, P. D. (1987). Internal tides and sediment transport at the shelf break in the Celtic Sea. *Continental Shelf Research*, 7(5), 485-517. https://doi.org/10.1016/0278-4343(87)90092-6

Héquette, A., Hemdane, Y. & Anthony E. J. (2008). Sediment transport under wave and current combined flows on a tide-dominated shoreface, northern coast of France. *Marine Geology*, 249, 226-242. https://doi.org/10.1016/j.margeo.2007.12.003

Herrling, G & Winter, C. (2018). Tidal inlet sediment bypassing at mixed-energy barrier islands. *Coastal Engineering*, 140, 342-354. https://doi.org/10.1016/j.coastaleng.2018.08.008

Holt, J. T. & Proctor, R. (2008). The seasonal circulation and volume transport on the northwest European continental shelf: A fine-resolution model study. *Journal of Geophysical Research: Oceans, 113, C06021.* https://doi.org/10.1029/2006JC004034

Holt, J. T., Hyder, P., Ashworth, M., Harle, J., Hewitt, H. T., Liu, H. et al. (2017). Prospects for improving the representation of coastal and shelf seas in global ocean models. *Geoscientific Model Development*, 10, 499-523. https://doi.org/10.5194/gmd-10-499-2017

Holt, J. T., James, I. D. & Jones, E. J. (2001). An s coordinate density evolving model of the northwest European continental shelf: 2. Seasonal currents and tides. *Journal of Geophysical Research: Oceans*, 106(C7), 14035-14053. https://doi.org/10.1029/2000JC000303

Holt, J., Wakelin, S., Lowe, J. & Tinker, J. (2010). The potential impacts of climate change on the hydrography of the northwest European continental shelf. *Progress in Oceanography*, 86(3-4), 361-379. https://doi.org/10.1016/j.pocean.2010.05.003

Hopkins, J., Elgar, S., & Raubenheimer, B. (2015). Observations and model simulations of wave-current interaction on the inner shelf. *Journal of Geophysical Research: Oceans*, 121, 198–208. https://doi.org/10.1002/2015JC010788

Houthuys, R., Trentesaux, A., & De Wolf, P. (1994). Storm influences on a tidal sandbank's surface (Middelkerke Bank, southern North Sea). *Marine Geology*, 121(1–2), 23–41. https://doi.org/10.1016/0025-3227(94)90154-6

IHO. (2008). *Standardization of Undersea Feature Names: Guidelines Proposal form Terminology*, (4th ed.). International Hydrographic Organisation and Intergovernmental Oceanographic Commission, Monaco.

Isobe, M. & Horikawa, K. (1982). Study on water particle velocities of shoaling and breaking waves. *Coastal Engineering in Japan*, 25(1). https://doi.org/10.1080/05785634.1982.11924340

Jennings, S., Orford, J. D., Canti, M., Devoy, R. J. N. & Straker, V. (1998). The role of relative sea-level rise and changing sediment supply on Holocene gravel barrier development: the example of Porlock, Somerset, UK. *The Holocene*, 8(2), 165-181. https://doi.org/10.1191/095968398667901806

Kalkwijk, J. P. T. & Booij, R. (1986). Adaptation of secondary flow in nearly horizontal flow. *Journal of Hydraulic Research*, 24(1), 19-37. https://doi.org/10.1080/00221688609499330

Kanevski, M., Pozdnukhov, A . & Timonin, V. (2009). *Machine Learning for Spatial Environmental Data: Theory, Applications, and Software*. Lausanne, Switzerland: EPFL Press.

Kemp, P. H. & Simmons, R. R. (1982). The interaction between waves and a turbulent current: waves propagating with the current. *Journal of Fluid Mechanics*, 116, 227-250. https://doi.org/10.1017/S0022112082000445

Kemp, P. H. & Simmons, R. R. (1983). The interaction of waves and a turbulent current: waves propagating against the current. *Journal of Fluid Mechanics*, 130, 73-89. https://doi.org/10.1017/S0022112083000981

King, E. V., Conley, D. C., Masselink, G., Leonardi, N., McCarroll, R. J., & Scott, T. (2019). The impact of waves and tides on residual sand transport on a sediment-poor, energetic, and macrotidal continental shelf. *Journal of Geophysical Research: Oceans*, 124, 4974 – 5002. https://doi.org/10.1029/2018JC014861

King, E. V., Conley, D. C., Masselink, G., Leonardi, N., McCarroll, R. J., Scott, T., & Valiente, N. G. (2021). Wave, Tide and Topographical Controls on Headland Sand Bypassing. *Journal of Geophysical Research: Oceans*, 126, e2020JC017053. https://doi.org/10.1029/2020JC017053

Klein, A.H.F., Ferreira, Ó., Dias, J.M.A., Tessler, M.G., Silveira, L.F., Benedet, L., de Menezes, J.T. & de Abreu, J.G.N. (2010). Morphodynamics of structurally controlled headland-bay beaches in southeastern Brazil: A review. *Coastal Engineering*, 57, 98–111. https://doi.org/10.1016/j.coastaleng.2009.09.006

Klein, A. H. F., Vieira da Silva, G., Taborda, R., da Silva, A. P. & Short, A. D. (2020). Headland bypassing and overpassing: form, processes and applications. In Jackson, D. & Short, A. (Eds.), *Sandy Beach Morphodynamics* (Vol. 1, pp. 557 – 591). Amsterdam, Netherlands: Elsevier.

Klopman, G. (1994). Vertical structure of the flow due to waves and currents. *Progress report H840.30, Part II.* Delft Hydraulics.

Knaapen, M. A. F. (2005). Sandwave migration predictor based on shape information. *Journal of Geophysical research: Earth Surface*, 110, F04S11. https://doi.org/10.1029/2004JF000195

Komen, G., Hasselmann S. & Hasselmann, K. (1984). On the existence of a fully developed wind-sea spectrum. *Journal of Physical Oceanography*, 14, 1271 – 1285. https://doi.org/10.1175/1520-0485(1984)014<1271:OTEOAF>2.0.CO;2

Kristensen, S., Dronen, N., Deigaard, R. and Fredsoe, J. (2012). Hybrid morphological modelling of shoreline response to a detached breakwater. *Coastal Engineering*, 71, 13 – 27. https://doi.org/10.1016/j.coastaleng.2012.06.005

Lary, D. J., Alavi, A. H., Gandomi, A. H., & Walker, A. L. (2016). Machine learning in geosciences and remote sensing. *Geoscience Frontiers*, 7(1), 3–10.

Lee, T. R., Phrampus, B. J., Obelcz, J., Wood, W. T., & Skarke, A. (2020). Global marine isochore estimates using machine learning. *Geophysical Research Letters*, 47, e2020GL088726. https://doi.org/10.1029/2020GL088726

Lee, T. R., Wood, W. T., & Phrampus, B. J. (2019). A machine learning (kNN) approach to predicting global seafloor total organic carbon. *Global Biogeochemical Cycles*, 33, 37–46. https://doi.org/10.1029/2018GB005992

Leonardi, N., Kolker, A. S. & Fagherazzi, S. (2015). Interplay between river discharge and tides in a delta distributary. *Advances in Water Resources*, 80, 69 – 78. https://doi.org/10.1016/j.advwatres.2015.03.005

Leonardi, N., & Plater, A. J. (2017). Residual flow patterns and morphological changes along a macro- and meso-tidal coastline. *Advances in Water Resources*, 109, 290-301. https://doi.org/10.1016/j.advwatres.2017.09.013

Lesser, G. R., Roelvink, J. A., Van Kester, J. A. T. M. & Stelling, G. S. (2004). Development and validation of a three-dimensional morphological model. *Coastal Engineering*, 51(8), 883-915. https://doi.org/10.1016/j.coastaleng.2004.07.014

Levin, L. A. (1995). Influence of sediment transport on short-term recolonization by seamount infauna. *Marine Ecology Progress Series*, 123, 163-175. https://doi.org/10.3354/meps123163

Lewis, M. J., Neill, S. P. & Elliot, A. J. (2015). Interannual variability of two offshore sand banks in a region of extreme tidal range. *Journal of Coastal Research*, 31(2), 265-275. https://doi.org/10.2112/JCOASTRES-D-14-00010.1

Lin, B., & Falconer, R. A. (2001). Numerical modelling of 3-d tidal currents and water quality indicators in the Bristol Channel. *Proceedings of the Institution of Civil Engineers - Water and Maritime Engineering*, 148(3), 155-166. https://doi.org/10.1680/wame.2001.148.3.155

Lopez, G., Conley, D. C. & Greaves, D. (2016). Calibration, validation, and analysis of an empirical algorithm for the retrieval of wave spectra from HF radar sea echo. *Journal of Atmospheric and Oceanic Technology*, 33, 245-261. https://doi.org/10.1175/JTECH-D-15-0159.1

Luijendijk A. P., Ranasinghe, R., de Schipper, M. A., Huisman, B. A., Swinkels, C. M., Walstra, D. J. R. & Stive, M. J. F. (2017). The initial morphological response of the Sand Engine: A process-based modelling study. *Coastal Engineering*, 119, 1-14. https://doi.org/10.1016/j.coastaleng.2016.09.005

Lyddon, C., Brown, J. M., Leonardi, N. and Plater, A. J. (2018). Flood Hazard Assessment for a Hyper-Tidal Estuary as a Function of Tide-Surge-Morphology Interaction. *Estuaries and Coasts*, 1-22. https://doi.org/10.1007/s12237-018-0384-9

Madsen, O., Poon Y. K. & Graber, H. (1988). Spectral wave attenuation by bottom friction: Theory. *Proceedings 21th International Conference Coastal Engineering*, ASCE, 492 – 504. https://doi.org/10.9753/icce.v21.34

Mandelbrot, B. (1967). How long is the coast of Britain? Statistical self-similarity and fractal dimension. *Science*, 156 (3775), 636 – 638. https://doi.org/10.1126/science.156.3775.636

Marmorino, G. O. & Hallock, Z. R. (2001). On estimating wind velocity using an upward-looking ADCP. *Journal of Atmospheric and Oceanic Technology*, **8**(5), 791-798. https://doi.org/10.1175/1520-0426(2001)018<0791:OEWVUA>2.0.CO;2

Martin, K. M., Wood, W. T., & Becker, J. J. (2015). A global prediction of seafloor sediment porosity using machine learning. *Geophysical Research Letters*, 42, 10,640–10,646. https://doi.org/10.1002/2015GL065279

Masselink, G., Castelle, B., Scott, T., Dodet, G., Suanez, S., Jackson, D. & Floc'h, F. (2016). Extreme wave activity during 2013/14 winter and morphological impacts along the Atlantic coast of Europe. *Geophysical Research Letters*, 43, 2135-2143. https://doi.org/10.1002/2015GL067492

Masselink, G., Scott, T., Poate, T., Russell, P., Davidson, M. & Conley, D. (2015). The extreme 2013/14 winter-storms: hydrodynamic forcing and coastal response along the southwest coast of England. *Earth Surface Processes and Landforms*, 41(3), 378-391. https://doi.org/10.1002/esp.3836

MathWorks. (2020). *Statistics and Machine Learning Toolbox™ User's Guide*. September, 2020. Natick, MA: The MathWorks, Inc. Retrieved 29/10/2020: https://uk.mathworks.com/help/pdf_doc/stats/stats.pdf

McCarroll, R. J., Brander, R. W., Turner, I. L. & Van Leeuwen, B. (2016). Shoreface storm morphodynamics and mega-rip evolution at an embayed beach: Bondi Beach, NSW, Australia. *Continental Shelf Research*, 116, 74 – 88. https://doi.org/10.1016/j.csr.2016.01.013

McCarroll, R. J., Masselink, G., Valiente, N. G., Scott, T., Wiggins, M., Kirby, J. –A. & Davidson, M. (2021a). A rules-based shoreface translation and sediment budgeting tool for estimating coastal change: ShoreTrans. *Marine Geology*, 435, 106466. https://doi.org/10.1016/j.margeo.2021.106466

McCarroll, R. J., Masselink, G., Valiente, N. G., King, E. V. Scott, T., Stokes, C. & Wiggins, M. (2021b). An XBeach derived parametric expression for headland bypassing. *Coastal Engineering*, 103860. https://doi.org/10.1016/j.coastaleng.2021.103860

McCarroll, R. J., Masselink, G., Valiente, N. G., Scott, T., King, E. V. & Conley, D. (2018). Wave and Tidal Controls on Embayment Circulation and Headland Bypassing for an Exposed, Macrotidal Site. Journal of Marine Science and Engineering, 6(3), 94. https://doi.org/10.3390/jmse6030094

McCarroll, R. J., Masselink, G., Wiggins, M., Scott, T., Billson, O., Conley, D. C. & Valiente, N. G. (2019). High-efficiency gravel longshore sediment transport and headland bypassing over an extreme wave event. *Earth Surface Processes and Landforms*, 44, 2720 – 2727. https://doi.org/10.1002/esp.4692

McCarron, C. J., Van Landeghem, K. J. J., Baas, J. H., Amoudry, L. O. & Malarkey, J. (2019). The hiding-exposure effect revisited: A method to calculate the mobility of bimodal sediment mixtures. *Marine Geology*, 410, 22-31. https://doi.org/10.1016/j.margeo.2018.12.001

McConnell, N., King, R., Tonani, M., O'Dea, E., Martin, M., Sykes, P. & Ryan, A. (2017). North West European Shelf Production Centre NORTHWESTSHELF_ANALYSIS_FORECAST_PHYS_004_001_b. *Quality Information Document.* Issue 3.5. Copernicus Marine Environment Monitoring Service.

McLaren, P., Collins, M. B., Gao, S. & Powys, R. I. L. (1993). Sediment dynamics of the Severn Estuary and inner Bristol Channel. *Journal of the Geological Society,* 150, 589-603. https://doi.org/10.1144/gsjgs.150.3.0589

Mori, N., Sizuki, T. & Kakuno, S. (2007). Noise of acoustic Doppler velocimeter data in bubbly flows. *Journal of Engineering Mechanics*, 133(1), 122-125. https://doi.org/10.1061/(ASCE)0733-9399(2007)133:1(122)

Moriarty, J. M., Harris, C. K. & Hadfield, M. G. (2014). A hydrodynamic and sediment transport model for the Waipaoa Shelf, New Zealand: sensitivity of fluxes to spatially-varying erodibility and model nesting. *Journal of Marine Science and Engineering*, 2(2), 336-369. https://doi.org/10.3390/jmse2020336

Motyka, J. M. & Brampton, A. H. (1993). Coastal Management. Mapping of littoral cells. HR Wallingford Ltd, Report SR 328. http://eprints.hrwallingford.co.uk/748/1/SR328.pdf

Mouragues, A., Bonneton, P., Castelle, B., Marieu, V., McCarroll, R. J., Rodriguez-Padilla, I., Scott, T. & Sous, D. (2020). High-energy surf zone currents and headland rips at a geologically constrained mesotidal beach. *Journal of Geophysical Research: Oceans*, 125, e2020JC016259. https://doi.org/10.1029/2020JC016259

Murphy, A. H. & Epstein, E. S. (1989). Skill scores and correlation coefficients in model verification. *Monthly Weather Review*, 117, 572-582. https://doi.org/10.1175/1520-0493(1989)117<0572:SSACCI>2.0.CO;2

Neill, S. P., Scourse, J. D. & Uehara, K. (2010). Evolution of bed shear stress distribution over the northwest European shelf seas during the last 12,000 years. *Ocean Dynamics*, 60, 1139-1156. https://doi.org/10.1007/s10236-010-0313-3

Németh, A. A., Hulscher, S. J. M. H., & de Vriend, H. J. (2003). Offshore sand wave dynamics, engineering problems and future solutions. *Pipeline & Gas Journal*, 230(4), 67. http://search.epnet.com/login.aspx?direct=true&db=bsh&an=9562236

Nielsen, P. (1992). *Coastal bottom boundary layers and sediment transport*. Singapore: World Scientific Publishing Co. Pte. Ltd. https://doi.org/10.1142/1269

O'Dea, E. J., Arnold, A. K., Edwards, K. P., Furner, R., Hyder, P., Martin, M. J., et al. (2012). An operational ocean forecast system incorporating NEMO and SST data assimilation for the tidally driven European North-West shelf. *Journal of Operational Oceanography*, 5(1), 3-17. https://doi.org/10.1080/1755876X.2012.11020128

Olabarrieta, M., Medina, R., & Castenedo, S. (2010). Effects of wave–current interaction on the current profile. *Coastal Engineering*, 57(7), 643–655. https://doi.org/10.1016/j.coastaleng.2010.02.003

Orford, J. and Jennings, S. (1998). 8: The importance of different time-scale controls on coastal management strategy: the problem of Porlock gravel barrier, Somerset, UK. In Hooke, J. M. (Ed.), *Coastal defence and earth science conservation* (pp .87-102). Bath, UK: The Geological Society.

Oyedotun, T. D. T. (2020). Compositional and multivariate statistical analyses for grain-size characterisation of intertidal sedimentary facies in an estuarine environment. *Geology, Ecology and Landscapes*, 4 (4). https://doi.org/10.1080/24749508.2020.1814186

Pattiaratchi, C. & Collins, M. C. (1988). Wave influence on coastal sand transport paths in a tidally dominated environment. *Ocean & Shore Management*, 11, 449-465. https://doi.org/10.1016/0951-8312(88)90025-2

Phrampus, B. J., Lee, T. R., & Wood, W. T. (2020). A global probabilistic prediction of cold seeps and associated SEAfloor FLuid Expulsion Anomalies (SEAFLEAs). *Geochemistry, Geophysics, Geosystems*, 21, e2019GC008747. https://doi.org/10.1029/2019GC008747

Pingree, R. D. & Griffiths, D. K. (1979). Sand transport paths around the British Isles resulting from M_2 and M_4 tidal interactions. *Journal of the Marine Biological Association of the United Kingdom*, 59(2), 497-513. https://doi.org/10.1017/S0025315400042806

Pingree, R. D. & Griffiths, D. K. (1980) Currents driven by a steady uniform wind stress on the shelf areas around the British Isles. *Oceanologica Acta*, 3, 227-236. http://archimer.ifremer.fr/doc/00121/23265/

Pingree, R. D. & Le Cann, B. (1989). Celtic and Amorican slope and shelf residual currents. *Progress in Oceanography*, 23(4), 303-338. https://doi.org/10.1016/0079-6611(89)90003-7

Pingree, R. D. & Maddock, L. (1977). Tidal eddies and coastal discharge. *Journal of the Marine Biological Association of the United Kingdom*, 57(3), 869-875. https://doi.org/10.1017/S0025315400025224

Pingree, R. D. & Maddock, L. (1979). The tidal physics of headland flows and offshore tidal bank formation. *Marine Geology*, **32**(3-4), 269-289. https://doi.org/10.1016/0025-3227(79)90068-9

Porter-Smith, R., Harris, P. T., Andersen, O. B., Coleman, R., Greenslade, D. & Jenkins, C. J. (2004). Classification of the Australian continental shelf based on predicted sediment threshold exceedance from tidal currents and swell waves. *Marine Geology*, 211, 1-20. https://doi.org/10.1016/j.margeo.2004.05.031

Prodger, S., Russell, P. & Davidson, M. (2017). Grain-size distributions on high-energy sandy beaches and their relation to wave dissipation. *Sedimentology*, 64, 1289-1302. https://doi.org/10.1111/sed.12353

Prodger, S., Russell, P., Davidson, M., Miles, J. & Scott, T. (2016). Understanding and predicting the temporal variability of sediment grain size characteristics on high-energy beaches. *Marine Geology*, **376**, 109 – 117. https://doi.org/10.1016/j.margeo.2016.04.003

Reiss, H., Degraer, S., Duineveld, G. C. A., Kröncke, I., Aldridge, J., Craeymeersch, J., Eggleton, J. D., Hillewaert, H., Lavaleye, M. S. S., Moll, A., Pohlmann, T., Rachor, E., Robertson, M., vanden Berghe, E., van Hoey, G., & Rees, H. L. (2010). Spatial patterns of infauna, epifauna, and demersal fish communities in the North Sea. *ICES Journal of Marine Science*, 67, 278–293. https://doi.org/10.1093/icesjms/fsp253

Restreppo, G. A., Wood, W. T. & Phrampus, B. J. (2020). Oceanic sediment accumulation rates predicted via machine learning algorithm: towards sediment characterization on a global scale. *Geo-Marine Letters*, 40, 755–763. https://doi.org/10.1007/s00367-020-00669-1

Reynaud, J. –Y., Tessier, B., Berné, S., Hervé, C., & Debatist, M. (1999). Tide and wave dynamics on a sand bank from the deep shelf of the Western Channel approaches. *Marine Geology*, 161, 339-359. https://doi.org/10.1016/S0025-3227(99)00033-X

Ribeiro, M. S. A. (2017). *Headland sediment bypassing processes* (Doctoral dissertation). University of Lisbon. 229 p. https://pdfs.semanticscholar.org/e6be/c734b7b57592213848201567a80e1157d2b7.pdf

Ridderinkhof, W., Swart, H. E., Vegt, M., & Hoekstra, P. (2016). Modeling the growth and migration of sandy shoals on ebb-tidal deltas. *Journal of Geophysical Research: Earth Surface*, 121, 1351– 1372. https://doi.org/10.1002/2016JF003823

Robinet, A., Idier, D., Castelle, B., & Marieu, V. (2018). A reduced-complexity shoreline change model combining longshore and cross-shore processes: the LX-Shore model. *Environmental modelling & software*, 109, 1 – 16. https://doi.org/10.1016/j.envsoft.2018.08.010

Robinet, A., Castelle, B., Idier, D., Harley, M. D., & Splinter, K. D. (2020). Controls of local geology and cross-shore/longshore processes on embayed beach shoreline variability. *Marine Geology*, 106118. https://doi.org/10.1016/j.margeo.2020.106118

Roelvink, D., Huisman, B., Elghandour, A., Ghonim, M., & Reyns, J. (2020). Efficient modeling of complex sandy coastal evolution at monthly to century time scales. *Frontiers in Marine Science*, *7*, 535. https://doi.org/10.3389/fmars.2020.00535

Roetert, T., Raaijmakers, T., & Borsje, B. (2017). Cable route optimization for offshore wind farms in Morphodynamic areas. Paper presented at the 27th International Ocean and Polar Engineering Conference, San Francisco, California, USA.

Saha, S., Moorthi, S., Wu, X., Wang, J., Nadiga, S., Tripp, P., Behringer, D., Hou, Y. T., Chuang, H. Y., Iredell, M., Ek, M., Meng, J., Yang, R., Mendez, M. P., van den Dool, H., Zhang, Q., Wang, W., Chen, M., & Becker, E. (2014). The NCEP Climate Forecast System version 2. *Journal of Climate*, 27(6), 2185 – 2208. https://doi.org/10.1175/JCLI-D-12-00823.1

Saulter, A. (2017). North West European Shelf Production Centre: NORTHWESTSHELF_ANALYSIS_FORECAST_WAV_004_012. Quality Information Document. Issue 1.0. Copernicus Marine Environment Monitoring Service.

Scott, T., Austin, M., Masselink, G. & Russell, P. (2016a). Dynamics of rip currents associated with groynes — Field measurements, modelling and implications for beach safety. *Coastal Engineering*, 107, 53 – 69. https://doi.org/10.1016/j.coastaleng.2015.09.013

Scott, T., Masselink, G., O'Hare, T., Saulter, A., Poate, T., Russell, P., Davidson, M. & Conley, D. (2016b). The extreme 2013/2014 winter storms: Beach recovery along the southwest coast of England. *Marine Geology*, 382, 224-241. https://doi.org/10.1016/j.margeo.2016.10.011

Short, A. D. & Masselink, G. (1999). Structurally Controlled Beaches. In Handbook of Beach and Shoreface Morphodynamics; Short, A.D., Ed.; JohnWiley and Sons Ltd.: Chichester, UK, 1999; pp. 230–250.

Short, A. D. (1985). Rip-current type, spacing and persistence, Narrabeen Beach, Australia. *Marine Geology*, 65(1 – 2), 47 – 71. https://doi.org/10.1016/0025-3227(85)90046-5

Soulsby, R. L., Hamm, L., Klopman, G., Myrhaug, D., Simons, R. R., & Thomas, G. P. (1993). Wave-current interaction within and outside the bottom boundary layer. *Coastal Engineering*, 21(1-3), 41 – 69. https://doi.org/10.1016/0378-3839(93)90045-a

Stride, A. H. (1963). Current-swept sea floors near the southern half of Great Britain. *Quarterly Journal of the Geological Society*, 119, 175-197. https://doi.org/10.1144/gsjgs.119.1.0175

Stride, A. H., & Belderson, R. H. (1990). A reassessment of sand transport paths in the Bristol Channel and their regional significance. *Marine Geology*, 92, 227-236. https://doi.org/10.1016/0025-3227(90)90005-5

Stride, A. H., & Belderson, R. H. (1991). Sand transport in the Bristol Channel east of Bull Point and Worms Head: a bed-load parting model with some indications of mutually evasive sand transport paths. *Marine Geology*, 101, 203-207. https://doi.org/10.1016/0025-3227(91)90071-B

Sutherland, J., Peet, A. H. & Soulsby, R. L. (2004). Evaluating the performance of morphological models. *Coastal Engineering*, 51, 917-939. https://doi.org/10.1016/j.coastaleng.2004.07.015

Tambroni, N., Blondeaux, P. & Giovanna, V. (2015). A simple model of wave-current interaction. *Jounral of Fluid Mechanics*, 775, 328-348. https://doi.org/10.1017/jfm.2015.308

Taylor, G. I. (1921). Tides in the Bristol Channel. *Mathematical Proceedings of the Cambridge Philosophical Society*, 20, 320-325.

Thom B. G., Eliot, I., Eliot, M., Harvey, N., Rissik, D., Sharples, C., Short, A. D. & Woodroffe, C. D. (2018). National sediment compartment framework for Australian coastal management. *Ocean and Coastal Management*, 154, 103 – 120. https://doi.org/10.1016/j.ocecoaman.2018.01.001

Thompson, C. E. L., Williams, M. E., Amoudry, L., Hull, T., Reynolds, S., Panton, A., & Fones, G. R. (2019). Benthic controls of resuspension in UK shelf seas: Implications for resuspension frequency. *Continental Shelf Research*, in press, in press. https://doi.org/10.1016/j.csr.2017.12.005

Toimil, A., Losada, I. J., Camus, P., & Diaz-Simal, P. (2017). Managing coastal erosion under climate change at the regional scale. *Coastal Engineering*, 128, 106 – 122. https://doi.org/10.1016/j.coastaleng.2017.08.004

Tonani M. & Saulter, A. (2020). For NWS Ocean Waves Reanalysis Product NWSHELF_REANALYSIS_WAV_004_015. Product User Manual. Issue 1.0. Copernicus Marine Environment Monitoring Service.

Tonani, M., Sykes, P., King, R. R., McConnell, N., Péquignet A-C., O'Dea, E., Graham, J. A., Polton, J. & Siddorn, J. (2019). The impact of a new high-resolution ocean model on the Met Office North-West European Shelf forecasting system. *Ocean Science*, 15, 1133–1158. https://doi.org/10.5194/os-15-1133-2019

Turner, J. F., Iliffe, J. C., Ziebart, M. K., Wilson, C. & Horsburgh, K. J. (2010). Interpolation of Tidal Levels in the Coastal Zone for the Creation of a Hydrographic Datum. *Journal of Atmospheric and Ocean Technology*, 27, 605-613. https://doi.org/10.1175/2009JTECHO645.1

Umeyama, M. (2005). Reynolds stresses and velocity distributions in a wave–current coexisting environment. *Journal of Waterway, Port, Coastal and Ocean Engineering,* 131(5), 203-212. https://doi.org/10.1061/(ASCE)0733-950X(2005)131:5(203)

Uncles, R. J. (1982). Computed and observed residual currents in the Bristol Channel. *Oceanologica Acta*, 5(1), 11-20. http://archimer.ifremer.fr/doc/00120/23148/

Uncles, R. J. (1984). Hydrodynamics of the Bristol Channel. *Marine Pollution Bulletin*, 15(2), 47-53. https://doi.org/10.1016/0025-326X(84)90461-2

Uncles, R. J. (2010). Physical properties and processes in the Bristol Channel and Severn Estuary. *Marine Pollution Bulletin*, 61(1-3), 5– 20. https://doi.org/10.1016/j.marpolbul.2009.12.010

Uncles, R. J., Clark, J. R., Bedington, M. & Torres, R. (2020). Chapter 31 - On sediment dispersal in the Whitsand Bay Marine Conservation Zone: Neighbour to a closed dredge-spoil disposal site. In J. Humphreys, R. W. E. Clark (Eds.), *Marine Protected Areas* (pp. 599 – 629). Amsterdam, Elsevier. https://doi.org/10.1016/B978-0-08-102698-4.00031-9

Valiente, N. G., Masselink, G., Scott, T., Conley, D. C. & McCarroll, R. J. (2019a). Role of waves and tides on depth of closure and potential for headland bypassing. *Marine Geology*, 407, 60-75. https://doi.org/10.1016/j.margeo.2018.10.009

Valiente, N. G., McCarroll, R. J., Masselink., G., Scott, T. & Wiggins, M. (2019b). Multi-annual embayment sediment dynamics involving headland bypassing and sediment exchange across the depth of closure. *Geomorphology*, 343, 48 – 64. https://doi.org/10.1016/j.geomorph.2019.06.020

Valiente, N. G., Masselink., G., McCarroll, R. J., Scott, T., Conley, D. C. & King, E. V. (2020). Nearshore sediment pathways and potential sediment budgets in embayed settings over a multi-annual timescale. *Marine Geology*, 427, 106270. https://doi.org/10.1016/j.margeo.2020.106270

van der Molen, J. (2002). The influence of tides, wind and waves on the net sand transport in the North Sea. *Continental Shelf Research*, 22, 2739-2762. https://doi.org/10.1016/S0278-4343(02)00124-3

van Dijk, T. A. G. P., & Kleinhans, M. G. (2005). Processes controlling the dynamics of compound sand waves in the North Sea, Netherlands, Journal of Geophysical Research: Earth Surface, 110, F04S10. https://doi.org/10.1029/2004JF000173

van Leeuwen, S., Tett, P., Mills, D., and van der Molen, J. (2015), Stratified and nonstratified areas in the North Sea: Long-term variability and biological and policy implications, *Journal of Geophysical Research: Oceans*, 120, 4670–4686. https://doi.org/10.1002/2014JC010485

Van Oyen, T. & Blondeaux, P. (2009). Tidal sand wave formation: Influence of graded suspended sediment transport. *Journal of Geophysical Research: Oceans*, 114, C07004. https://doi.org/10.1029/2008JC005136

Van Oyen, T., de Swart, H. & Blondeaux, P. (2011). Formation of rhythmic sorted bed forms on the continental shelf: An idealised model. *Journal of Fluid Mechanics*, 684, 475-508. https://doi.org/10.1017/jfm.2011.312

van Rijn, L. C. (2007a). Unified view of sediment transport by currents and waves. I: Initiation of motion, bed roughness, and bed-load transport. *Journal of Hydraulic Engineering*, 133(6), 649 – 667. https://doi.org/10.1061/(ASCE)0733-9429(2007)133:6(649

van Rijn, L. C. (2007b). Unified view of sediment transport by currents and waves. II: Suspended transport. *Journal of Hydraulic Engineering*, 133(6), 668 – 689. https://doi.org/10.1061/(ASCE)0733-9429(2007)133:6(668

van Rijn, L. C., Walstra, D. J. R., van Ormondt, M. (2007). Unified View of Sediment Transport by Currents and Waves. IV: Application of Morphodynamic Model. *Journal of Hydraulic Engineering*, 133(7), 776 – 793. https://doi.org/10.1061/(ASCE)0733-9429(2007)133:7(776)

van Rijn, L. C. (2014). A simple general expression for longshore transport of sand, gravel and shingle. *Coastal Engineering*, 90, 23 – 39. https://doi.org/10.1016/j.coastaleng.2014.04.008

van Rijn, L. C., Walstra, D. J. R. & van Ormondt, M. (2004). Description of TRANSPOR2004 and implementation in Delft3D-ONLINE, Final Report. Report Z3748.10. Delft, The Netherlands: WL Delft Hydraulics.

van Rijn, L. C., Roelvink, J. A. & Horst, W. T. (2000). Approximation formulae for sand transport by currents and waves and implementation in DELFT-MOR. Technical Report Z3054.40. Delft, The Netherlands: WL Delft Hydraulics.

van Rijn, L. C., Tonnon, P. K. & Walstra, D. J. R. (2011). Numerical modelling of erosion and accretion of plane sloping beaches at different scales. *Coastal Engineering*, 58(7), 637 – 655. https://doi.org/10.1016/j.coastaleng.2011.01.009

van Santen, R. B., de Swart, H. & Van Dijk, T. A. G. P. (2011). Sensitivity of tidal sand wave characteristics to environmental parameters: A combined data analysis and modelling approach. *Continental Shelf Research*, 31(9), 966-978. https://doi.org/10.1016/j.csr.2011.03.003

Verschelling, E, Deijl, E, Perk, M, Sloff, K & Middelkoop, H. (2017). Effects of discharge, wind, and tide on sedimentation in a recently restored tidal freshwater wetland. *Hydrological Processes*, 31(6), 2827 – 2841. https://doi.org/10.1002/hyp.11217

Vieira da Silva, G., Toldo Jr, E. E., Klein, A. H. da F., Short, A. D. & Woodroffe, C. D. (2016). Headland sand bypassing – Quantification of net sediment transport in embayed beaches, Santa Catarina Island North Shore, Southern Brazil. *Marine Geology*, 379, 13-27. https://doi.org/10.1016/j.margeo.2016.05.008

Vieira da Silva, G., Toldo, E. E., Klein, A. H. D. F. & Short, A. D. (2018). The influence of wave-, wind-and tide-forced currents on headland sand bypassing–Study case: Santa Catarina Island north shore, Brazil. *Geomorphology*, 312, 1 – 11. https://doi.org/10.1016/j.geomorph.2018.03.026

Vitousek, S., Barnard, P. L., Limber, P., Erikson, L., & Cole, B. (2017). A model integrating longshore and cross-shore processes for predicting long-term shoreline response to climate change. *Journal of Geophysical Research: Earth Surface*, 122(4), 782 – 806. https://doi.org/10.1002/2016JF004065

Wang Z., Liang, B., Wu, G. & Borsje, B. W. (2019). Modeling the formation and migration of sand waves: The role of tidal forcing, sediment size and bed slope effects. *Continental Shelf Research*, 190, 103986. https://doi.org/10.1016/j.csr.2019.103986

Ward, S. L., Neill, S. P., Van Landeghem, K. J. J., & Scourse, J. D. (2015). Classifying seabed sediment type using simulated tidal-induced bed shear stress. *Marine Geology*, 367, 94–104. https://doi.org/10.1016/j.margeo.2015.05.010

Welshby, J. & Motyka, J. M. (1989). A macro review of the coastline of England and Wales. Volume 6. The South West Coast. Portland Bill to Avonmouth. Hydraulics Research Limited, Report SR 192. http://eprints.hrwallingford.co.uk/1263/1/SR192.pdf

Wiggins, M., Scott, T., Masselink, G., Russell, P. & McCarroll, R. J. (2019). Coastal embayment rotation: Response to extreme events and climate control, using full embayment surveys. *Geomorphology*, 327, 385 – 403. https://doi.org/10.1016/j.geomorph.2018.11.014

Willmott, C. J. & Matsuura, K. (2005). Advantages of the mean absolute error (MAE) over the root mean square error (RMSE) in assessing average model performance. *Climate Research*, 30, 79-82. https://doi.org/10.3354/cr030079

Willmott, C. J., Robeson, S. M. & Matsuura, K. (2012). A refined index of model performance. *International Journal of Climatology*, 32, 2088-2094. https://doi.org/10.1002/joc.2419

Wilson, R. J., Spiers, D. C., Sabatino, A. & Heath, M. R. (2018). A synthetic map of the north-west European Shelf sedimentary environment for applications in marine science. Earth System Science Data, 10(1), 109-130. https://doi.org/10.5194/essd-10-109-2018

Xia, J., Falconer, R. A. & Lin, B. (2010). Numerical model assessment of tidal stream energy resources in the Severn Estuary, UK. *Proceedings of the Institution of Mechanical Engineers, Part A: Journal of Power and Energy*, 224(7), 969-983. https://doi.org/10.1243/09576509JPE938

Xing, F., Wang, Y. P. & Wang, H. V. (2012). Tidal hydrodynamics and fine-grained sediment transport on the radial sand ridge system in the southern Yellow Sea. *Marine Geology*, 291-294, 192-210. https://doi.org/10.1016/j.margeo.2011.06.006

Xu, K., Mickey, R. C., Chen, Q., Harris, C. K., Hetland, R. D., Hu, K. & Wang, J. (2016). Shelf sediment transport during hurricanes Katrina and Rita. *Computers and Geosciences*, **90**(B), 24-39. https://doi.org/10.1016/j.cageo.2015.10.009

Young, I. R., Zieger, S., & Babanin, A. V. (2011). Global trends in wind speed and wave height. *Science*, 332(6028), 451 – 455. https://doi.org/10.1126/science.1197219

Zhang, W., Cui, Y., Santos, A. I. & Hanebuth, T. J. J. (2016). Storm-driven bottom sediment transport on a high-energy narrow shelf (NW Iberia) and development of mud depocenters. *Journal of Geophysical Research: Oceans*, 121(8), 5751-5772. https://doi.org/10.1002/2015JC011526

Zimmerman, J. T. F. (1978). Topographic generation of residual circulation by oscillatory (tidal) currents. *Geophysical and Astrophysical Fluid Dynamics*, 11, 35-47. https://doi.org/10.1080/03091927808242650

Appendices

Appendix A: Figures

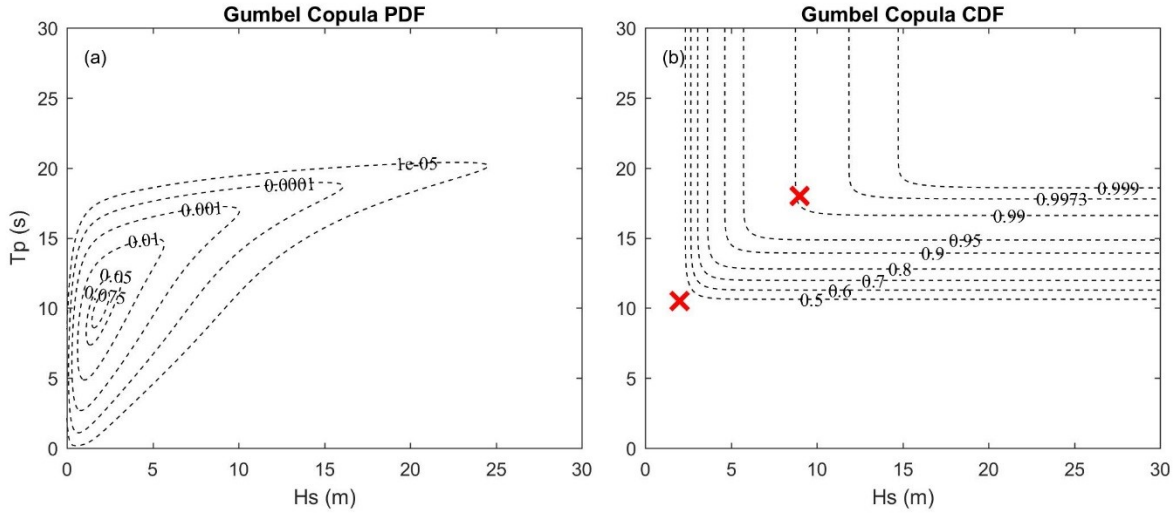

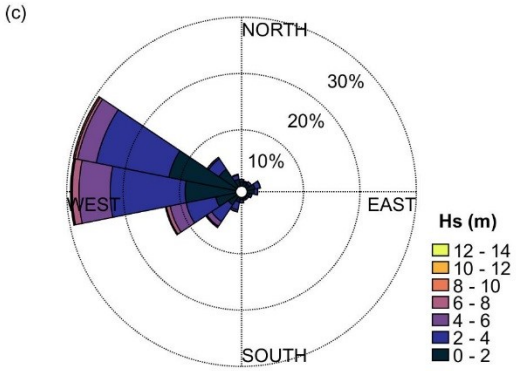

(d)

Dir (°)	Hs ∩ Tp	Hs ∩ Tp
292.5°	50% (2m , 10.5s)	1% (9m , 18s)
270°	50% (2m , 10.5s)	1% (9m , 18s)

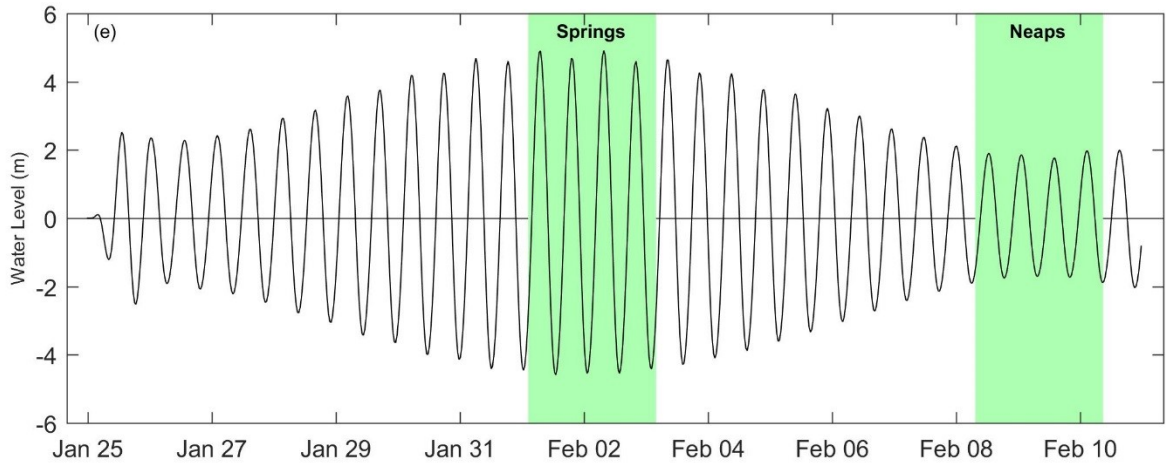

Figure A1: (a-b) Gumbel copula probability- and cumulative-density functions for Hs and Tp; (c) Wave rose for Hs. (d) Wave conditions simulated are shown. (e) An example of the simulated tidal signal taken from Ilfracombe. Shaded areas are the four spring/ neap tidal cycles extracted and averaged for a representative spring and neap cycle respectively. Tidal forcing varies along the open boundaries.

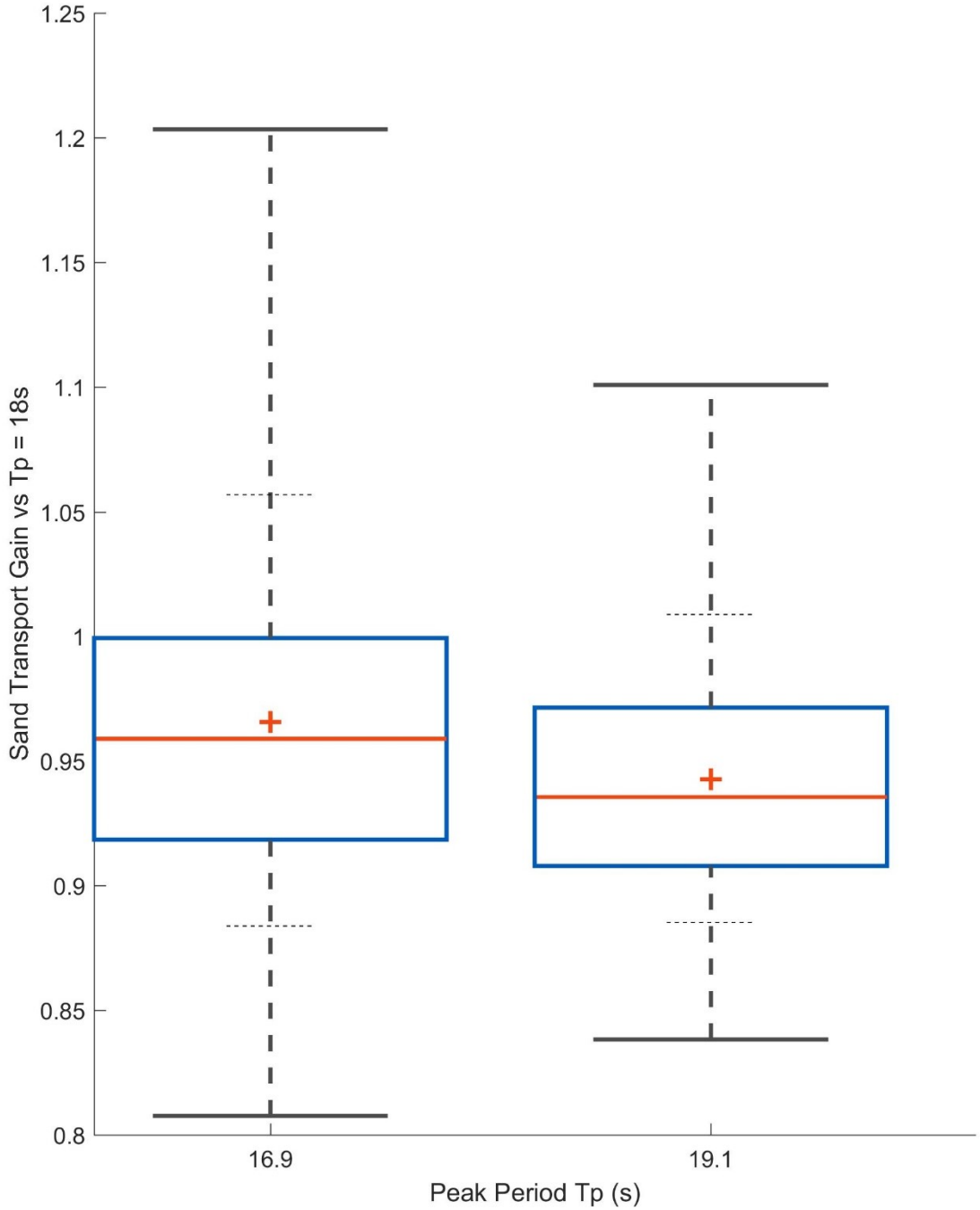

Figure A2: Sand transport gain for extreme waves at springs, defined as the sand transport for the scenario using the new peak period value divided by the sand transport for Tp = 18s. The red centre line represents the median of the data, the mean is shown by a red +, the boxes span the 25th and 75th percentiles, the dashed whiskers are the 9th and 91st percentiles and the solid whiskers span the 2nd and 98th percentiles. Data where gain > 5 or < 0.2 were excluded (N = 30 ≈ 0.05%).

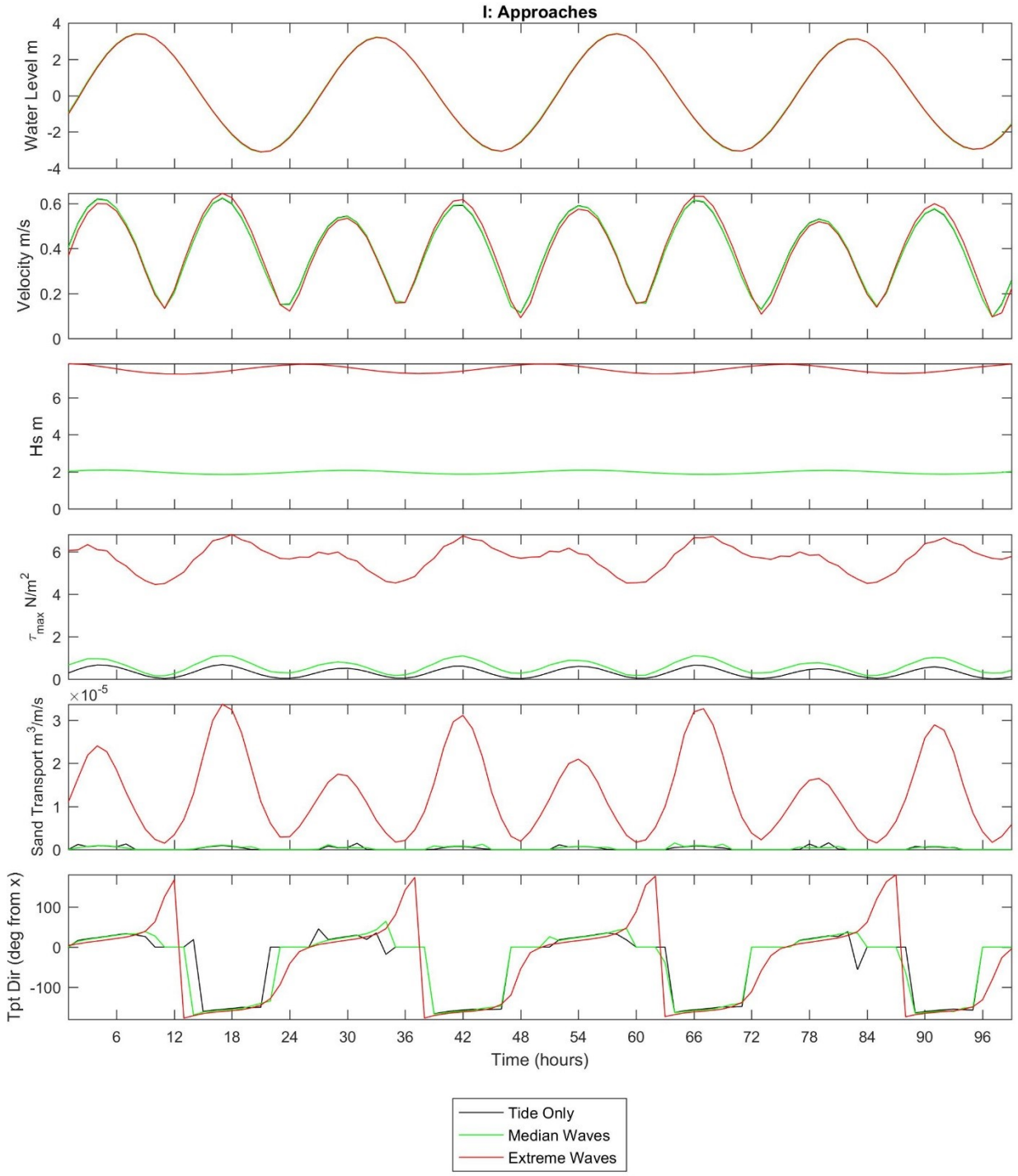

Figure A3: Hydrodynamic, wave and sand transport parameters for point I shown in Figure 9 (Section 2.5.1). Tide only (black), median wave (green) and extreme wave (red) conditions are shown for WNW waves at spring tide. Direction is degrees anticlockwise from East.

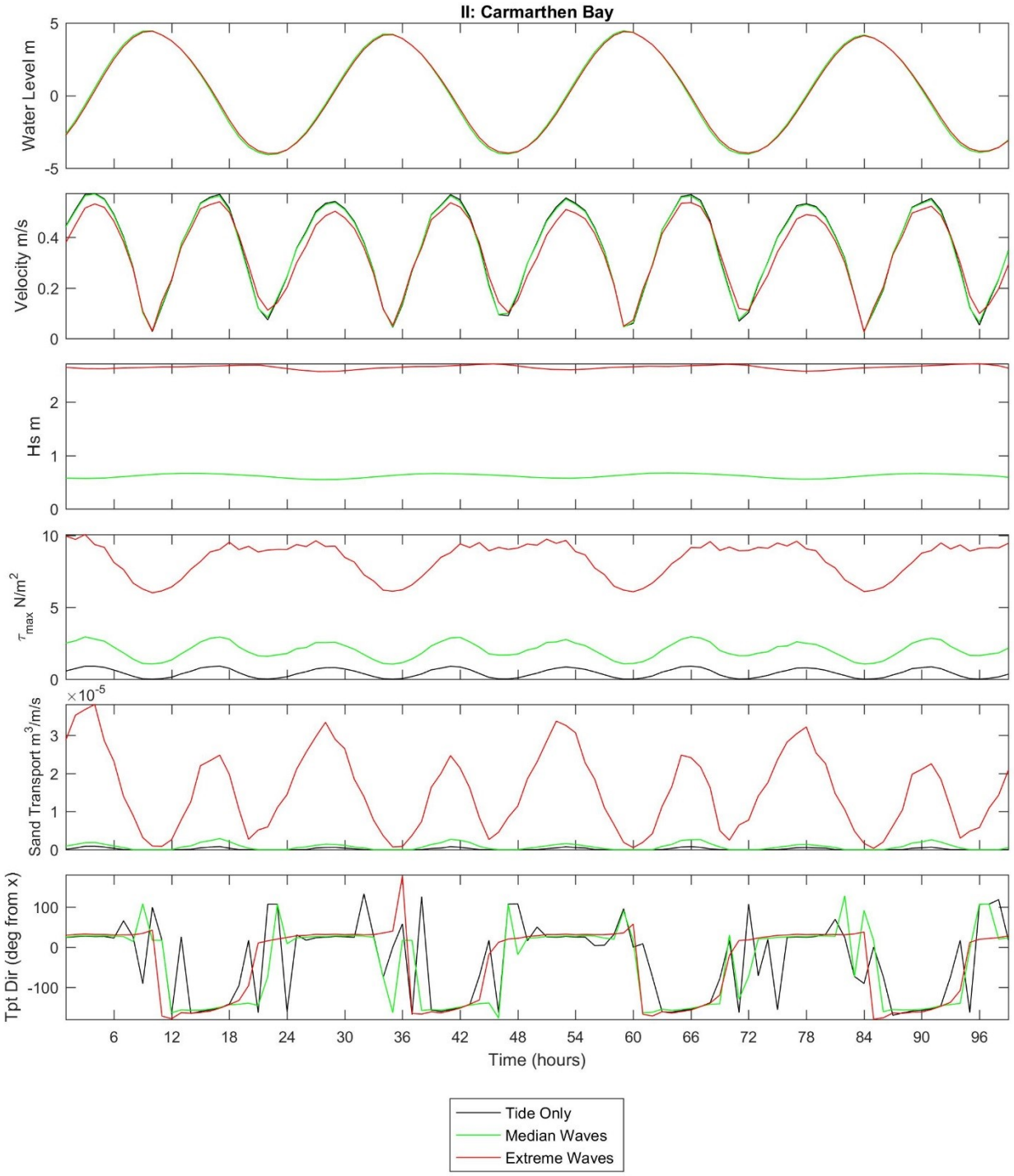

Figure A4: Hydrodynamic, wave and sand transport parameters for point II shown in Figure 9 (Section 2.5.1). Tide only (black), median wave (green) and extreme wave (red) conditions are shown for WNW waves at spring tide. Direction is degrees anticlockwise from East.

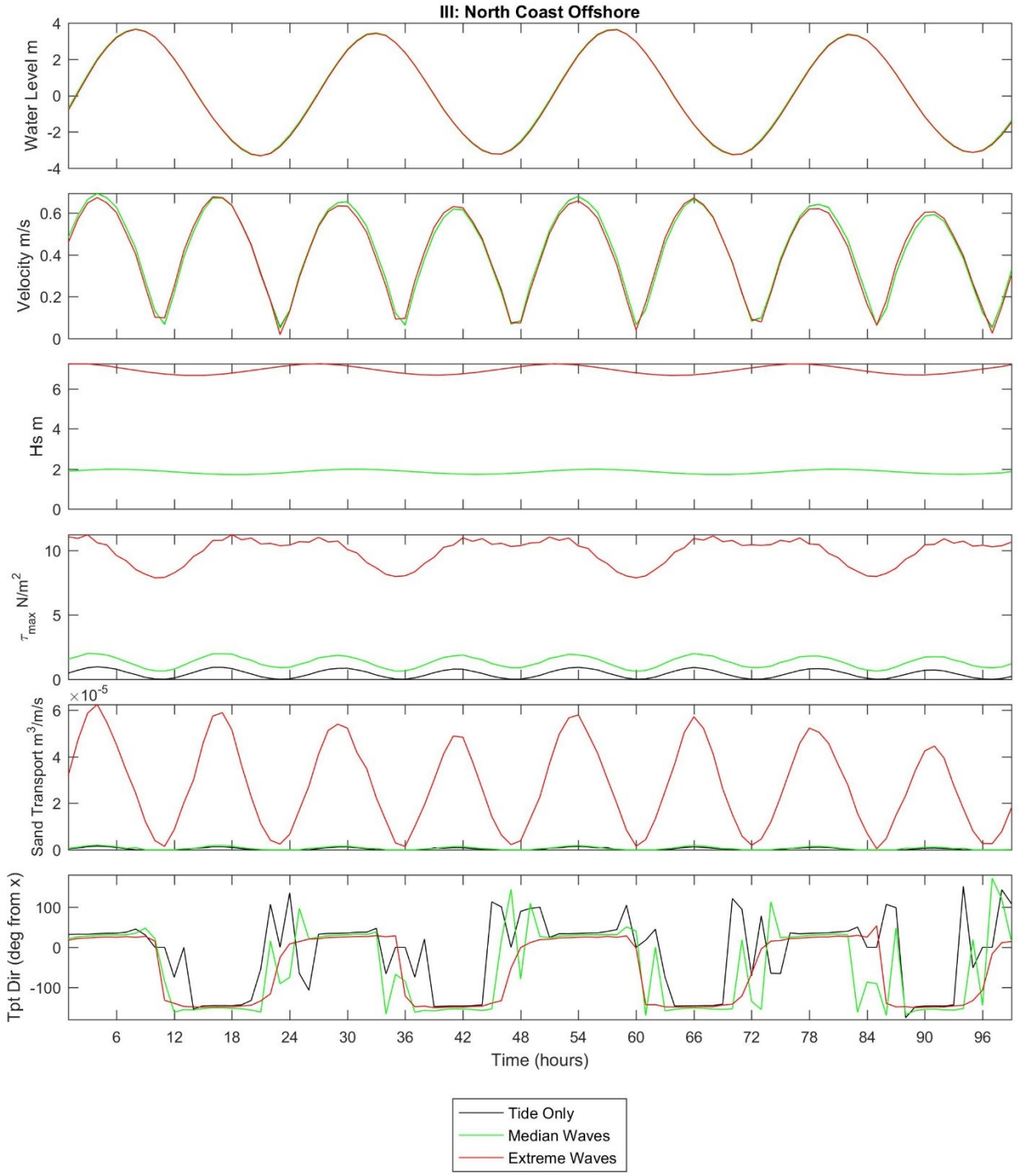

Figure A5: Hydrodynamic, wave and sand transport parameters for point III shown in Figure 9 (Section 2.5.1). Tide only (black), median wave (green) and extreme wave (red) conditions are shown for WNW waves at spring tide. Direction is degrees anticlockwise from East.

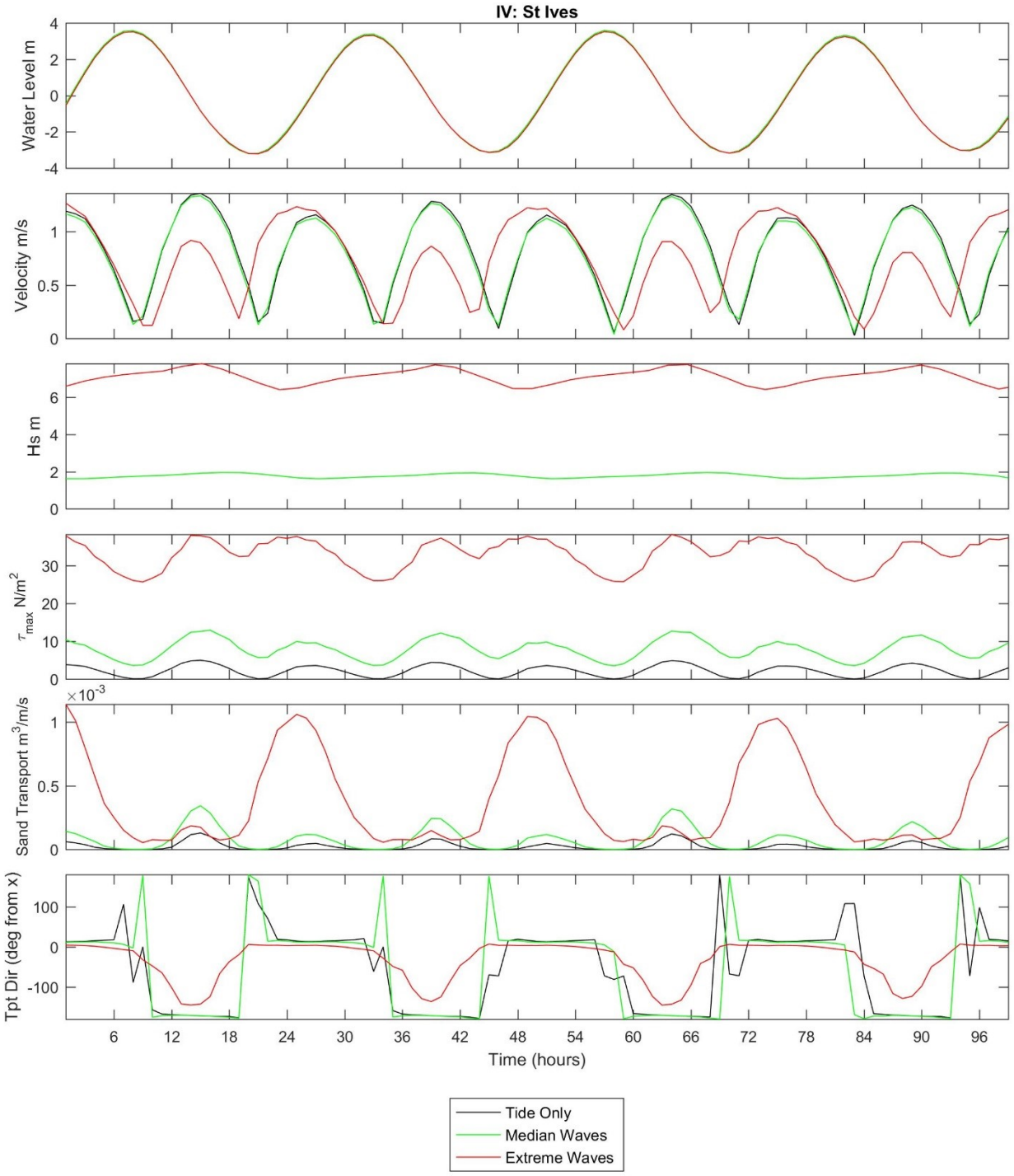

Figure A6: Hydrodynamic, wave and sand transport parameters for point IV shown in Figure 9 (Section 2.5.1). Tide only (black), median wave (green) and extreme wave (red) conditions are shown for WNW waves at spring tide. Direction is degrees anticlockwise from East.

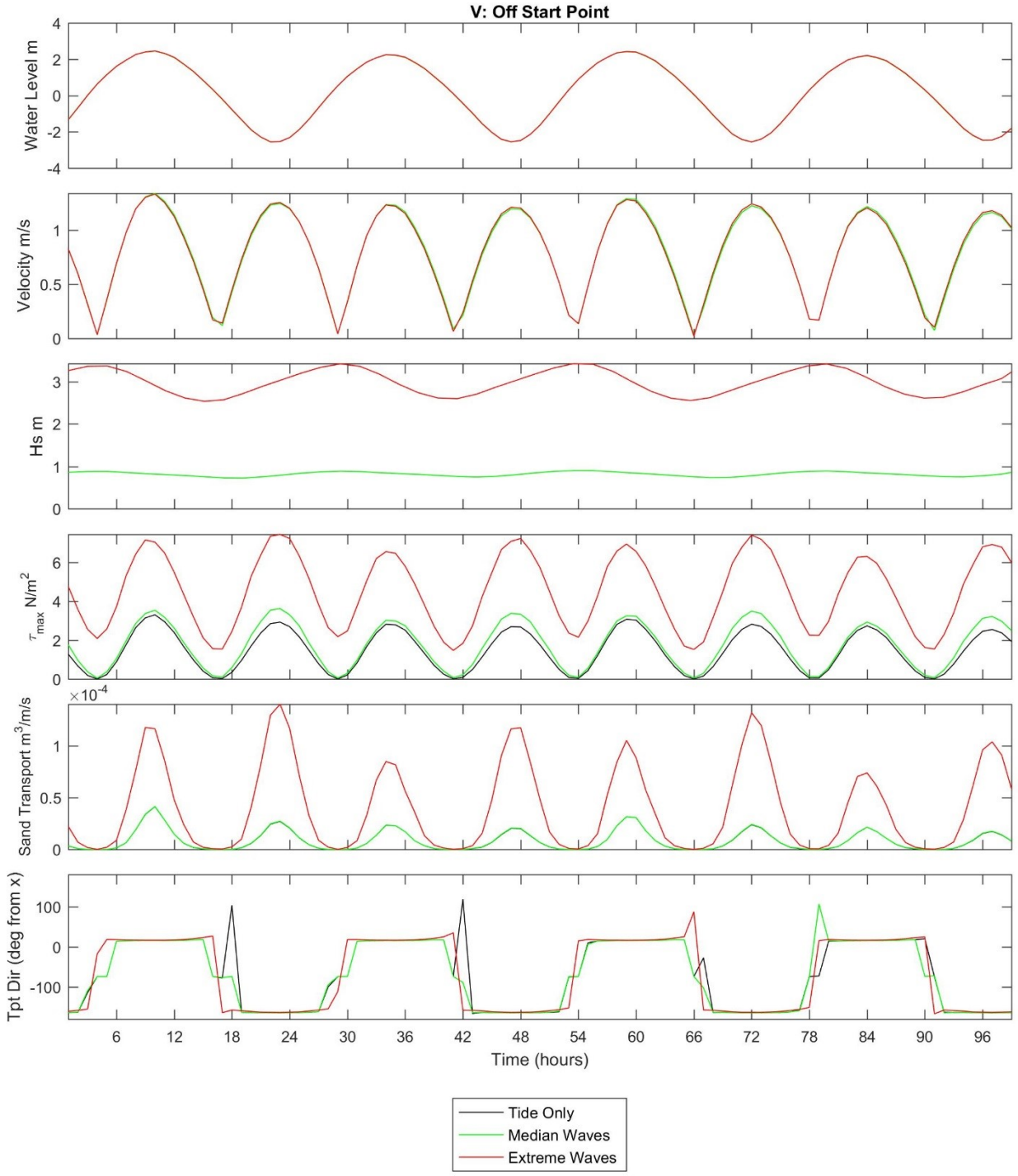

Figure A7: Hydrodynamic, wave and sand transport parameters for point V shown in Figure 9 (Section 2.5.1). Tide only (black), median wave (green) and extreme wave (red) conditions are shown for WNW waves at spring tide. Direction is degrees anticlockwise from East.

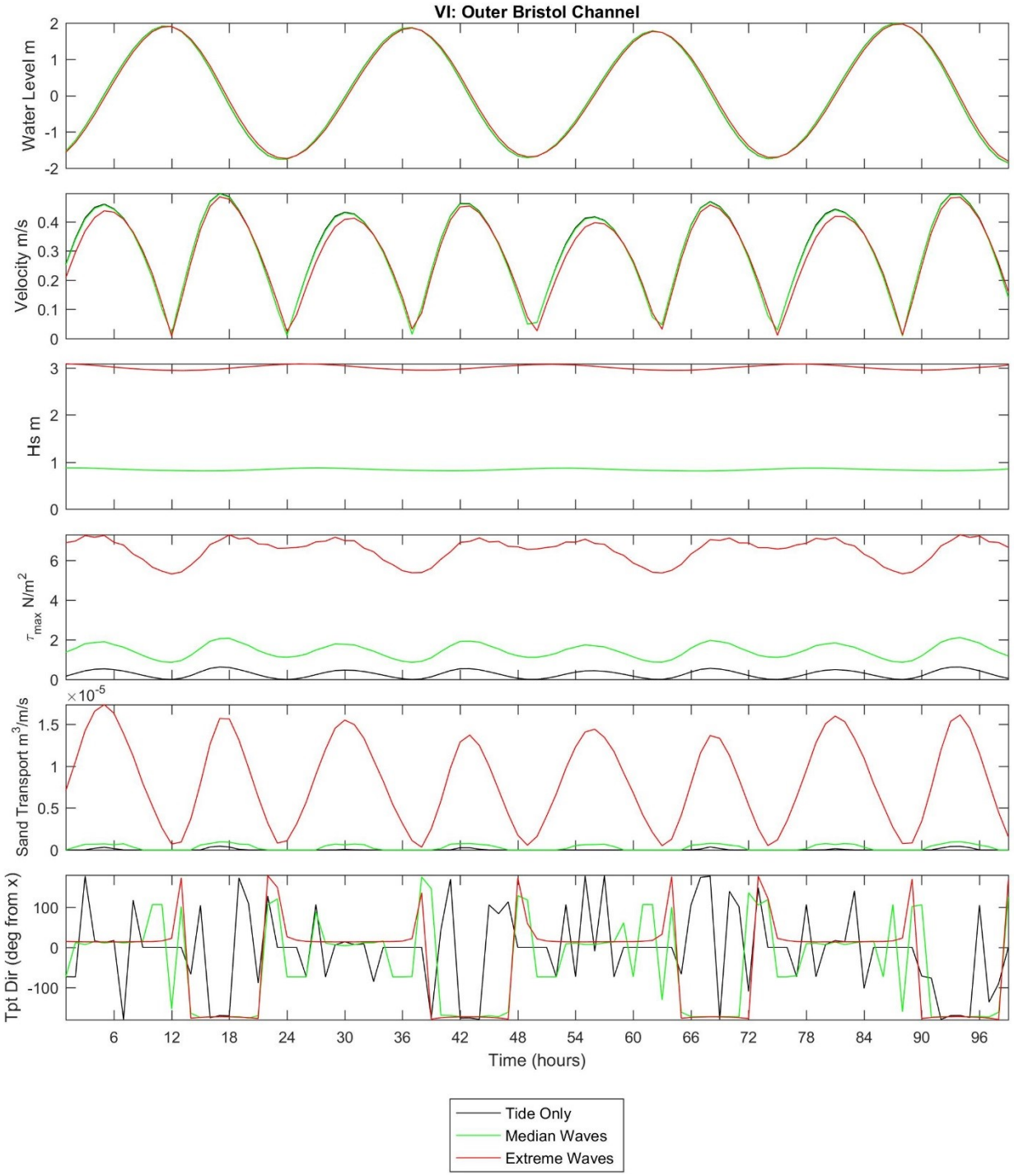

Figure A8: Hydrodynamic, wave and sand transport parameters for point VI shown in Figure 9 (Section 2.5.1). Tide only (black), median wave (green) and extreme wave (red) conditions are shown for WNW waves at neap tide. Direction is degrees anticlockwise from East.

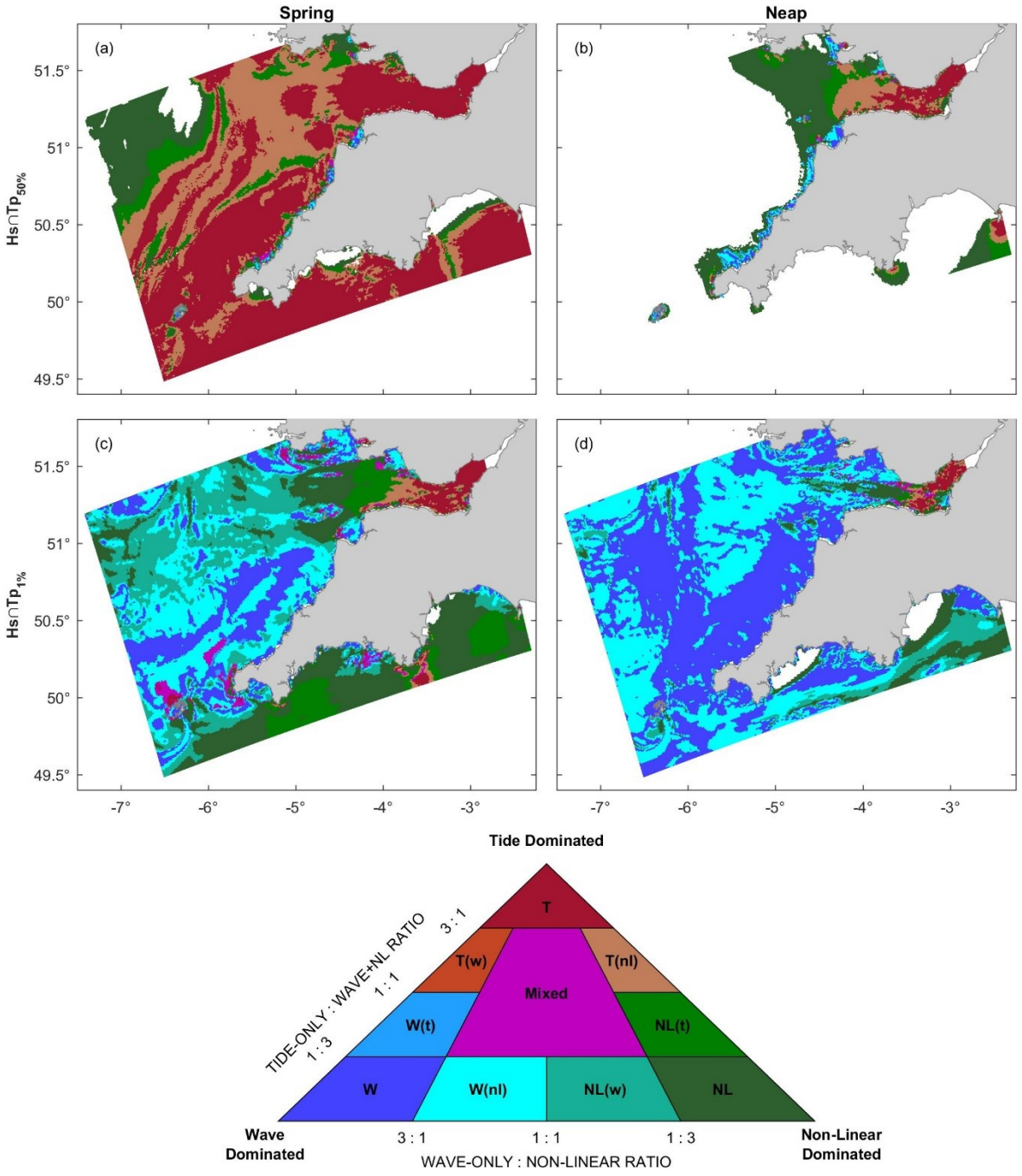

Figure A9: Wave-tide dominance classification of the South West UK during different wave and tide forcing for the 3D scenarios, accounting for the relative influence of non-linear wave-tide interactions. Based on potential net sand transport magnitude per tidal cycle. Areas where wave+tide sand transport was < 0.00016m^3/m/cycle have been removed based on the transport formulation validation in van Rijn (2007b).

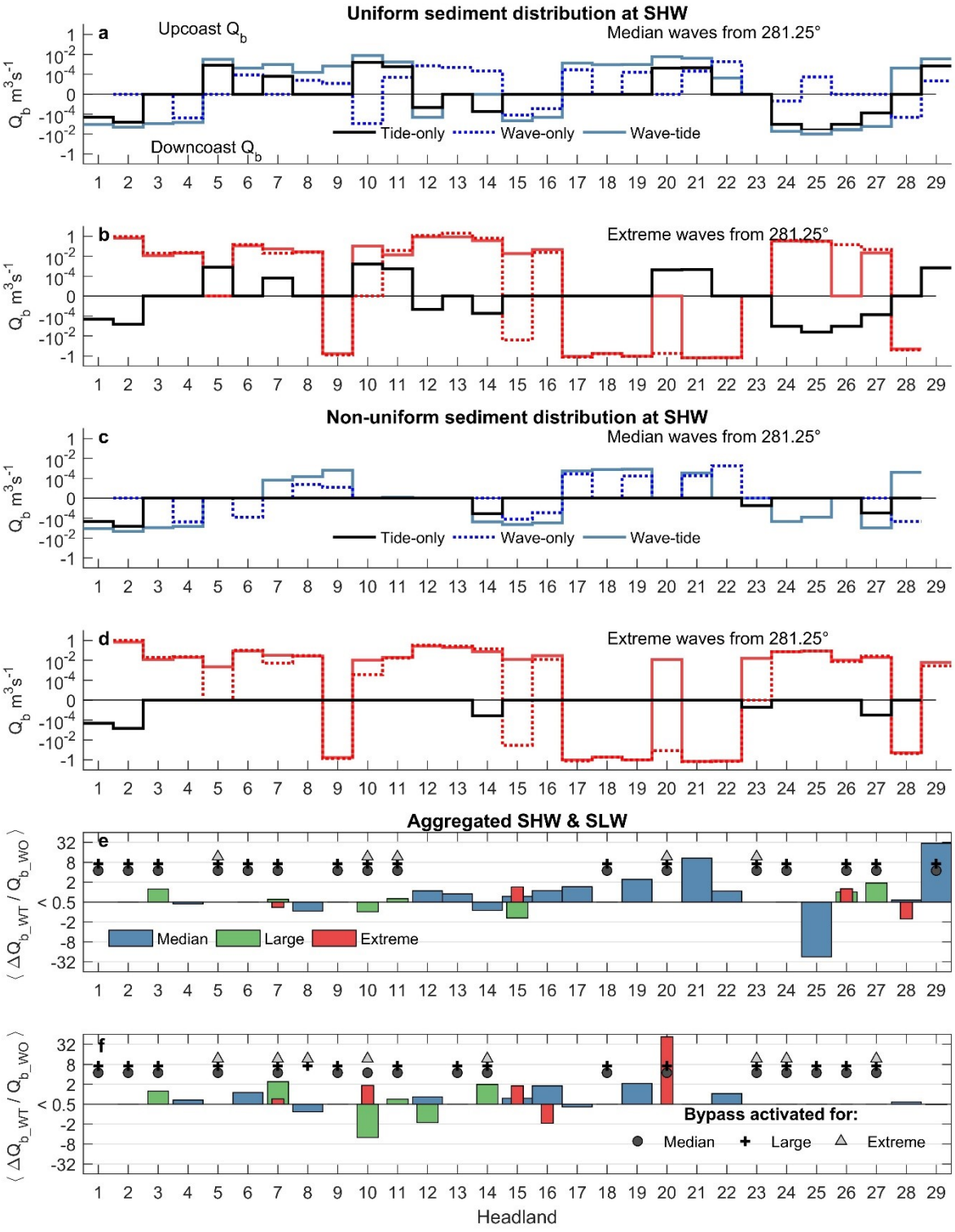

Figure A10: Comparison between tide-only, wave-only and wave-tide bypassing rates, for waves from the modal wave direction 281.25°. Instantaneous bypassing rates are presented for median and extreme waves for uniform sediments (a, b) and non-uniform sediments (c, d) for tide-only (black solid line), wave-only (coloured solid line) and wave-tide (coloured dashed line). Positive values represent upcoast bypassing, and downcoast bypassing for negative values. Values are for each headland. (e, f) Relative differences for uniform sediments (e) and non-uniform sediments (f) per headland. Values are an average over all water levels and wave directions. Bars are coloured for each wave condition. Symbols indicate wave conditions where bypassing was activated by wave-tide forcing Q_{b_WT} but not by wave only forcing Q_{b_WO} for at least one condition. The y-scale increases in $\log_2$ increments.

Appendix B: North Coast Model Parameters

Table A1: Hydrodynamic physical parameters.

Parameter	Value	Units
Horizontal eddy viscosity	1	$m^2 s^{-1}$
Horizontal eddy diffusivity	10	$m^2 s^{-1}$
Gravitational acceleration	9.81	$m s^{-2}$
Water density	1025	$kg m^{-3}$
Water temperature	15	°C
Salinity	35	PPT
Wave related bottom stress formulation	Fredsøe (1984)	-
Wind drag coefficients	$2e^{-3}$, 0, $7.23e^{-3}$, 100, $7.23e^{-3}$, 100	-,$m s^{-1}$
Air density	1	$kg m^{-3}$
Spiral motion	Included in 3D hydrodynamics	-
Bottom friction formulation	Manning	-
Bottom friction coefficient u, v	$2.75e^{-2}$, $2.75e^{-2}$	$s m^{-1/3}$
Drying/ flooding threshold depth	0.05	m

Table A2: Hydrodynamic numerical parameters.

Parameter	Value	Units
Computational time step	0.2	mins
Iterations in continuity equation	2	-
Number of sigma layers	10	-
Sigma layer thickness (surface – bed)	20,20,15,12,10,8,6,4,3,2	% depth
If depth < threshold, set whole cell to dry	YES	-
Depth determination at water level points when all vertices wet	MEAN	-
Depth determination at velocity points when all vertices wet	MEAN	-
Drying/ flooding threshold	0.05	m
Marginal depth in shallow areas	-999	m
Smoothing time at start of simulation	1440	mins
Numerical method for advective terms	Cyclic-method	-
Numerical method for momentum terms	Cyclic	-
Output storage time interval	60	mins
Communication time interval with WAVE	60	mins

Table A3: Wave physical processes and parameters.

Process/ Parameter	Value	Units
Water level correction	0	m
Water levels	From FLOW	-
Currents	From FLOW	-
Gravitational acceleration	9.81	$m\ s^{-2}$
Water density	1025	$kg\ m^{-3}$
North direction	90°	Cartesian
Minimum depth	0.05	m
Physics	3rd Generation	-
Wave breaking	true	-
Alpha coefficient for wave breaking	1	-
Gamma coefficient for wave breaking	0.73	-
Non-linear triad interactions	true	-
Triad alpha proportionality coefficient	0.1	-
Triad beta max frequency ratio	2.2	-
Bed friction formulation	Madsen et al. (1988)	-
Bed friction coefficient	0.05	$m^2\ s^{-3}$
Diffraction	false	-
Wind growth	false	-
Whitecapping formulation	Komen (1984)	-
Quadruplets	false	-
Refraction	true	-
Frequency shifting	true	-
Method of wave force computation	dissipation 3d	-

Table A4: Wave numerical parameters.

Process/ Parameter	Value	Units
Computational mode	Non-stationary	-
Computational time step	10	mins
Discretisation in directional space	0.5	-
Discretisation in frequency space	0.5	-
Relative change of wave height or mean wave period with respect to local value	0.05	-
Relative change of wave height with respect to model-wide average wave height	0.05	-
Relative change of mean wave period with respect to model-wide average mean wave period	0.05	-
Percentage accuracy criteria	98	%
Maximum number of iterations	15	-
Directional resolution	10	°
Frequency min, max	0.05, 1	Hz
N frequency bins	24	-

Appendix C: Skill Metrics

Skill was assessed using the following metrics: R^2, *BIAS*, mean absolute error *MAE*, Willmott Index of Agreement *WIA* and Brier Skill Score *BSS*. This appendix covers the calculation of the *BIAS*, *MAE*, *WIA*, and *BSS* metrics. *BIAS* was determined as:

$$BIAS = \frac{\sum_{i=1}^{n}(P_i - O_i)}{n}, \tag{A1}$$

Where P_i is the i^{th} model prediction and O_i is the i^{th} observed value, n is the total number of data points for comparison. *MAE* was determined as:

$$MAE = \frac{\sum_{i=1}^{n}(|P_i - O_i|)}{n}, \tag{A2}$$

WIA (Willmott et al., 2012) is given by:

$$WIA = \begin{cases} 1 - \dfrac{\sum_{i=1}^{n}|P_i - O_i|}{2\sum_{i=1}^{n}|O_i - \bar{O}|}, when \\ \sum_{i=1}^{n}|P_i - O_i| \leq 2\sum_{i=1}^{n}|O_i - \bar{O}| \\ \dfrac{2\sum_{i=1}^{n}|O_i - \bar{O}|}{\sum_{i=1}^{n}|P_i - O_i|} - 1, when \\ \sum_{i=1}^{n}|P_i - O_i| > 2\sum_{i=1}^{n}|O_i - \bar{O}| \end{cases}, \tag{A3}$$

Where $\bar{P}$ and $\bar{O}$ are the mean prediction and observation, respectively. *WIA* varies from -1 to 1, indicating the magnitude of the summed predictive error relative to the summed observed deviations about the mean observation. A value >0 indicates the summed error magnitudes is less than the summed magnitude of the observed variation about the mean (by half for *WIA* = 0.5).

BSS is determined following Davidson et al., (2010) as:

$$BSS = 1 - \frac{\langle (|P_i - O_i| - \epsilon)^2 \rangle}{\langle (|F_i - O_i|)^2 \rangle} \quad \text{(A4)}$$

Where F_i represents the i^{th} value interpolated from a linear fit to the observation data and ε is the observation error. Observation errors used were 0.1 m for H_s, 1 s for T_p, 5° for direction and 0.02 ms^{-1} for currents, in accordance with McCarroll et al., (2018). Angle brackets represent the time mean.